

DISS. ETH No. 19297

Lattice QCD at strong coupling: thermodynamics and nuclear physics

A dissertation submitted to

ETH ZURICH

for the degree of
Doctor of Sciences

presented by

Michael Fromm

Dipl. Phys., Eberhard-Karls-University, Tübingen
born 13. March 1981
citizen of Germany

accepted on the recommendation of

Prof. Dr. M. Troyer, examiner
Dr. Ph. de Forcrand, co-examiner
Prof. Dr. U.-J. Wiese, co-examiner

2010

Abstract

QCD, the theory of strong interactions between quarks and gluons, describes accurately the physics of a single hadron, the color-singlet bound state of quarks and gluons. It should also describe the residual, van der Waals-like interactions between hadrons, i.e. nuclear physics. To study nuclear physics from first principles, that is from QCD, present day non-perturbative approaches are effective theories and Lattice QCD. The latter relies on the probabilistic interpretation of the measure that characterizes the QCD partition function. In the presence of a finite density of nucleons (baryons) or, equivalently, at finite baryon chemical potential the positivity of the measure is lost and the minus-sign problem arises. To study systems containing only a few baryons already requires an immense computational effort and the approach is essentially reserved to only a few large collaborations worldwide.

The strong coupling limit considered in the larger part of this thesis neglects the gauge part of the Lattice QCD action as the inverse bare gauge coupling is set to zero. While in principle this implies “infinite coarseness” of the lattice and the presence of large lattice artifacts, it allows us to bypass the conventional numerical approach as its advantage is threefold: Firstly in our model gauge fields can be integrated out exactly. A good part of the sign fluctuations of the path integral measure at finite chemical potential is exactly taken into account rather than probabilistically. The minus-sign problem is thus milder in the resulting model. Secondly, integration over the gauge fields immediately results in a formulation of the system in color-singlet degrees of freedom - the mesons and baryons. This makes the interpretation of the results more transparent. Thirdly, with these degrees of freedom the model can be formulated as a loop gas. Recent algorithmic developments like the worm algorithm allow to sample such a system with high efficiency.

The main part of the thesis is thus devoted to Lattice QCD at strong coupling with $N_f = 1$ flavor of staggered quarks. With the help of the worm algorithm and the snake algorithm we uncover the strong coupling variant of nuclear physics by measuring the nucleon-nucleon potential precisely. Our potential shows essential features such as a repulsive hard core and a medium-range attraction. Eventually, by considering the perturbation of the pion gas caused by the nucleon, we are able to show that the nuclear potential is of Yukawa form at large distances. Using a similar technique we further study composite objects of nucleons, the nuclei of our model, and find their mass to fall on top of the curve predicted by the phenomenological Bethe-Weizsäcker mass formula. In addition, due to the mild sign problem, we can determine the phase diagram of our model in the whole (μ_B, T) -plane and determine the location of the tricritical point predicted by mean-field theory. Giving the quark mass nonzero values, we

observe that the behavior of the QCD critical point is in agreement with the scaling prediction of the classical theory. Finally, we extend our study of strong coupling QCD to $N_f = 2$ flavors. There, contrary to the one-flavor case where the explicit expression of the partition function formulated in color singlet degrees of freedom was long known, these preparatory steps have to be carried out. We explicitly map the partition function for gauge group $U(N = 2, 3)$ to that of a dimer model in a way easily generalizable to higher N_f . Doing so, we uncover a sign problem which we are however able to tame by practical methods. This opens the way to the study of nuclear physics in the presence of up and down quarks.

Zusammenfassung

Die Theorie der starken Wechselwirkung zwischen Quarks und Gluonen, Quantenchromodynamik (QCD), beschreibt die Physik der Hadronen, also der farblosen Bindungszustände von Quarks und Gluonen. Die Theorie sollte aber auch die daraus resultierende, Van-der-Waals-ähnliche Wechselwirkung *zwischen* den Hadronen beschreiben, also auch die Kernwechselwirkung. Modern Ansätze um Kernphysik mit der ihr zugrundeliegenden Theorie (QCD) zu behandeln, sind sogenannte Effektive Theorien und Gitter-QCD. Letztere beruht auf der Interpretation des Maßes der Zustandssumme als Wahrscheinlichkeitsmaß. Bei endlicher Baryondichte oder endlichem chemischen Potential ist dieses Maß aber nicht mehr positiv semi-definit und man spricht vom Vorzeichenproblem. Um Systeme mit nur wenigen Baryonen zu untersuchen, benötigt man einen immensen Rechenaufwand, so daß dieser Zugang eigentlich nur den großen Kollaborationen weltweit vorbehalten ist.

Im Grenzwert unendlicher Eichkopplung, wie in dieser Arbeit betrachtet, kann man jedoch den Eichanteil der Wirkung, welche im Wahrscheinlichkeitsmaß auftritt, vernachlässigen. Obwohl dies grundsätzlich eine unkontrollierbare Approximation darstellt, da es eine Diskretisierung mit unendlicher Gitterkonstanten impliziert, so erlaubt es uns doch den herkömmlichen numerischen Weg zu verlassen und folgende Vorteile zu nutzen: Erstens können im Limes unendlicher Eichkopplung die Eichfelder *exakt* ausintegriert werden. Ein guter Teil der Fluktuationen des Maßes der Zustandssumme bei endlichem chemischen Potential ist damit exakt berücksichtigt worden und nicht nur probabilistisch. Das Vorzeichenproblem des daraus entstehenden Modells ist daher schwächer. Zweitens kann die Theorie durch die Integration über Eichfelder in den farblosen, hadronischen Freiheitsgraden — den Mesonen und Baryonen — formuliert werden. Drittens wird das Modell in dieser Formulierung zu einem “loop-gas”-Modell, welches z.B. mit dem “worm”-Algorithmus effizient simuliert werden kann.

Der Hauptteil dieser Arbeit beschäftigt sich also mit Gitter-QCD bei unendlicher Eichkopplung, speziell für den Fall nur eines Flavors ($N_f = 1$) von elementaren Kogut-Susskind-Fermionen. Mit Hilfe des worm-Algorithmus und des “snake”-Algorithmus untersuchen wir die daraus resultierende Kernphysik und bestimmen insbesondere das Zweikörperpotential. In der Tat besitzt dieses Potential wichtige Charakteristika wie z.B. eine starke Repulsion für kleine Abstände und einen attraktiven Anteil bei mittleren Distanzen. Betrachtet man schließlich die Störung der bosonischen Freiheitsgrade durch ein statisches Baryon, so kann man zeigen, daß das Potential die Form eines Yukawa-Potentials für große Distanzen besitzt.

Mit den genannten Algorithmen lassen sich aber auch aus Baryonen zusammengesetzte Objekte (Kerne) untersuchen. Die Masse dieser Kerne wird in der Tat durch die semi-phänomenologische Bethe-Weizsäcker-Formel beschrieben.

Darüber hinaus untersuchen wir das Phasendiagramm unseres Modells für endliche Temperatur und Dichten im chiralen Limes, d.h. für masselose Quarks. Insbesondere finden wir einen trikritischen Punkt, welcher bereits von der Molekularfeld-Theorie vorhergesagt wurde. Im Falle massiver Quarks untersuchen wir das Verhalten des dann auftretenden kritischen Punktes und finden, daß es in der Nähe des trikritischen Punktes durch die klassische Landau-Theorie beschrieben wird.

Schließlich wenden wir uns der Erweiterung des Modells zu $N_f = 2$ Quark-Flavors zu. Wir schreiben hierzu die Gitter QCD-Zustandssumme als Zustandssumme eines “dimer”-Modells.

Jedoch finden wir selbst für eine rein bosonische Theorie (Eichgruppe $U(N = 2, 3)$) ein Vorzeichenproblem, welches sich aber durch praktische Methoden wenn nicht lösen, so doch gut kontrollieren läßt. Diese Schritte schaffen die Voraussetzung, nun auch die resultierende Kernphysik für $N_f = 2$ Flavors, d.h. mit “up” - und “down”-Quarks zu untersuchen.

Contents

1	Motivation and outline	1
2	Introduction	5
2.1	QCD Lagrangian, symmetries	7
2.2	QCD on the lattice	9
2.2.1	Discretizing the gauge action	9
2.2.2	Fermions on the lattice	11
2.2.3	Finite temperature and chemical potential	14
2.3	Some concepts in statistical mechanics	15
2.3.1	Tricriticality	16
2.3.2	The worm algorithm for classical spin models	19
3	Tricriticality in the $q = 3$ Potts model for $d = 2 + 1$	25
3.1	Introduction	25
3.2	The Potts model	26
3.2.1	Conjectured behavior	26
3.2.2	Tricriticality	27
3.3	Numerical Experiments	28
3.3.1	Observables and results	28
3.4	Conclusion	33
4	Nuclear physics from Lattice QCD at strong coupling	35
4.1	Partition function, worm formulation, cross checks	35
4.1.1	Partition function	35
4.1.2	The worm algorithm in strong coupling QCD	40
4.1.3	Consistency checks	46
4.2	Mean field results, symmetries, earlier results, μ_c puzzle	49
4.2.1	Mean-field results	49
4.2.2	Determination of the baryon mass m_B by Monte Carlo	54
4.2.3	Qualitative understanding of the baryon mass m_B	56
4.2.4	Determination of $\mu_{B,c}$	59
4.3	Nuclear Physics at strong coupling	59
4.3.1	The nucleon-nucleon potential V_{NN} at strong coupling	59
4.3.2	Nuclear matter at strong coupling	62
4.3.3	The size of a nucleon	65
4.4	Summary and Conclusions	69
5	Phase diagram of Lattice QCD at strong coupling	71
5.1	Introduction, early work, expectations	71
5.1.1	Symmetries and expected phases, connection to real QCD	71

5.1.2	Existing mean-field and Monte-Carlo results	72
5.2	Results in the chiral limit, $\mathbf{am}_q = \mathbf{0}$	77
5.2.1	Observables	77
5.2.2	Results	80
5.2.3	Sign problem	83
5.3	Results for $\mathbf{m}_q > \mathbf{0}$	85
5.3.1	Results	87
5.4	Summary and Conclusions	88
6	Strong coupling Lattice QCD with $N_f = 2$ flavors	91
6.1	Motivation	91
6.2	Partition function for gauge group \mathbf{G} and N_f flavors	92
6.2.1	$\mathbf{G} = \mathbf{U}(\mathbf{3})$	93
6.2.2	Taming the sign problem	97
6.3	Conclusions	99
7	Outlook	101
8	Appendix	1
8.1	One-link integral, $N_f = 1$	1
8.2	One-link integral, $N_f = 2$	3
8.2.1	$\mathbf{G} = \mathbf{U}(\mathbf{3})$	3
8.2.2	$\mathbf{G} = \mathbf{U}(\mathbf{2})$	6
8.3	A useful relation	7
8.3.1	Relating the decay mass M and the continuum pole mass m	7
8.4	Algorithmic details	8
8.4.1	Resummation in the MDP-algorithm	8
8.4.2	Proving detailed balance for the mesonic worm	9
8.4.3	Mesonic worm estimators	12
	Bibliography	17
	List of Figures	21
	List of Tables	25

1 Motivation and outline

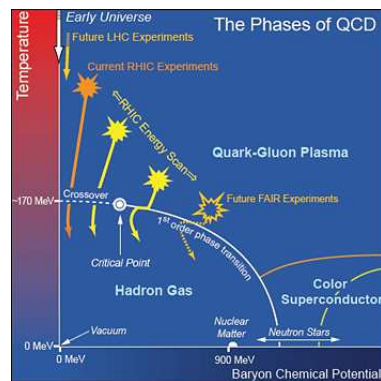
Quantum Chromodynamics (QCD), the theory of the strong force, describes the interactions between quarks and gluons. At low temperature QCD predicts confinement, i.e. quarks and gluons can only occur in bound states (baryons, mesons, glueballs) whose color charge is zero, see Fig.1.1(a). On the other hand, baryons such as protons and neutrons as well as compound objects of baryons, the nuclei, interact. This nuclear interaction is a residual interaction resulting from the strong force between hadronic composites. Nuclear physics should therefore be described by QCD if we neglect the effects due to weak and electromagnetic interactions. Considering now the statistical properties of an ensemble of quarks and gluons with the temperature T and quark density ρ (or equivalently the baryonic chemical potential μ) Fig.1.1(b) shows the current conjectured phase diagram of QCD. The for this work relevant features are: At low temperature there exists a hadronic phase (of confined quarks and gluons). Nuclear matter exists at very low temperature and high chemical potential of order of the proton mass $m_p \approx 1$ GeV. The confined phase is connected by a crossover to a deconfined phase where quarks and gluons form a plasma (QGP). This crossover region is the “shadow”¹ of an approximate symmetry restoration and may turn into an actual transition of first or second order at higher chemical potential.

Coming to the theoretical approaches to solve QCD, the situation is as follows: QCD cannot

¹Numerical results support the existence of two nearly coincident crossover phenomena: one corresponds to the deconfinement transition, the other restores what would be a chiral symmetry in the limit of massless quarks.



(a)



(b)

Figure 1.1: (a) Sketch of a baryon and a meson, bound states of three and two quarks, respectively. (b) The conjectured QCD phase diagram featuring a hadronic, QGP and color superconducting phase as well as a deconfinement transition of first order ending in the QCD critical endpoint. The picture has been taken from [1].

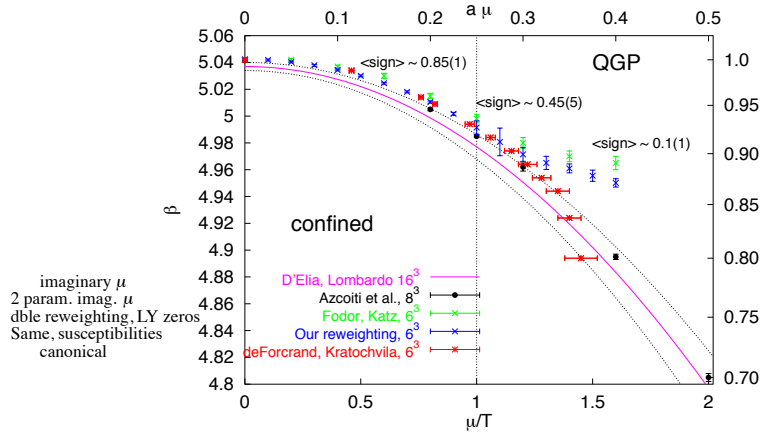


Figure 1.2: The QCD phase diagram [2] as obtained by various lattice methods, all restricted to $\mu/T \leq 1$. Also shown is the severity of the sign problem encoded in the average sign $\langle \text{sign} \rangle$ which approaches zero when going to the right.

be solved with perturbative methods for a wide range in temperature and chemical potential (in particular at low T and μ) because its coupling constant is large. One therefore has to revert to non-perturbative methods.

On the numerical side, Lattice QCD discretizes space-time and uses Monte-Carlo methods to evaluate the QCD functional integral. At zero chemical potential this approach is successful in that it predicts for example the above mentioned finite temperature crossover to the deconfined phase [3, 4] and can also obtain the zero temperature spectrum of the theory [5]. But the QCD functional is a functional of bosons (gluons) and fermions (quarks). Mathematically, the latter are integrated over, yielding a contribution to the path integral measure that can take complex, i.e. not real-positive, values at non-zero chemical potential. Monte-Carlo methods relying on the probabilistic interpretation of this measure fail. This *sign problem* when dealing with fermionic systems is ubiquitous, also appearing for example in the fermionic Hubbard model of condensed matter physics.

For the QCD phase diagram a summary of different approaches of Lattice QCD to determine the critical line of the finite temperature, finite chemical potential transition is shown in Fig. 1.2, taken from [2]. Avoiding direct numerical simulations at $\mu > 0$ because of the sign problem, alternative techniques were used: The fermionic measure turns out to be real for imaginary μ , thus allowing for Monte-Carlo simulations. The results on the critical line can be fitted with an ansatz which is continued to $\mu^2 > 0$. Alternatively, one can use the fact that a statistical ensemble at $\mu = 0$ (i.e. in the absence of the sign problem) contains information about the sector $\rho > 0$ which is made visible by *reweighting* its statistical weight. Note however that these various attempts are all restricted to small physical volumes and to the region $\mu/T \lesssim 1$ due to the sign problem.

In view of the non-perturbative character of QCD and the failure of Monte-Carlo methods for full Lattice QCD at finite density, the possible alternatives are effective models. For the phase diagram these are models with four-fermi interaction [6] like the NJL-model or random matrix models, see [7, 8] for an overview.

Here we instead consider a “toy” model of QCD: Lattice QCD in the limit of infinite bare gauge coupling as first studied numerically by Karsch & Mütter [9]. There are numerous reasons to pursue a study of this model. Firstly, Karsch et al. showed that the sign problem at finite

chemical potential is not an obstacle any more in this parameter regime and high densities of nuclear matter could be reached with what are now table-top computing resources.

Secondly, even though the model is obtained as unphysical limit of the full Lattice QCD Lagrangian, the main non-perturbative properties of QCD, confinement and chiral symmetry breaking, are preserved. We can therefore gain qualitative insight into the QCD phase diagram. Thirdly, the model has been a theoretical playground for 30 years now, starting with mean-field approaches [10] continuing up to now [11]. The approximate theoretical predictions should be checked against numerical methods using exact algorithms.

Furthermore, it is possible, in the future, to systematically approach a relevant parameter regime (albeit with yet unknown computer effort) by means of inclusion of corrections to strong coupling action.

Finally, apart from the above motivation, the strong coupling limit turned out also to be physically interesting, as Karsch et al. found that the model has a strong first order phase transition at low temperature and finite chemical potential, separating a phase of dilute hadrons from that of dense nuclear matter. Interestingly, this transition appeared at a value of μ_B considerably smaller than the measured baryon mass m_B in lattice units, $\mu_{B,c} < m_B$. Using mean-field theory the finite density transition was investigated earlier [12] with similar results, but it was only realized later [13, 14] that this apparent mismatch must be due to a strong nuclear attraction in this model.² This fact essentially triggered the investigation leading to this thesis as strong coupling QCD promised to be an excellent laboratory of nuclear interactions which seemed to be considerably enhanced in this limit.

The outline of this work is the following: in Ch.2 we give the necessary concepts and introduce QCD, its symmetries and formulation on the lattice. On the side of statistical mechanics we discuss tricriticality and introduce the worm algorithm for classical statistical spin models.

Ch.3 is devoted to a study of the $q = 3$ Potts model. Not only is the model important due to its Z_3 symmetry, shared with $SU(3)$ -Yang-Mills on the lattice, but we also practice the finite size scaling, which is the essential tool to study pseudo-phase transitions in a finite volume. It also serves to familiarize ourselves with the worm algorithm.

Ch.4 contains the main part of the thesis: The nuclear physics content of Lattice QCD at strong coupling. After introduction of the formalism at infinite gauge coupling and a summary of mean-field predictions, we present results on the nucleon-nucleon potential and the masses of nuclei at strong coupling. We conclude the chapter by investigating the origin of nuclear interactions in this model.

In Ch.5 the phase diagram at strong coupling will be presented. Of particular interest are the tricritical point predicted by mean-field theory in the chiral limit, and the critical endpoint for nonzero quark mass.

Finally, Ch.6 concerns the extension of the model to $N_f > 1$. The formalism to map the partition function to a dimer model for more than one quark flavor is presented and a resulting sign problem discussed. We conclude the thesis with an outlook on future directions in Ch.7.

²Contrary to nature where the transition is expected at $\mu_{B,c} \approx m_B$ due to the large difference in the scale of the baryon mass of $\mathcal{O}(1)$ GeV and nuclear binding energies which add up to only a few MeVs.

2 Introduction

According to the standard model of particle physics (see Fig.2.1(a)) three out of the four fundamental interactions¹ — the weak, the electromagnetic and the strong interaction — arise from the exchange of gauge bosons between fermionic matter fields. The fermionic sector contains the six leptons e^- , ν_e , μ^- , ν_μ , τ^- , ν_τ and their antiparticles which do not take part in the strong interactions but feel the electro-weak force mediated by the W^\pm and Z_0 bosons on the weak side and the photon on the electromagnetic side. Fermions that do feel the strong force mediated by the gluons G^a ($a = 1, \dots, 8$) are the $N_f = 6$ quarks denoted by u, d, s, c, b, t which themselves form bound states subject to the strong interactions (hadrons).

As an example of some gauge boson mediated process involving many of the elementary particles of the standard model, Fig.2.1(b) shows a diagram corresponding to beta decay of a neutron n to a proton p , an electron e and its antineutrino $\bar{\nu}_e$. This process involves the W^- -boson.

In quantum field theory, the strength of the interaction is expressed by coupling constants or

¹A formulation of gravity as quantum field theory has yet to be found.

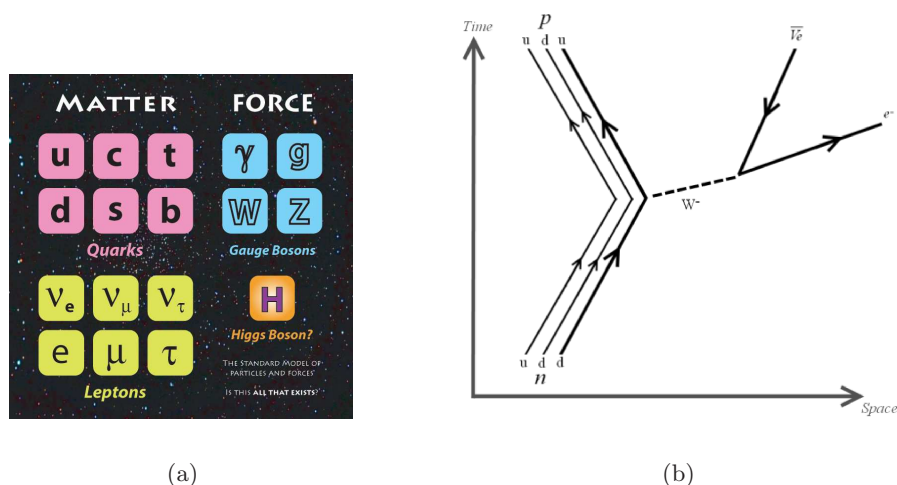


Figure 2.1: (a) The particle content of the Standard Model. Three generations of quarks and leptons, respectively, make up matter. Fundamental force carriers are the gauge bosons. The origin of the elementary particle masses is only effectively understood by means of spontaneous symmetry breaking involving the Higgs boson, the search for which is currently ongoing at the Large Hadron Collider. The table was taken from [15]. (b) Beta decay $n \rightarrow p + e^- + \bar{\nu}_e$ as an example of a process mediated by a (weak) gauge boson involving many of the elementary particles of (a). The diagram figure was taken from [16].

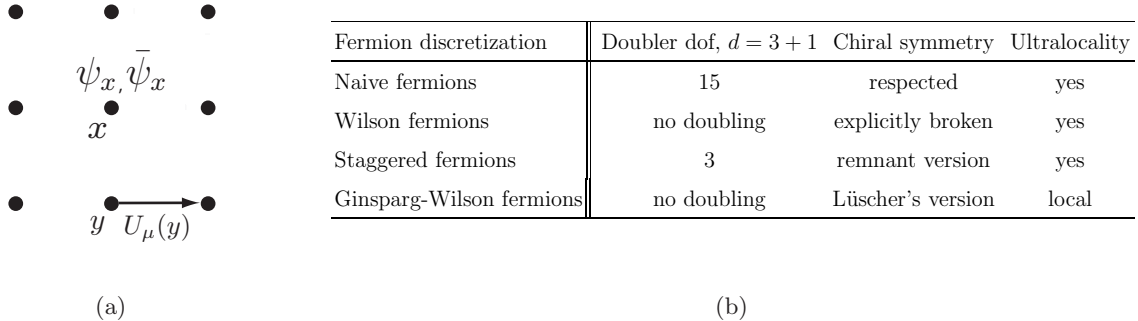


Figure 2.2: (a) A simple hypercubic lattice with fermionic matter fields $\psi_x, \bar{\psi}_x$ defined on lattice sites and gauge bosons $U_\mu(x)$ located on the links connecting these sites. (b) Overview of possible choices of discrete fermions currently used: We use the staggered formalism, offering a compromise between the computational cost, symmetry properties and the number of (unwanted) doubler degrees of freedom.

charges e, g_w, g_s of the elementary particles with respect to the interaction. These “constants” depend however on the distance or energy scale μ of the interaction. For instance, while the coupling constant of Quantum Electrodynamics (QED) is measured at the scale of the electron mass $m_e \approx 0.5$ MeV using the Josephson effect to give $\alpha(m_e) = \frac{e^2}{4\pi} \approx \frac{1}{137}$, when “run up” to the scale of the W^\pm , $m_W \approx 80$ GeV, it is $\alpha(m_W) \approx \frac{1}{128}$. Thus, it increases at shorter distances but still remains small, s.t. QED can be treated by perturbative methods which rely on the expansion of physical quantities in terms of $\alpha(\mu)$. In contrast, for Quantum Chromodynamics (QCD), the theory underlying strong interactions, perturbative methods fail at relevant distances: When the strong coupling α_s , measured at the scale of the Z^0 -boson mass $m_Z \approx 90$ GeV to give $\alpha_s(m_Z) \approx 0.12$, is run “down” to the scale of $\mu = \mathcal{O}(100)$ MeV, it becomes “strong”, $\alpha_s \gtrsim 1$. In natural units ($\hbar = c = 1$) this mass scale defines an (inverse) length scale since $\frac{1}{\text{fm}} \approx 197.5$ MeV. The property of QCD we just described is called “infrared slavery” and implies that any perturbative calculations in α_s at the scale of the size of a baryon (1 fm) must fail. Taken in the other direction, i.e. going to smaller distance ($\ll 1$ fm), the QCD coupling vanishes logarithmically and leads to “asymptotically free” quarks and gluons. Because perturbative methods fail when applied to the low energy regime of QCD, non-perturbative (numerical) approaches have to be used.

Lattice field theory discretizes space-time and replaces the continuum theory by a theory defined on a regular, in most cases hypercubic, lattice of the appropriate dimension. The (fermionic) matter fields are now defined on lattice sites, $\psi(x) \rightarrow \psi_x$, see Fig.2.2(a). Gauge bosons carry an additional Lorentz index and are defined on the links of length a connecting neighboring sites, $A_\mu \rightarrow U_\mu(x) = \exp(iaA_\mu(x))$. This follows the prescription first chosen by K.Wilson [17] to discretize gauge theory: While the continuous Poincaré symmetry of the continuum is reduced to a discrete translational and rotational symmetry on the lattice, the gauge symmetry and thus the gauge principle is preserved. However, while the discretization of bosons is essentially straight forward, defining fermions on the lattice is accompanied by the doubling problem (see Sect.2.2.2.1): A naive discretization of fermions does not lead to the correct continuum theory one started with but rather describes additional, “double” degrees of freedom. The Nielsen-Ninomiya theorem sets up systematic constraints on the fermionic action and symmetries it possesses, eventually leading to the currently available choices of

fermions listed in Fig.2.2(b), see [18] for an overview. While the formulation using Wilson fermions completely removes doubling by adding a term to the action that corresponds to a lattice Laplacian, it explicitly breaks chiral symmetry which is only recovered in the continuum after a fine-tuning of the bare quark mass. As an example of Ginsparg-Wilson fermions we mention domain wall fermions that instead use the Wilson-Dirac operator in five dimensions and let the mass term be a particular function of the fifth dimension. This formulation removes the doubler degrees of freedom as it is the case with Wilson fermions. In addition it obeys a discrete (lattice) version of chiral symmetry that turns into the continuum version as $a \rightarrow 0$. In this work we chose the staggered formulation of fermions which is numerically the simplest to study and simulate at the cost of leaving four of the sixteen doubler fermions of the four-dimensional theory using the naive discretization.

Before we turn to a more thorough description of Lattice QCD, we shortly introduce QCD in the language of field theory in the next section. As it will be necessary for numerical computations, this is done in the Euclidean formulation, i.e. with imaginary time $t = -i\tau$.

2.1 QCD Lagrangian, symmetries

The QCD Lagrangian in Euclidean time is given by

$$\mathcal{L}_E = \frac{1}{2} \text{tr}(F_{\mu\nu} F_{\mu\nu}) + \sum_{\alpha} \bar{\psi}^{\alpha} (\gamma_{\mu} [\partial_{\mu} + igA_{\mu}] + m^{\alpha}) \psi^{\alpha} \quad (2.1)$$

where summation over a repeated index is implied and we defined the following quantities:

$F_{\mu\nu} = \partial_{\mu} A_{\nu} - \partial_{\nu} A_{\mu} + ig[A_{\mu}, A_{\nu}]$	Non-Abelian field strength for gauge group $G = SU(N)$.
$F_{\mu\nu} = F_{\mu\nu}^a t^a$	t^a are the hermitian, traceless generators of $SU(N)$.
$A_{\mu} = A_{\mu}^a t^a$	A_{μ}^a represents the (gauge) gluon field.
$\psi_i^{\alpha}, m^{\alpha}$	Quark field of bare mass m^{α} .
$a = 1, \dots, N^2 - 1$	Adjoint color index.
$i = 1, \dots, N$	Fundamental color index.
$\alpha = 1, \dots, N_f$	Flavor index.
$\mu = 0, \dots, d$	Euclidean space-time index in $d + 1$ -dimensions.
g	Bare gauge coupling.
γ_{μ}	Euclidean Dirac γ matrices fulfilling $\{\gamma_{\mu}, \gamma_{\nu}\} = 2\delta_{\mu,\nu}$, $\gamma_{\mu}^{\dagger} = \gamma_{\mu}$.

For QCD the numbers of colors is $N = 3$. The generators t^a , spanning the Lie-Algebra of $SU(3)$ with $[t^a, t^b] = if^{abc}t^c$ and structure constants f^{abc} , are then taken to be $t^a = \lambda^a/2$, where λ^a are the Gell-Mann matrices normalized s.t. $\text{tr}(\lambda^a \lambda^b) = 2\delta_{a,b}$ (see for example [19]).

We have $N_f = 6$ quark flavors in nature. The lightest (termed ‘‘up’’ (u), ‘‘down’’ (d) and ‘‘strange’’ (s)) have masses $m_u = 1.5 - 4$ MeV, $m_d = 4 - 8$ MeV and $m_s = 80 - 130$ MeV and dominate the dynamics of QCD. In the absence of the quarks, Eq.(2.1) represents a Yang-Mills theory of self-interacting gluons A_μ^a , invariant under local gauge transformations

$$A_\mu(x) \rightarrow \Omega(x)A_\mu(x)\Omega^{-1}(x) - \frac{i}{g}\Omega(x)\partial_\mu\Omega^{-1}(x) \quad (2.2)$$

with $\Omega(x) \in SU(3)$. The quark fields transform according to

$$\psi^\alpha(x) \rightarrow \Omega(x)\psi^\alpha(x), \quad \bar{\psi}(x)^\alpha \rightarrow \bar{\psi}(x)^\alpha\Omega^{-1}(x). \quad (2.3)$$

Apart from this local symmetry, for $m^\alpha = 0$ the Lagrangian Eq.(2.1) is invariant under transformations

$$\Psi \rightarrow e^{i\theta_V^a t^a + i\gamma_5 \theta_A^a t^a} \Psi, \quad \bar{\Psi} \rightarrow \bar{\Psi} e^{-i\theta_V^a t^a + i\gamma_5 \theta_A^a t^a}, \quad (2.4)$$

where we denoted by Ψ the vector in flavor space with $(\Psi)^\alpha = \psi^\alpha$, $\gamma_5 = \gamma_0\gamma_1\gamma_2\gamma_3$ and t^a are the generators of $SU(N_f)$. The massless Lagrangian further has a $U_V(1) \times U_A(1)$ symmetry

$$U_V(1) : \quad \bar{\Psi} \rightarrow \bar{\Psi} e^{-i\theta_V}, \quad \Psi \rightarrow e^{i\theta_V} \Psi, \quad (2.5)$$

$$U_A(1) : \quad \bar{\Psi} \rightarrow \bar{\Psi} e^{i\gamma_5 \theta_A}, \quad \Psi \rightarrow e^{i\gamma_5 \theta_A} \Psi. \quad (2.6)$$

In the quantized theory the $U_A(1)$ symmetry Eq.(2.6) is explicitly broken by Instantons in the continuum (the so called ‘‘axial anomaly’’ see for example [20]). To see that the full symmetry group is actually $U(N_f) \times U(N_f)$, we define $\psi^\alpha = \psi_L^\alpha + \psi_R^\alpha$ where $\psi_{R/L}^\alpha = \frac{1}{2}(1 \pm \gamma_5)\psi^\alpha =: P_{R/L}\psi^\alpha$ are the right and left handed quark fields, respectively. Thanks to the properties of γ_5 ,² P_R and P_L are projectors with properties $P_{R/L}^2 = P_{R/L}$, $P_R + P_L = 1$, $P_L P_R = P_R P_L = 0$. $\psi_{R/L}^\alpha$ have right and left handed *chirality*, $\gamma_5 \psi_{R/L}^\alpha = \pm \psi_{R/L}^\alpha$, respectively. Further we rewrite the two sets of generators $t^a, \gamma_5 t^a$ of Eq.(2.4) as two commuting sets of generators t_R^a, t_L^a

$$t_R^a = \frac{1}{2}(1 + \gamma_5)t^a, \quad t_L^a = \frac{1}{2}(1 - \gamma_5)t^a. \quad (2.7)$$

The massive Lagrangian Eq.(2.1) in this basis becomes

$$\mathcal{L}_E = \frac{1}{2}\text{tr}(F_{\mu\nu}F_{\mu\nu}) + \sum_\alpha \bar{\psi}_R^\alpha \gamma_\mu (\partial_\mu + igA_\mu) \psi_R^\alpha + \bar{\psi}_L^\alpha \gamma_\mu (\partial_\mu + igA_\mu) \psi_L^\alpha + m^\alpha (\bar{\psi}_R^\alpha \psi_L^\alpha + \bar{\psi}_L^\alpha \psi_R^\alpha) \quad (2.8)$$

and in the chiral limit is seen to have a $U(N_f) \times U(N_f) = SU_L(N_f) \times SU_R(N_f) \times U_V(1) \times U_A(1)$ symmetry with the transformations given by Eqs.(2.5,2.6) and

$$SU_L(N_f) : \quad \bar{\Psi}_L \rightarrow \bar{\Psi}_L e^{-it_L^a \theta_L^a}, \quad \Psi_L \rightarrow e^{it_L^a \theta_L^a} \Psi_L, \quad (2.9)$$

$$SU_R(N_f) : \quad \bar{\Psi}_R \rightarrow \bar{\Psi}_R e^{-it_R^a \theta_R^a}, \quad \Psi_R \rightarrow e^{it_R^a \theta_R^a} \Psi_R. \quad (2.10)$$

Note that the transformation given in Eq.(2.4) can be written as $e^{i\theta_V^a t^a + i\gamma_5 \theta_A^a t^a} = e^{i\gamma_5 \theta_A^a t^a} e^{i\theta_V^a t^a}$ with parameters θ_A^a, θ_V^a which depend on θ_A^b, θ_V^b . In this notation $U(N_f) \times U(N_f)$ can loosely

² $\gamma_5^\dagger = \gamma_5$, $\gamma_5^2 = \mathbf{1}$, $\{\gamma_5, \gamma_\mu\} = 0$.

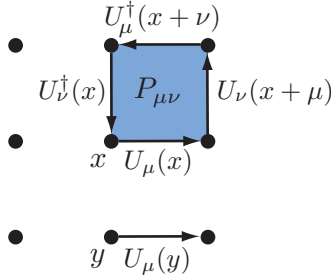


Figure 2.3: Plaquette $P_{\mu\nu}$ and fundamental link $U_{\hat{\mu}}(x)$.

be rewritten as $U(N_f) \times U(N_f) = "SU_A(N_f)" \times SU_V(N_f) \times U_A(1) \times U_V(1)$ where " $SU_A(N_f)$ " now does not denote a group but the right coset space $SU_L(N_f) \times SU_R(N_f)/SU_V(N_f)$ with generators $\gamma_5 t^a$ and $SU_V(N_f) = SU_{L=R}(N_f)$ is a subgroup generated by the t^a . For $m^a > 0$ the symmetry group $SU_L(N_f) \times SU_R(N_f)$ is explicitly broken down to this subgroup because of the noninvariant term $\bar{\Psi}\Psi = \bar{\Psi}_R\Psi_L + \bar{\Psi}_L\Psi_R$ which couples to the quark mass in Eq.(2.8). In the chiral limit, this breaking happens spontaneously and the expectation value $\langle\bar{\Psi}\Psi\rangle$, the chiral condensate, represents an order parameter signaling this break down as it transforms nontrivially under " $SU_A(N_f)$ " chiral transformations. In the chirally symmetric phase it must hence be zero but can take a non-vanishing value in the broken phase, representing a contribution to the constituent quark mass.

In the above discussion we have already anticipated the expectation value of observables. Formally we define the generating functional Z for systems with the Lagrangian \mathcal{L}_E in Euclidean time by

$$Z = \int \mathcal{D}\bar{\Psi}\mathcal{D}\Psi\mathcal{D}A e^{-\frac{1}{\hbar} \int d^4x \mathcal{L}_E(A, \bar{\Psi}, \Psi)}, \quad (2.11)$$

from which expectation values of observables \hat{O} are obtained,

$$\langle\hat{O}\rangle = \frac{1}{Z} \int \mathcal{D}\bar{\Psi}\mathcal{D}\Psi\mathcal{D}A O e^{-\frac{1}{\hbar} \int d^4x \mathcal{L}_E(A, \bar{\Psi}, \Psi)}. \quad (2.12)$$

Perturbatively the theory with "partition function" Z is not properly defined without fixing a gauge and a subsequent regularization (see e.g. [20]). As we will see in the next section, on the lattice a momentum cut-off $1/a$ with the lattice spacing a is introduced and the theory is thus regularized without any need for gauge-fixing. In fact, the lattice is the only known regulator that is non-perturbative and gauge-covariant.

2.2 QCD on the lattice

2.2.1 Discretizing the gauge action

Throughout this thesis we work with the discretized version of the QCD-Lagrangian Eq.(2.1). The discretization is formally presented in two separate steps: This section will shortly intro-

duce how the Yang-Mills part of the QCD action is formulated on a lattice where we take the gauge group to be $G = SU(N)$. Sect.2.2.2 then treats the fermionic part.

In the following we will refer to the “lattice” as the discrete set of points $x(t, i, j, k) = (t\mathbf{e}_0 + i\mathbf{e}_1 + j\mathbf{e}_2 + k\mathbf{e}_3)a$, with a being the lattice constant and $\mathbf{e}_\mu (a\mathbf{e}_\mu = \hat{\mu})$ the unit-vector in the μ th direction of Euclidean space-time. t, i, j, k take integer values, $t, i, j, k = 1, \dots, L$ and we choose periodic boundary conditions for the corresponding finite space-time volume. To obtain a discretized expression for $S_{\text{YM}} = \int d^4x \frac{1}{2} \text{tr}(F_{\mu\nu} F_{\mu\nu})$ that is invariant under the discretized form of the gauge transformations, Eq.(2.2), we introduce the discrete version of parallel transport. The parallel transporter that connects neighboring lattice sites is referred to as *link* $U_{\hat{\mu}} \in G$ and has the form

$$U_{\hat{\mu}}(x) = P \exp \left(ig \int_x^{x+a\hat{\mu}} A_\nu dx^\nu \right) \xrightarrow{a \rightarrow 0} \exp(igaA_\mu(x) + \mathcal{O}(a^2)). \quad (2.13)$$

Under a gauge transformation, Eq.(2.2), $U_{\hat{\mu}}$ transforms according to $U_{\hat{\mu}}(x) \rightarrow U'_{\hat{\mu}}(x) = \Omega(x)U_{\hat{\mu}}(x)\Omega^{-1}(x + \hat{\mu})$ and we can now construct parallel transport along different paths γ on the lattice out of these elementary links. The smallest, closed Wilson line, the 1×1 -*Wilson loop* $P_{\mu\nu}$ (see Figure 2.3) is given by

$$P_{\mu\nu} = U_{\hat{\mu}}(x)U_{\hat{\nu}}(x + \hat{\mu})U_{\hat{\mu}}^\dagger(x + \hat{\nu})U_{\hat{\nu}}^\dagger(x) \xrightarrow{a \rightarrow 0} \exp(iga^2 F_{\mu\nu} + \mathcal{O}(a^3)) \quad (2.14)$$

where $e^A e^B = e^{A+B+\frac{1}{2}[A,B]+\dots}$ and $F_{\mu\nu}(x) = \partial_\mu A_\nu - \partial_\nu A_\mu + ig[A_\nu, A_\mu]$ with $A_\mu(x + \hat{\nu}) = A_\mu(x) + a\partial_\nu A_\mu(x) + \mathcal{O}(a^2)$ were used. Eq.(2.14) serves as a definition for the lattice field strength $F_{\mu\nu}$, usually referred to as *plaquette*. In the limit of small lattice spacing a we can expand Eq.(2.14) to $\mathcal{O}(a^4)$ and see that

$$\text{tr} P_{\mu\nu} \xrightarrow{a \rightarrow 0} N - \frac{1}{2}g^2 a^4 (F_{\mu\nu})^2 + \mathcal{O}(a^5),$$

where terms linear in the generators vanish due to their zero trace. The following sum is the simplest choice of a lattice action (the Wilson action [17]) reproducing the Yang-Mills action in the continuum limit $a \rightarrow 0$:

$$S[U] := \beta \sum_{x, \mu < \nu} \left[1 - \frac{1}{2N} \text{tr} (P_{\mu\nu} + P_{\mu\nu}^\dagger) \right] = \frac{\beta}{2} \sum_{x, \mu\nu} \left[1 - \frac{1}{N} \text{Re tr} P_{\mu\nu} \right] \xrightarrow{a \rightarrow 0} \frac{\beta g^2}{4N} \int_M d^4x \text{tr} (F_{\mu\nu} F^{\mu\nu}), \quad (2.15)$$

taking into account both orientations of $P_{\mu\nu}$ (Figure 2.3) to ensure hermiticity of $S[U]$. The free parameter β of the lattice theory thus has to satisfy $\beta = 2N/g^2$. The partition function can be defined by

$$Z = \int_G \mathcal{D}U e^{-S[U]}, \quad (2.16)$$

where the measure $\mathcal{D}U$, with $\mathcal{D}U = \prod_{x, \mu} dU_{x, \mu}$, involves the Haar measure dU of the gauge group. It is normalized s.t. $\int_G dU = 1$ and enjoys invariance under left and right multiplication with

elements of the group

$$\int_G dU f(U) = \int_G dU f(VU) = \int_G dU f(UW), \quad \forall V, W \in G. \quad (2.17)$$

An expectation value of an observable $\hat{O}(U)$ is given by

$$\langle \hat{O} \rangle = \frac{1}{Z} \int_G \mathcal{D}U O(U) e^{-S[U]}. \quad (2.18)$$

where the invariance Eq.(2.17) ensures that it is non-vanishing only for gauge invariant expressions $O(U)$.

2.2.2 Fermions on the lattice

2.2.2.1 The Doubling problem

Special care has to be taken when discretizing fermions. We consider for example a free theory with one flavor,

$$S_{F,free} = \int d^4x \bar{\psi}(x) (\gamma_\mu \partial_\mu + m) \psi(x) = \int d^4x \bar{\psi}(x) (D + m) \psi(x),$$

with Dirac operator D . Replacing the derivative by a central difference on the lattice leads to

$$S_{F,free, lat} = a^4 \sum_x \left\{ \sum_{\mu=0}^3 \bar{\psi}_x \gamma_\mu \frac{\psi_{x+\hat{\mu}} - \psi_{x-\hat{\mu}}}{2a} + m \bar{\psi}_x \psi_x \right\}. \quad (2.19)$$

Here, $\psi_y, \bar{\psi}_y$ are anti-commuting (Grassmann) variables, $\psi_y \bar{\psi}_y = -\bar{\psi}_y \psi_y$.

If we look at the free fermion propagator $\Delta_F(x, y)$ obtained by going to momentum space in Eq.(2.19), taking the inverse of the discrete Dirac operator and transforming back, then

$$\Delta_F(x, y) = \int_{-\pi/a}^{\pi/a} d^4p \frac{-i\gamma_\mu \hat{p}_\mu + m}{\sum_\mu \hat{p}_\mu^2 + m^2} e^{i(x-y)}, \quad (2.20)$$

where $\hat{p}_\mu = \frac{1}{a} \sin(p_\mu a)$ and $p_\mu \in [-\pi/a, \pi/a]$ varies in the first Brillouin zone (BZ). In the continuum a relativistic particle has dispersion relation $E(p) = \sqrt{p^2 + m^2}$. On the lattice, setting $p_0 = iE$, the integrand in Eq.(2.20) has poles at $\sinh^2(Ea) = a^2 m^2 + \sum_{i=1}^3 \sin^2(p_i a)$. Taking the limit $a \rightarrow 0$, for small momenta p_i we indeed find $E = \sqrt{m^2 + p^2}$, i.e. a particle state with the correct dispersion relation. But for $a \rightarrow 0$ the integral Eq.(2.20) also receives contributions from momenta at the corners of the BZ at $p_i \approx \pm\pi/a$, where $E_\delta = \sqrt{m^2 + \sum_i (p_i - \delta_i \pi/a)^2}$, with $\delta_i = 0, 1$. Together with the choice $p_0 = iE + \delta_0 \pi/a$, we recover $2^{d+1} = 16$ degenerate particle states, i.e. the action Eq.(2.19) describes a theory of 16 degenerate Dirac particles, instead of one, which is referred to as ‘‘doubling’’ problem.

In the next section we will encounter an alternative formulation of discrete fermions. It follows from the Nielsen-Ninomiya theorem [21] that any formulation of fermions on the lattice with discretized Dirac operator D_{xy} cannot satisfy simultaneously the following conditions:

- **Locality:** The contribution to the sum $\sum_y D_{xy}\psi_y$ from terms at $y = z$ decays exponentially with the distance $|x - z|$. Practically it means that, given x , D only couples terms via D_{xy} for y in the neighborhood of x , shrinking to $\delta(x)$ as $a \rightarrow 0$.
- **Chiral symmetry:** $\{\gamma_5, D\} = 0$.
- The formulation is doubler free.
- In momentum space $D(p)$ behaves like $D(p) = i\gamma_\mu p_\mu$ for small p .

Staggered fermions, described in the next section, reduce the number of doublers from 16 to 4 in $d + 1 = 4$ dimensions and have a reduced chiral symmetry. They will be used throughout this thesis.

2.2.2.2 Staggered fermions

Starting from the naive discretization Eq.(2.19), the change of variables

$$\psi(x) = T(x)\hat{\chi}(x), \quad \bar{\psi}(x) = \hat{\chi}(x)T^\dagger(x) \quad (2.21)$$

with unitary matrices T is made, s.t.

$$T^\dagger(x)\gamma_\mu T(x + \hat{\mu}) = \eta_{\hat{\mu}}(x) \quad \text{with } \eta_{\hat{\mu}}(x) \in \mathbb{C}. \quad (2.22)$$

A constraint is given by the condition $\eta_{\hat{\mu}}(x)\eta_{\hat{\nu}}(x + \hat{\mu})\eta_{\hat{\mu}}^\dagger(x + \hat{\nu})\eta_{\hat{\nu}}^\dagger(x) = -1$. A possible choice is $T(x) = \gamma_0^{x_0}\gamma_1^{x_1}\gamma_2^{x_2}\gamma_3^{x_3}$, which yields $\eta_{\hat{\mu}}(x) = (-1)^{\sum_{\nu < \mu} x_\nu}$. The action then reads

$$S_{F,\text{free, lat}} = a^4 \sum_x \left\{ \sum_{\mu=0}^3 \eta_{\hat{\mu}}(x) \left(\sum_{j=0}^3 \hat{\chi}_{x,j} \frac{\hat{\chi}_{x+\hat{\mu},j} - \hat{\chi}_{x-\hat{\mu},j}}{2a} \right) + m \sum_j \hat{\chi}_{x,j} \hat{\chi}_{x,j} \right\}, \quad (2.23)$$

and now describes 4 independent sets of fields $\hat{\chi}_{x,j}, \bar{\chi}_{x,j}$. By taking only one component $\hat{\chi}_x, \bar{\chi}_x$ per site x , the number of doublers is reduced from 16 to 4. Alternatively, one may interpret the index j as a staggered flavor index α , $\alpha = 1, \dots, N_f$, since now the mass in Eq.(2.23) can be chosen independently for each j . The free staggered action now reads (defining dimensionless fields by $\chi = a^{3/2}\hat{\chi}$)

$$S_{F,\text{free, stag}} = \sum_x \sum_{\alpha=1}^{N_f} \left\{ \sum_{\mu=0}^3 \eta_{\hat{\mu}}(x) \left(\bar{\chi}_x^\alpha \frac{\chi_{x+\hat{\mu}}^\alpha - \chi_{x-\hat{\mu}}^\alpha}{a} \right) + am^\alpha \bar{\chi}_x^\alpha \chi_x^\alpha \right\}, \quad (2.24)$$

and really describes a theory of $4N_f$ flavors due to the presence of doublers. In Lattice QCD each variable $\chi_x^\alpha, \bar{\chi}_x^\alpha$ is an N -component object, $(\chi_x^\alpha)_a, a = 1, \dots, N$, representing the color degree of freedom. To account for a local, i.e. gauge invariance of the action Eq.(2.24) under transformations

$$\chi_x^\alpha \rightarrow \Omega(x)\chi_x^\alpha, \quad \bar{\chi}_x^\alpha \rightarrow \bar{\chi}_x^\alpha \Omega^{-1}(x), \quad (2.25)$$

we have to replace the finite difference scheme of the lattice derivative by the covariant derivative on the lattice. The modified expression of the action Eq.(2.24) given by

$$S_{F,\text{stag}} = \sum_x \sum_{\alpha=1}^{N_f} \left\{ \sum_{\mu=0}^3 \eta_{\hat{\mu}}(x) \left(\bar{\chi}_x^\alpha U_{\hat{\mu}}(x) \chi_{x+\hat{\mu}}^\alpha - \bar{\chi}_{x+\hat{\mu}}^\alpha U_{\hat{\mu}}^\dagger(x) \chi_x^\alpha \right) + 2am^\alpha \bar{\chi}_x^\alpha \chi_x^\alpha \right\}, \quad (2.26)$$

is gauge invariant as the links U transform according to $U_{\hat{\mu}}(x) \rightarrow \Omega(x) U_{\hat{\mu}}(x) \Omega^{-1}(x + \hat{\mu})$ under gauge transformations Eq.(2.25). Expanding the links to $U_{\hat{\mu}}(x) = 1 + igA_{\hat{\mu}}(x)a + \mathcal{O}(a^2)$, we indeed see that for $a \rightarrow 0$ the lattice finite difference in Eq.(2.26) reduces to $D_\mu = \partial_\mu + igA_\mu$ which is the covariant derivative in the continuum.

As it stands, the action Eq.(2.26) has a global $U(N_f) \times U(N_f) = SU_L(N_f) \times SU_R(N_f) \times U_V(1) \times U_{A'}(1)$ symmetry for $m^\alpha = 0 \forall \alpha$,

$$\begin{aligned} \chi_{x_e}^\alpha &\rightarrow V^{\alpha\beta} e^{i\theta_{A'} + i\theta_V} \chi_{x_e}^\beta & \bar{\chi}_{x_e}^\alpha &\rightarrow \bar{\chi}_{x_e}^\beta e^{i\theta_{A'} - i\theta_V} W^{\dagger,\beta\alpha} \\ \chi_{x_o}^\alpha &\rightarrow W^{\alpha\beta} e^{-i\theta_{A'} + i\theta_V} \chi_{x_o}^\beta & \bar{\chi}_{x_o}^\alpha &\rightarrow \bar{\chi}_{x_o}^\beta e^{-i\theta_{A'} - i\theta_V} V^{\dagger,\beta\alpha} \end{aligned} \quad (2.27)$$

with matrices $V, W \in SU(N_f)$ and an even-odd decomposition of our hypercubic lattice in sites x_e, x_o defined via parity $\epsilon(x_e) = 1, \epsilon(x_o) = -1$ where $\epsilon(x) = (-1)^{\sum_\mu x_\mu}$. As the notation suggests $SU_L(N_f) \times SU_R(N_f)$ is the chiral symmetry of the lattice action. In the case $N_f = 1$ the above symmetry reduces to $U_{A'}(1) \times U_V(1)$ which in the limit $a \rightarrow 0$ is enhanced to a $SU_L(4) \times SU_R(4) \times U_V(1)$ symmetry due to the symmetry between the 4 doublers or ‘‘tastes’’. The ‘‘axial’’ symmetry $U_{A'}(1)$ is thus a subgroup of the $SU_L(4) \times SU_R(4)$ chiral group and is not related to the anomalous, axial $U_A(1)$ broken explicitly by the appearance of instantons in the continuum. It is the remnant chiral symmetry of staggered fermions on the lattice.

For $m^\alpha = m > 0$ the symmetry under transformations Eq.(2.27) is reduced to $SU(N_f) \times U_V(1)$, i.e. taking $V = W$ in Eq.(2.27) and we thus have a flavor symmetry and a symmetry corresponding to fermion number conservation (see below).

If we consider the free case again, Eq.(2.24), with $N_f = 1$ we can recover an action describing 4 tastes (flavors with degenerate mass) of Dirac spinors by dividing the lattice in hypercubic blocks with coordinate y , s.t. a site x can be written $x = 2y + \delta$, where the 4-vector δ has components $\delta_i = 0, 1$ and labels the corners of the hypercube. Defining (see e.g. [22])

$$\psi_y^{\hat{a}b} = \frac{1}{8} \sum_\delta T(\delta)^{\hat{a}b} \chi_{2y+\delta}, \quad \bar{\psi}_y^{\hat{a}b} = \frac{1}{8} \sum_\delta \left(T^\dagger(\delta) \right)^{\hat{a}b} \bar{\chi}_{2y+\delta}, \quad (2.28)$$

with matrices $T^{\hat{a}b}(\delta) = (\gamma_0^{\delta_0} \gamma_1^{\delta_1} \gamma_2^{\delta_2} \gamma_3^{\delta_3})^{\hat{a}b}$ which we already used in Eq.(2.22), we recover not only the spinor index (here taken as the second index b) but also make visible the taste-multiplicity with the taste index \hat{a} . This will become important once we want to assign quantum numbers to correlation functions involving the staggered quark fields $\bar{\chi}, \chi$, see Sect.4.1.3.2. The taste *symmetry* of the free action and the interacting theory with gauge fields is broken at nonzero lattice spacing a .

The Lattice QCD partition function is now given by

$$Z = \int \mathcal{D}U \mathcal{D}\chi \mathcal{D}\bar{\chi} e^{-S_{YM} - S_F}, \quad (2.29)$$

where S_{YM}, S_F are defined in Eq.(2.15) and (2.26), respectively. The fermion path integral

measure $\mathcal{D}\chi\mathcal{D}\bar{\chi} = \prod_{x,\alpha,i} d\chi_{x,i}^\alpha d\bar{\chi}_{x,i}^\alpha$ relies on the definition of the Grassmann integration which we will use extensively: For Grassmann numbers $\xi, \bar{\xi}$, we define

$$\int d\xi \xi = 1, \quad \int d\bar{\xi} \bar{\xi} = 1, \quad \int d\xi d\bar{\xi} \bar{\xi} \xi = 1. \quad (2.30)$$

The partition function Eq.(2.29) is the starting point to derive an alternative representation at infinite gauge coupling $\beta = 6/g^2 = 0$, called the ‘‘strong coupling’’ limit. For $a > 0$ the taste and spin rotational symmetries of the continuum action are broken to discrete shifts and rotations on the lattice. The breaking of the taste symmetry leads to mass splitting of taste multiplets. In the strong coupling limit this splitting is maximal, having little in common with the continuum theory of four degenerate quarks tastes. When working in the $\chi, \bar{\chi}$ -basis which is a set of variables without spinor index but with the correct anticommutation relation we therefore adopt the point of view of studying the physics of one flavor of spinless quarks on a hypercubic lattice.

2.2.3 Finite temperature and chemical potential

An Euclidean field theory at finite temperature T is obtained by compactifying the Euclidean time direction ($\hat{0}$ -direction), where the physical temperature T is identified with the inverse extent in time, i.e. $t \in [0, 1/T]$. Compactness in time means that we have to impose boundary conditions (bc) in time for the fields A_μ (or U) and ψ (χ). If we denote by $Z(T)$ the partition function of a system at finite temperature T with fields ϕ , then

$$Z(T) = \int \mathcal{D}\phi e^{-\int_0^{1/T} dx_0 \int d^3x \mathcal{L}_E(\phi, \partial\phi)} \Big| \quad (2.31)$$

where $|$ denotes a set of suitable bc on the field. We want to motivate why $\phi(\vec{x}, t + \frac{1}{T}) = c\phi(\vec{x}, t)$ with $c = 1$ for bosons and $c = -1$ for fermions, respectively, by alluding to quantum statistical mechanics and write $Z(T)$

$$Z(T) = \text{Tr}(e^{-\hat{H}/T}) := \int d\varphi \langle \varphi | e^{-\hat{H}/T} | \varphi \rangle. \quad (2.32)$$

The 2-pt function $G(\vec{x}_1, t_1, \vec{x}_2, t_2) = \langle \mathcal{T} \hat{\phi}(\vec{x}_1, t_1) \hat{\phi}(\vec{x}_2, t_2) \rangle$ is then given by

$$G(\vec{x}_1, t_1, \vec{x}_2, t_2) = \frac{1}{Z} \text{Tr} \left(e^{-\hat{H}/T} \mathcal{T} \hat{\phi}(\vec{x}_1, t_1) \hat{\phi}(\vec{x}_2, t_2) \right), \quad (2.33)$$

with time-ordering \mathcal{T} defined by ($c = 1$ bosons, $c = -1$ fermions)

$$\mathcal{T} \hat{\phi}(\vec{x}_1, t_1) \hat{\phi}(\vec{x}_2, t_2) := \hat{\phi}(\vec{x}_1, t_1) \hat{\phi}(\vec{x}_2, t_2) \theta(t_1 - t_2) + c \hat{\phi}(\vec{x}_2, t_2) \hat{\phi}(\vec{x}_1, t_1) \theta(t_2 - t_1).$$

Taking $t_1 = t > t_2 = 0$ we obtain

$$\begin{aligned}
G(\vec{x}_1, t, \vec{x}_2, 0) &= \frac{1}{Z} \text{Tr} \left(e^{-\hat{H}/T} \mathcal{T} \hat{\phi}(\vec{x}_1, t) \hat{\phi}(\vec{x}_2, 0) \right) = \frac{1}{Z} \text{Tr} \left(e^{-\hat{H}/T} \hat{\phi}(\vec{x}_1, t) \hat{\phi}(\vec{x}_2, 0) \right) \\
&= \frac{1}{Z} \text{Tr} \left(\hat{\phi}(\vec{x}_2, 0) e^{-\hat{H}/T} \hat{\phi}(\vec{x}_1, t) \right) = \frac{1}{Z} \text{Tr} \left(e^{-\hat{H}/T} e^{+\hat{H}/T} \hat{\phi}(\vec{x}_2, 0) e^{-\hat{H}/T} \hat{\phi}(\vec{x}_1, t) \right) \\
&= \frac{1}{Z} \text{Tr} \left(e^{-\hat{H}/T} \hat{\phi}(\vec{x}_2, 1/T) \hat{\phi}(\vec{x}_1, t) \right) = c \frac{1}{Z} \text{Tr} \left(e^{-\hat{H}/T} \mathcal{T} \hat{\phi}(\vec{x}_1, t) \hat{\phi}(\vec{x}_2, 1/T) \right) \\
&= cG(\vec{x}_1, t, \vec{x}_2, 1/T), \tag{2.34}
\end{aligned}$$

which implies $\phi(\vec{x}, t + \frac{1}{T}) = c\phi(\vec{x}, t)$ for the fields in Eq.(2.31).

On the lattice we proceed in the same way and compactify the $\hat{0}$ -direction with extent $N_t a$ ($N_t \ll L$), defining the temperature by $T = 1/N_t a$. Finally the boundary conditions $U_{\hat{\mu}}(\vec{x}, t + N_t) = U_{\hat{\mu}}(\vec{x}, t)$, $\chi(\vec{x}, t + N_t) = -\chi(\vec{x}, t)$ are imposed.

To introduce a quark chemical potential μ on the lattice we first observe that the global $U_V(1)$ symmetry Eq.(2.5) in the continuum leads to a conserved current $j_\mu^V = \bar{\psi} \gamma_\mu \psi$ by Noether's theorem. The conserved charge under this symmetry, $n = \int_V d^3x \bar{\psi} \gamma_0 \psi$, corresponds to quark number. As in statistical mechanics where the particle number is controlled via the chemical potential, μ should couple to the quark number in the Lagrangian Eq.(2.1) via a term $\mu \bar{\psi} \gamma_0 \psi$ which can be achieved by letting $\partial_0 \rightarrow \partial_0 + \mu$. Hence we obtain

$$\mathcal{L} = \frac{1}{2} \text{tr}(F_{\mu\nu} F_{\mu\nu}) + \bar{\psi}(\gamma_\nu[\partial_\nu + igA_\nu + \mu\delta_{\nu,0}] + m)\psi, \tag{2.35}$$

and we see that the chemical potential is introduced as the imaginary part of 0.th component of the gauge potential. On the lattice we proceed in an analogous way. Remembering that the gauge potential was introduced by inserting the links $U_\mu(x)$ in the finite difference, see Eq.(2.26), the replacement $U_{\hat{0}}(x) \rightarrow e^{a\mu} U_{\hat{0}}(x)$, $U_{\hat{0}}^\dagger(x) \rightarrow e^{-a\mu} U_{\hat{0}}^\dagger(x)$ leads to the expression

$$S_{F,\text{stag}} = \sum_x \sum_{\alpha=1}^{N_f} \left\{ \sum_{\nu=0}^d \eta_{\hat{\nu}}(x) \left(\bar{\chi}_x^\alpha e^{a\mu^\alpha \delta_{\nu,0}} U_{\hat{\nu}}(x) \chi_{x+\hat{\nu}}^\alpha - \bar{\chi}_{x+\hat{\nu}}^\alpha e^{-a\mu^\alpha \delta_{\nu,0}} U_{\hat{\nu}}^\dagger(x) \chi_x^\alpha \right) + 2am^\alpha \bar{\chi}_x^\alpha \chi_x^\alpha \right\} \tag{2.36}$$

where the discrete difference term reduces to $(\partial_\nu + igA_\nu + \mu\delta_{\nu,0})$ in the limit $a \rightarrow 0$, as seen by an expansion to $\mathcal{O}(a^2)$.

With the lattice action Eq.(2.36) we have the necessary tool to investigate strong coupling QCD as done in Ch.4. We now turn to some topics in statistical mechanics.

2.3 Some concepts in statistical mechanics

In the previous sections we used the terms ‘‘partition function’’ and ‘‘generating functional’’ alternately to denote the expression

$$Z = \int \mathcal{D}U \mathcal{D}\chi \mathcal{D}\bar{\chi} e^{-S_{YM} - S_F}, \tag{2.37}$$

thereby exploiting the analogy between statistical mechanics and Euclidean quantum field theory on a lattice (see for example [22]). The lattice actions S_{YM} and S_F defined in Eqs.(2.15)

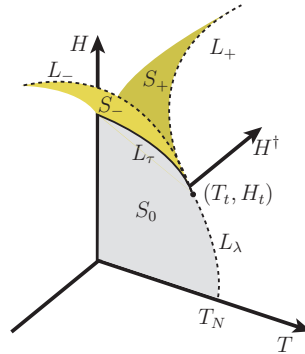


Figure 2.4: Schematic phase diagram of a metamagnet.

and (2.36), respectively, contain the parameters $\beta = 6/g^2$, $aT = \frac{1}{N_t}$, $a\mu$ and the bare quark mass am_q which determine the state of the system described by Eq.(2.37). As a particular example in Chs.4 and 5 we will consider the case $N_f = 1, \beta = 0$. Then for $m_q = 0$, the remnant chiral symmetry Eq.(2.27) will be broken spontaneously for low temperature T and chemical potential μ with order parameter $\langle \bar{\chi}\chi \rangle$. As one of the parameters (say $a\mu$) is varied smoothly, this state might change abruptly, a phase transition leading to a chirally symmetric state occurs. Generally, one possibility a phase transition may happen is through the coexistence of two or more competing phases with different macroscopic properties (such as the value of the order parameter in each phase) at the transition point, implying a finite (possibly large) correlation length in the fluctuations of microscopic observables. Slightly away from the transition the system is in a unique phase whose properties are that of one of the coexisting phases. The transition is therefore discontinuous (or first order). Tuning another thermodynamic parameter (for example temperature), the macroscopic distinction between the competing phases along the transition line can become weaker, the correlation length grows and finally diverges. The competing phases become a unique, critical phase and the system undergoes a continuous transition at a critical point. As the correlation length diverges, the microscopic properties of the system (such as the details of the interaction in the action) become less relevant and global properties, for example the symmetries and dimension of the system characterize its behavior, the model falls into a universality class. For the particular case of three coexistent phases at the first order transition, the critical point is named tricritical point. The next section will give an example of a system exhibiting tricriticality and shortly summarizes the analytic predictions on the shape of the transition line in the vicinity of this point.

2.3.1 Tricriticality

2.3.1.1 General remarks

An example for a system with tricritical behavior is a metamagnet such as Fe_2Cl which is a particular type of antiferromagnet. Like all antiferromagnets it exhibits as a function of temperature a continuous phase transition at Néel temperature T_N , separating a high-temperature paramagnetic phase from a low-temperature phase of antiferromagnetic order of the atomic spins. As shown in the phase diagram Fig.2.4 turning on a magnetic field H , the Néel point becomes a Néel line L_λ of critical points which — for a metamagnet — turns into a first order

transition at $(T, H) = (T_t, H_t)$. If the metamagnet has a strong uniaxial anisotropy (i.e. an “easy” axis of magnetization) a simplified model is given by the Ising model on a cubic lattice which is partitioned into two sublattices A, B which interact antiferromagnetically. One such partition would be the natural bipartition of the hypercubic lattice, s.t. a site of A has only neighbors which are elements of B . The Hamiltonian is given by

$$\mathcal{H} = - \sum_{ij} J_{ij} s_i s_j - H \sum_i s_i - H^\dagger \left(\sum_{i \in A} s_i - \sum_{i \in B} s_i \right), \quad (2.38)$$

with Ising spins $s_i = \pm 1$ and

$$J_{ij} = \begin{cases} J_1 > 0, & \text{if } i, j \text{ are nearest neighbors (n.n) on the same sublattice } A \text{ or } B \\ J_2 < 0, & \text{if } i, j \text{ are n.n. but } i \in A \text{ and } j \in B \text{ and vice versa} \\ 0, & \text{else} \end{cases} \quad (2.39)$$

The magnetic fields H, H^\dagger are the non-ordering uniform field and the staggered field, respectively. H couples to the magnetization $M = \sum_i s_i$ and thus respects the symmetry between the two sublattices A, B , whereas the conjugate variable to H^\dagger (which explicitly breaks this symmetry) is the staggered magnetization $M^\dagger = \sum_{i \in A} s_i - \sum_{i \in B} s_i$. For $H^\dagger = 0$ it is the order parameter distinguishing the paramagnetic ($M^\dagger = 0$) from the antiferromagnetic phase ($M^\dagger \neq 0$). The area S_0 in the plane $H^\dagger = 0$ of Fig.2.4 corresponds to the surface of coexistence of the “vacua” $M^\dagger \gtrless 0$ which are reached in the limit $H^\dagger \rightarrow 0_\pm$, respectively. This two-phase coexistence turns into a three-phase coexistence ($M^\dagger \gtrless 0$ and $M^\dagger = 0$) at high magnetic field H on the line of first order transitions L_τ . The three-phase coexistence ends at the *tricritical* point $(T_t, H^\dagger = 0, H_t)$ when the three phases turn into one phase. The terminology is hence chosen in analogy to a critical point which marks the endpoint of a two-phase coexistence such as the liquid-gas transition line of water or the transition to nuclear matter in strong coupling QCD at nonzero bare quark mass. For $H^\dagger \neq 0$ the phases $M^\dagger \gtrless 0$ at low temperature and low magnetic field H are inequivalent. Increasing H a first order transition traces out the coexistence surfaces S_+, S_- of the phases $M^\dagger > 0, M^\dagger < 0$ with the phase of low staggered magnetization $M^\dagger \approx 0$, respectively. This coexistence ends on the wing-lines L_\pm of critical endpoints which terminate at the tricritical point (TCP). In the following we will be interested in the scaling predictions for L_\pm close to tricriticality.

2.3.1.2 Scaling predictions in the vicinity of the tricritical point

The scaling analysis starts by choosing an appropriate set of variables in the vicinity of the TCP. In the case of the antiferromagnet we define the scaling variables

$$t = \frac{T - T_t}{T_t}, \quad h = H - H_t - at, \quad h^\dagger = H^\dagger \quad (2.40)$$

where $a = \left. \frac{dH}{dT} \right|_{T_t}$ is the slope of the lambda line L_λ (see Fig.2.4) at the tricritical temperature T_t . If Z is the partition function of the system and $G = -T \log Z$ its free energy, a scaling hypothesis for G in the neighborhood of the TCP can be formulated. In our case it reads [23, 24]

$$G = G(t, h^\dagger, h) \sim |t|^{2-\alpha} \mathcal{G}^\pm(h^\dagger/|t|^{\phi_1}, h/|t|^\phi) \quad (2.41)$$

asymptotically close to the tricritical point for $t \geq 0$, respectively. Here α, ϕ, ϕ_1 are tricritical exponents and \mathcal{G} denotes the scaling function. Classical (Landau) theory makes predictions for the exponents and we point to the next section for a motivation why for $d = 3$ these exponents are expected to be correct.

The scaling hypothesis Eq.(2.41) now constrains the shape of the wing-lines L_{\pm} drawn in Fig.2.4 by the following argument: By definition G has a singularity at any point on L_{\pm} . If this point is given by $(t, h_{\pm}^{\dagger}(t), h_{\pm}(t))$ close to the TCP, then Eq.(2.41) implies that G has the same singularity at a point $(\lambda t, \lambda^{\phi_1} h_{\pm}^{\dagger}(t), \lambda^{\phi} h_{\pm}(t))$, $\lambda \in R$, provided we are still in the scaling region. But this means that $\lambda^{\phi} h_{\pm}(t) = h_{\pm}(t\lambda)$ and $\lambda^{\phi_1} h_{\pm}^{\dagger}(t) = h_{\pm}^{\dagger}(t\lambda)$. Choosing $\lambda = |t|^{-1}$ and taking into account the symmetry of the lines L_{\pm} yields ($t < 0$ on the wing lines)

$$\boxed{h_{\pm}(t) \sim |t|^{\phi}, h_{\pm}^{\dagger}(t) \sim \pm |t|^{\phi_1}}. \quad (2.42)$$

The geometry of the wing-lines close to the TCP is thus largely constrained once the critical exponents are known. A TCP is predicted in the phase diagram of strong coupling QCD in the chiral limit (see Sect.5.1.1), where the quark mass m_q plays the role of the symmetry breaking (ordering) field h^{\dagger} . The scaling predictions Eq.(2.42) in the tricritical region will determine the ‘‘movement’’ of the QCD critical endpoint as m_q is increased, see Sect.5.3.

2.3.1.3 Ginzburg criterion & upper critical dimension

	α	β	γ	ν	η
critical	0	$\frac{1}{2}$	1	$\frac{1}{2}$	0
tricritical	$\frac{1}{2}$	$\frac{1}{4}$	1	$\frac{1}{2}$	0

Table 2.1: Critical and tricritical exponents of the classical theory.

Classical (Landau) theory relies on the expansion of the underlying thermodynamic potential in powers of the order parameter ψ of the system. If G is the free energy of the last section and $F(t, m^{\dagger}, h) = G(t, h^{\dagger}, h) + h^{\dagger} m^{\dagger}$ its Legendre transform, then the potential is given by $\Phi(\psi; t, h) = F(t, \psi, h)$ in the absence of the external field h^{\dagger} . In this notation Φ is a functional of $\psi(h, t)$ and is minimized by $\psi(h, t) = m^{\dagger}(h, t)$. In the presence of the external field $\Phi(\psi; t, h^{\dagger}, h) = F(t, \psi, h) - h^{\dagger} \psi$ is expanded near a critical point,

$$\Phi(\psi; t, h^{\dagger}, h) = \Phi_{reg} - h^{\dagger} \psi + r \psi^2 / 2 + u \psi^4 / 4! + \psi^6 / 6! \quad (2.43)$$

where the spatial dependence $\psi(x)$ is typically neglected. Subsequently it is assumed that the coefficients u, r depend analytically on the scaling variables t, h . A condition for the validity of these assumptions is given by the Ginzburg-criterion [23]: If we consider a subvolume $\Omega = \xi^d$ of our d -dimensional metamagnet to be correlated, fluctuations $\Delta = \int_{\Omega} dx (\psi(x) - m^{\dagger})$ of the order parameter $\psi(x)$ around its mean value m^{\dagger} in this volume are negligible if

$$\langle \Delta^2 \rangle = \int_{\Omega} dx \int_{\Omega} dy \langle (\psi(x) - m^{\dagger})(\psi(y) - m^{\dagger}) \rangle \ll m^{\dagger 2} \xi^{2d}. \quad (2.44)$$

But the expression in the middle is the correlation function $G(\vec{r} = x - y) \sim e^{-r/\xi}/r^{d-2+\eta}$. With $\int_{\Omega} dx \int_{\Omega} dy G(x, y) = C\xi^{d+2-\eta}$, the above inequality thus becomes $\xi^{-(d-2+\eta)}m^{\dagger-2} \ll C'$ or

$$|t|^{\nu(d-2+\eta)-2\beta} \ll \tilde{C} \quad (2.45)$$

if the scaling laws $m^{\dagger} \sim |t|^{\beta}$ and $\xi \sim |t|^{-\nu}$ are used. In the limit $t \rightarrow 0$, for the inequality Eq.(2.45) to hold, we obtain the lower bound

$$d^* = \begin{cases} 3, & \text{tricritical point} \\ 4, & \text{critical point} \end{cases}, \quad (2.46)$$

when the exponents obtained from the classical theory (Tab.2.1) are used. $d = 3$ thus corresponds to the upper critical dimension for tricriticality, above which the classical theory is assumed to be correct. When studying strong coupling QCD in 3+1 dimensions at finite temperature (Ch.5) we will therefore exploit this criterion and use classical exponents in the phase diagram region where tricritical scaling is expected. At the upper critical dimension logarithmic corrections to scaling are expected [23] which are however numerically hard to detect. We further note that for $d < d^*$ Eq.(2.45) specifies a region, namely when the parameter $|t|$ becomes small, where mean-field scaling must fail.

2.3.2 The worm algorithm for classical spin models

Before we turn to an actual investigation of a classical spin model exhibiting tricritical behavior using the example of the $q = 3$ -state Potts model in Ch.3, this section addresses the practical question of how the model can be studied efficiently using a worm algorithm [25]. We start by stating the Potts partition function Z ,

$$Z = \sum_{\{s\}} e^{K \sum_{\langle ij \rangle} \delta_{s_i, s_j}}, \quad (2.47)$$

where the Potts spins $s_i \in \{1, \dots, q\}$ are located on a d -dimensional hypercubic lattice and $K = \beta J$ includes the inverse temperature $\beta = 1/T$ and the Potts coupling $J > 0$. More details about the Potts model and its phase diagram will be given in Sect.3.2. Standard Monte Carlo algorithms to sample the partition function Eq.(2.47) written in the Potts spin degrees of freedom, s_i , are cluster algorithms [26, 27]. The worm algorithm [25], on the other hand, relies on the reformulation of the partition function in terms of link-variables n_b , see below. As we will take advantage of the worm algorithm in Lattice QCD at strong coupling, Chs.4 - 6, a demonstration of the change of variables and the subsequent application of the worm algorithm seems useful.

2.3.2.1 Rewriting the partition function

We start by noting that the properties of the system Eq.(2.47) remain unchanged under a shift of the energy $E = -J \sum_{\langle ij \rangle} (\delta_{s_i, s_j}) \rightarrow -J \sum_{\langle ij \rangle} (\delta_{s_i, s_j} - 1)$, as a (K -dependent) factor will drop out when calculating expectation values. In the following equalities between partition

functions will be understood as possibly containing such constants. Therefore we write

$$\begin{aligned} Z &= \sum_{\{s\}} e^{K \sum_{\langle ij \rangle} (\delta_{s_i, s_j} - 1)} = \sum_{\{s\}} e^{K/3 \sum_{\langle ij \rangle} [e^{i(\phi_i - \phi_j)} + e^{-i(\phi_i - \phi_j)} - 2]} \\ &= \sum_{\{s\}} \prod_{\langle ij \rangle} e^{K/3 [e^{i(\phi_i - \phi_j)} + e^{-i(\phi_i - \phi_j)}]}, \end{aligned}$$

where $\phi_k = 2\pi s_k/3$. Using $e^{K/3 [e^{i(\phi_i - \phi_j)} + e^{-i(\phi_i - \phi_j)}]} = A (1 + B/2 [e^{i(\phi_i - \phi_j)} + e^{-i(\phi_i - \phi_j)}])$ with $A = \frac{1}{3} (e^{\frac{2}{3}K} + 2e^{-\frac{1}{3}K})$ and $B = 2 \left(\frac{e^K - 1}{e^K + 2} \right)$ we obtain

$$\begin{aligned} Z &= \sum_{\{s\}} \prod_{\langle ij \rangle} A \left(1 + B/2 [e^{i(\phi_i - \phi_j)} + e^{-i(\phi_i - \phi_j)}] \right) \\ &= \sum_{\{s\}} \prod_{\langle ij \rangle} A \left(1 + B/2 [\psi_i \psi_j^* + \psi_i^* \psi_j] \right) \quad \text{with } \psi_k = e^{i\phi_k} \\ &= \sum_{\{s\}} \prod_{b=\langle ij \rangle} \sum_{(n_b, m_b)} W_{(n_b, m_b)} [\psi_i \psi_j^*]^{n_b} [\psi_i^* \psi_j]^{m_b}. \end{aligned} \quad (2.48)$$

In the last line the sum over link configurations of the link b includes the configurations $(n_b, m_b) \in \{(0, 0), (1, 0), (0, 1)\}$ and the configuration weight $W_{(n_b, m_b)}$ is defined as

$$W_{(n_b, m_b)} = \begin{cases} A, & \text{if } (n_b, m_b) = (0, 0) \\ AB/2, & \text{if } (n_b, m_b) = (0, 1) \text{ or } (1, 0), \end{cases} \quad (2.49)$$

Now the terms in Eq.(2.48) are reordered:

$$\begin{aligned} Z &= \sum_{\{n_b, m_b\}} \left(\prod_b W_{(n_b, m_b)} \right) \prod_{i=1}^N \sum_{s_i=1}^3 [\psi_i]^{p_i} [\psi_i^*]^{q_i} \\ &= \sum_{\{n_b, m_b\}} \left(\prod_b W_{(n_b, m_b)} \right) \prod_{i=1}^N \sum_{s_i=1}^3 [\psi_i]^{p_i} [\psi_i^*]^{q_i}, \end{aligned} \quad (2.50)$$

where q_i, p_i are the numbers of incoming and outgoing currents at site i , respectively. The crucial step is now to see that

$$\sum_{s_i=1}^3 [\psi_i]^{p_i} [\psi_i^*]^{q_i} = 1 + e^{i2\pi/3(p_i - q_i)} + e^{i4\pi/3(p_i - q_i)} = \begin{cases} 3, & \text{if } p_i = q_i \pmod{3} \\ 0, & \text{else} \end{cases}, \quad (2.51)$$

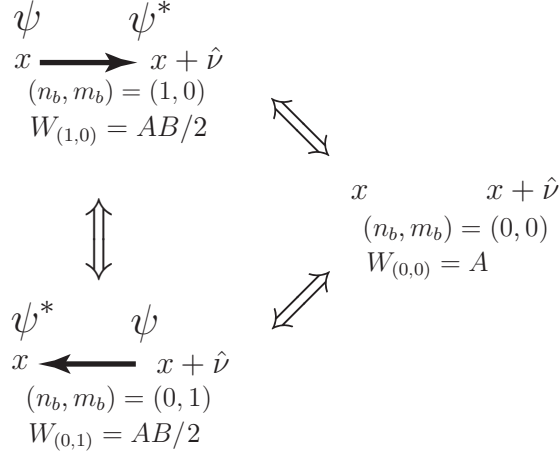


Figure 2.5: Elementary link update for the link $b = (x, \hat{\nu})$ with states $(n_b, m_b) = (0, 0), (1, 0), (0, 1)$.

i.e. for configurations $\{n_b, m_b\}$ contributing to the partition function at each site i current conservation modulo 3 has to be fulfilled,

$$\underbrace{\sum_{\mu} (n_{i, \hat{\mu}} + n_{i, -\hat{\mu}})}_{p_i} = \underbrace{\sum_{\mu} (m_{i, \hat{\mu}} + m_{i, -\hat{\mu}})}_{q_i} \pmod{3}. \quad (2.52)$$

The final expression for Z thus reads

$$Z = \sum_{\{n_b, m_b\}, CP} \left(\prod_b W_{(n_b, m_b)} \right) = \sum_{\{n_b, m_b\}, CP} W_Z, \quad (2.53)$$

where the label CP (“closed paths”) indicates that in configurations contributing to Z with weight W_Z the “paths” made out of links form closed (mod 3) intersecting loops.

If we return to Eq.(2.48), we see that for the 2-pt function $G(k, l)$,

$$G(k, l) = \frac{1}{Z} \sum_{\{s\}} \psi_k^* \psi_l \prod_{b=\langle ij \rangle} \sum_{(n_b, m_b)} W_{(n_b, m_b)} [\psi_i \psi_j^*]^{n_b} [\psi_i^* \psi_j]^{m_b} \quad (2.54)$$

this derivation remains unchanged, except that at the sites k, l , Eq.(2.52) now is changed to $p_k = q_k + 1 \pmod{3}$ and $p_l + 1 = q_l \pmod{3}$, respectively. We therefore have

$$G(k, l) = \frac{1}{Z} \sum_{\{n_b, m_b\}, CP_{kl}} \left(\prod_b W_{(n_b, m_b)} \right) = \frac{1}{Z} \sum_{\{n_b, m_b\}, CP_{kl}} W_{G(k, l)}. \quad (2.55)$$

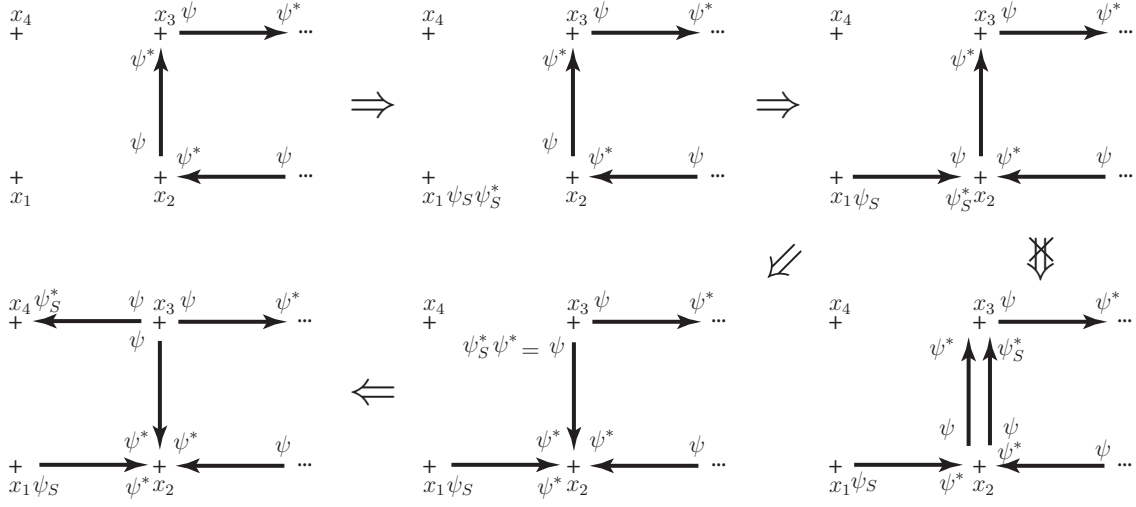


Figure 2.6: Sequence of worm updates starting with a CP-configuration (upper left). After the two “charges” $\psi_S \psi_S^*$ are placed at site x_1 , a sequence of shifts of ψ_S^* introduces incoming and outgoing currents at the involved sites until the path closes at x_1 and source and sink are removed.

2.3.2.2 The worm algorithm

Instead of sampling the partition function Z with weights $W_{(n_b, m_b)}$, the worm algorithm samples the correlation function G as described in the following.

The degrees of freedom are now the link variables (n_b, m_b) . Each link $b = (i, \hat{\nu})$ can be in one of the three states $(0, 0)$, $(0, 1)$, $(1, 0)$. From Eq.(2.48) we see that these correspond to terms $(\psi_x \psi_{x+\hat{\nu}}^*)^0$, $\psi_x \psi_{x+\hat{\nu}}^*$, $\psi_x^* \psi_{x+\hat{\nu}}$ in the expansion of Z . In Fig.(2.5) we display the three states along with their weight $W_{(n_b, m_b)}$. An elementary link update among them can be done using a Metropolis acceptance [25]. It is however clear that such update — when carried out on a single link — will violate the constraint Eq.(2.52) for configurations of Z but not that of $G(x, x + \hat{\nu})$. In Fig.2.6 we display an update sequence starting with a closed-path configuration (upper left configuration). In the second step we introduce a pair of charges $\psi_S \psi_S^*$ at site x_1 , chosen randomly. This step is carried out with probability 1 as it does not change the configuration weight in the case of the Potts model (contrary to e.g. the XY model or $|\phi|^4$ theory, see [25]). In the next step the charge ψ_S^* is moved in a direction chosen at random and an outgoing current is created. This step marks the transition from a configuration contributing to Z to a configuration of $G(x_1, x_2)$ as it violates the constraint Eq.(2.52) at x_1, x_2 . The step is accepted with Metropolis probability $W_{G(x_1, x_2)}/W_{G(x_1, x_1)} = B/2$. During the next move (from the upper right to the lower right configuration) a pair $\psi \psi^*$ is created at x_2 and ψ_S^* is shifted in the new, randomly chosen direction. The resulting link configuration of the chosen link $b = (x_2, x_3 - x_2)$ would be $(2, 0)$. From Fig.(2.5) we see that such a configuration formally does not exist. Indeed using the identity $(\psi^*)^2 = \psi$ for the complex spins of the $q = 3$ Potts model, this configuration actually corresponds to the one displayed in the middle of the lower row of Fig.2.6. The step is accepted with probability $W_{G(x_1, x_3)}/W_{G(x_1, x_2)} = 1$ and at site x_2 the constraint Eq.(2.52) is fulfilled again, the charges ψ_S, ψ_S^* being now located at x_1, x_3 , respectively. The update proceeds until ψ_S^* reaches ψ at site x_1 and the path closes.

The estimator for the 2-pt function $G(\vec{r} = l - k)$ is given by

$$G(\vec{r}) = \frac{\sum_{\{n_b, m_b\}, CP(ij)} W_{G(i,j)} \delta(\vec{r} - (j - i))}{\sum_{\{n_b, m_b\}, CP} W_Z} = \frac{\sum_{K, CP(ij)} \delta(\vec{r} - (j - i))}{\sum_{K_{CP}}}. \quad (2.56)$$

The numerator of the right hand side sums over all Monte-Carlo configurations K with sources located at sites i and j , contributing only if $\vec{r} = j - i$ and the denominator is given by the number of path closures. We will encounter similar estimators in strong coupling QCD, Ch.4, where often a direct measurement, i.e. a measurement of an expectation value taken with respect to configurations of Z , is *not* possible without expensive extrapolations in a parameter such as the quark mass m_q .

3 Tricriticality in the $q = 3$ Potts model for $d = 2 + 1$

Throughout this work finite size scaling (FSS) will be the essential tool to locate a phase transition and to determine its order. In Chs.4 and 5 we will encounter strong first order and continuous (second order and tricritical) phase transitions predicted in the phase diagram of strong coupling Lattice QCD. Here, we practice FSS for the case of a classical spin model — the Potts model — by addressing the interesting question of a change in the order of the phase transition from discontinuous to continuous when tuning the finite extent of a compact dimension of a d -dimensional system.

3.1 Introduction

Quite generally, we consider a system that exhibits a phase transition in d and $d-1$ dimensions. We are interested in the situation where the order of the transition is different in these two cases. If we compactify one dimension of the d -dimensional system choosing the extent N_t in the compact direction to be finite, we can study the evolution of the order with N_t . If our system is a lattice gauge theory model (LGT) and the boundary conditions are properly set for its degrees of freedom, then the inverse extent plays the role of temperature, $aT = 1/N_t$, see Sect.2.2. As an example we take $U(1)$ LGT in $d = 4$ dimensions,

$$S_{U(1)LGT} = -\beta \sum_{x,\mu<\nu} \cos \theta_{\mu\nu}(x), \quad \beta = \frac{1}{e^2}, \quad (3.1)$$

where $\theta_{\mu\nu}(x) = \arg [U_{\hat{\mu}}(x)U_{\nu}(x + \hat{\mu})U_{\mu}^{\dagger}(x + \hat{\nu})U_{\nu}^{\dagger}(x)]$ is the “plaquette” angle and $U_{\mu}(x) \in U(1)$. It undergoes a first order transition in β , separating the strong-coupling confining phase where planar Wilson loops W_C ,

$$W_C = \text{Re} \left(\prod_{\ell \in C} U_{\ell} \right) \quad (3.2)$$

show an area law, $\langle W_C \rangle \sim e^{-c \text{area}(C)}$, from the Coulomb phase where $\langle W_C \rangle \sim e^{-c' \partial C}$. At finite temperature, i.e. in $d = 3 + 1$ with one compact dimension of finite extent $aN_t = 1/T$, the model has a phase transition as a function of β , between the confining phase and a weak coupling phase. In the latter, the global $U(1)$ symmetry

$$P_{\vec{x}} := \prod_{t=0}^{N_t-1} U_{\hat{0}}(t, \vec{x}) \rightarrow e^{i\phi} P_{\vec{x}} \quad (3.3)$$

of the Polyakov loop $P_{\vec{x}}$ is spontaneously broken and only spatial Wilson loops show an area law, while Wilson loops extending in time direction obey a perimeter law [28]. For $N_t = 1$ the partition function with action defined in Eq.(3.1) factorizes into $Z_{U(1)LGT,d=3} \cdot Z_{XY,d=3}$ where the latter has a 2nd order phase transition at a finite value of β , whereas $U(1)$ LGT is confining for all values of the gauge coupling β in $d = 3$ dimensions. The change in the order of the phase transition with varying N_t has been studied in [28, 29].

In this chapter we study instead a classical spin system and take as a representative the q -states Potts model in $d = 2, 3$. Section 3.2 will introduce our expectations before we turn to the numerical work in Section 3.3.

3.2 The Potts model

The q -state Potts model [30] is a classical spin-model with Hamiltonian

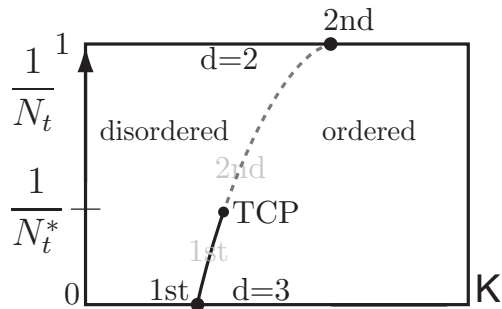
$$-\beta H = K \sum_{\langle ij \rangle} \delta_{s_i s_j}, \quad K = \beta J \quad (3.4)$$

and Potts spins $s_i \in \{1, \dots, q\}$. Here we consider the ferromagnetic case ($J > 0$, setting $J = 1$) on a simple cubic lattice in $d = 2$ and 3 dimensions, respectively. The *simple* Potts model as defined in (3.4) represents one generalization of the Ising model ($q = 2$), and exhibits a phase transition between an ordered (low temperature, Z_q symmetry broken) phase and a symmetric high temperature phase. For $d = 2$, the location of the critical point is known to be $K_c = \log(1 + \sqrt{q})$, where the phase transition is continuous (second order) for $q \leq 4$ and first order for $q > 4$ [31, 32]. In general, renormalization group arguments [33] show that in d dimensions the q -state Potts model has a continuous phase transition for $q \leq q_c(d)$ ($q_c(2) = 4$, $q_c(3) < 3$). Thus, a change of the order of the phase transitions for dimensionally reduced systems, as advertised for the case of $U(1)$ -LGT in the introduction, can be examined in the $q = 3, 4$ Potts models in $d = 2$ and 3 dimensions.

For $q = 4, d = 2$ the Potts model shows large logarithmic corrections (additive and multiplicative) to finite size scaling (FSS) [34], which complicate the disentanglement of (weak) first and second order signals. Therefore, we consider $q = 3$.

3.2.1 Conjectured behavior

In Figure 3.1(a) we sketch the conjectured phase diagram for a $N_t \times L^2$, $L \rightarrow \infty$ lattice (with periodic boundary conditions) in the plane of parameters K and $1/N_t$. For $N_t = 1$ the system is two-dimensional as our degrees of freedom are located on the sites x and the extra-coupling in $\pm t$ -direction will only contribute a constant shift in energy. Thus the system will be at criticality for $K_c(N_t = 1) = K_{c,d=2} = \log(1 + \sqrt{3}) \approx 1.00505$ and the phase transition will be of second order. Taking on the other hand $N_t = L, L \rightarrow \infty$ we will obtain the $d = 3$ model with a weak first order transition at $K_{c,d=3} = 0.550565(10)$ [35]. For systems having $N_t > 1$ fixed, and $L \rightarrow \infty$, the phase boundary will be continued into the $(1/N_t, K)$ plane, separating the disordered phase on the left from the ordered phase on the right. We speculate about the order of the transition for $N_t > 1$: Starting from $d = 2$ the system could, for fixed N_t , exhibit a second order phase transition until we reach some N_t^* beyond which the phase transition is



(a)

	α	γ	ν	$\eta = 2 - \gamma/\nu$
crit.	$\frac{1}{3}$	$\frac{13}{9}$	$\frac{5}{6}$	$\frac{4}{15}$
tricrit.	$\frac{5}{6}$	$\frac{19}{18}$	$\frac{7}{12}$	$\frac{4}{21}$

(b)

Figure 3.1: (a) Expected phase diagram for $q = 3$. (b) Exponents of the $d = 2, q = 3$ critical and tricritical Potts universality class [32].

of first order. We note that along the first order line of our conjecture, $(q + 1)$ phases coexist (q equivalent ordered phases and one disordered phase). The point $(N_t^*, K_c(N_t^*))$ where this 4-phase coexistence ends should then be termed “multicritical” point. However, traditionally the notion “tricritical” point (TCP) from 3-phase coexistence (see Sect.2.3) is kept in use and we point to Sect.3.2.2 for more details.

In fact, there was an attempt to study this scenario [36] using renormalization group methods. There, results for N_t^* were dependent on the renormalization group procedure and yielded the range $2^5 < N_t^* < 2^{13}$. While this window is rather large at least the lower bound meets our expectations: The $d = 3$ phase transition is weakly first order with correlation lengths in the ordered and disordered phase $\xi_o/a \approx \xi_d/a \approx 10$ [35]. Thus, it is expected that systems with $N_t \gg \xi$ will behave three-dimensionally and cross over to two-dimensional behavior when $N_t \sim \mathcal{O}(\xi) = \mathcal{O}(10)$. It is this scenario that we find the most natural and we probed the system at finite thickness N_t for such behavior in the following.

3.2.2 Tricriticality

As argued in the scenario above, for $N_t = N_t^*$ and $K = K_c(N_t)$ we expect a multicritical point. Tri - or multicritical behavior of $d = 2$ Potts models occurs for example for the dilute Potts model or Potts lattice gas (PLG) [23, 33] which introduces vacancies through an additional site

variable $t_i \in \{0, 1\}$ for the vacant (occupied) site i ,

$$-\beta H_{\text{PLG}} = K \sum_{\langle ij \rangle} t_i t_j \delta_{s_i s_j} - \Delta \sum_i t_i. \quad (3.5)$$

In the extended parameter space of q , K and the vacancy chemical potential Δ , the $d = 2$, $q \leq 4$ transition can be driven to first order by increasing the vacancy concentration. Thus for a particular parameter set ($q \leq 4, K_t(q), \Delta_t(q)$) the PLG will exhibit multicritical behavior which, strictly speaking, only for $q = 2$ corresponds to a TCP. Traditionally, the literature [23, 32, 33] does not make a distinction here and the term “tricritical” is used to denote the change from first to second order behavior. The exponents of this $d = 2, q = 3$ “tricritical” universality class are given in Tab.3.1(b). In our case we want to drive the model (3.4) first order by increasing its thickness, i.e. by “dimensional crossover”. As the correlation length ξ diverges, $\xi/a \gg N_t$, our system will be effectively two-dimensional at or near the TCP and we expect it to be in the same universality class as the two-dimensional *PLG*.

3.3 Numerical Experiments

Using standard techniques such as the Wolff single cluster algorithm [27] and the worm algorithm [25], we simulated the Potts model (3.4) for successive system sizes $L^2 \times N_t$, $L = 2^n$, $n = 6, \dots, 9$ and $N_t = 2, \dots, 22$ with periodic b.c. in all directions.

3.3.1 Observables and results

3.3.1.1 Collapse of probability distributions

We want to distinguish a weak first order from a second order and a tricritical transition. At continuous phase transitions like the latter two we can make a finite-size scaling ansatz for observables in a finite volume. In particular the specific heat $c_V = V(\langle e^2 \rangle - \langle e \rangle^2)$ or magnetic susceptibility $\chi_m = V(\langle |m|^2 \rangle - \langle |m| \rangle^2)$ will depend on the ratio L/ξ and behave as $c_V \sim L^{\alpha/\nu} \tilde{c}(tL^{1/\nu})$ and $\chi_m \sim L^{\gamma/\nu} \tilde{\chi}(tL^{1/\nu})$, respectively, where $e = 1/V \sum_{\langle ij \rangle} \delta_{s_i, s_j}$, $m = 1/V \sum_k \exp(i2\pi/3s_k)$ and $|t| = |\frac{K-K_c}{K_c}| \sim \xi^{-1/\nu}$. Instead of the magnetization density m as defined above, we consider the components of magnetization v_i , that is the fraction of spins in state $q_i = 1, 2, 3$. In the disordered phase we will have $\langle v_i \rangle \approx 1/q = 1/3$ as each spin fluctuates independently. In the ordered phase, the distribution $P(v_i)$ will be strongly peaked at small values close to zero and near 1. If we approximate $P(v)$ by $P_{L \rightarrow \infty} = \frac{1}{q}((q-1)\delta(0) + \delta(1))$ in the disordered phase or at the transition in case of coexistence by $P_{L \rightarrow \infty} = \frac{1}{q+1}((q-1)\delta(0) + \delta(1/q) + \delta(1))$, we see that $\langle v_i \rangle = 1/q$ remains valid. To locate the tricritical point our method is the following: Coming from large values of N_t we determine the distributions $P_{N_t, L}(e)$, $P_{N_t, L}(v)$ for various $L \gg N_t$ for systems of size $L^2 \times N_t$ tuned to their (pseudo)critical $K_c(N_t)$ (see below). At a continuous transition the scaling assumption

$$P_{N_t, L}(o) = L^y P_{N_t}^*(L^y o, \xi/L) = L^y \tilde{P}_{N_t}(x_o, t \cdot L^{1/\nu}) \quad (3.6)$$

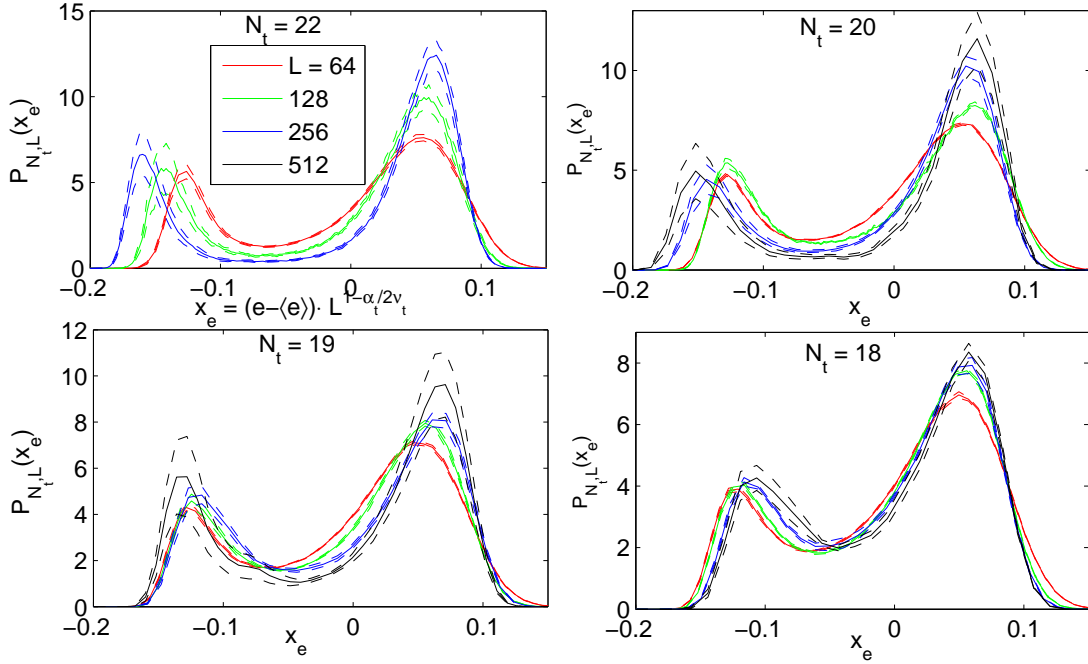


Figure 3.2: Distributions $P_{N_t, L}(x_e)$ with $x_e = (e - \langle e \rangle) \cdot L^{1 - \alpha_t / 2\nu_t}$ and tricritical exponents α_t, ν_t . An approximate collapse is obtained only for $N_t = 18$.

with an appropriate critical exponent y for the observable o and the reduced temperature $t = T/T_c - 1$ lies at the heart of Binder's [37, 38] scaling analysis. In the last step we used $\xi \sim |t|^{-\nu}$ and defined $x_o = L^y(o - \langle o \rangle)$ as well as the universal scaling function $P_{N_t}^*, \tilde{P}_{N_t}$. Note that for distributions P, P^*, \tilde{P} of unit norm, Eq.(3.6) implies universal variance of the latter two

$$\int dx_m x_m^2 \tilde{P}(x_m, t \cdot L^{1/\nu}) = L^{2y} L^{\gamma/\nu - d} \tilde{\chi}_m(t \cdot L^{1/\nu}), \quad (3.7)$$

for $2y = d - \gamma/\nu$ and our choice of $o = |m|$ with the magnetization density m . Thus, using Eq.(3.6) at a continuous transition we can obtain the universal distribution function \tilde{P} . Conversely, by rescaling the argument $o = e, v$ of the distribution $P_{N_t, L}(e), P_{N_t, L}(v)$ to

$$x_e = (e - \langle e \rangle) L^{1 - \alpha_{c,t} / (2\nu_{c,t})} \quad \text{and} \quad x_v = (v - \langle v \rangle) L^{1 - \gamma_{c,t} / (2\nu_{c,t})}, \quad (3.8)$$

where $\gamma_{c,t}, \alpha_{c,t}, \nu_{c,t}$ are the exponents of the critical and tricritical $q = 3, d = 2$ Potts universality class (see Tab.3.1(b)), $P_{N_t, L}(x_e)$ and $P_{N_t, L}(x_v)$ should collapse to a universal scaling curve if the transition is second order or the system is at its tricritical point, respectively. In Fig.3.2 we display the attempted collapse of $P_{N_t, L}(x_e)$ for $N_t = 22, 20 - 18$ using tricritical exponents. For $N_t > 18$ the distributions develop two δ -peaks as $L \rightarrow \infty$ while for $N_t = 18$ an approximate collapse can be achieved, indicating that the system is at or close to the tricritical point. This becomes even much clearer when using v instead of e : In Fig.3.3 we display the same series of figures showing that for $N_t = 18$, the curves $P_{18, L}(x_v)$ fall approximately on top of each other using tricritical exponents while for $N_t \leq 17$ critical scaling can be observed, see Fig.3.4.

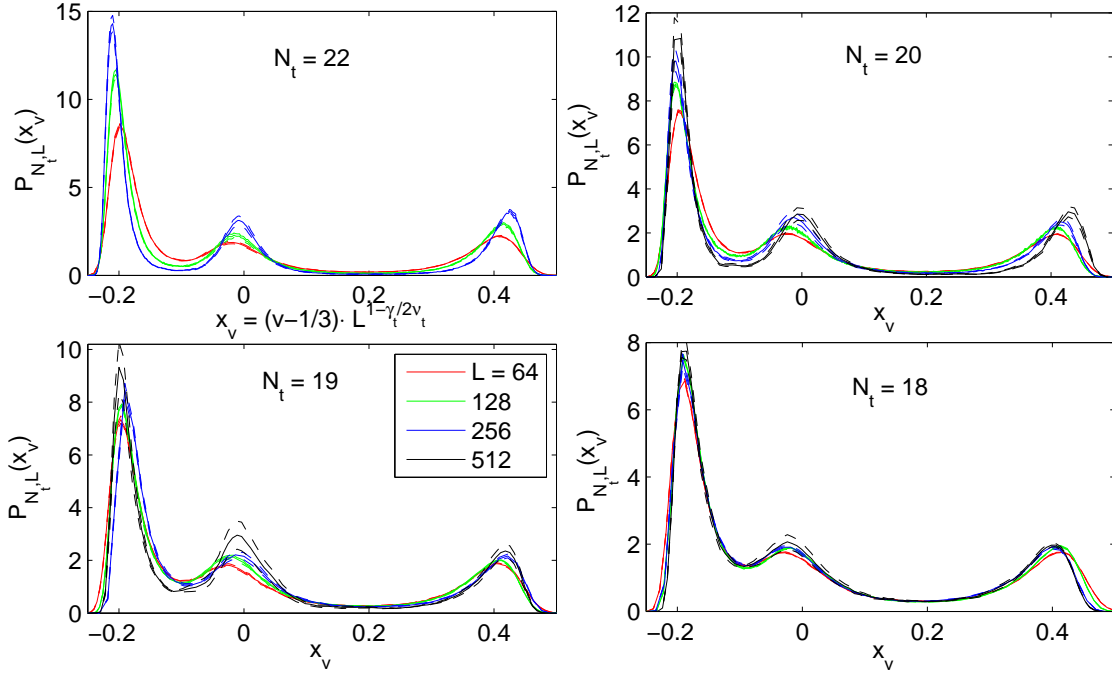


Figure 3.3: Rescaled distributions $P_{N_t, L}(x_v)$ for $N_t = 20 - 18$ using tricritical exponents γ_t, ν_t . A satisfying collapse is visible for $N_t = 18$ (right) indicating that the systems is at its TCP.

We note that there are several definitions of $K_c(N_t)$ in a finite volume, all equivalent in infinite volume. For the case of the distribution $P_{N_t, L}(e)$ and a first order transition, a convenient definition is the *ratio-of-weights* [35], which requires that the areas below the curve $P_{N_t, L}(e)$ left and right of the minimum e_0 , are in proportion 1 : 3 at criticality. We employed this definition of $K_c(N_t)$ for $P_{N_t, L}(x_e)$ within errorbars and reweighted to K_c . In the case of $P_{N_t, L}(x_v)$ we tried to adjust the areas below the three peaks to the ratio 2 : 1 : 1, taking the respective minima to be the interval boundaries.

3.3.1.2 Interface tension

A first order phase transition is characterized by the coexistence of the ordered phases with the disordered phase. Quite generally, the probability distribution of an extensive variable such as the energy E with value E_o in the q ordered phases and E_d in the disordered phase, is given by the ansatz

$$P(E) = qP_o(E) + P_d(E) + P_m(E), \quad (3.9)$$

where $P_{o/d} = c_{1,o/d} e^{-\beta f_{o/d}(T)V} e^{-(E-E_{o/d})^2/c_{2,c/d}^2}$ and $f_{o/d}(\beta)$ denotes the free energy of the respective phases. The probability of the mixed phase, i.e. in the presence of two interfaces of area A separating the portion of the volume V_o in an ordered state from the disordered volume V_d , can be approximated by

$$P_m(E) = c_m e^{-\beta(f_o V_o + f_d V_d)} e^{-2\beta\sigma A}, \quad (3.10)$$

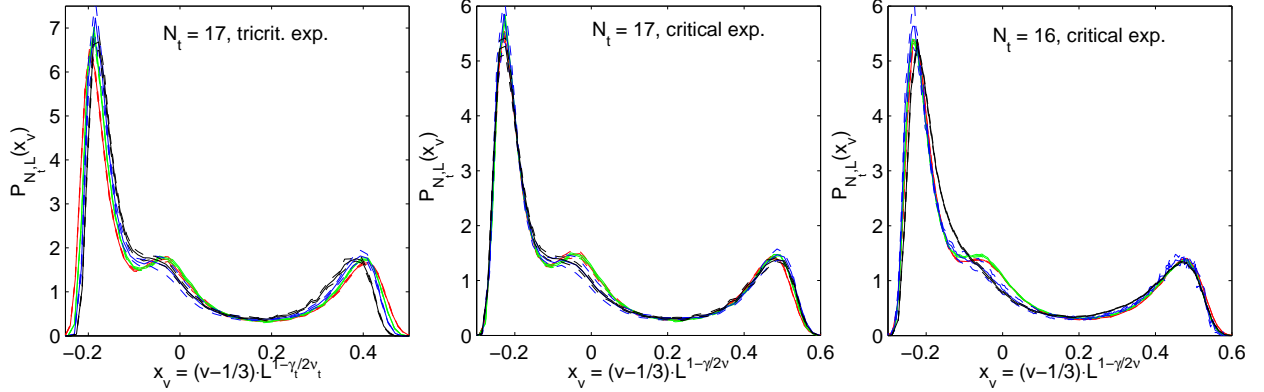


Figure 3.4: Rescaled $P_{N_t, L}(v)$ for $N_t = 17, 16$. Using critical exponents γ, ν for $N_t = 17$ (middle) yields a better collapse compared to tricritical exponents (left). Also shown is the $N_t = 16$ system at criticality (right).

where $E = E_o V_o + E_d V_d$ and σ is the surface tension. In a finite volume, in the vicinity of the pseudocritical β , $P(E)$ will have maxima $P_{\max, o}$ and $P_{\max, d}$ at E_o/d and a minimum in the coexistence region described by P_m at $E_{\min} = \alpha_o E_o + \alpha_d E_d$. If we define

$$\beta\sigma_L = -\ln \frac{P_{\min}}{(P_{\max, o})^{\alpha_o} (P_{\max, d})^{\alpha_d}} / (2A) \quad (3.11)$$

then $\sigma = \lim_{L \rightarrow \infty} \sigma_L$. In our case of a volume $L^2 \times N_t$, interfaces with area L^2 in the plane perpendicular to the t -direction are exponentially suppressed in L compared to interfaces forming in the (t, x_i) -plane ($x_i = x, y$) with area LN_t . If we reweight the distributions $P_{N_t, L}(E)$ in K such that the peaks $P_{\max, o/d}$ in the ordered and disordered phase are of equal height, then Eq.(3.11) becomes

$$\beta\sigma_{N_t, L} = -\ln (P_{\min, N_t, L}(E) / P_{\max, N_t, L}(E)) / (2N_t L) \quad (3.12)$$

as $\alpha_o + \alpha_d = 1$. For a first order behavior in a $L^2 \times N_t$ volume, $\sigma_{N_t, L}$ will be related to the infinite volume ($L \rightarrow \infty$) interface tension σ_{N_t} by $\sigma_{N_t, L} = \sigma_{N_t} - \frac{c}{LN_t}$, $c > 0$ [39]. In Fig.3.5 we show $a^2\beta\sigma_{N_t, L}$ as a function of $1/L$ for $N_t = 16-20, 22$. Our data show a linear relation, having a slope opposite in sign to the prediction. Clearly, finite volume corrections are of different origin at this cross over from second order to first order behavior but qualitatively similar to [40]. We therefore extrapolate linearly and obtain for $N_t = 19$, $a^2\beta\sigma_{N_t=19} = (4 \pm 1) \cdot 10^{-5}$ which is an order of magnitude smaller than $a^2\beta\sigma_{d=3} = 8.15(10) \cdot 10^{-4}$ [35]. $N_t \leq 18$ gives an estimate consistent with zero, indicating that for $N_t \leq 18$ the system has a continuous phase transition without coexisting domains.

3.3.1.3 Correlation function

In ref. [25] an alternative representation of the Potts partition function suitable for the worm algorithm was presented. After a change of variables from the Potts spins $s_i = 1, \dots, 3$ to

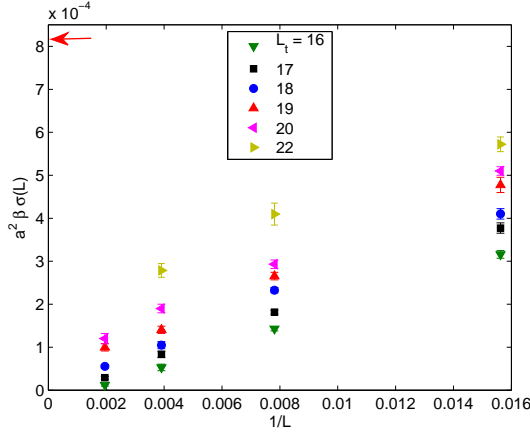


Figure 3.5: $\sigma_{N_t, L}$ as function of $1/L$ for $N_t = 16 - 20, 22$. The arrow denotes $a^2 \beta \sigma_{d=3}$ [35].

oriented bond occupation numbers $n_b, m_b = 0, 1$, ($b = (x, \mu)$) the partition function reads

$$Z = \sum_{\{n_b, m_b\}, CP} \prod_b W_{(n_b, m_b)}, \quad \text{with } W_{(n_b, m_b)} = \begin{cases} A, & \text{if } (n_b, m_b) = (0, 0) \\ AB/2, & \text{if } (n_b, m_b) = (0, 1) \text{ or } (1, 0), \end{cases} \quad (3.13)$$

where $A = \frac{1}{3} \left(e^{\frac{2}{3}K} + 2e^{-\frac{1}{3}K} \right)$ and $B = 2 \left(\frac{e^K - 1}{e^K + 2} \right)$. n_b, m_b represent the numbers of incoming and outgoing currents on bond $b = (x, \mu)$, respectively. At each site i the constraint

$$\underbrace{\sum_{\mu} n_{i, \mu} + n_{i, -\mu}}_{p_i} = \underbrace{\sum_{\mu} m_{i, \mu} + m_{i, -\mu}}_{q_i} \pmod{3}, \quad (3.14)$$

has to be satisfied which we denote by CP(closed paths) in Eq.(3.13). For the two-point function $G(i, j) = \langle s_i s_j \rangle$ this constraint is modified at the sites i and j to $p_i = q_i + 1 \pmod{3}$ and $p_j = q_j - 1 \pmod{3}$, and one obtains [25] $G(i, j) = \frac{1}{Z} \sum_{\{n_b, m_b\}, CP_{ij}} \prod_b W_{(n_b, m_b)}$. $G(i, j)$ and $\frac{d}{dK} G(i, j)$ can be measured efficiently during the worm update, say at Potts coupling K_0 . Thus we can determine the two-point function in a narrow range in K with a single run at K_0 via $G(i, j)_K = G(i, j)_{K_0} + \frac{d}{dK} G(i, j)_{K_0} (K - K_0) + \mathcal{O}((K - K_0)^2)$.

At a continuous phase transition in infinite volume $G(\vec{r} = \vec{r}_i - \vec{r}_j) \sim \frac{1}{r^{\eta+d-2}}$ with the exponent η of the critical or tricritical Potts universality class. In a finite volume this behavior will be modified according to $G(\vec{r}) \sim \frac{1}{L^\eta} f(r/L)$ by a renormalization group argument, with a universal scaling function $f(r/L)$. We further note, that if the correlation length ξ/a diverges, an $L^2 \times N_t$ system will be dimensionally reduced to $d = 2$. Using the worm algorithm, we therefore determined $G_{N_t, L}(\vec{r})$ and $\frac{d}{dK} G_{N_t, L}(\vec{r})$ for systems at or close to their pseudo critical $K_c(N_t)$, averaging over the t -direction. In Fig.3.6 we display the so obtained $G_{N_t, L}(r_{2D}) \cdot L^\eta$ for $N_t = 18$ as a function of r_{2D}/L and $L = 32, 64, 128$. Using the tricritical (right) exponent η_t , the curves fall on top of each other, but fail to collapse when critical scaling is assumed (left).

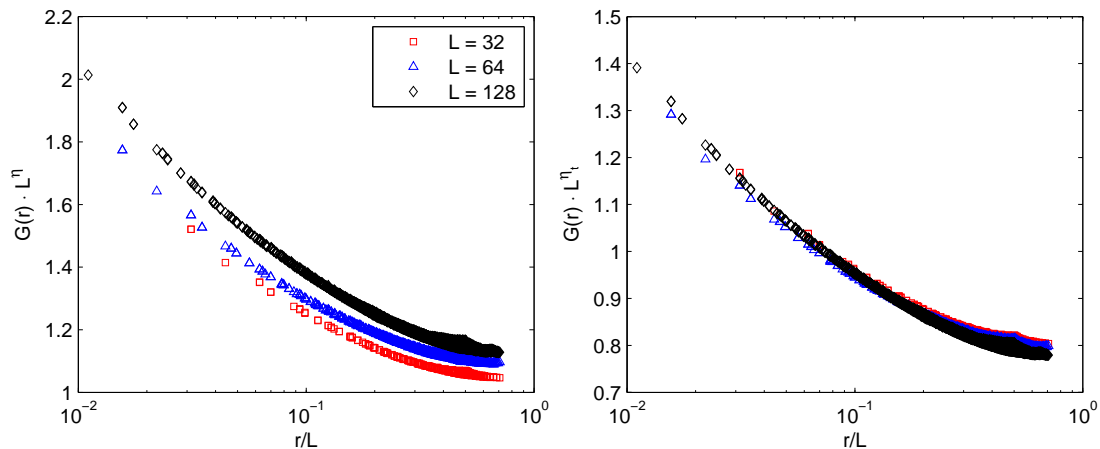


Figure 3.6: $N_t = 18$: Failing collapse $G(r) \cdot L^\eta$ (left), collapse $G(r) \cdot L^{\eta_t}$ (right)

3.4 Conclusion

Choosing as criteria the scaling of probability distributions and correlation functions at criticality as well as the interface tension, our data support that the system has a first order transition for $N_t > 18$, while being second order for $N_t < 18$. At $N_t = 18$ the transition is most likely either second or first order as tricriticality corresponds to fine-tuning in N_t which is a discrete variable in our setup. Further, tricritical scaling in the vicinity of the TCP implies that the exponents depend on the directions taken towards the transition point. A better strategy would therefore require to introduce anisotropic couplings K_t, K_s for the time-like and space-like directions, respectively to approach the tricritical point from directions other than $N_t = n = \text{const}$, $n \in N$ in the $(K, 1/N_t)$ -plane.

Our result confirms the naive expectation that the tricritical behavior occurs when $N_t^* \sim \xi^{\text{1st order}}$ and has to be contrasted with that of an old renormalization group study [36] which found $N_t^* > 32$, a result that strongly depended on the details of the RG transformation.

The significance of our result is ambivalent: In the case of a LGT at finite temperature, one is commonly interested in taking the continuum limit $a \rightarrow 0$ while keeping the temperature $T = 1/(aN_t)$ fixed, tuning the inverse bare coupling β appropriately. A change in the order of the transition with increasing N_t would then be considered as a lattice artifact as one is eventually interested in the $N_t \rightarrow \infty$ limit for fixed T . On the other hand, in the context of classical statistical models, our finding is interesting on its own: Cross over from first to second order behavior is usually associated with a tunable parameter such as a symmetry breaking field or chemical potential. Here we add to this list the cross over due to finite thickness, which breaks a geometric symmetry.

4 Nuclear physics from Lattice QCD at strong coupling

In Ch.1 we pointed out that the ultimate goal of studying Lattice QCD at finite density is severely hindered by the sign problem. Here we consider Lattice QCD at strong coupling, starting from the original work of Rossi & Wolff [41] where the partition function of Lattice QCD at infinite gauge coupling was mapped onto that of a dimer system. This rewriting of the partition function is the essential ingredient of their approach and will be presented in detail. Karsch & Mütter [9] developed an efficient algorithm to study the resulting model and could in particular solve the fermionic sign problem present even for zero quark chemical potential in this formulation. In [42] however it was realized that the algorithm suffered from ergodicity problems. In the following chapter we show, based on the work of [43], how the worm algorithm can be applied to this model. Having overcome the practical (algorithmic) questions we turn to the physics and find two central features of Lattice QCD at strong coupling: Firstly, the theory has its own (strong coupling) variant of nuclear physics which will be part of this chapter. Secondly, the sign problem arising at finite baryon density remains mild and enables us to study the phase diagram of the model in Ch.5. The results presented are based on a publication with Ph. de Forcrand [44].

4.1 Partition function, worm formulation, cross checks

4.1.1 Partition function

We start by restating the lattice QCD partition function Eq.(2.29)

$$Z(\mu, T, m_q) = \int \mathcal{D}\chi \mathcal{D}\bar{\chi} \mathcal{D}U e^{S_F}, \quad (4.1)$$

now in the limit of infinite bare gauge coupling $\beta = 0$ with one flavor of staggered fermions¹,

$$S_F = \sum_x \left\{ \sum_{\mu=0,d} \eta_{\hat{\mu}}(x) \left(\bar{\chi}_x U_{\hat{\mu}}(x) \chi_{x+\hat{\mu}} - \bar{\chi}_{x+\hat{\mu}} U_{\hat{\mu}}^\dagger(x) \chi_x \right) + 2am_q \bar{\chi}_x \chi_x \right\}. \quad (4.2)$$

We take $U_{\hat{\mu}}(x) \in SU(N)$ and suppress color indices. The system is defined on an $L^d \times N_t$ lattice with anti-periodic boundary conditions (bc) in direction $\hat{0}$ and periodic bc elsewhere. In

¹The staggered quark fields appearing in Eq.(2.29) have been rescaled with $\chi, \bar{\chi} \rightarrow i\sqrt{2}\chi, i\sqrt{2}\bar{\chi}$, thus canceling the factor $\frac{1}{2}$ conventionally appearing in the action and introducing an additional minus-sign which cancels the minus-sign in front of the action. As a consequence the mass term is multiplied by 2. This convention is advantageous in the context of the one-link integral Eq.(4.6).

the presence of a quark chemical potential μ and an asymmetry γ which in the weak coupling limit fulfills $\gamma = a/a_t$, the links $U_{\pm\hat{0}}(x)$ receive an additional factor $\gamma \exp(\pm a_t \mu)$. Further, we recall (see Sect.2.2.2.2) that for $am_q = 0$, the action (4.2) satisfies a $U_A(1)$ symmetry

$$\bar{\chi}_x \rightarrow \bar{\chi}_x e^{i\epsilon(x)\theta_A}, \quad \chi_x \rightarrow e^{i\epsilon(x)\theta_A} \chi_x, \quad \epsilon(x) = (-1)^{\sum_{\mu} x_{\mu}}, \quad (4.3)$$

in addition to the usual $U_V(1)$ symmetry

$$\bar{\chi}_x \rightarrow \bar{\chi}_x e^{-i\theta_B}, \quad \chi_x \rightarrow e^{i\theta_B} \chi_x, \quad (4.4)$$

which corresponds to baryon number conservation. Because $\beta = 0$, the link integration $\int \mathcal{D}U = \int \prod_{x,\mu} dU_{\hat{\mu}}(x)$ in Eq.(4.1) factorizes

$$\begin{aligned} Z &= \int \prod_x \left(d\chi_x d\bar{\chi}_x e^{2am_q \bar{\chi}_x \chi_x} \prod_{\mu} \left[dU_{\hat{\mu}}(x) e^{\eta_{\hat{\mu}}(x) (\bar{\chi}_x U_{\hat{\mu}}(x) \chi_{x+\hat{\mu}} - \bar{\chi}_{x+\hat{\mu}} U_{\hat{\mu}}^{\dagger}(x) \chi_x)} \right] \right) \\ &=: \int \prod_x \left(d\chi_x d\bar{\chi}_x e^{2am_q \bar{\chi}_x \chi_x} \prod_{\mu} z(x, \mu) \right). \end{aligned} \quad (4.5)$$

In the second step we defined the *one-link integral* $z(x, \mu)$ which is of the form

$$z(x, \mu) = \int_G dg e^{\text{tr}(gm^{\dagger} + mg^{\dagger})}, \quad (4.6)$$

where G denotes the gauge group with elements g . Taking $y = x + \hat{\mu}$, we set $(m)_{ij} = \chi_{x,i} \bar{\chi}_{y,j}$ and $(m^{\dagger})_{kl} = -\chi_{y,k} \bar{\chi}_{x,l}$ with explicit color indices i, j, k, l .

Integrals of the type (4.6) are known for various gauge groups [45–48] in the sense that these references give closed expressions for $z(x, y)$ in terms of group invariants. In the present case of one flavor of staggered fermions with gauge group $U(N)$ or $SU(N)$ one obtains (see Sect.8.1 for details)

$$\begin{aligned} z(x, y) &= \sum_{k=0}^N \left\{ \frac{(N-k)!}{N!k!} ((\eta_{\hat{\mu}}(x) \gamma^{\delta_{0,\mu}})^2 \bar{\chi}_x \chi_x \bar{\chi}_y \chi_y)^k \right\} + \\ &\quad + \frac{\kappa}{N!} ((\rho(x, y) \bar{\chi}_x \chi_y)^N + (-1)^N (\rho(y, x) \bar{\chi}_y \chi_x)^N) \\ &= \sum_{k=0}^N \left\{ \frac{(N-k)!}{N!k!} ((\eta_{\hat{\mu}}(x) \gamma^{\delta_{0,\mu}})^2 M(x) M(y))^k \right\} + \\ &\quad + \kappa (\rho(x, y)^N \bar{B}(x) B(y) + (-1)^N \rho(y, x)^N \bar{B}(y) B(x)), \end{aligned} \quad (4.7)$$

where

$$\kappa = \begin{cases} 1, & SU(N) \\ 0, & U(N) \end{cases} \quad \text{and} \quad \rho(x, y) = \eta_{(y-x)}(x) \begin{cases} \gamma \exp(\pm a_t \mu), & (y-x)_0 = \pm 1 \\ 1, & \text{otherwise} \end{cases}.$$

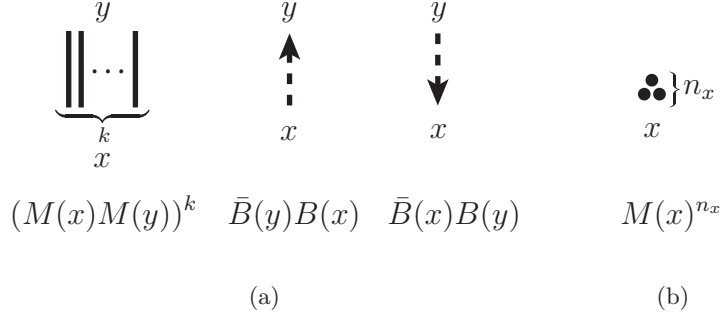


Figure 4.1: (a) Mesonic and baryonic links as defined in Eq.(4.7). (b) Graphical notation for a monomer term.

Here we denote by

$$M(z) = \bar{\chi}_z \chi_z \quad \text{and} \quad B(z) = \frac{1}{N!} \varepsilon_{i_1 \dots i_N} \chi_{z, i_1} \dots \chi_{z, i_N} \quad (4.8)$$

the bosonic (“mesonic”) and fermionic (“baryonic”, $\kappa = 1$) color-singlet states, respectively, of the underlying gauge group.² As it will be useful for the following discussion we introduce a pictorial representation of the new degrees of freedom in Fig.4.1(a).

We now turn to the remaining Grassmann integral of Eq.(4.5). The integration is done per site x and relies on the relation

$$\int \prod_a [d\chi_{a,x} d\bar{\chi}_{a,x}] e^{2am_q \bar{\chi}_x \chi_x} (\bar{\chi}_x \chi_x)^k = \frac{N!}{n_x!} (2am_q)^{n_x}, \quad n_x = N - k \quad (4.9)$$

which is obtained by using the definition of the Berezin-integral $\int d\xi d\bar{\xi} \xi \bar{\xi} = 1$ for Grassmann numbers $\bar{\xi}, \xi$. The integration rule (4.9) is applied to evaluate the integral Eq.(4.5), where $z(x, \mu)$ is given by (4.7). There, when taking the product over x and μ a constraint arises in order to have non-vanishing contribution to the partition function: At every site x , all degrees of freedom $\bar{\chi}_{x,i}, \chi_{x,i}$ have to be “paired”. This can happen

- in form of a meson hopping from site x to a neighboring site y , forming a non-oriented link (dimer) $(M(x)M(y))^k$, see Fig.4.1(a). This defines the link-occupation number $k \equiv k_{\hat{\mu}} \in \{0, \dots, N\}$, $\hat{\mu} = y - x$.
- in form of baryon hopping ($\kappa = 1$) from x to y to form an oriented baryonic link $\bar{B}(y)B(x)$ ($B(x)B(y)$), Fig. 4.1(a). In this case, as a baryon $B(x)$ employs all of the $\chi_{x,i}$ ($i = 1, \dots, N$) the site x must be paired with another site z with a pair of the form $\bar{B}(x)B(z)$. This way one recognizes that baryons must form self-avoiding, oriented loops (ℓ) to yield a non-vanishing contribution to (4.5). As a loop ℓ enters a site x from an incoming direction, say $\hat{\mu}$ and leaves the site in an outgoing direction $\hat{\nu} \neq \hat{\mu}$, we can assign to each

²Note that $B(z)$ as defined in Eq.(4.8) transforms under gauge transformations $\Omega \in G$ according to $B(z) = \frac{1}{N!} \varepsilon_{i_1 \dots i_N} \chi_{z, i_1} \dots \chi_{z, i_N} \rightarrow \frac{1}{N!} \varepsilon_{i_1 \dots i_N} \Omega_{i_1, j_1} \chi_{z, j_1} \dots \Omega_{i_N, j_N} \chi_{z, j_N} = \frac{1}{N!} \varepsilon_{i_1 \dots i_N} \chi_{z, i_1} \dots \chi_{z, i_N} \det \Omega$. Baryons B are therefore *not* gauge invariant if $\Omega \in U(N)$ and we have to set $\kappa = 0$ for $G = U(N)$ in Eq.(4.7).

site the baryonic link variable $b_{\hat{\rho}}(x) \in \{-1, 0, 1\}$, $\hat{\rho} = \pm\hat{0}, \dots, \pm\hat{d}$ to obtain the constraint

$$\sum_{\hat{\rho}=\pm\hat{0},\dots,\pm\hat{d}} b_{\hat{\rho}}(x) = 0, \quad (4.10)$$

where $b_{\hat{\rho}}(x) = -1, 0, 1$ stand for an incoming, non-occupied and outgoing baryonic link, respectively. Although the partition function Z in Eq.(4.12) below depends on the baryonic degrees of freedom in terms of loops ℓ , the link variables $b_{\hat{\rho}}$ will be particularly useful for the formulation of the loop update in Sect.4.1.2.

- at the site x itself, thus forming monomer terms $M(x)^{n_x}$, $n_x \in \{0, \dots, N\}$ which we depict in Fig.4.1(b), where

$$n_x + \sum_{\hat{\mu}=\pm\hat{0},\dots,\pm\hat{d}} k_{\hat{\mu}} = N. \quad (4.11)$$

In the following we specialize to the case $SU(3)$. The final expression after integration can now be given as a sum over configurations $\{k, n, \ell\}$ with non-vanishing contribution,

$$Z = \sum_{\{k, n, \ell\}} \prod_{b=(x, \hat{\mu})} \frac{(3 - k_b)!}{3!k_b!} \gamma^{2k_b \delta_{\hat{0}, \hat{\mu}}} \prod_x \frac{3!}{n_x!} (2am_q)^{n_x} \prod_{\ell} w(\ell), \quad (4.12)$$

where the first term is obtained from meson hopping, the second term is the contribution from monomers and the third term accounts for baryonic world lines (loops ℓ) with weight $w(\ell)$. If a baryon loop ℓ has $N_{\hat{0}}$ links in (positive and negative) $\hat{0}$ -direction and winding number r_{ℓ} in this direction, it is given by

$$w(\ell) = \frac{1}{\prod_{x \in \ell} 3!} \sigma(\ell) \gamma^{3N_{\hat{0}}} \exp(3N_t r_{\ell} a_t \mu) \quad (4.13)$$

with a geometry dependent *sign* $\sigma(\ell) = (-1)^{r+N_-(\ell)+1} \prod_{b=(x, \hat{\mu}) \in \ell} \eta_{\hat{\mu}}(x)$. Here $N_-(\ell)$ is the number of links in all negative directions. Important parameters entering Z in Eq.(4.12) are the bare quark mass am_q , the chemical potential $a_t \mu$, the asymmetry γ and the number of lattice sites in $\hat{0}$ -direction, N_t . This concludes the reformulation of the partition function Z . We now comment on important features of the model defined by (4.12).

4.1.1.1 Configuration space

In Fig.4.2(a) we draw a 4×4 sample configuration. We distinguish two types of self-avoiding loops: Baryonic (dashed) loops with a natural orientation can be either trivially closed as in the middle of the figure or wind around the lattice in any direction. Loops winding in $\hat{0}$ -direction contribute to the baryon number (discussed in Sect.4.1.1.3) and can thus be associated with propagating (anti)-baryons. Another type of loop consists of sequences of alternating $k_b = 1, 2$ dimers. These *Polymer* loops always have positive weight unlike the baryons.

If a site x is not traversed by a baryonic loop, the constraint (4.11) has to be fulfilled. For a neighboring pair of sites x and y this can be achieved in a number of ways, e.g. by a $k_b = 3$ dimer or a pair of monomers at either site combined with a 2-dimer in between, see Fig.4.2(a).

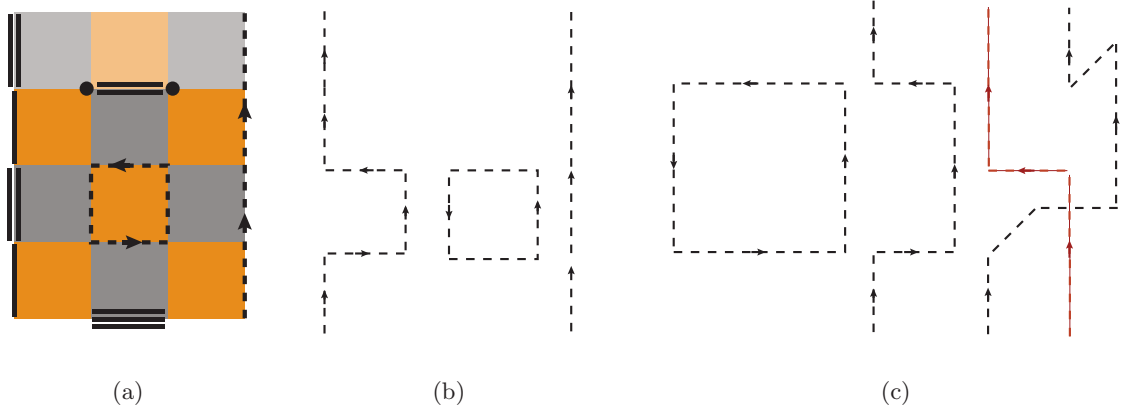


Figure 4.2: (a) 4×4 Example configuration. The transparent plaquettes imply periodic continuation in $\hat{0}$ -direction. (b) Three typical baryonic loops with $\sigma(\ell) = +1$. To this class belongs the straight line on the right, corresponding to a static baryon. (c) A sample of baryonic loops with $\sigma(\ell) = -1$. The rightmost loop, winding twice in $\hat{0}$ -direction represents an exchange in the spatial position of two baryons thus carrying a minus-sign as compared to two parallel, static world lines.

4.1.1.2 Sign $\sigma(\ell)$

The sign $\sigma(\ell)$, given below Eq.(4.13), is associated with the (composite) fermionic degrees of freedom. The model thus has a minus-sign problem which seems to be present even at zero quark chemical potential $\mu = 0$. Karsch and Mütter [9] however showed that at least at $\mu = 0$ the minus sign can be removed completely by a change of variables (see Sect.8.2). In Fig.4.2(b) and 4.2(c) we display samples of loops with $\sigma = +1, -1$, respectively. Note that the static baryon (straight, vertical line) has $\sigma = +1$. We will be concerned with the severity of the sign problem for finite μ in Sect.5.2.3 where we give also a more detailed account of the effectiveness of Karsch's trick.

4.1.1.3 Observables

With the partition function Z , (4.12), we can now define important observables and their corresponding expressions in terms of the new degrees of freedom.

- The chiral condensate $\langle \bar{\psi}\psi \rangle$ is given by

$$a^3 \langle \bar{\psi}\psi \rangle = \frac{1}{V_s N_t} \frac{\partial}{\partial (2am_q)} \log Z = \frac{1}{2am_q V_s N_t} \langle \sum_x n_x \rangle =: \frac{1}{2am_q} \langle n_M \rangle. \quad (4.14)$$

The last term defines the monomer density $n_M = N_M/V$ with total number of monomers N_M .

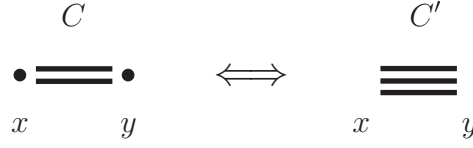


Figure 4.3: Example of a MDP-update: A pair of monomers on neighboring sites x, y is replaced by a dimer, thus turning the configuration C into a configuration C' and vice versa.

- The baryon density ρ_B is given by

$$a^3 \rho_B = \frac{1}{V_s N_t} \frac{\partial}{\partial (3a_t \mu)} \log Z = \frac{1}{V_s} \left\langle \sum_{\ell} r_{\ell} \right\rangle. \quad (4.15)$$

r_{ℓ} already occurred in Eq.(4.13) and denotes the winding number in t -direction of the baryon loop ℓ . Due to the self-avoiding nature of baryon loops, $|a \rho_B|$ cannot exceed 1, i.e. 1 baryon or antibaryon per spatial site.

- To obtain an expression for the energy density ϵ , defined by

$$a^3 \epsilon = - \frac{1}{V_s} \frac{\partial}{\partial \beta} \log Z \Big|_{a_t \mu} = - \frac{1}{V_s N_t} \frac{\partial}{\partial a_t} \log Z \Big|_{a_t \mu} = - \frac{1}{V_s N_t a} \frac{\partial}{\partial \gamma} \log Z \Big|_{a_t \mu} \frac{\partial \gamma}{\partial h(\gamma)} \quad (4.16)$$

one needs to know the function $f(\gamma) = 1/h(\gamma)$ relating the spatial and temporal lattice spacings a, a_t via $f(\gamma) = \frac{a}{a_t}$ at strong coupling. While in the weak coupling regime $f(\gamma) = \gamma$ [49], this relation does not hold for $g \rightarrow \infty$ and indeed mean-field theory [13] finds that $\frac{a}{a_t} = \gamma^2$ in the limit of large γ on the $T = 0$ and $\mu = 0$ axis. We are thus left with the expression

$$a^4 \epsilon = - \frac{1}{V_s N_t} \frac{1}{\gamma} \frac{\partial \gamma}{\partial h(\gamma)} \langle 2N_{Dt} + 3N_{Bt} \rangle, \quad (4.17)$$

where $N_{Dt} = \sum_x k_{\hat{0}}(x)$ and $N_{Bt} = \sum_x |b_{\hat{0}}(x)|$ are the total number of dimer- and (anti)baryonic links in $\hat{0}$ -direction, respectively.

4.1.2 The worm algorithm in strong coupling QCD

The partition function (4.12) was first systematically studied for small systems and $am_q > 0$ in [9]. The degrees of freedom involved, namely monomers, dimers and polymers gave rise to the name MDP-formalism. In view of the constraint Eq.(4.11), the algorithmic strategy consists of a local update using Metropolis dynamics:

4.1.2.1 MDP-update

The update relies on the fact that every configuration which contributes to the partition function Z has to fulfill the constraint (4.11). In Fig.4.3 we depict two configurations C, C' of neighboring sites x and y . The local update replaces, with probability $P(C'|C)$, a pair of adjacent monomers by a dimer, which has to be balanced by the reverse step with probability

$P(C|C')$. Probabilities for either replacement have to fulfill a balance equation which we choose to be detailed balance,

$$P(C'|C)W(C) = P(C|C')W(C'), \quad (4.18)$$

with the configuration weight $W(C)$. If we define $P(C'|C) = P_{\text{acc}}P_{\text{prop}}$, then one solution for the acceptance probability P_{acc} is given by the Metropolis acceptance $P_{\text{acc}}(C'|C) = \min \left\{ 1, \frac{W(C')P_{\text{prop}}(C|C')}{W(C)P_{\text{prop}}(C'|C)} \right\}$, where P_{prop} is the probability to propose such an update. In our specific example Fig.4.3, to go from C to C' , we see that the ratio $W(C')/W(C) \sim \frac{1}{(2am_q)^2}$. The efficiency of this algorithm thus depends on the quark mass am_q which is not surprising, given the fact that each monomer contributes with a weight $\sim 2am_q$. In the absence of monomers ($am_q = 0$) this algorithm is not applicable and in the limits of very light and very heavy quarks (see [42]) the local update will produce very little change in configuration C due to a low acceptance ratio.

4.1.2.2 Worm, preliminary remarks

In ref. [43], the authors studied various aspects of $U(3)$ lattice gauge theory, i.e. in the absence of baryons. Being aware of the shortcomings of the local monomer update in the chiral limit, they developed a worm-type algorithm, the directed path algorithm (dpa), itself being an adaptation of the directed loop algorithm put forth in [50]. The dpa is essentially a worm algorithm [25, 51] with the special feature of the exclusion of backtracking during the worm update. In the following, we show its applicability and usefulness for $SU(3)$ LGT at strong coupling.

Use of the worm algorithm (WA) has already been made in the case of a classical spin model in Ch.3 (see also Sect.2.3.2). There, the first step consisted of a high-temperature expansion (steps leading to Eq.(2.48)) which resulted in a change of variables from Potts spins φ_x to link occupation numbers $(n_{\hat{\mu}}(x), m_{\hat{\mu}}(x))$, which had to fulfill the constraint

$$\sum_{\hat{\mu}=\pm\hat{0},\dots,\pm\hat{d}} n_{\hat{\mu}}(x) = \left(\sum_{\hat{\mu}} m_{\hat{\mu}}(x) \right) \pmod{3}. \quad (4.19)$$

It is interesting to note that for QCD at strong coupling these preparatory steps have already been carried out, starting in Eq.(4.5). In this context the expansion Eq.(4.7) is the analogue of a high temperature expansion. The change of variables $(\bar{\chi}(x), \chi(x)) \rightarrow (k_{\hat{\mu}}(x), n(x), b_{\hat{\mu}}(x))$ is accompanied by the constraint (4.11), together with the closed loop constraint satisfied by baryons.

We now take our model in the chiral limit, $am_q = 0$, and consider the two-point function

$$G(y, z) = \langle \bar{\chi}\chi_y \bar{\chi}\chi_z \rangle = \frac{1}{Z} \int \prod_x (d\chi_x d\bar{\chi}_x) \bar{\chi}\chi_y \bar{\chi}\chi_z \prod_{x,\mu} z(x, \mu). \quad (4.20)$$

We see that the derivation which led to (4.12) with the constraint (4.11) now has to be only slightly modified and take into account the sources M_y and M_z which will represent monomers at y and z . In the chiral limit, i.e. in the absence of monomers, configurations which contribute

to the monomer-two-point function will have to satisfy the constraint $\sum_{\hat{\mu}} k_{\hat{\mu}} + \delta_{x,y} + \delta_{x,z} = N$. Thus, contrary to configurations which contribute to the partition function Z , configurations of G will contain two monomers at y and z which do not carry a weight $2am_q$. For $am_q > 0$, if we insist on the distinction between monomers and sources, the constraint will read $\sum_{\hat{\mu}} k_{\hat{\mu}} + n_x + \delta_{x,y} + \delta_{x,z} = N$.

Further, for $am_q = 0$, under a symmetry transformation Eq.(4.3), $G(y, z)$ transforms according to

$$G(y, z) = \langle \bar{\chi} \chi_y \bar{\chi} \chi_z \rangle \rightarrow e^{i2\theta_A(\epsilon(y)+\epsilon(z))} \langle \bar{\chi} \chi_y \bar{\chi} \chi_z \rangle, \quad (4.21)$$

so that $G(y, z)$ can be non-zero only if y, z are lattice sites of opposite parity, $\epsilon(y) = -\epsilon(z)$. For $am_q > 0$, this symmetry is broken explicitly and the lattice will be populated by a finite density of monomers. The role of the quark mass is thus comparable to a magnetic field h breaking the Z_3 symmetry of the Potts model, discussed in Ch.3.

Taking these preliminary remarks into account, we now turn to the practical question of the realization of the worm update. Our model contains both mesonic and baryonic degrees of freedom (dof). The former are present in terms of intersecting loops, possibly terminating in source variables, the monomers, for $am_q > 0$. Baryons form self-avoiding loops without monomer-terms. The WA thus has to update two different kinds of loop gases, including the presence of sources. This can be generalized starting from [43, 52] as follows.

4.1.2.3 Worm, mesonic part

This part of the worm algorithm updates the mesonic dof only. Hence, it cannot change the sign $\sigma(C) = \sigma(\{n, k, b\})$ of a configuration. Since our lattice is bipartite, we can choose to decompose the set of sites into active and passive sites $x_{p/a}$, respectively, and rewrite the partition function Z given by Eq.(4.12) into the form

$$Z = \sum_{\{n, k, b\}} \prod_{x_a} W_a(x_a) \prod_{x_p} W_p(x_p) \sigma(\{n, k, b\}), \quad (4.22)$$

where

$$W_a(x) = \prod_{\hat{\nu}=\pm\hat{0}, \dots, \pm\hat{d}} \left(\frac{(N - k_{\hat{\nu}})!}{N! k_{\hat{\nu}}!} \exp(3b_{\hat{\nu}}(\delta_{\hat{\nu}, \hat{0}} + \delta_{\hat{\nu}, -\hat{0}}) a_t \mu) \right) \frac{N!}{n_x!} (2ma)^{n_x} \quad (4.23)$$

$$W_p(x) = \prod_{\hat{\nu}=\pm\hat{0}} \left(\gamma^{2k_{\hat{\nu}}+3|b_{\hat{\nu}}|} \right) \frac{N!}{n_x!} (2ma)^{n_x}. \quad (4.24)$$

Here we made use of the baryonic link variables $b_{\hat{\nu}}(x)$, satisfying the constraint Eq.(4.10). We represent the state of an active or passive site x by the tuple of parameters $(n_x, k_{\hat{\mu}}, b_{\hat{\mu}}, \hat{\mu} = \pm\hat{0}, \dots, \pm\hat{d})$. In the following we describe the update and show in Sect.8.4.2 that it satisfies detailed balance.

1. We start by choosing with uniform probability a site x that is not member of a baryon loop. The active set of sites is defined as the set that contains all sites with parity $\epsilon(x)$. We should begin by placing a worm head and tail in terms of two monomers at x . Due to the constraint (4.11) this could only happen if we separate head and tail immediately

by erasing a dimer in direction $\hat{\nu}$, with $k_{\hat{\nu}} \neq 0$, and increase the number of monomers $n_x \rightarrow n_x + 1$, $n_{x+\hat{\nu}} \rightarrow n_{x+\hat{\nu}} + 1$. Note that in the chiral limit, this represents going from the set of Z -configurations to configurations that contribute to the two-point function G , Eq.(4.20). Practically however, we introduce only one monomer at x and erase a dimer in direction $\hat{\mu}$ with probability $P_{\hat{\mu}}$

$$P_{\hat{\mu}} = \frac{k_{\hat{\mu}}}{N}. \quad (4.25)$$

We have split the operation ($n_x \rightarrow n_x + 1, k_{\hat{\mu}}(x) \rightarrow k_{\hat{\mu}}(x) - 1, n_y \rightarrow n_y + 1, k_{-\hat{\mu}}(y) \rightarrow k_{-\hat{\mu}}(y) - 1$) in two parts, postponing the change at $y = x + \hat{\mu}$ to the next step. Note that we explicitly distinguish the link occupation numbers $k_{\hat{\mu}}(x)$ and $k_{-\hat{\mu}}(x + \hat{\mu})$, allowing for $k_{\hat{\mu}}(x) \neq k_{-\hat{\mu}}(x + \hat{\mu})$ if the link connecting x and $x + \hat{\mu}$ is updated.

The remaining option at x , to leave the site without any change, is chosen with probability

$$P_x = \frac{n_x}{N}. \quad (4.26)$$

2. The site y is a passive site. The update will change the state of the site by choosing a direction $\hat{\rho}$ and letting ($k_{-\hat{\rho}}(y) \rightarrow k_{-\hat{\rho}}(y) - 1, k_{\hat{\rho}}(y) \rightarrow k_{\hat{\rho}}(y) + 1$). All directions $\hat{\rho}$ are weighted with $W_{\hat{\rho}} = \gamma^{2\delta_{\hat{\rho}, \pm\hat{0}}}$ if the site $y + \hat{\rho}$ is not a member of a baryon loop, otherwise with $W_{\hat{\rho}} = 0$ and the step is carried out using a heat-bath probability

$$P_{\hat{\rho}} = \frac{W_{\hat{\rho}}}{W_D(y)}, \quad W_D(y) = \sum_{\hat{\nu}} W_{\hat{\nu}}. \quad (4.27)$$

3. The site $z = y + \hat{\rho}$ is an active site. In the chiral limit, only the starting site x (by definition an active site) carries a monomer, the worm tail. An active site gives thus the possibility to close the path by erasing a monomer. If we choose this step with a directed path probability P_z , then

$$P_z = \frac{n_z}{N - k_{-\hat{\rho}}}, \quad (4.28)$$

where $k_{-\hat{\rho}}$ is the dimer number of the incoming direction. We then change the site state of site z by ($n_z \rightarrow n_z - 1, k_{-\hat{\rho}} \rightarrow k_{-\hat{\rho}} + 1$) which ends the worm update. The remaining choice is to continue the path by choosing an outgoing direction $\hat{\mu} \neq -\hat{\rho}$ with directed path probability

$$P_{\mu} = \frac{k_{\hat{\mu}}}{N - k_{-\hat{\rho}}}. \quad (4.29)$$

This last step excludes backtracking by omitting steps in direction $-\hat{\rho}$. After letting ($k_{-\hat{\rho}} \rightarrow k_{-\hat{\rho}} + 1, k_{\hat{\mu}} \rightarrow k_{\hat{\mu}} - 1$), the update continues with step 2.

The mesonic worm update satisfies (detailed) balance as shown in Sect.8.4.2. Let us note that backtracking in step 2 cannot be avoided as the site y might be surrounded by baryonic sites. Likewise, in step 1, the site x might be already occupied by N monomers, thus preventing the creation of an additional one.

4.1.2.4 Worm, baryonic part

The purpose of this part of the algorithm is twofold: It completes the above by updating the baryonic loops, i.e. it changes the shape and size of a baryon loop. On the other hand, in order to achieve ergodicity, we should be able to convert mesonic into baryonic dof and vice versa. The update realizes the latter by the ability to turn triple dimers into pairs of baryonic sites along with the reverse.

1. We choose with uniform probability a site x which can be either a site connected to a triple dimer or is traversed by a baryonic loop. Again we consider the partition into active (defined by x) and passive sites with weights given by Eqs.(4.23) and (4.24), respectively. If x is a baryonic site, then $b_{\hat{\mu}} = \pm 1$ for exactly one pair of links. We symbolically place a baryonic source at x (this way conserving the constraint at x) and choose the direction $\hat{\mu}$ whose link will be updated to be that with $b_{\hat{\mu}} = -1$. We set $b_{\hat{\mu}} = 0$ and move to the neighboring site $y = x + \hat{\mu}$. If instead the site x has a link with occupation number $k_{\hat{\mu}} = 3$, then we set $k_{\hat{\mu}} = 0$ and $b_{\hat{\mu}} = 1$.
2. The site y is a passive site. The update changes the state of the site by choosing an outgoing direction $\hat{\rho}$. Possible directions are weighted with $W_{\hat{\rho}} = \gamma^{3\delta_{\hat{\rho},\pm\hat{0}}} \exp(3a_t\mu(\delta_{\hat{\rho},+\hat{0}} - \delta_{\hat{\rho},-\hat{0}}))$ if the site $y + \hat{\rho}$ is a member of a baryon loop or is touched by a triple dimer, otherwise with $W_{\hat{\rho}} = 0$ and the step is carried out using a heat-bath probability

$$P_{\hat{\rho}} = \frac{W_{\hat{\rho}}}{\sum_{\hat{\nu}} W_{\hat{\nu}}}. \quad (4.30)$$

We let $(b_{-\hat{\mu}} \rightarrow b_{-\hat{\mu}} - 1, k_{-\hat{\mu}} = 0, b_{\hat{\rho}} \rightarrow b_{\hat{\rho}} + 1)$ and if $b_{\hat{\rho}} = 0$, then $k_{\hat{\rho}} = 3$.

3. For the active site $z = y + \hat{\rho}$ there are three possible choices:
 - If the site contains a baryonic source, introduced in a first step, then the update ends with probability $P_z = 1$ given by the directed path probabilities. We let $b_{-\hat{\rho}} \rightarrow b_{-\hat{\rho}} - 1$ and if $b_{-\hat{\rho}} = 0$, then $k_{-\hat{\rho}} = 3$.
 - If the site is touched by a triple dimer in direction $\hat{\mu}$, then we change its state with probability $P_{\hat{\mu}} = 1$ according to $(b_{-\hat{\rho}} \rightarrow b_{-\hat{\rho}} - 1, b_{\hat{\mu}} = 1, k_{\hat{\mu}} = 0)$ and continue with step 2.
 - If the site is traversed by a baryon loop s.t. there is a direction $\hat{\mu}$ with $b_{\hat{\mu}} = -1$, then we change its state with probability $P_{\hat{\mu}} = 1$ according to $(b_{-\hat{\rho}} \rightarrow b_{-\hat{\rho}} - 1, b_{\hat{\mu}} = 0)$ and continue with step 2.

The proof of detailed balance for the baryonic worm is very similar to that of the mesonic worm in Sect.8.4.2 and will hence be omitted. We point to [43, 52] for additional details. As the baryonic worm changes the number and shape of baryonic loops the sign $\sigma(C)$ of a configuration changes. Practically, we determine the sign of a configuration once the baryonic worm has closed. Mesonic and baryonic worm updates are performed independently, not necessarily with equal frequency.

4.1.2.5 Worm estimators

It is possible to define worm estimators for relevant observables of our model. Starting from a closed path configuration, i.e. a configuration satisfying the constraint in Eq.(4.11), we introduce head and tail of a mesonic worm and carry out mesonic worm update steps. Let $O(\bar{\psi}\psi)$ and $O(G(x_1, x_2))$ be observables continuously accumulated during the worm update, s.t.

$$\langle \bar{\psi}\psi \rangle = 2am_q N \frac{O(\bar{\psi}\psi)}{K_{CP}} \quad (4.31)$$

$$G(x_1, x_2) = N \frac{O(G(x_1, x_2))}{K_{CP}}, \quad (4.32)$$

where K_{CP} is the number of mesonic worm updates, taking into account the sign $\sigma(C) = \pm 1$ of the configuration updated by the mesonic worm. As the mesonic worm does not touch any baryonic site this sign is not changed throughout the update. In practice K_{CP} will be the difference of the number of closed paths on configurations with positive sign and negative sign. As usual $N = 3$ denotes the number of colors and am_q is the bare quark mass. In Sect.8.4.3.1 we show that during each update of a passive site, say x , $O(\bar{\psi}\psi)$ has to be updated according to

$$O(\bar{\psi}\psi) \rightarrow O(\bar{\psi}\psi) + \frac{V_D}{V} \frac{\sigma(C)}{W_D(x)}, \quad (4.33)$$

where $W_D(x)$ was defined in step (2) of the mesonic worm, V_D denotes the total number of dimer sites (i.e. sites that are not traversed by a baryonic loop) and V is the total number of sites. $\sigma(C) = \pm 1$ is the sign of the current configuration (or equivalently the configuration from which the worm started).

$O(G(x_1, x_2))$ can be accumulated similarly (see Sect.8.4.3.2): During a mesonic worm update with head at the passive site x and tail at the active site y , we update $O(G(x_1, x_2)) \forall x_1, x_2 \in V$ by the prescription

$$O(G(x_1, x_2)) \rightarrow O(G(x_1, x_2)) + V_D \frac{\sigma(C)}{W_D(x)} (\delta_{x,x_1} \delta_{y,x_2} + n_{x_2} \delta_{x,x_1}). \quad (4.34)$$

In the chiral limit $n_{x_2} = 0 \forall x_2 \in V$ except $x_2 = y$ and the last term in Eq.(4.34) vanishes. To see the importance of Eq.(4.34) we note that we can measure the chiral susceptibility χ_σ , defined by

$$\chi_\sigma = \frac{1}{V} \frac{\partial^2}{\partial (2am_q)^2} \log Z = \frac{1}{(2am_q)^2 L^3 N_t} (\langle N_M^2 \rangle - \langle N_M \rangle^2 - \langle N_M \rangle), \quad (4.35)$$

even in the chiral limit, i.e. in the absence of partition function configurations with nonzero N_M , by using the alternative definition

$$\chi_\sigma = \frac{1}{V} \sum_{x_1, x_2} G(x_1, x_2). \quad (4.36)$$

This relation will be of particular importance for the investigation of the phase diagram in the chiral limit, see Sect.5.2.

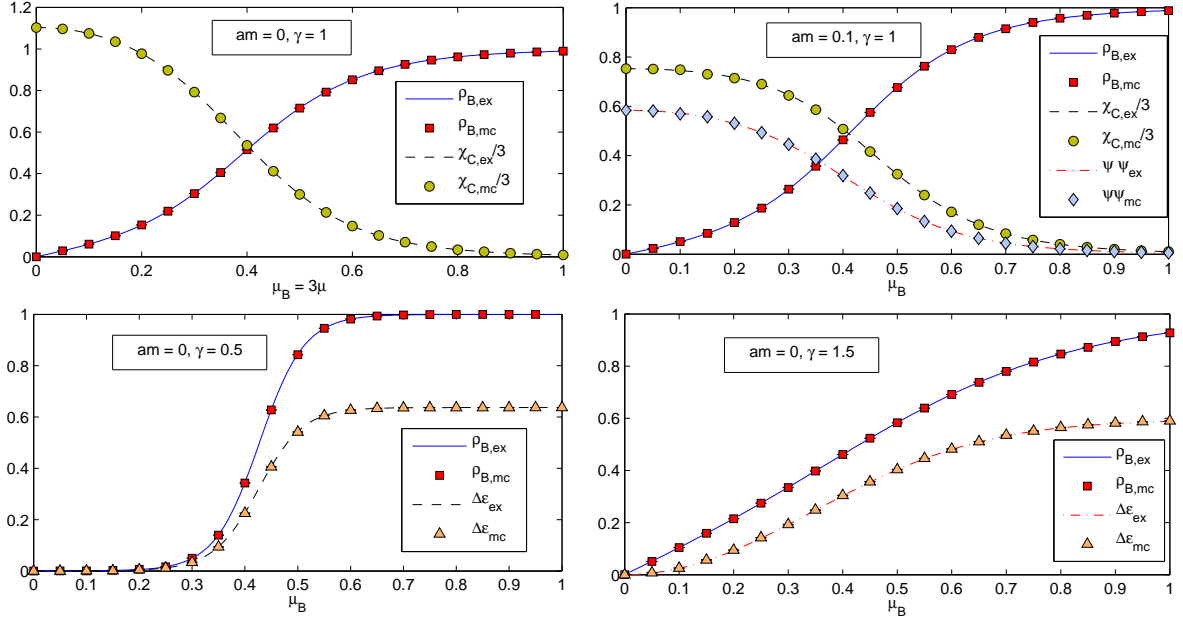


Figure 4.4: Comparing exact (solid and dashed lines) and numerical results (symbols) on a 2×2 system for the baryon density (ρ_B), the energy density (ϵ), the chiral condensate ($\langle\bar{\psi}\psi\rangle$) and its susceptibility (χ_C) using different parameter sets.

4.1.3 Consistency checks

There are limiting cases of the model in which the correctness of our formulation and its implementation can be cross-checked. A simple and basic check can be carried out on a 2×2 lattice where an exact enumeration of all configurations contributing to Z is possible. Moreover, one conventional algorithmic approach to lattice QCD is given by the Hybrid Monte Carlo (HMC) algorithm. Simulations at $\beta = 0, a\mu = 0$ are here easy to perform and results on observables such as $\langle\bar{\psi}\psi\rangle$ or decays of correlation functions represent a non-trivial reference to compare with.

4.1.3.1 Exact enumeration

The partition function (4.12) is of polynomial form in am_q with even powers due to the invariance under $m_q \rightarrow -m_q$. Every site can be occupied by a maximum of $n_{max} = 3$ monomers, Z has therefore degree $3V = 12$, $V = L^d \times N_t = 2 \times 2$. It is convenient to employ the form of (4.12) as used by Karsch and Mütter [9] in which baryonic and mesonic loops are combined into polymers (see Sect.8.2)

$$Z = \sum_C W(C) = \sum_{C=\{k,n,\ell\}} \gamma^{2N_{D\hat{0}}} (2am_q)^{N_M} \frac{1}{3}^{N_{D_1}+N_{D_2}} \prod_x w(x) \prod_\ell w(\ell), \quad (4.37)$$

where $N_{D\hat{0}} = \sum_x k_{\hat{0}}(x)$, $N_M = \sum_x n_x$ and $N_{D_i} = \sum_x \sum_{\mu=0}^d \delta_{i,k_{\hat{\mu}}(x)}$. In this formulation the loop weights are given by $w(\ell) = 1 + \gamma^{n_{\hat{0}}(\ell)} \sigma(\ell) \cosh(3r_\ell a_t \mu N_t)$ with $n_{\hat{0}}(\ell) = 3N_{\hat{0}}(\ell) - 2N_{D\hat{0}}(\ell)$.

$N_{\hat{0}}(\ell)$ and $N_{D\hat{0}}(\ell)$ are the number of steps and the number of dimers, respectively, in $\pm\hat{0}$ -directions. The site weights $w(x)$ are tabulated in [9].

To further simplify the calculation of the partition function, we considered two distinct cases for the parameters am_q, γ and arbitrary $a_t\mu$: First we enumerate all possible configurations with $am_q \geq 0, \gamma = 1$. We weight each configuration C according to $W(C)$ given in (4.37) and thus find

$$\begin{aligned} Z(a_t\mu, am_q) &= \frac{980}{9} + 16 \cosh(6a_t\mu) + 4 \cosh^2(6a_t\mu) + \left[\frac{9760}{3} + 160 \cosh(6a_t\mu) \right] (am_q)^2 + \\ &+ [21248 + 384 \cosh(6a_t\mu)] (am_q)^4 + [50944 + 256 \cosh(6a_t\mu)] (am_q)^6 + (4.38) \\ &+ 53248(am_q)^8 + 24576(am_q)^{10} + 4096(am_q)^{12}, \end{aligned}$$

from which most observables defined in Sect.4.1.1 can be obtained. Further, from the configurations labelled above our expression for $Z = Z(a_t\mu, \gamma \neq 1, am_q = 0)$ reads

$$Z(a_t\mu, \gamma, am_q = 0) = 4 + \frac{400}{9}(\gamma^4 + \gamma^8) + 16 \left(1 + \cosh(6a_t\mu) + \frac{1}{4} \cosh^2(6a_t\mu) \right) \gamma^{12}, \quad (4.39)$$

It allows us to verify our implementation for $\gamma \neq 1$. In Fig.4.4 we display the baryon density ρ_B , the energy density ϵ , the chiral condensate $\langle \bar{\psi}\psi \rangle$ ($am_q \neq 0$) and the chiral susceptibility χ_C as a function of $a_t\mu$ for $am_q = 0, \gamma = 1$ (top, left), $am_q = 0.1, \gamma = 1$ (top, right) and $am_q = 0, \gamma = 0.5$ (bottom, left), $am_q = 0, \gamma = 1.5$ (bottom, right), showing complete agreement between exact results and Monte-Carlo estimators which we checked to high precision.

4.1.3.2 Meson spectrum

The spectrum of low-lying hadronic bound states represents a more thorough check of correctness when comparing the worm approach of strong coupling QCD with the standard algorithmic technique of HMC. We saw in Sect.2.2.2.2 that n distinct staggered fermion fields $\bar{\chi}_x^i, \chi_x^i$ in $d = 3 + 1$, describe $4n$ spinor fields $\bar{\psi}_y^{\alpha bi}, \psi_y^{\alpha bi}$ in the continuum, $a \rightarrow 0$, with spinor index $\alpha = 0, \dots, 3$, taste index $b = 1, \dots, 4$ and flavor index $i = 1, \dots, n$. We defined in particular

$$\psi_y^{\alpha b} = \frac{1}{8} \sum_{\delta} \Omega_{\delta}^{\alpha b} \chi_{2y+\delta} \quad \text{with} \quad \Omega_{\delta} = \gamma_0^{\delta_0} \gamma_1^{\delta_1} \gamma_2^{\delta_2} \gamma_3^{\delta_3}. \quad (4.40)$$

The 4-vector δ has components 0 or 1 and labels the corners of the hypercube with origin at $2y$. Thus, to specify the quantum numbers of a mesonic observable $O_{DT}(y)$ we need a Dirac kernel Γ_D for which we have sixteen different choices such as $\gamma_{\mu}, \gamma_{\mu}\gamma_5$ etc. Additionally, for staggered fermions, the taste kernel Γ_T , which we choose in the same basis of γ -matrices, gives another sixteen possibilities,

$$O_{DT}(y) = \bar{\psi}^{\beta b}(y) \Gamma_D^{\beta\alpha} \Gamma_T^{*ba} \psi^{\alpha a}(y) = \frac{1}{16} \sum_{\delta, \delta'} \bar{\chi}_{2y+\delta} \chi_{2y+\delta'} g_{\delta, \delta'}^{DT}, \quad (4.41)$$

with $g_{\delta, \delta'}^{DT} = \text{Tr}(\Omega_{\delta}^{\dagger} \Gamma_D \Omega_{\delta'} \Gamma_T^{\dagger})/4$. If we take a vector meson as example then $\Gamma_D = \gamma_i$. If we choose $\Gamma_T = \gamma_i^*$, then $g_{\delta, \delta'}^{ii} = -(-1)^{\sum_{\nu} \delta'_{\nu}} (-1)^{\delta'_i} \delta_{\delta, \delta'}$. It is true in general that for $\Gamma_D = (\Gamma_T)^* g_{\delta, \delta'}^{DT} \sim \delta_{\delta, \delta'}$. The sum over δ in Eq.(4.41) still straddles two different time slices with $\delta_0 = 0, 1$

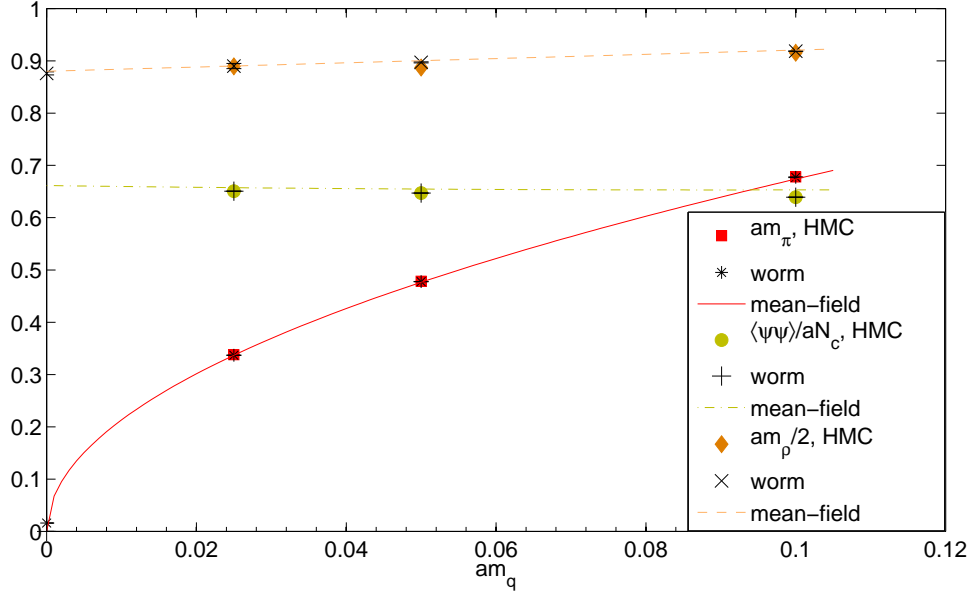


Figure 4.5: Comparison of results on the spectrum using HMC (squares) and the worm formulation (stars). Plotted are m_π , $m_\rho/2$ and $\langle\bar{\psi}\psi\rangle/3$ as a function of am_q . The Monte-Carlo data show excellent agreement and are well described by mean-field theory [53, 54], see Sect.4.2.1.

which will be impractical if we want to measure the decay of correlations $\langle O_{DT}^\dagger O_{DT} \rangle$ in time direction. To restrict the sum to one time slice we can replace the Dirac - taste - kernel $\Gamma_D \otimes \Gamma_T$ by

$$\Gamma_D \otimes \Gamma_T \pm \Gamma_D \gamma_0 \gamma_5 \otimes (\Gamma_T \gamma_0 \gamma_5)^*, \quad (4.42)$$

then, for $\Gamma_D = \Gamma_T^*$, Eq.(4.41) will be modified according to $g_\delta^{DT} \rightarrow g_\delta^{DT}(1 \pm (-1)^{\delta_0})$ and the contribution of $\delta_0 = 0$ or $\delta_0 = 1$ drops out depending on the sign chosen in Eq.(4.42). Coming back to $\Gamma_D = \Gamma_T^* = \gamma_i$, we can now compute the correlator with zero spatial momentum to

$$C(t) = \sum_{\vec{y}} \sum_{\delta, \delta_0=0} \sum_{\delta', \delta'_0=0} \langle \bar{\chi}_\delta \chi_\delta \bar{\chi}_{2y+\delta'} \chi_{2y+\delta'} \rangle (-1)^{\delta+\delta'+\delta_i+\delta'_i} \quad (4.43)$$

$$\sim \sum_{\vec{x}} \langle \bar{\chi}_0 \chi_0 \bar{\chi}_{\vec{x},t} \chi_{\vec{x},t} \rangle (-1)^{x_j+x_k} \quad j = i+1, k = i+2, \text{cyclic}. \quad (4.44)$$

The coordinate $x = (\vec{x}, t)$ runs over all sites of the original lattice with even t . For arbitrary t , we obtain a phase $(-1)^{x_0+x_j+x_k}$ in Eq.(4.44). Since the quantum numbers are determined by the Dirac-taste-kernel (4.42) with $\Gamma_D = \Gamma_T^* = \gamma_i$, the decay of $C(t)$ will be governed by the vector particle with taste assignment γ_i and its parity partner - an axial vector particle - with taste assignment $\gamma_j \gamma_k$. If we denote by $g_\delta^{D05T05} = \text{Tr}(\Omega_\delta^\dagger \Gamma_D \gamma_0 \gamma_5 \Omega_{\delta'} (\Gamma_T \gamma_0 \gamma_5)^\dagger)/4$ then $g_\delta^{D05T05} = g_\delta^{DT} (-1)^{\delta_0}$ and we see that the contributions will be of the form

$$C(t) \sim \exp(-mt) + (-1)^t \exp(-m't), \quad (4.45)$$

with mass assignment $m = m_{AV}$, $m' = m_V$ if the phase is chosen as in Eq.(4.44) for all t . For a general Dirac-taste-kernel ($\Gamma_D = \Gamma_T^*$) with

$$C(t) = \sum_{\vec{x}} \langle \bar{\chi}_0 \chi_0 \bar{\chi}_{\vec{x},t} \chi_{\vec{x},t} \rangle g_x^D, \quad (4.46)$$

we list the sign g_x^D and the corresponding continuum states in Tab.4.1. We note that the correlation function appearing in (4.46) is the monomer-monomer correlation $G(x, y)$ which can be determined for $am_q \geq 0$ by means of the worm estimator given by Eq.(4.32). For periodic boundary condition Eq.(4.45) has to be replaced by

$$C(t) = A \{ \exp(-amt) + \exp(-am(N_t - t)) \} + (-1)^t B \{ \exp(-am't) + \exp(-am'(N_t - t)) \}. \quad (4.47)$$

Of particular interest for us are the phases $g_x^D = (-1)^{x+y+z}$ and $g_x^D = (-1)^{x_j+x_k}$, $j \neq k$ which yield a pion correlator ($\gamma_5 \otimes \gamma_5^*$) and rho correlator ($\gamma_i \otimes \gamma_i^*$), respectively, in the $(-1)^t$ -channel of Eq.(4.47). These are the two lightest mesons. In Fig.4.6 we show $C(t)$ and the corresponding fit for $am_q = 0.025, 0.05, 0.1$ and $\Gamma_D \otimes \Gamma_T^* = \gamma_5 \otimes \gamma_5^*$, i.e. a pion channel on a the $L^3 \times N_t = 8^3 \times 16$ lattice. The masses m_π thus obtained are given in Fig.4.5 along with the mass of the vector channel which we call m_ρ and the chiral condensate $\bar{\psi}\psi$ as a function of quark mass am_q . These data have to be compared with those obtained by the standard approach (HMC) [55] plotted in the same figure. The two sets of data show good agreement and are well described by the mean-field results (continuous lines) described in the following section.

g_x^D		$(-1)^t$
$(-1)^{x_i}$	$\gamma_i \gamma_5 \otimes (\gamma_i \gamma_5)^*$	$\gamma_i \gamma_0 \otimes (\gamma_i \gamma_0)^*$
$(-1)^{x_j+x_k}$	$\gamma_j \gamma_k \otimes (\gamma_j \gamma_k)^*$	$\gamma_i \otimes \gamma_i^*$
$(-1)^{x+y+z}$	$\gamma_0 \otimes \gamma_0^*$	$\gamma_5 \otimes (\gamma_5)^*$
1	$1 \otimes 1$	$\gamma_0 \gamma_5 \otimes (\gamma_0 \gamma_5)^*$

Table 4.1: The sign g_x^D defined in Eq.(4.46). The second and third column assign quantum numbers with kernel ($\Gamma_D \otimes \Gamma_T, \Gamma_D = \Gamma_T^*$) to the states with masses m, m' of (Eq.4.45), respectively.

4.2 Mean field results, symmetries, earlier results, μ_c puzzle

4.2.1 Mean-field results

4.2.1.1 $T = 0, \mu = 0$

We know of three different approaches to obtain results in a mean-field approximation [10, 53, 56] at zero temperature and zero chemical potential ($T = 0, \mu = 0$). In [10, 57] external sources

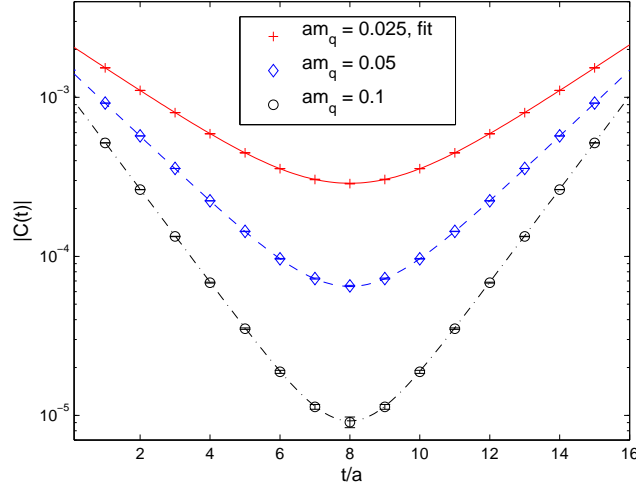


Figure 4.6: Absolute value of the zero spatial momentum transform $C(t)$ (see Eq.(4.46)) of the pion correlator for various quark masses on a $8^3 \times 16$ -lattice. The continuous lines correspond to the fitting ansatz given in Eq.(4.47). The masses m_π thus extracted are plotted against m_q in Fig.4.5.

$J(x), \bar{\eta}(x), \eta(x)$ for the fields $M(x), B(x), \bar{B}(x)$, respectively, are introduced in the action which is then treated in an $1/N$ expansion resulting in an effective action. Refs. [56, 58] follow a different approach by first carrying out the Grassmann integration in Eq.(4.1). The resulting expression for Z is then given as a series in $1/m_q$. In the limit $N \rightarrow \infty$ (the bare gauge coupling g being infinite) this corresponds to summing closed quark-antiquark paths of zero enclosed area (tree graphs). In this limit, the summation leads to exact expressions for expectation values such as $\langle \bar{\chi}\chi \rangle$.

The most popular approach [53, 54], which we now want to motivate, is an expansion in $1/d$ (where d is the space-time dimension) and a subsequent Hubbard-Statonovich transformation. Taking as a starting point the partition function of Lattice QCD with staggered fermions at strong coupling, Eq.(4.1), we rewrite it in the familiar form

$$Z = \int \prod_x (d\chi_x d\bar{\chi}_x) e^{2am_q \sum_x \bar{\chi}_x \chi_x + \sum_{x,\nu} \log z(x,\nu)} \quad (4.48)$$

where an expansion for $z(x,\nu)$ was given in Eq.(4.7) from which $w(x,\nu) := \log z(x,\nu)$ follows [46] with

$$w(x,\nu) = \sum_{n=1}^3 \tilde{a}_n (M(x)M(x+\hat{\nu}))^n + \kappa \eta_{\hat{\nu}}(x)^3 (\bar{B}(x)B(x+\hat{\nu}) - \bar{B}(x+\hat{\nu})B(x)) \quad (4.49)$$

$$=: \tilde{a}_1 M(x)M(x+\hat{\nu}) + F_\kappa(x, x+\hat{\nu}) \quad (4.50)$$

and coefficients $\tilde{a}_1 = 1/3, \tilde{a}_2 = 1/36, \tilde{a}_3 = -5/108$. If we now consider the sum $\sum_{x,\nu} w(x,\nu)$ in Eq.(4.48) to be finite in the limit of large d and take into account that summing over directions results in a factor of d because of isotropy, then the staggered quark fields scale as $\chi, \bar{\chi} \sim d^{-1/4}$ since the term in $w(x,\nu)$ that contains the least quark fields is $\sim M(x)M(x+\hat{\nu})$. It follows

that baryonic terms $\bar{B}(x)B(x+\hat{\nu})$ should scale as $d^{-3/2}$ and are therefore suppressed by $1/\sqrt{d}$ whereas summing over the terms $(M(x)M(x+\nu))^2$, $(M(x)M(x+\hat{\nu}))^3$ only contributes to order $1/d$ and $1/d^2$, respectively. These subleading terms serve to define F_κ in Eq.(4.50), where $\kappa = 0, 1$ for gauge group $U(N)$, $SU(N)$, respectively.

We continue by rewriting Eq.(4.48) using the expansion for $w(x, \mu)$ ($M_x = M(x)$)

$$\begin{aligned} Z &= \int \prod_x (d\chi_x d\bar{\chi}_x) e^{2am_q \sum_x M_x + \sum_{x,y} M_x V_{xy} M_y / 2 + \mathcal{O}(1/\sqrt{d})} \\ &= \int \prod_x (d\chi_x d\bar{\chi}_x d\sigma_x) e^{-\sum_{x,y} \sigma_x V_{xy}^{-1} \sigma_y / 2 + \sum_x (\sigma_x + 2am_q) M_x + \mathcal{O}(1/\sqrt{d})}. \end{aligned} \quad (4.51)$$

where $V_{xy} = 1/3 \sum_\mu (\delta_{x+\hat{\nu}, y} + \delta_{x-\hat{\nu}, y})$ and we have introduced the field $\sigma(x)$ by a gaussian integral (dropping constant factors) to linearize the leading term $M_x V_{xy} M_y$. Considering the gauge group $U(3)$ for simplicity ($\kappa = 0$ in Eq.(4.49)), it follows that $F_0(x, x+\hat{\nu}) \equiv F_0(M(x)M(x+\hat{\nu}))$ is of order $\mathcal{O}(1/d)$ and can be entirely rewritten as a derivative term

$$\begin{aligned} Z &= \int \prod_x (d\chi_x d\bar{\chi}_x d\sigma_x) e^{-\sum_{x,y} \sigma_x V_{xy}^{-1} \sigma_y / 2} e^{\sum_{x,\nu} F(\frac{\partial}{\partial \sigma_x} \frac{\partial}{\partial \sigma_{x+\hat{\nu}}})} e^{\sum_x (\sigma_x + 2am_q) M_x} \\ &= \int \prod_x (d\sigma_x) e^{-\sum_{x,y} \sigma_x V_{xy}^{-1} \sigma_y / 2} e^{\sum_{x,\nu} F(\frac{\partial}{\partial \sigma_x} \frac{\partial}{\partial \sigma_{x+\hat{\nu}}})} e^{3 \sum_x \log(\sigma_x + 2am_q)} \\ &=: \int \prod_x (d\sigma_x) e^{-S_{\text{eff}}}. \end{aligned} \quad (4.52)$$

In the second step the Grassmann-integration has been carried out and the resulting expression in the exponential defines an action S_{eff} . Eq.(4.52) is then subject to two nested expansions: The loop expansion around the classical minimum σ_{cl} of S_{eff} is done order by order³ in $1/d$ because of the more complicated terms contained in $F(\frac{\partial}{\partial \sigma_x} \frac{\partial}{\partial \sigma_{x+\hat{\nu}}})$. The free energy $f = -\frac{1}{VN} \log Z$ can then be expressed as a series in $1/d$ [53, 54]. It allows to obtain results for the chiral condensate $\langle \bar{\psi} \psi \rangle$, the correlation function $\langle M(x)M(0) \rangle$ and - in general for $SU(N)$ in the presence of source terms $\bar{B}(x)J_B(x)$, $\bar{J}_B(x)B(x)$ in Eq.(4.48) - for the correlation function $\langle \bar{B}(x)B(0) \rangle$. As in Eq.(4.46) the poles of the zero spatial momentum projected correlation functions define meson masses m_M and baryon masses m_B , respectively. We state the results to lowest order in $1/d$ [53]:

$$\begin{aligned} \frac{a^3}{N} \langle \bar{\psi} \psi \rangle &\approx \sqrt{\frac{2}{d}} (\bar{\lambda} - 2\bar{m}) \\ \cosh am_M &= d(\bar{\lambda}^2 - 1) + 2j + 1, \quad j = 0, \dots, d-1 \\ \sinh am_B &= \frac{1}{2} \bar{\lambda}^N (2d)^{N/2}, \end{aligned} \quad (4.53)$$

with $\bar{\lambda} = \bar{m} + \sqrt{\bar{m}^2 + 1}$ and $\bar{m} = \frac{am_q}{\sqrt{2d}}$. For $d = 4$, $j = 0, \dots, 3$ and $N = 3$, $am_M(j)$ is traditionally assigned to be mass of the pion (π), the vector (ρ), the pseudo-vector (a_1) and the scalar (a_0/f_0) particle, respectively. If we follow the later adopted, more systematic classification (see for example [59, 60] or [61]) we should call the particles corresponding to these states the $\pi(5)$, $\rho(i)$, $\rho(0i)$ and $\pi(05)$ where we gave the taste assignment in parenthesis, e.g. $\pi(05)$ is the

³The parameter d appears in the calculation by explicitly rescaling the fields $\bar{\chi}, \chi$ as described above.

pion with taste kernel $\Gamma_T = \gamma_0\gamma_5$. For $am_q \ll \sqrt{2d}$ this results in

$$a^3 \langle \bar{\psi}\psi \rangle \approx 2.12 - 0.75am_q \quad (4.54)$$

$$(am_{\pi(5)})^2 \approx 5.66am_q \quad (4.55)$$

$$am_{\rho(i)} \approx 1.76 + am_q \quad (4.56)$$

$$am_B \approx 3.12 + 1.06am_q \quad (4.57)$$

In [54] the authors included leading order corrections in the $1/d$ expansion for $\langle \bar{\psi}\psi \rangle$, $m_{\pi(5)}$ and m_B and obtain

$$a^3 \langle \bar{\psi}\psi \rangle \approx N \sqrt{\frac{2}{d}} \left(1 - \frac{1}{4d} + \bar{m} \left(-1 + \frac{1}{d}\right)\right) = 1.99 - 0.56am_q \quad (4.58)$$

$$(am_{\pi(5)})^2 \approx 2\sqrt{2d}am_q \left(1 - \frac{3}{4d}\right) = 4.6am_q \quad (4.59)$$

$$\sinh am_B = \frac{1}{2} \bar{\lambda}^N (2d)^{N/2} \left[1 - \frac{N}{4d} + \left(1 + \frac{1}{4d}\right) \frac{Nm}{\sqrt{2d}}\right] \rightarrow am_B \approx 2.93 + 1.99am_q \quad (4.60)$$

Relations (4.56), (4.58) and (4.59) are shown in Fig.4.5 as a function of quark mass m_q . The same figure displays data obtained by Monte-Carlo with the worm algorithm and HMC, respectively, which show excellent mutual consistency, and good agreement with mean-field predictions. The three sets of data are also listed in Tab.4.2.

It is important to note that mean-field theory predicts a non-zero expectation value for $\langle \bar{\psi}\psi \rangle$, Eq.(4.58) for $T = 0, \mu = 0, m_q = 0$ which means that the chiral symmetry Eq.(4.3) is spontaneously broken. This symmetry can and will be restored at high temperature and non-zero chemical potential.

4.2.1.2 $\mu > 0$

With the mean-field results for $T = 0, \mu = 0$ above in mind, in particular the relation (4.60) for the baryon mass m_B , we turn to the behavior of $f = -\frac{1}{NV} \log Z$ for finite quark chemical potential μ . This and the ultimate goal of the determination of the whole phase diagram in the (T, μ) -plane has been the subject of numerous mean-field studies [12–14, 62–66].

The $1/d$ expansion for finite chemical potential μ follows the line that leads to Eq.(4.51) with the important difference that link integration is done for spatial links $U_i(x)$ only and thus corresponds to an expansion in $\frac{1}{d-1}$. In the mean-field approximation, the field $\sigma(x)$ is replaced by a constant $\sigma(x) = \sigma$ and the remaining Grassmann- and U_0 link-integration can be done exactly [66], giving for $T = 0$

$$f_{\text{eff}}(\sigma, \mu_B) = \frac{N(d-1)}{4} \sigma^2 - \max\{a\mu_B, NE(\sigma)\}, \quad E(\sigma) = \text{asinh}\left(\frac{d-1}{2}\sigma\right), \quad (4.61)$$

where we set $\mu_B = N\mu$. This function has local minima at $\sigma = 0$ and $\sigma_0 = \pm \sqrt{\frac{2\sqrt{1+(d-1)^2}-2}{(d-1)^2}}$ with $f_{\text{eff}}(0, \mu_B) = -\mu_B$ and $f_{\text{eff}}(\sigma_0, \mu_B) = NE(\sigma_0) - \frac{N(d-1)}{4}\sigma_0^2$. Specializing to $N = 3, d = 4$, then for $a\mu_B = a\mu_{B,c} = 3E(\sigma_0) - \frac{9}{4}\sigma_0^2$ the system changes its state from $\sigma = \sigma_0$ to $\sigma = 0$, this corresponds to a first order phase transition with order parameter σ . From the mean-field treatment for the auxiliary field $\sigma(x) = \sigma$ it follows that $\sigma = -\frac{1}{a}\langle \bar{\psi}\psi \rangle$. The phase transition

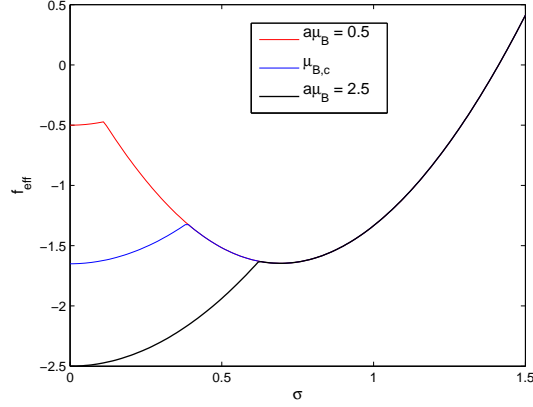


Figure 4.7: f_{eff} as a function of σ for $a\mu_B = 0.5, a\mu_{B,c}, 2.5$.

then corresponds to a transition from the chirally broken phase at low $\mu_B < \mu_{B,c}$ to the chirally restored phase at high μ_B . The baryon density $\rho_B = -\frac{\partial}{\partial a\mu_B} f_{\text{eff}}$ takes values

$$\rho_B = \begin{cases} 0, & \text{for } \mu_B < \mu_{B,c} \\ 1, & \text{for } \mu_B > \mu_{B,c} \end{cases},$$

in particular the high density, chirally restored phase shows saturation of baryons.

At $T = 0$ the transition thus separates a phase of a dilute gas of hadrons (mesons) from the high-density baryonic phase at high μ_B . For non-interacting baryons (see Sect.5.1.1) the transition should occur at $\mu_{B,c} = m_B$, i.e. the cost in free energy to place a baryon into the dilute bath of mesons is given by its mass. Here instead we find

$$a\mu_{B,c} = 3E(\sigma_0) - \frac{9}{4}\sigma_0^2 \approx am_B - \frac{9}{4}\sigma_0^2 = 1.63, \quad (4.62)$$

where $3E(\sigma_0) \approx 2.73 \approx am_B$ and $\sigma_0 \approx 0.7$. The sizable relative difference

$$\Delta/m_B = \frac{m_B - \mu_{B,c}}{m_B} \approx 0.4 \quad (4.63)$$

must then be due to a strong nuclear attraction as already pointed out in [13].

However, the comparison Eq.(4.63) is based on $\mu_{B,c}, E(\sigma_0)$, obtained in a mean-field approximation using an effective action which itself is the result of a $\frac{1}{d-1}$ expansion of the original action, taking only leading contributions into account and neglecting terms of order $\mathcal{O}(\frac{1}{\sqrt{d-1}})$ for $d = 3 + 1$.⁴ These approximate predictions should be carefully compared with results of Monte-Carlo simulations.

⁴Contrary to that, the results for the spectrum at $T = \mu = 0$, Eqs.(4.58)-(4.60), were obtained discarding terms of order $\mathcal{O}(1/d)$.

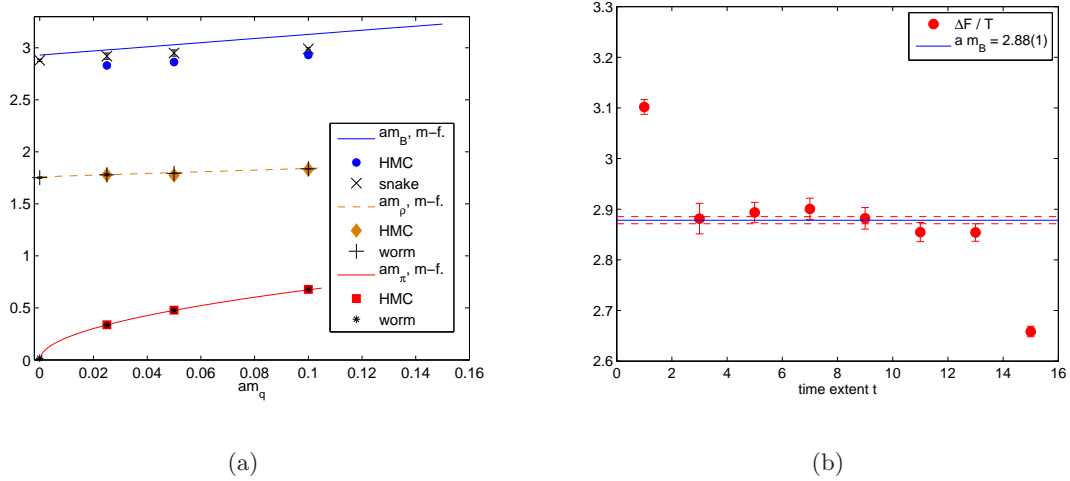


Figure 4.8: (a) The masses m_B, m_ρ and m_π obtained by mean-field theory, Sect.4.2.1, HMC and the snake algorithm described below. (b) $-\log(Z_{l_{||}}^{(N_t-2n)}/Z_{l_{||}}^{(N_t-2n-2)})/2$ as a function of $t = N_t - 2n + 1$, obtained on a $8^3 \times 16$ lattice for $\mu = m_q = 0$. We extract am_B from the approximate plateau, neglecting the effects stemming from the beginning and ending of the world line which correspond to finite-size effects and become negligible as $T \rightarrow 0$.

4.2.2 Determination of the baryon mass m_B by Monte Carlo

When we introduced the worm formulation for strong coupling QCD in Sect.4.1.1 we gave a pictorial representation of the (new) hadronic degrees of freedom (dof) in Fig.4.1. Due to the Grassmann property, baryon world lines form self-avoiding loops which may carry a minus sign due to their fermionic character, see Fig.4.2. In particular, a *static* baryon is represented by a non-trivial closed loop in $\hat{0}$ -direction such as the loop ℓ in Fig.4.9. This loop is built of links $\bar{B}(x')B(x)$ representing a baryon “hopping” by annihilation and creation of a baryon at site $x = (\vec{x}, t)$ and $x' = (\vec{x}, t + 1)$, respectively. At low temperature $T = \frac{1}{N_t a}$ and for $\mu_B = 0$, the probability for this baryon *hopping* is given by $p_{\bar{B}(x')B(x)} \sim \exp(-am_B)$ such that we recover for the whole loop ℓ displayed in Fig.4.9

$$p_\ell \sim \exp(-am_B N_t) = \exp(-m_B/T) = \exp(-\Delta F/T) \quad (4.64)$$

where ΔF is the difference in free energy between those configurations contributing to Z that contain one baryon (world line) at \vec{x} and the vacuum configurations with $\rho_B = 0$. Rewriting this as a ratio of partition functions then

$$\exp(-\Delta F/T) = \frac{Z_\ell}{Z_0}, \quad (4.65)$$

and we obtain $Z_\ell/Z_0 \sim \mathcal{O}(10^{-21})$ for an $N_t = 16$ lattice and assuming the mean-field result $m_B \approx 3$. Thus, extracting the baryon mass m_B directly as a ratio of partition functions via Eq.(4.65) seems impossible.

We note however, that for $\mu = 0$ the static baryon loop ℓ carries a total weight $w_{tot}(\ell) = w(\ell) \prod_{x \in \ell} 3! = +1$ which we observe from the expressions (4.12),(4.13) for Z and $w(\ell)$, respec-

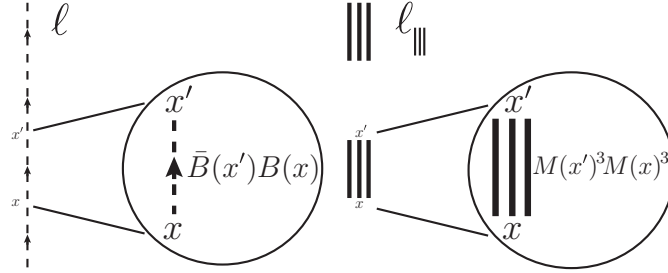


Figure 4.9: Example of a static baryon loop ℓ (left) with weight $w_{tot}(\ell) = 1$ for $N_t = 4$. On the right, the loop ℓ has been replaced by a sequence of triple dimers $\ell_{|||}$ which also carries weight $w_{tot}(\ell_{|||}) = 1$.

tively. From the same expression it follows, that a sequence of triple dimers $\ell_{|||}$ at site \vec{x} as sketched in Fig.4.9 carries a weight $w_{tot}(\ell_{|||}) = 1$ as well. Thus, replacing the baryon loop ℓ by a loop $\ell_{|||}$ does not change the configurational weight, i.e. $Z_\ell = Z_{\ell_{|||}}$. The advantage of such replacement becomes clear if we rewrite Eq.(4.65) in factorized form as used in the snake algorithm [67],

$$\frac{Z_\ell}{Z_0} = \frac{Z_{\ell_{|||}}}{Z_0} = \frac{Z_{\ell_{|||}}}{Z_{\ell_{|||}}^{(N_t-2)}} \frac{Z_{\ell_{|||}}^{(N_t-2)}}{Z_{\ell_{|||}}^{(N_t-4)}} \cdots \frac{Z_{\ell_{|||}}^{(2)}}{Z_0}, \quad (4.66)$$

and we define the $Z_{\ell_{|||}}^{(N_t-2n)}$ to be partition functions with configurations that contain a sequence of triple dimers at site \vec{x} of length $(N_t - 2n)$, starting at $x = (\vec{x}, 0)$. Note that a similar factorization for the baryon loop ℓ would lead us from configurations that contribute to Z to those contributing to the baryon 2-pt function G_B . No such complication arises in the case of $\ell_{|||}$ and each factor $Z_{\ell_{|||}}^{(N_t-2n)} / Z_{\ell_{|||}}^{(N_t-2n-2)}$ appearing in Eq.(4.66) should be of order $\mathcal{O}(10^{-3})$.

4.2.2.1 Practical implementation

We express the ratio $Z_{\ell_{|||}}^{(N_t-2n)} / Z_{\ell_{|||}}^{(N_t-2n-2)}$ as an expectation value with respect to the denominator. In order to measure the ratio we exclude the volume corresponding to the sequence $\ell_{|||}^{(N_t-2n-2)}$ at site \vec{x} or equivalently we impose the sequence $\ell_{|||}^{(N_t-2n-2)}$ of triple dimers to be frozen during the Monte Carlo run. Such a frozen dimer sequence can and will be extended during a simulation by another, dynamic sequence as sketched in Fig.4.10. Measuring the triple-dimer occupation rate of the subsequent link thus yields $Z_{\ell_{|||}}^{(N_t-2n)} / Z_{\ell_{|||}}^{(N_t-2n-2)} = \exp(-2am_B)$.

In Fig.4.8(b) we plot $-\log(Z_{\ell_{|||}}^{(N_t-2n)} / Z_{\ell_{|||}}^{(N_t-2n-2)})/2$ as a function of $t = N_t - 2n + 1$, obtained on a $8^3 \times 16$ lattice for $\mu = m_q = 0$. Up to deviations corresponding to the starting and ending of the world line we extract $am_B = 2.88(1)$ from the plateau values. Repeating this for quark masses $am_q = 0.025, 0.05, 0.1$, we can compare our values with those obtained from HMC at $\beta = 0$ [55] and mean-field theory [54], displayed in Fig.4.8(a), confirming the validity of our approach. The numerical data are listed in Tab.4.2 along with the results on the meson spectrum and $\langle \bar{\psi}\psi \rangle$.

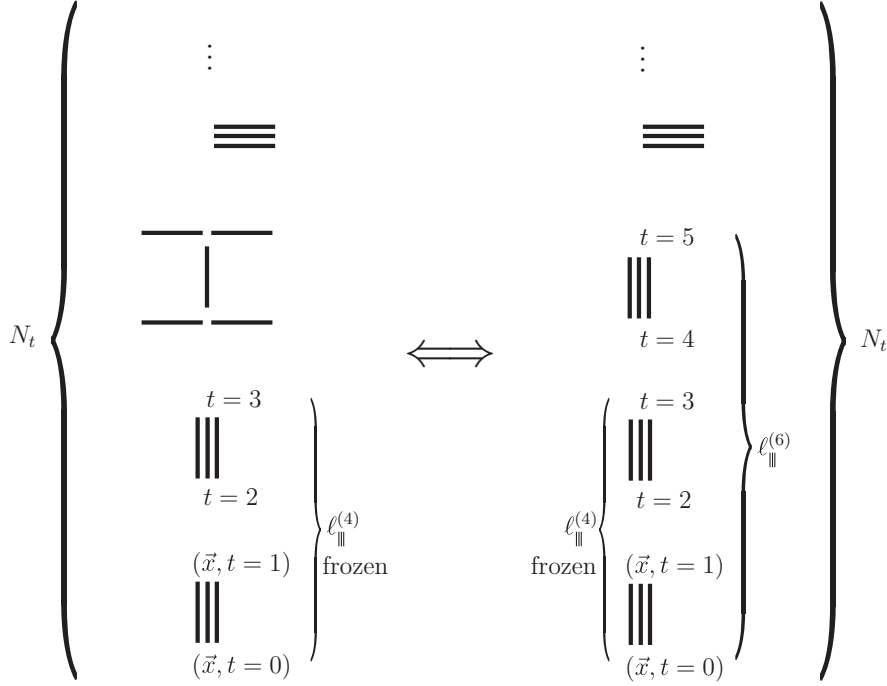


Figure 4.10: Example of a pair of configurations that contribute to the sector $Z_{\ell_{||}}^{(4)}$ (left) and $Z_{\ell_{||}}^{(6)}$ (right), respectively: The frozen sequence of triple dimers $\ell_{||}^{(4)}$ starting at $(\vec{x}, t=0)$ on the left has been extended to $\ell_{||}^{(6)}$ when going from left to right. The relative occurrence of configurations of either sector serves to calculate the factor $Z_{\ell_{||}}^{(6)}/Z_{\ell_{||}}^{(4)}$ in the factorization Eq.(4.66).

4.2.3 Qualitative understanding of the baryon mass m_B

At $T=0$ we can equate the internal energy E and the free energy F , defined as Legendre transform of the former, $F = E - TS$. Thus, our findings for $m_B = \Delta F$ should be consistent with the increase in internal energy ΔE of the system after adding the static baryon to the dilute gas of mesons. However, at strong coupling the definition of energy,

$$a^4 \epsilon = -\frac{1}{L^3 N_t} \frac{1}{\gamma} \frac{\partial \gamma}{\partial h(\gamma)} \langle 2N_{Dt} + 3N_{Bt} \rangle \quad (4.67)$$

relies on the knowledge of the functional behavior $1/h(\gamma) = f(\gamma) = \frac{a}{a_t}$, where $f(\gamma) \rightarrow \gamma^2$ for $\gamma \gg 1$ [13, 68]. Our measurement of am_B above was carried out for $\gamma = 1$ and can thus not be easily compared to ΔE . Strictly speaking a continuum extrapolation of $am_B(\gamma)$, $\gamma \rightarrow \infty$, while keeping $\gamma^2/N_t = \text{const}$ is required to carry out a meaningful comparison.

Still, we can qualitatively understand the origin of the baryon mass by noting from Eq.(4.67) that $a^4 \epsilon \sim \langle 2k_{\hat{0}} + 3|b_{\hat{0}}| \rangle$, where $k_{\hat{0}}$, $|b_{\hat{0}}|$ represent the dimer and baryon link occupation number in $\hat{0}$ -direction, respectively.⁵ Note that, in the absence of baryons and for $\gamma = 1$, $am_q = 0$, the average occupation number $\langle k_{\mu} \rangle = N/(2d) = 3/8$ as we have N links per site x that will

⁵We thus see that ϵ is proportional to the number (density) of quarks and antiquarks propagating in Euclidean time direction.

	am_q	snake/worm	HMC [55]	mean-field
am_B	0	2.88(1)	—	2.930, Eq.(4.60)
	0.025	2.92(3)	2.831(10)	2.980
	0.05	2.95(3)	2.863(5)	3.030
	0.1	2.99(1)	2.931(3)	3.129
am_ρ	0	1.752(6)	—	1.760, Eq.(4.56)
	0.025	1.78(1)	1.779(1)	1.785
	0.05	1.794(2)	1.774(4)	1.810
	0.1	1.837(1)	1.831(2)	1.860
am_π	0	0.016 (finite volume)	—	0, Eq.(4.59)
	0.025	0.3368(2)	0.3379(1)	0.3390
	0.05	0.4778(3)	0.4784(1)	0.4794
	0.1	0.6773(6)	0.6780(1)	0.6780
$a^3\langle\bar{\psi}\psi\rangle$	0	0 (finite volume)	—	1.990, Eq.(4.58)
	0.025	1.95174(3)	1.9520(6)	1.9747
	0.05	1.94133(1)	1.9413(3)	1.9606
	0.1	1.91723(1)	1.9172(2)	1.9325

Table 4.2: Comparison of results for the mass of the baryon (am_B), the rho particle (am_ρ) and the pion (am_π) as well as the chiral condensate $a^3\langle\bar{\psi}\psi\rangle$ at the listed quark masses using the snake and worm algorithm, HMC and mean-field results (Sect.4.2.1). Monte-Carlo simulations were done on a $8^3 \times 16$ lattice.

be isotropically distributed over the $2d$ directions, provided we have an isotropic four-volume $V = L^4$. This estimate turns out to be correct to high precision even when baryons are included because the smallest baryon loop (a loop around a plaquette) has probability $\sim e^{-4am_B} \approx e^{-12}$. Going back to $SU(N)$ and relation (4.67) we see that a static baryon world line contributes $\sim 3N_t$ in lattice units to the internal energy. But placing a static baryon at site x will have a twofold effect: We increase the internal energy at the site but we will also distort the link-occupation numbers of the neighboring sites as we excluded the site x from the surrounding meson bath. This simple geometric effect is demonstrated for $d = 2 + 1$ in Fig.4.11(a). For the nearest neighbors of a site x traversed by the baryon loop, this site is no longer available for a pairing $M(x)M(x + \hat{\nu})$, therefore at distance $R/a = 1$, link occupation numbers $k_{\hat{\mu}}, \hat{\mu} \neq -\hat{\nu}$ will show an increase, away from $\langle k_{\hat{\mu}} \rangle = \langle \frac{3}{2d} \rangle$, leading to an increase in internal energy at sites $x + \hat{i}$. Points of distance $R/a = \sqrt{2}$ to the baryonic site x will contribute a decreased energy density, as their link-occupation number $k_{\hat{i}}$ in the spatial directions \hat{i} pointing to the nearest neighbors of the baryon will be increased, leaving less occupation probability for remaining directions. This distortion thus propagates to large spatial distances and describes the effect of a static baryon loop on the meson-vacuum which we will examine more closely in Sect.4.3.3. In Fig.4.11(b) we show the difference $a^4\delta\epsilon := \langle 2k_{\hat{0}} + 3|b_{\hat{0}}| \rangle - 3/4$ as a function of spatial distance R/a to a static baryon at the origin, obtained on a 16^4 lattice for $am_q = 0$ and $\gamma = 1$. Note that while the simple sketch in Fig.4.11(a) explains the fluctuations in the sign of $\delta\epsilon$, we have

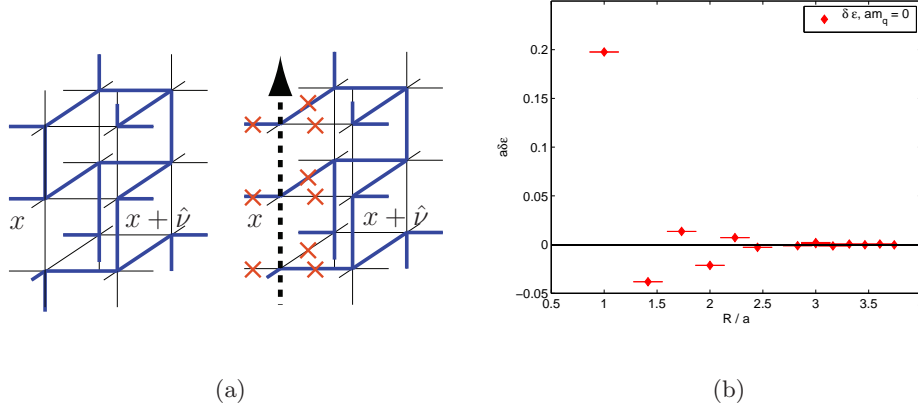


Figure 4.11: (a) Example configurations for $d = 2 + 1$: On the left we show a vacuum configuration (purely mesonic links). On the right we added a static baryon loop. The sites it traverses can no longer be touched by pionic links (crossed). This increases the link occupation number in $\hat{0}$ direction at the nearest neighbors. (b) $\delta\epsilon(R) = \langle 2k_{\hat{0}} + 3|b_{\hat{0}}| \rangle - 3/4$ as obtained from a 16^4 lattice for $am_q = 0$ and $\gamma = 1$.

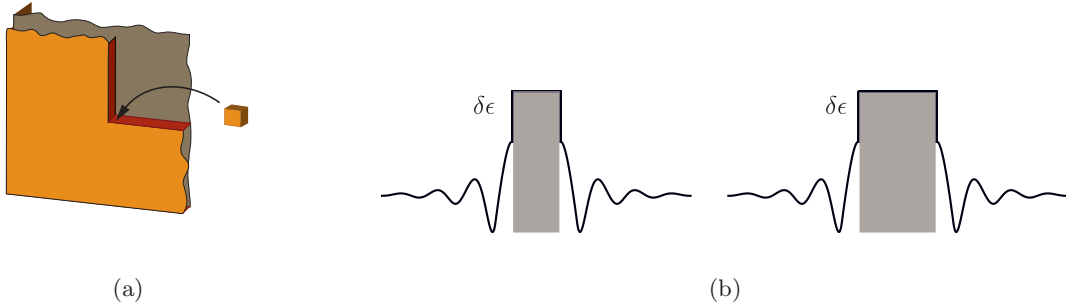


Figure 4.12: (a) Adding a baryon to grow an additional layer of bulk nuclear matter. Each new baryon binds to 3 baryonic nearest neighbors. (b) Profile of $\delta\epsilon$ for two configurations containing a baryon volume (flat piece) in the middle. When going from left to right the baryonic volume has grown, say by one site and the distortion of the energy density (oscillatory part) of the pion cloud has just shifted. The increase in total energy is thus just the difference in energy of a baryonic site and a vacuum site.

to revert to Monte Carlo to obtain answers on its actual magnitude.

As we have measured $\delta\epsilon$ with sufficient accuracy we can estimate ΔE employing as a test the weak coupling relation $h(\gamma) = 1/\gamma$ in Eq.(4.67), giving

$$a\Delta E|_{h(\gamma)=\gamma} = a^4 \sum_R \delta\epsilon(R) = 3.05(3)$$

a value not too far from $am_B = 2.88(1)$. Note that with higher accuracy one can use this approach to determine $\frac{\partial\gamma}{\partial h(\gamma)}$ in Eq.(4.67).

4.2.4 Determination of $\mu_{B,c}$

We can use the same strategy of extending a triple dimer line little by little into the dilute gas of hadrons in a modified manner: The $T = 0$ transition separates the hadronic phase with baryon density $a^3\rho_B = 0$ and that of dense nuclear matter with baryon density $a^3\rho_B = 1$. At the transition, i.e. for $\mu_B = \mu_{B,c}$, in a finite cubic box the two phases will coexist forming an interface as shown in Fig.4.12(a). We can then determine the free energy necessary to extend the volume occupied by nuclear matter by one more “slice” of shape $L \times L \times a$ in our finite volume $L^3 \times N_t$. Breaking this layer into the L^2 elementary contributions, we can add static baryons one by one as sketched in Fig.4.12(a), “attaching” each to three baryonic nearest neighbors. Measuring the free energy ΔF of this elementary increment on a $8^3 \times 16$ lattice for $m_q = 0$ by the snake algorithm described above we obtained

$$a\Delta F = a\mu_{B,c} = 1.78(1), \quad (4.68)$$

a value roughly consistent with earlier Monte-Carlo [9] extrapolations from small lattices ($a\mu_{B,c}^{\text{Karsch}} = 1.89(6)$) and not too far from the mean-field prediction [66], $a\mu_{B,c}^{\text{mf}} = 1.63$.

While this agreement seems satisfying and will be supported by findings for the nucleon-nucleon potential V_{NN} , Sect.4.3.1, the reasoning of the previous section applies: In order to compare $\Delta F = \mu_{B,c}$ with the increase in energy ΔE after the insertion of the additional baryon, we should study both quantities in the time continuum limit $\gamma \rightarrow \infty$, $\gamma^2/N_t = \text{const}$. In Fig.4.12(b) we have drawn two profiles of the energy density $\delta\epsilon$ for configurations in $d = 1 + 1$: For a baryonic volume in the middle the energy density is constant and oscillates to the left and right of the interface. As the baryonic volume is increased by adding an additional baryon to it we go from the left to the right configuration. We see that the distortion (oscillatory part) has just been translated, the net effect being the replacement of an undistorted site at large distance from the interface by a site occupied by one baryon. Even though this example takes place in $d = 1 + 1$ this effect carries over to $d = 3 + 1$. We should therefore expect

$$a\mu_{B,c} \approx a\Delta E = \frac{1}{\gamma} \frac{\partial \gamma}{\partial h(\gamma)} (3 - \langle 2k_{\hat{0}} + 3|b_{\hat{0}}| \rangle). \quad (4.69)$$

4.3 Nuclear Physics at strong coupling

In view of the numerical values for $a\mu_{B,c} = 1.78(1)$ and $am_B = 2.88(1)$ obtained with the snake algorithm for $\gamma = 1$, we are left with the puzzle why $\mu_{B,c} \neq m_B$? As pointed out in the context of mean-field theory [13] and below Eq.(4.63), the mismatch must be due to a strong attractive interaction between baryons. We now study this interaction by measuring the nuclear potential, i.e. the change of energy caused by the introduction of two static nucleons at zero temperature.

4.3.1 The nucleon-nucleon potential V_{NN} at strong coupling

We can use the snake algorithm to determine the potential $V_{NN}(R)$ in a manner similar to Sects.4.2.2 and 4.2.4 by measuring the cost in free energy of adding a baryonic world line at distance R from a baryon at the origin as sketched in Fig.4.13(a). In Fig.4.13(b) we plot V_{NN}

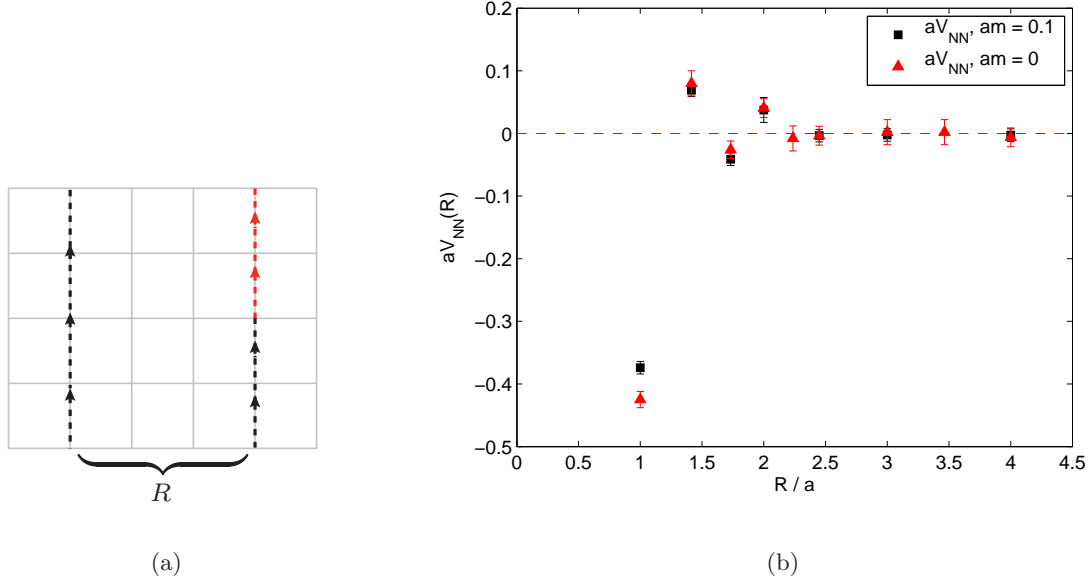


Figure 4.13: (a) Extending a static baryonic world line at distance R from another static baryon at the origin. As with the mass am_B and the chemical potential $\mu_{B,c}$, the free energy ΔF necessary for the extension (red) can be measured with the snake algorithm. (b) The nuclear potential $V_{NN}(R)$ obtained on an $8^3 \times 16$ lattice for $am_q = 0, 0.1$ and $\gamma = 1$. Apart from the hardcore repulsion the potential shows a strong nearest-neighbor attraction of $V_{NN}(a) \approx -120$ MeV.

obtained on a $8^3 \times 16$ lattice for $am_q = 0, 0.1$ ($\gamma = 1$). We comment on the important features:

- In our model baryons form non-intersecting loops which followed from the Grassmann property of the field χ and the fact that we have only one pair of staggered variables $\chi_a, \bar{\chi}_a$ per color a and site x . This results trivially in a hard-core repulsion present in V_{NN} .
- V_{NN} exhibits a strong nearest-neighbor attraction at distance $R/a = 1$. If we set the scale using the proton mass, $m_B = 938$ MeV, then $V_{NN}(a) \approx -120$ MeV. Using instead the mass of the Delta baryon, $m_\Delta = 1232$ MeV [69], yields $V_{NN}(a) \approx -160$ MeV. This large attraction can again be qualitatively understood by considering a system of two baryons and the surrounding mesonic sites drawn in Fig.4.14(a). In the middle, Fig.4.14(b), we have plotted, for $am_q = 0, 0.1$, the change in energy density $a^4\delta\epsilon$ due to a single baryon at the origin. On a hypercubic lattice in $d = 3 + 1$ a single, static baryon will be surrounded by 6 mesonic, nearest-neighbor sites, each with increased energy density $\delta\epsilon(R = a)$. Placing two baryons next to each other, this number is reduced from 12 to 10. Contrary to that, at distance $R/a = \sqrt{2}$, the two baryons lead to an increase larger than $\delta\epsilon(R = a)$ at the white sites in Fig.4.14(c), thus resulting in a net repulsion. Like the baryon mass am_B in our model, V_{NN} has its origin in a *steric effect* and it is therefore clear that its shape depends on the particular choice of lattice discretization.

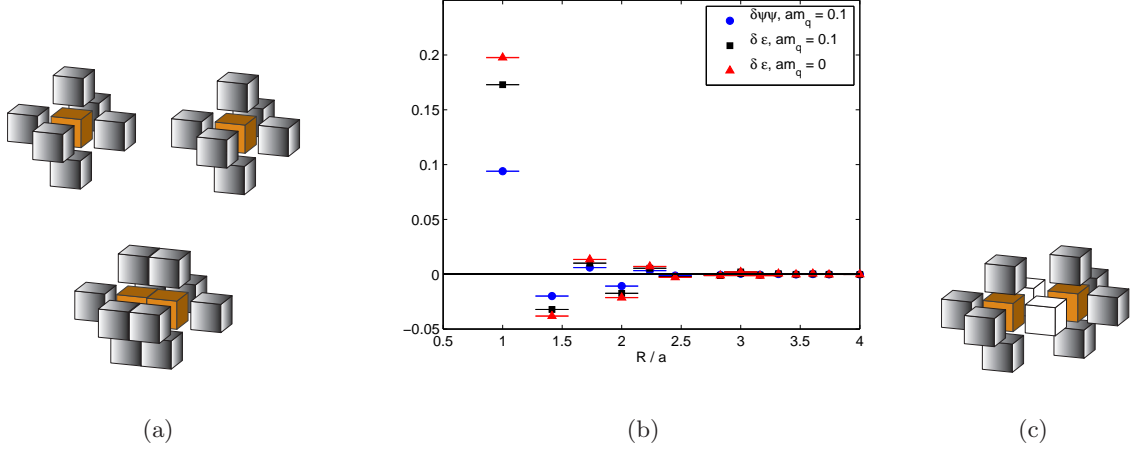


Figure 4.14: (a) The upper part of the figure shows generically the steric effect: Two single baryons (orange cubes), each surrounded by 6 mesonic sites (grey metallic), can “bind” (lower part) to reduce the number of mesonic sites with increased energy density $\delta\epsilon$. (b) The change in energy density $a^4\delta\epsilon = \langle 2k_{\bar{0}}(R) + 3|b_{\bar{0}}|(R) \rangle_{B=1} - \langle 2k_{\bar{0}} + 3|b_{\bar{0}}| \rangle_{\text{vac}}$ as function of distance from a baryon at the origin. Also shown is the change $\delta\bar{\psi}\psi = \langle \bar{\psi}\psi(R) \rangle_{B=1} - \langle \bar{\psi}\psi \rangle_{\text{vac}}$ in the condensate density for $am_q = 0.1$. (c) The steric effect leading to a net repulsion of baryons at distance $R/a = \sqrt{2}$. The white cubes (sites) represent mesonic sites with increased energy density $> \langle 2k_{\bar{0}} + 3|b_{\bar{0}}| \rangle_{\text{vac}} + a^4\delta\epsilon(a)$.

- The quantitative change of V_{NN} and $\delta\epsilon$ with the introduction of a non-zero quark mass m_q supports this simple argument: For $am_q > 0$, the staggered $U_A(1)$ -symmetry Eq.(4.3) is broken explicitly, allowing for a non-zero density of monomers n_M with $\frac{1}{2am_q}\langle n_M \rangle = \langle \bar{\psi}\psi \rangle$, at low temperature T and baryon chemical potential μ_B . The formation of a chiral condensate density through a monomer at site y , lowers the energy density at this site from the $am_q = 0$ - value $\epsilon_{\text{vac}, am_q=0} \sim 3/4$ to e.g. $\epsilon_{\text{vac}, am_q=0.1} \sim 0.7$ at $am_q = 0.1$, up to the same proportionality constant. Placing a static baryon loop at the origin will still distort the energy density of the surrounding mesonic sites. Besides this effect already encountered in the chiral limit, also the condensate density $\bar{\psi}\psi(x)$ will be distorted. The change $\delta\bar{\psi}\psi(R) = \langle \bar{\psi}\psi(R) \rangle_{B=1} - \langle \bar{\psi}\psi \rangle_{\text{vac}}$ takes a similar oscillating shape as $\delta\epsilon(R)$, which itself is smaller in magnitude than at $am_q = 0$ (see Fig.4.14(b)) due to the additional contribution in form of $\delta\bar{\psi}\psi$. As a consequence, for $am_q > 0$ the nearest-neighbor attraction present in V_{NN} (Fig.4.13(b)) decreases when compared to the $am_q = 0$ - value.
- We reconsider the geometry displayed in Fig.4.12(a), leading to an estimate of $\mu_{B,c}$ for $am_q = 0$: Each baryon added to the dense phase binds to 3 nearest-neighbors. This reduces the cost in free energy to

$$a\Delta F_{\text{bulk}} \approx am_B + 3aV_{NN}(a) \approx 1.7, \quad (4.70)$$

which is roughly consistent with $\mu_{B,c}$, indicating that additional interactions are small.

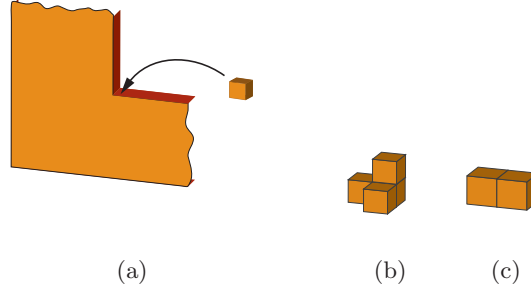


Figure 4.15: (a) Generic sketch of a single slice of nuclear matter in the dilute phase. Each baryon binds to 2 baryonic nearest neighbors instead of 3 in the bulk, Fig.4.12(a), leading to a surface tension of $\sigma = |V_{NN}(a)|/2a^2$. (b) Example of a nucleus in our 1-flavor strong coupling model. Each baryon is nearest neighbor to at least one other baryon, here for the case of a nucleus with mass number $A = 4$. (c) Sketch of a deuteron.

- From a similar geometry, now consisting of a single layer of baryons (see Fig.4.15(a)) we can estimate the surface tension of nuclear matter in our model as follows: When building a first slice of nuclear matter in the dilute phase, each baryon added, binds to 2 baryonic nearest-neighbors, resulting in an increase in free energy $\Delta F_{\text{surf}} \approx am_B + 2V_{NN}(a)$. Thus, when increasing the area of the interface in Fig.4.15(a) by $2a^2$ we have to invest a surplus of $|V_{NN}(a)|$ compared to ΔF_{bulk} (Eq.(4.70)) where we added a baryon to a bulk of nuclear matter. This corresponds to a surface tension

$$\sigma \approx |V_{NN}(a)|/2a^2 \approx 150 - 400 \text{ MeV/fm}^2. \quad (4.71)$$

This large surface tension will determine the stability of the *nuclei* of our model, to be studied in the next section.

4.3.2 Nuclear matter at strong coupling

Our measurement of the nuclear potential V_{NN} , in particular the determination of the nearest-neighbor attraction $V_{NN}(a)$, paves the way for another fruitful application of the snake algorithm: We can determine the masses of particular geometries consisting of *several*, say A static baryons, each nearest neighbor to another, see Fig.4.15(b) as an example. These “bound” objects of A baryons represent the nuclei of our model. For the important case of the “deuteron” ($A = 2$) in Fig.4.15(c), we see that

$$m(A = 2) = 2m_B + V_{NN}(a). \quad (4.72)$$

Adding baryons one by one we can determine the masses of nuclei of mass number A by successively measuring the change in free energy ΔF_i , $i = 1, \dots, A$, yielding $m(A) = \sum_i \Delta F_i$. As usual the single change in free energy, ΔF_j , is determined by extending step by step the world line of the baryon to be added to the nucleus. Starting with $A = 3$, there will exist several nuclei of equal mass number A but different geometry, see Fig.4.16(b). These “isomers” will have different masses $m^{(\alpha)}(A = 3)$ owing to the particular form of the nuclear potential and

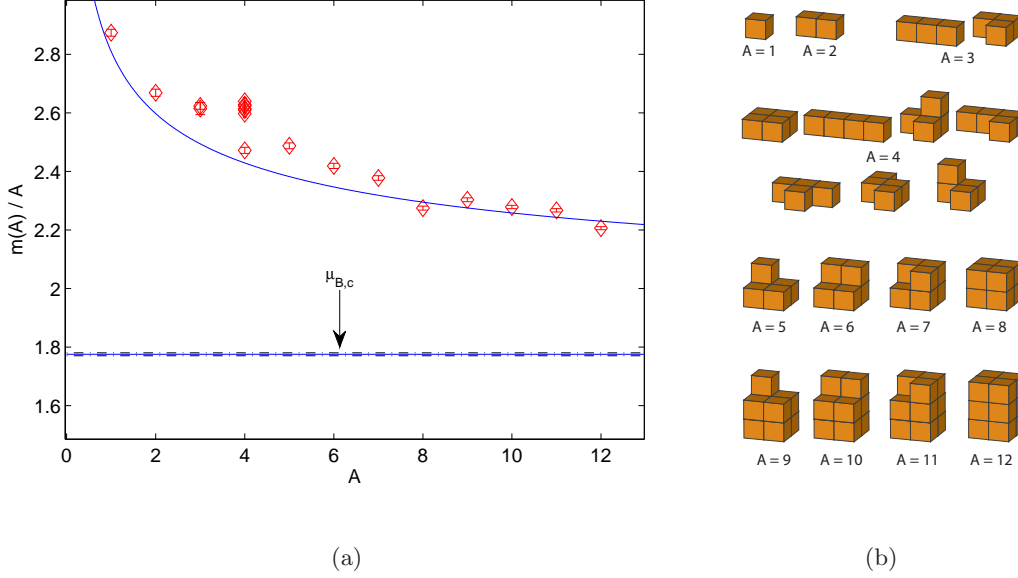


Figure 4.16: (a) The average mass per nucleon, $m(A)/A$, for $A = 1, \dots, 12$ obtained on a $8^3 \times 16$ lattice at $am_q = 0$. For $A = 3, 4$ all geometric isomers have been considered, showing increased stability for the square geometry of $A = 4$. The solid line shows the parameter-free Bethe-Weizsäcker Eq.(4.73) with the surface tension $\sigma = |V_{NN}(a)|/2a^2$. (b) Corresponding nuclear geometries in order of increasing mass $m(A)$.

ultimately the large interface tension σ .

In Fig.4.16(a) we have plotted $m(A)/A$ for mass numbers $A = 1, \dots, 12$, studying exhaustively the masses of shape isomers for $A = 3$ and 4 only. The corresponding geometries are given on the right. We now discuss the qualitative features:

4.3.2.1 Semiempirical mass-formula

As shown in Fig.4.16(a) the masses $m(A)$ are approximately described by the Bethe-Weizsäcker phenomenological formula

$$m(A)/A = \mu_{B,c} + (36\pi)^{\frac{1}{3}} \sigma a^2 A^{-\frac{1}{3}}, \quad (4.73)$$

given by the solid line. This can be understood as follows: In the liquid-drop model (see e.g. [70]) - where the nucleus is the analogue to the liquid droplet and the nucleons play the role of the molecules within the droplet - the mass $m(A)$ of a nucleon of mass number A can be decomposed into several terms,

$$m(A) = \sum_i f_i(A), \quad (4.74)$$

where $f_0(A) = m_B A$. The leading contributions are

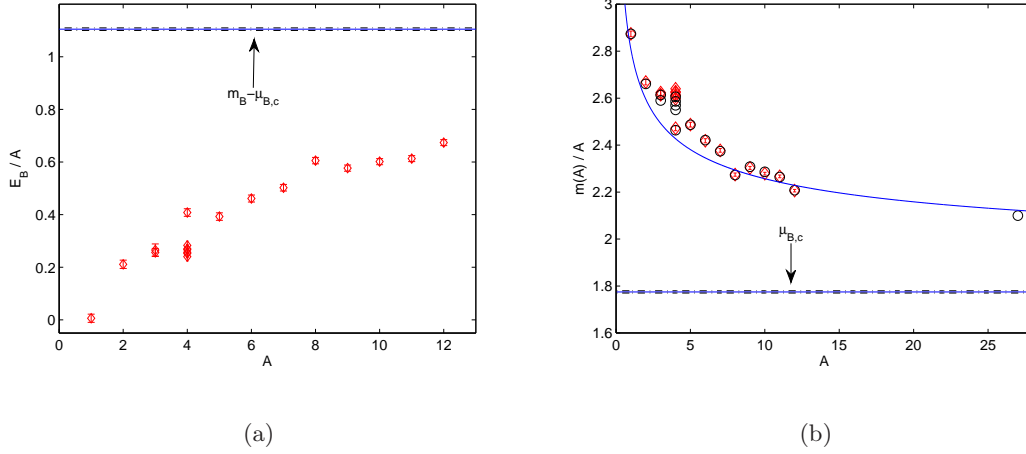


Figure 4.17: (a) Binding energy per nucleon $E_B/A = m_B - m(A)/A$ as a function of A . For nuclear matter ($A \rightarrow \infty$) we obtain $E_B/A \approx 250$ MeV, compared to the real-world value of 16 MeV neglecting the Coulomb interaction and taking $N = Z$. (b) The masses $m(A)/A$ and their predictions $m_V(A)/A$ (black circles) based on Eq.(4.77), including the nucleus of cubic shape with $A = 27$ (“Aluminium”).

- The *volume* term f_1 : In the real world, the nuclear interaction - approximately represented by the two-body interaction V_{NN} of our model - is short-range. As a consequence a nucleon within the nucleus will only “feel” the effect of the nucleons immediately surrounding it. We have already exploited this fact to explain, in the approximation of a nearest-neighbor interaction, the value of $\mu_{B,c}$ in Eq.(4.70). The volume- or bulk-contribution to $m(A)$ now encodes the assumption that each of the A baryons contributes $m_B + \Delta V$, with the baryon mass m_B and the interaction with the surrounding baryons ΔV . But this is exactly the reasoning that led to our determination of $\mu_{B,c}$ as sketched in Fig.(4.12(a)). We thus find for our model

$$f_0(A) + f_1(A) = (m_B + \Delta V)A \underset{A \rightarrow \infty}{=} \mu_{B,c}A. \quad (4.75)$$

Real nuclei can be approximately treated as homogeneously charged spheres of radius R , obeying $R = r_0 A^{1/3}$ with $r_0 \approx 1$ fm [70] showing the volume dependence of the terms Eq.(4.75). Note that as our model is defined on a hypercubic lattice, the volume V of a nucleus is given by $V = Aa^3$.

- The *surface* term f_2 : The bulk contribution Eq.(4.75) neglects the fact that nuclei at the surface contribute less binding energy, leading to a positive contribution to $m(A)$. The effect is quantified by the surface tension of nuclear matter. In a first approximation we treat the nuclei of our model as spherical, thus equating $Aa^3 = V = \frac{4}{3}\pi R^3$. $f_2(A)$ will therefore be given by

$$f_2(A) = \sigma \times \text{surface area} = \sigma 4\pi R^2 = (36\pi)^{\frac{1}{3}} \sigma a^2 A^{\frac{2}{3}}, \quad (4.76)$$

where $a^2\sigma = |V_{NN}(a)|/2$ from the discussion leading to Eq.(4.71). Note that in the real world $f_{2,\text{real world}}(A) = a_2 A^{2/3}$ with $a_2 \approx 18$ MeV [70]. Setting $f_{2,\text{real world}} =$

$4\pi\sigma_{\text{real world}}R^2$, where the radius R of the nucleus with mass number A is given by $R = r_0A^{1/3}$ and taking the empirical value $r_0 \approx 1$ fm [70] we find $\sigma_{\text{real world}} \approx 1$ MeV/fm² compared to $\sigma \approx 200$ MeV/fm² in our model.

Other terms present in the original mass formula Eq.(4.73) have their origin in the Coulomb-interaction and the asymmetry in the number of protons Z and neutrons N of the nucleus. Both effects are absent in our one-flavor model.

4.3.2.2 Binding energy

In Fig.4.17(a) we plot the binding energy per nucleon $E_B(A)/A = m_B - m(A)/A$. The crudeness of our model becomes apparent if we compare the binding energy of the deuteron of our model ($E_B \approx 120$ MeV) with the real-world value of $E_{B,^2H} \approx 2$ MeV. A further important observable is the binding energy per nucleon in the limit $A \rightarrow \infty$, i.e. the binding energy of nuclear matter which we compare with the empirical value in the absence of Coulomb interaction and for $N = Z$: We find $\lim_{A \rightarrow \infty} E_{B,\text{model}}/A \approx 250$ MeV compared to $\lim_{A \rightarrow \infty} E_{B,\text{real-world}}/A \approx 16$ MeV [70]. Realistic theories are able to model the nucleon-nucleon interaction via a (repulsive) ω -meson exchange at short distances and a long-range (attractive) σ -meson exchange [70], leading to delicate cancellations which render the nucleon-nucleon interaction rather weak. In our model the strong attraction was heuristically explained by a steric effect in Sect.4.3.1, giving no direct evidence for a meson-exchange interaction. Yet, in Sect.4.3.3 this picture will receive corrections when we investigate the distortion of the energy density, $\delta\epsilon(R)$ (“the pion cloud”), in more detail.

4.3.2.3 Stability of particular geometries

The masses $m(A)/A$ displayed in Fig.4.16(a) show increased stability at values $A = 4, 8, 12$. The larger binding energy E_B (see Fig.4.17(a)) for the square ($A = 4$), cubic ($A = 8$) and parallelepipedic ($A = 12$) shape has its origin in the large interface tension, favoring spherical or cubic geometries. With the potential V_{NN} , Fig.4.13(b) at hand we can try to describe the mass $m(A)$ by decomposing the free energy ΔF_j necessary to add the j th baryon to the nucleus with mass number A , $j = 1, \dots, A$ according to

$$\Delta F_{j,V} \approx m_B + c_{nn,j}V_{NN}(a) + c_{nnn,j}V_{NN}(\sqrt{2}a), \quad (4.77)$$

where $c_{nn,j}$ and $c_{nnn,j}$ are the number of nearest and next-to-nearest baryonic neighbors, respectively, and neglecting small large-distance interactions. In Fig.4.17(b) we have plotted the nuclear masses $m_V(A)/A = \sum_j \Delta F_{j,V}/A$ thus obtained, extending this approximation to the cubic geometry with $A = 27$.

4.3.3 The size of a nucleon

In Sect.4.3.1 we have given a heuristic argument for the origin of the nuclear potential V_{NN} : A steric effect leading to the distortion of the energy density ϵ around a static baryon away from its vacuum value. Thus, while the baryons $B(x)$ in our model are *point-like*, the disturbance of the surrounding mesonic sites caused by a static, baryonic world-line has a *macroscopic* size

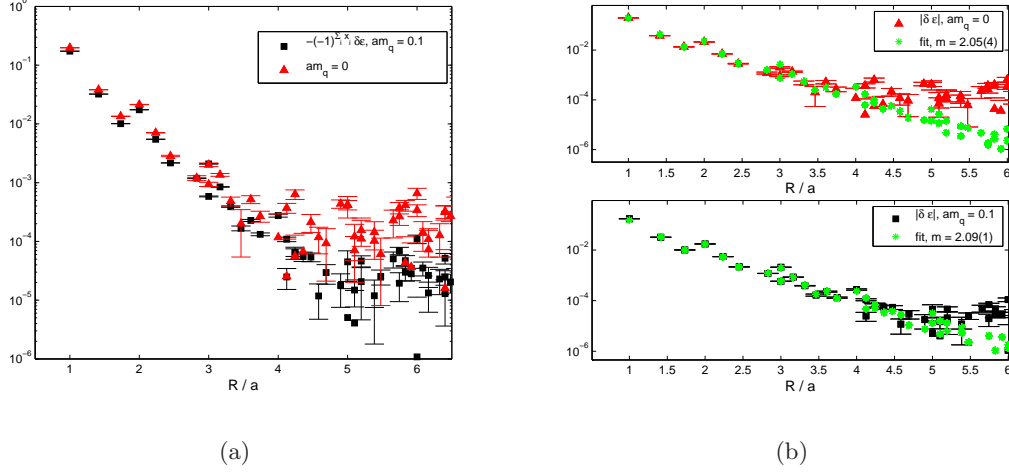


Figure 4.18: (a) $(-1)^{\sum_{i=1}^3 x_i+1} \delta\epsilon$, obtained for $am_q = 0, 0.1$ on a 16^4 - lattice, as a function of spatial distance R from the baryon at the origin. (b) The same data, now including the fit described above Eq.(4.80). For the upper plot ($am_q = 0$) we obtain $m = 2.05(4)$, for the lower ($am_q = 0.1$) $m = 2.09(1)$.

which we now want to study.

We have measured the distortion of the energy density $\delta\epsilon$ to high precision for $am_q = 0, 0.1$ on a 16^4 lattice, putting a static baryon at the origin. In Fig.4.18(a) we show $(-1)^{\sum_{i=1}^3 x_i+1} \delta\epsilon(R)$ on a semi-logarithmic scale. Clearly the profile of this “meson cloud” is governed - up to effects stemming from the lattice discretization - by an exponential decay, $\delta\epsilon \sim \exp(-R/r_0(m_q))$, where $r_0(m_q)$ shows a weak quark mass dependence.

To demonstrate that the observable $a^4 \delta\epsilon(R) = \langle 2k_{\hat{0}}(R) + 3|b_{\hat{0}}(R)| \rangle - 3/4$, which is the difference in link occupation of an ensemble with a baryon at distance R and the vacuum, corresponds to measuring link-link correlation in the presence of a source, we give a simple example in quantum mechanics in euclidean time τ : If we denote by \hat{O} , $|0\rangle, |\phi_s\rangle$, an observable, the ground state and some prepared state (containing the source in our case), respectively, then

$$\begin{aligned}
 \frac{\langle 0 | \hat{O}(\tau) | \phi_s \rangle}{\langle 0 | \phi_s \rangle} &= \sum_n \frac{\langle 0 | \hat{O}(\tau) | n \rangle \langle n | \phi_s \rangle}{\langle 0 | \phi_s \rangle} = \sum_n \frac{\langle 0 | e^{H\tau} \hat{O} e^{-H\tau} | n \rangle \langle n | \phi_s \rangle}{\langle 0 | \phi_s \rangle} \\
 &= \sum_n \frac{\langle 0 | e^{E_0\tau} \hat{O} e^{-E_n\tau} | n \rangle \langle n | \phi_s \rangle}{\langle 0 | \phi_s \rangle} \\
 &\approx \langle 0 | \hat{O} | 0 \rangle + \frac{\langle 0 | \hat{O} | 1 \rangle \langle 1 | \phi_s \rangle}{\langle 0 | \phi_s \rangle} e^{-(E_1 - E_0)\tau}
 \end{aligned} \tag{4.78}$$

for sufficiently large τ , where we labelled the basis of energy eigenstates $|n\rangle$ in order of increasing eigenvalue. The last statement holds, provided the overlap $\langle 1 | \phi_s \rangle \neq 0$. In the case of our model in $d = 3 + 1$, the static baryon acts as a source which, due to its translation invariance in $\hat{0}$ -direction, will have overlap with states of lattice momentum $p_0 = 0$. We note that in the continuum the propagator of a free boson with momentum $p_0 = 0$ gives rise to a profile of

Yukawa form

$$\int \frac{d^3k}{(2\pi)^3} \frac{e^{i\vec{k}\vec{r}}}{k^2 + m^2} = \frac{e^{-mr}}{4\pi r} \quad (4.79)$$

in position space. Our data support the $\frac{e^{-mr}}{r}$ behavior up to effects of the lattice discretization — after all our lattice is coarse and the rotational symmetry is broken. To establish the lattice equivalent of Eq.(4.79), we should use the discrete boson propagator in position space to describe our data. Writing $G(i-j)_{\text{lat}} = c \cdot (D^{-1})_{ij}$, where

$$D_{ij} = \frac{1}{2}(-\Delta_{ij} + (am)^2\delta_{ij}), \quad \Delta_{ij} = \sum_{\mu} \delta_{i-\mu,j} - 2\delta_{ij} + \delta_{i+\mu,j} \quad (4.80)$$

we fit $(-1)^{x+y+z}\delta\epsilon(\vec{R})$ to the functional form $G(\vec{R} = j-i)_{\text{lat}}$ leaving c and m (and possibly an additive constant) as fitting parameters. In Fig.4.18(b) we display the corresponding fit for $am_q = 0$ (upper part) and $am_q = 0.1$ (lower part): The data are extremely well described even at short distance where higher excited states might contribute in Eq.(4.78) and the fit yields masses $am = 2.05(4)$ and $am = 2.09(1)$, respectively. To relate these masses to the meson masses obtained in Sect.4.1.3 and [55], we have to recall that there the spectrum was extracted from the decay of the zero spatial momentum transform of the correlation function, $C(t)$. Taking as an example the free boson propagator in momentum space, $G(p)_{\text{lat}}$, at zero spatial momentum $\vec{p} = 0$, then (see Sect.8.3.1)

$$C(t) = \int_{-\pi/a}^{\pi/a} \frac{dp_0}{2\pi} \frac{e^{ip_0 t}}{4\sin^2(\frac{ap_0}{2}) + a^2m^2} = \frac{e^{-Mt}}{2\sinh aM}, \quad (4.81)$$

where M and m are related by $aM = \text{acosh}(1 + a^2m^2/2)$. Plugging in the masses $am = 2.05, 2.09$ of the above fit for quark masses $am_q = 0, 0.1$, respectively, we obtain $aM = 1.80(3)$ and $aM = 1.83(1)$ which corresponds to the ρ -mass [55], see also Tab.4.2. The size of the pion-cloud of the static nucleon, understood as the distortion of the surrounding mesonic “bath”, thus has a profile of Yukawa form with mass m_ρ , i.e.

$$\boxed{|\delta\epsilon(R)| \sim \frac{e^{-m_\rho R}}{R}}. \quad (4.82)$$

To motivate the appearance of m_ρ rather than the mass of the pion, we recall that the baryonic world line can be viewed as a sequence of triple monomers at sites $(t, \vec{x} = 0)$, $t = 0 \dots, N_t - 1$. This source is static in time and excites states with momentum $p_0 = 0$. The particle masses can be obtained from the poles of the propagator $G(p)$ in the 16 Brillouin subzones. In particular in mean-field theory to leading order in the $1/d$ -expansion and in the chiral limit [53],

$$G^{-1}(p) \sim \frac{1}{d} \sum_{i=0}^{d-1} \cos ap_i + 1 \quad (4.83)$$

with $ap = aP + P\delta$, $-\pi/2a \leq P_i \leq \pi/2a$, $-\pi/2a \leq p_i \leq 3\pi/2a$. The vector δ with components $\delta_i = 0, 1$ labels the $d^2 = 16$ Brillouin subzones in which P varies. Choosing $P^T = (iM, 0, 0, 0)$,

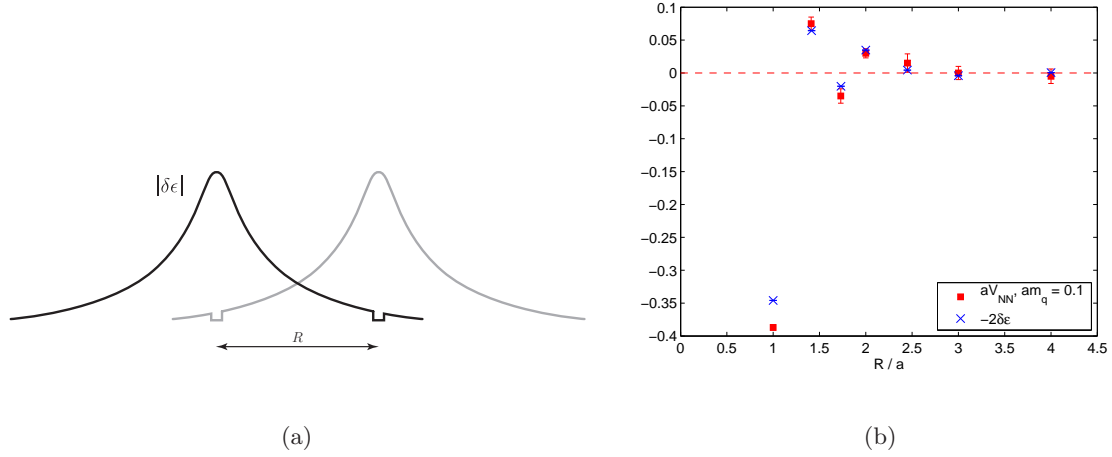


Figure 4.19: (a) The energy profile $|\delta\epsilon|$ of two baryons at distance R . The two pion-clouds overlap causing no disturbance to leading approximation, except at the location of the two baryons. (b) $V_{NN}(R)$ and $-2\delta\epsilon(R)$ at $am_q = 0.1$, showing good agreement at distances $R > 1$, confirming the relation Eq.(4.86).

the equation

$$\cosh(aM) \cos(\pi\delta_0) = - \left(\sum_{i=1}^{d-1} \cos(\pi\delta_i) + d \right) \quad (4.84)$$

has mean-field solutions for $ap^T = \pi(1, 1, 1, 1)$ ($aM^{(0)} = 0$), $ap^T = \pi(1, 0, 1, 1)$ ($aM^{(1)} = 1.76$), $ap^T = \pi(1, 0, 0, 1)$ ($aM^{(2)} = 2.29$) and $ap^T = \pi(1, 0, 0, 0)$ ($aM^{(3)} = 2.63$) + permutation in the last three entries. The $M^{(0)}$ corresponds to the pion, the Goldstone boson of the chiral symmetry Eq.(4.3) and has nonzero momentum in all components. $M^{(1)}$, $M^{(2)}$ and $M^{(3)}$ are traditionally assigned to be the masses of the vector (ρ), pseudo-vector (a_1) and scalar particle (a_0/f_0), respectively.⁶ Regarding the Yukawa form of $|\delta\epsilon(R)|$, the pion is thus ruled out as it requires momentum π/a in all components and cannot be excited by our source. The ρ has momentum $p_i = 0$ in one component. If we would have chosen a spatial direction in Eq.(4.84), this momentum component could be chosen to be p_0 , as in our case. The vector meson is the second lightest particle in the spectrum and should thus govern the long-distance behavior of the meson cloud.

We can also relate the potential $V_{NN}(R)$ to $\delta\epsilon(R)$ by considering a baryon sitting at the origin and its surrounding pion cloud. Adding a second baryon at site x with distance R from the origin, at long distance the two distortions $\delta\epsilon$ of either baryon will just be superimposed up to second order effects $\mathcal{O}(\delta\epsilon^2)$ in the perturbation $\delta\epsilon$. However, at the site x and the origin, each baryon annihilates the effect of the pion cloud of the other, as schematically depicted in

⁶A more systematic classification of staggered mesons [59, 60] at strong coupling shows that the latter two are actually taste partners of the ρ and π , respectively, see the comment below Eq.(4.53).

Fig.4.19(a). That is, the cost to add the baryon at site x , should then be

$$a\Delta E = c \left(3 - (3/4 + a^4\delta\epsilon(R)) + \sum_{x' \neq x, 0} a^4\delta\epsilon(x' - x) \right) = am_B - 2ca^4\delta\epsilon(R). \quad (4.85)$$

where the constant factor c has its origin in the definition of energy, Eq.(4.17). From the definition of $V_{NN}(R)$, $\Delta E = m_B + V_{NN}(R)$, we conclude that

$$\boxed{V_{NN}(R) \xrightarrow{R \gg 1} -2c\delta\epsilon(R) \sim (-1)^{x+y+z} \frac{e^{-m_\rho R}}{R}}. \quad (4.86)$$

Fig.4.19(b) confirms this expectation where we show $V_{NN}(R)$ and $-2\delta\epsilon(R)$ for $am_q = 0.1$. In nuclear physics, a potential of the form Eq.(4.86) is obtained from meson exchange [70]. In our one-flavor model, we have no meson exchange: The Pauli principle forbids the baryonic and mesonic world lines to intersect. We thus conclude this section with the original result that a Yukawa potential, Eq.(4.86), can be obtained from simple excluded-volume (steric) considerations, without the need for actual meson exchange.

4.4 Summary and Conclusions

In this chapter we have introduced the strong coupling formulation of Lattice QCD, carrying on the pioneering work of refs. [9, 41]. Using as an algorithmic approach the worm formulation [25] of our model [43], we compare our implementation with conventional Monte-Carlo techniques [55] finding exact agreement where this comparison is possible. We also find good agreement with existing results of mean-field theory [10, 53].

A further algorithmic technique, the snake algorithm, allows us to verify an important mismatch, so far only clearly exhibited within a mean-field treatment: The zero-temperature phase transition at finite baryon chemical potential, separating the hadronic from the chirally restored phase of dense nuclear matter, occurs at a chemical potential $\mu_{B,c}$ which is approximately 30% below its naive threshold - the baryon mass m_B - indicating a strong nuclear attraction.

We measure the nuclear potential directly, using the snake algorithm, and find a strong nucleonic nearest-neighbor attraction of ≈ 120 MeV, thus explaining why $\mu_{B,c} < m_B$.

The potential has its origin in a steric effect: A nucleon traveling through the meson vacuum distorts the vacuum in a way leading to an increase in energy density. Two static nucleons can minimize this increase by forming a nearest-neighbor pair, while baryons at e.g. distance $R = \sqrt{2}a$ repel each other as it is energetically less favorable.

The steric effect also serves to explain the large interface tension $\sigma \approx 200$ MeV/fm² of nuclear matter in our model. This led us to measure the masses of compound objects of A nearest-neighbor nucleons - the nuclei with mass number A of our model. In particular, we find that the average mass per nucleon $m(A)/A$ behaves as predicted by the liquid-drop model of nuclear physics, showing increased stability for nuclear geometries of spherical or cubic shape, owing to the large interface tension of our model.

To this point we had not considered the physical side of the steric effect: The distortion of the mesonic vacuum by a static nucleon, the mesonic “cloud”, lends the otherwise pointlike nucleon a macroscopic extent. Interestingly, we find its profile, $\delta\epsilon(R)$, to be of Yukawa form, governed

by the mass m_ρ of the ρ - meson in our model. This can be understood when interpreting the world line of a static nucleon as a t -invariant source exciting states with momentum $p_0 = 0$. Eventually, we relate $\delta\epsilon(R)$ and the potential $V_{NN}(R)$, showing that also the latter is of form $e^{-m_\rho R}/R$ even though direct meson exchange is absent in our model.

What is the relevance of this study? We have unravelled the strong coupling variant of nuclear physics in this chapter. And although it remains speculative up to which extent the steric effect described above also has consequences in real nuclear interactions, it is doubtless important to know the nuclear physics content of a model so extensively studied in the context of the QCD phase diagram, starting in the early 80's [10, 12], continuing up to now with statements about a quarkyonic phase [71].

5 Phase diagram of Lattice QCD at strong coupling

The sign problem of the strong coupling theory is mild, presumably by virtue of the exact integration over the gauge fields occurring in the partition function. Further, the efficiency of the worm algorithm does not degrade as the quark mass m_q is taken to zero. We can thus turn to the physically interesting question of the phase diagram at finite temperature T and quark chemical potential μ in the chiral limit, comparing our results to mean-field predictions. The material presented is based on publications with Ph. de Forcrand [72, 73].

5.1 Introduction, early work, expectations

5.1.1 Symmetries and expected phases, connection to real QCD

As we saw in the previous chapter, the low temperature transition in our model separates the phase of broken chiral symmetry, Eq.(4.3), at low μ from the chirally symmetric phase of dense nuclear matter. In the absence of interactions between the nucleons the naive threshold $\mu_c = m_B/N_c$ (see Sect.4.2.1) can be understood from the example of free, massive, charged fermions with Gibbs potential $G = E - \mu N$ with particle number N and total energy E . At low temperature, states i with one or more fermions carry energy $E_i/N_i = m_B$ and the potential will shift from its minimum $N = 0$ to $N > 0$ as soon as $\mu > \mu_c = \min_i\{E_i/N_i\}$. Then fermions will occupy all states in momentum space within the Fermi sphere of radius $p_F = \sqrt{\mu^2 - m^2}$, resulting in a particle density $\rho = N/V = \int_{V_F} d^3p n_p \sim p_F^3 = (\mu^2 - m^2)^{3/2}$, where $n_p \approx 1 \forall p \leq p_F$ is the occupation number for the state of momentum \vec{p} . Thus, this example not only motivates the threshold value μ_c but also demonstrates that already in the

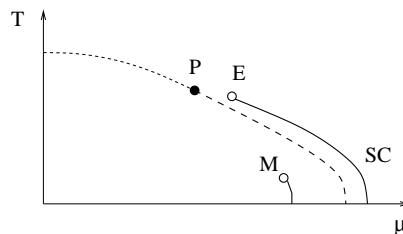


Figure 5.1: Phase diagram of 2-flavor QCD in and off the chiral limit: The first order nuclear transition (solid line) terminates in a critical endpoint M . The deconfinement, chiral symmetry restoring transition (dashed lines) changes from first order (low temperature) to second order at the tricritical point (P). For $m_{u/d} > 0$ the second order line turns into a crossover, leaving a first order line with critical endpoint E . The figure was taken from [7].

free case the density $\rho(\mu)$ shows a singularity at μ_c , its derivative becoming infinite.

In the presence of an attractive interaction, at the zero temperature transition, the system changes its state from $\rho_B = 0$ to the state of minimal energy per nucleon $E/N = m_B/N - E_B/N$, i.e. maximal binding energy E_B/N . In the absence of electromagnetic and isospin contributions as in our model, this is the state with $a^3\rho_B = 1$ following Eq.(4.73) and the discussion succeeding it.

It is instructive to compare our model to what is expected to be the phase diagram of QCD with two massless flavors [8, 74], Fig.5.1. In the absence of electromagnetic interaction, at the $T = 0$ transition, the density ρ_N will jump from 0 to $\rho_{N,0} \approx 0.16/\text{fm}^3$ which is a state containing a macroscopic volume of nuclear matter of density $\rho_{N,0}$. In complete analogy to our model, this is expected to happen at $\mu_0 = m_N - a_1$, where $m_N = 938$ MeV and the binding energy of nuclear matter $a_1 \approx 16$ MeV [70]. At strong coupling this transition coincides with the restoration of chiral symmetry. In the limit $m_q \rightarrow 0_+$, the chiral condensate $\langle \bar{\psi}\psi \rangle$, represented by the monomers of our model, see Eq.(4.14) drops to zero across the transition: The monomers are displaced by baryons. However, while QCD exhibits an additional deconfinement, chiral restoration transition at larger chemical potential, in our model quarks are confined into hadrons in the whole (μ, T) -plane. As shown in Fig.5.1, the QCD-chiral transition line (dashed line) must separate the two phases for nonzero T and μ in the chiral limit, possibly turning into a second order transition at a tricritical point (P). We now turn to mean-field predictions for the (μ, T) -phase diagram of strong coupling QCD in the chiral limit.

5.1.2 Existing mean-field and Monte-Carlo results

5.1.2.1 Mean-field results on isotropic lattices ($\gamma = 1$)

In Sect.4.2.1 we had already quoted results of mean-field calculations [12–14, 62–66] for the phase diagram, focusing on the $T = 0$ transition at $\mu_{B,c}$. Extending this summary for the full (μ_B, T) - plane, we show in Fig.5.2(a) the phase diagram obtained to leading order in a $\frac{1}{d-1}$ - expansion ($d = 4$) in the mean-field approximation [66] which has the following features:

- In the chiral limit, with intact symmetry Eq.(4.3), the chirally broken phase at low T and μ_B , is separated from the symmetric phase by a second order phase transition at $\mu_B = 0$, whose location is given by

$$aT_c = \frac{(d-1)(N+1)(N+2)}{6(N+3)} \quad (5.1)$$

for gauge group $SU(N)$, in particular $aT_c = 5/3$ for our model. The effect of baryons in this approximation can be estimated by looking at the same results, taking gauge group $U(N)$ with $aT_{c,U(N)} = \frac{(d-1)(N+2)}{6}$ [13], yielding $aT_{c,U(3)} = 5/2$, i.e. baryons decrease the transition temperature by a factor $2/3$.

- The transition line extends into the $\mu_B > 0$ region and changes into a first order transition at a tricritical point, $(a\mu_{B,t}, aT_t) \approx (1.73, 0.87)$, see Fig.5.2. The positive slope of the first

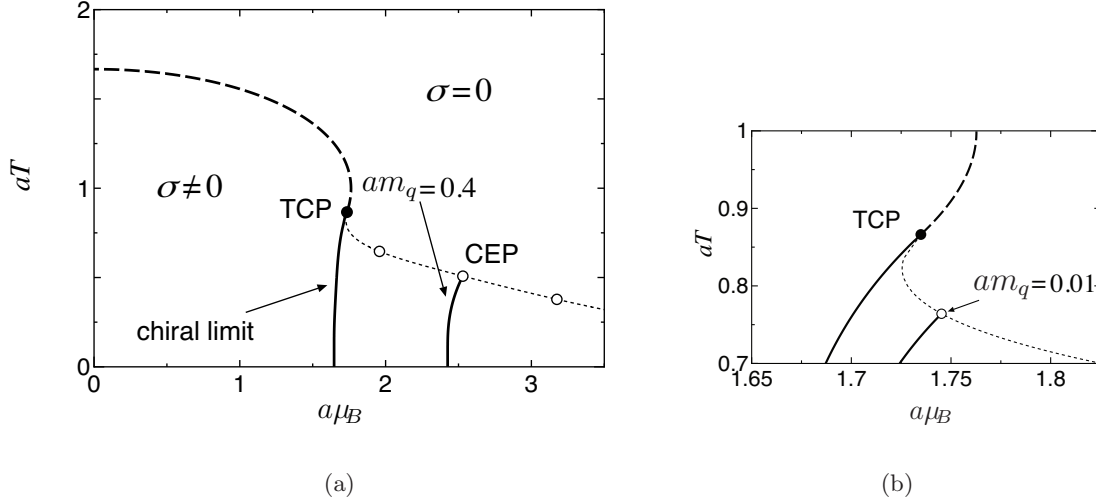


Figure 5.2: (a) Phase diagram of strong coupling QCD as obtained by mean-field theory in the $1/(d-1)$ expansion. The solid line denotes the first order transition turning second order (dashed line) in the chiral limit $am_q = 0$ at the tricritical point (TCP). Also shown is the trajectory (dotted line) of the critical endpoint (CEP) in the massive case, whose movement with changing am_q is obtained from a mean-field ansatz, see Sects.5.3 and 2.3. (b) Enlarged version of the tricritical region. The positive slope $dT/d\mu$ of the first order line close to the TCP can be motivated using relation Eq.(5.2). The figures are taken from [66], changing the labels to a compatible form.

order line just below the TCP can be understood using the Clausius-Clapeyron relation

$$\frac{dT}{d\mu} = -\frac{\Delta\rho_B}{\Delta s}, \quad (5.2)$$

where $\Delta\rho$ and Δs are the discontinuities of the baryon density and of the entropy per volume s , respectively. We know that $\Delta\rho_B > 0$, as $\frac{\partial\rho}{\partial\mu}$ diverges to positive infinity. Further, the author finds $\Delta s < 0$ and motivates the result by assuming the entropy S to be given only by the mixing entropy $S_m = N_1 \log(N/N_1) + N_2 \log(N/N_2)$ of a two-component system on a lattice with N sites. Taking $N = N_1 + N_2$ where N_1 denotes the number of baryonic sites and N_2 the number of empty sites, for our model, this results in $s = -\rho_B \log \rho_B - (1 - \rho_B) \log(1 - \rho_B)$. In the mean-field approximation one finds $1 > \rho_{B,+} > \rho_{B,-} > 1/2$ in the vicinity of the TCP which then leads to $\Delta s = s_{\rho_{B,+}} - s_{\rho_{B,-}} < 0$. With $\Delta\rho_B > 0$, $\Delta s < 0$, mean-field theory thus finds $\frac{dT}{d\mu} > 0$ and a reentrant phase diagram, Fig.5.2(b).

- For $am_q > 0$ the symmetry Eq.(4.3) is explicitly broken. The phase of dilute hadrons can thus be analytically connected to the dense phase. As a consequence, the $\mu = 0$, finite temperature transition present in the chiral limit turns into a crossover for nonzero quark mass and the $T = 0$ transition is found to terminate in a critical endpoint (CEP). For larger quark masses, $\mu_{B,c}$ is shifted to larger values of μ which explains the right-shift of the CEP with increasing am_q , starting at the TCP for $am_q = 0$. Remarkably, a quark mass as small as $am_q = 0.001$ lowers the value of T_E by 5%. As we will see in Sect.5.3,

the analytical form of the critical line $(\mu_E(m_q), T_E(m_q))$ in the vicinity of the chiral TCP can be obtained from a mean-field ansatz.

5.1.2.2 Mean-field results for an anisotropy $\gamma \neq 1$

We turn to mean-field calculations that make use of the staggered action Eq.(4.2) in the chiral limit with anisotropy $\gamma \neq 1$,

$$S_F = \sum_x \left[\sum_{\mu=1,d} \eta_{\hat{\mu}}(x) \left(\bar{\chi}_x U_{\hat{\mu}}(x) \chi_{x+\hat{\mu}} - \bar{\chi}_{x+\hat{\mu}} U_{\hat{\mu}}^\dagger(x) \chi_x \right) + \gamma \left(e^{a_t \mu} \bar{\chi}_x U_{\hat{0}}(x) \chi_{x+\hat{0}} - e^{-a_t \mu} \bar{\chi}_{x+\hat{0}} U_{\hat{0}}^\dagger(x) \chi_x \right) \right],$$

This is of particular importance for the Monte-Carlo approach which is limited to integer N_t and varies the temperature continuously via $T = 1/N_t a_t = f(\gamma)/N_t a$. where $f(\gamma) = a/a_t$. As pointed out in Sect.4.1.1, at infinite gauge coupling the weak coupling result $a/a_t = \gamma$ [49] must not necessarily hold. We note that the partition function Z of our model, given in Eq.(4.12), is a function of γ^2 , $Z = Z(\gamma^2)$. Using the $\frac{1}{d}$ -expansion in the mean-field approximation for $\gamma \neq 1$, refs. [13, 68] determine the critical anisotropy of the finite T , $\mu = 0$ transition to be

$$\gamma_c^2 = N_t \frac{(d-1)(N+1)(N+2)}{6(N+3)} \quad (5.3)$$

for fixed N_t and gauge group $SU(N)$. A sensible, i.e. N_t -independent, definition of the critical temperature is thus given by $aT_c = \frac{\gamma_c^2}{N_t}$. This implies $f(\gamma) = \gamma^2$ for $\mu = 0$, up to corrections of higher order in $1/d$. Taking $N_t \rightarrow \infty$ (zero temperature limit), the transition at finite μ is found [14] to occur at

$$a_t \mu_c = \operatorname{arcsinh}\left(\frac{\sigma_0}{\gamma}\right) - \frac{\sigma_0^2}{d-1} = \frac{3}{4} \frac{1}{\gamma^2} + \mathcal{O}\left(\frac{1}{\gamma^6}\right) \quad (5.4)$$

with $\sigma_0 = 1/\sqrt{2} \left(\sqrt{\gamma^4 + (d-1)^2} - \gamma^2 \right)^{1/2}$. Including $1/d$ corrections, the next to leading order in γ becomes $\mathcal{O}(1/\gamma^4)$. This implies $\gamma^2 a_t \mu_c = \gamma^2 a \mu_c / f(\gamma) \approx 3/4 = \text{const}$ for $\gamma \gg 1$ and thus $f(\gamma) \approx \gamma^2$ in agreement with the finite temperature result.

Finally, we remark that the particular value $a \mu_c = 3/4$ can also be obtained from the simple considerations at $\gamma = 1$ leading to Eq.(4.69)

$$3a \mu_c = a \mu_{B,c} \approx a \Delta E = (3 - \langle 2k_{\hat{0}} + 3|b_{\hat{0}}| \rangle) \approx 3 - 3/4, \quad (5.5)$$

however the last equation assumed the weak coupling relation $f(\gamma) = \gamma$ in the definition of energy, Eq.(4.17).

To summarize, mean-field theory finds to lowest order in $1/d_s$ ($d = d_s + 1$) at $\mu = 0$ that $f(\gamma) = \gamma^2$, with $f(\gamma) = a/a_t$, represents the correct anisotropy relation whereas at $T = 0$, $\mu > 0$ this relation is a good approximation for $\gamma \gg 1$ to leading and next-to-leading order in $1/d$.

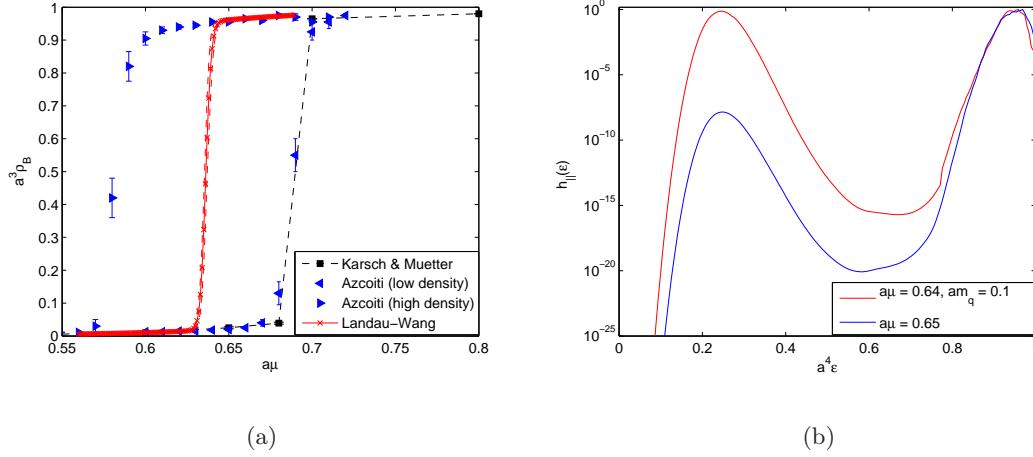


Figure 5.3: (a) Comparison of the baryon density ρ_B as a function of μ obtained by Karsch & Mütter [9] (black, dashed line) and Azcoiti et al. [42] (blue triangles) on a 4^4 lattice at $am_q = 0.1$. Thermalizing at low density leads to a phase transition to dense nuclear matter at $a\mu \approx 0.69$, compared to $a\mu \approx 0.58$ for thermalization at high density. The red curve results from reweighting, Eq.(5.9), where $h_{\parallel}(E)$, shown in (b) for $a\mu = 0.64, 0.65$, was obtained with the Wang-Landau algorithm [75]. Note that with Eq.(5.8) we extract a surface tension $\sigma_{L=4} \approx 200 \text{ MeV/fm}^2$, indicating a strong first order transition.

5.1.2.3 Previous Monte-Carlo results for $T \approx 0$ and their improvement

On the side of Monte-Carlo methods, the early, pioneering work of Karsch and Mütter [9] focused on the $T \approx 0$ transition. Equipped with the local MDP-update algorithm, described in Sect.4.1.2, the authors found for non-zero quark mass $am_q = 0.1$ a strong first order transition at $a\mu = 0.69(2)$ indicated by the jump in the baryon density ρ_B as motivated in Sect.5.1.1. These elementary results were however questioned as Azcoiti et al. [42] found that the algorithm suffered from ergodicity problems even for lattices as small as $V = 4^4$. This can be understood considering the MDP-update presented in Sect.4.1.2.1: An algorithm which relies solely on monomer-dimer replacements has average acceptance $\sim \min(am_q, 1/am_q)$. In Fig.5.3(a) we display their results (blue triangles) for ρ_B at $am_q = 0.1$. The two sets of data were obtained by simulations thermalized starting with an initial configuration containing a low (high) density of baryons, respectively. Also shown is ρ_B as obtained in [9] (black dashed line), presumably starting from low density and therefore indicating a transition at the upper limit, $a\mu \approx 0.69$, of the metastability region in μ .

More accurate results on μ_c for small systems can be obtained with the help of the now standard Wang-Landau algorithm [75]. If we take as an example a classical spin model with partition function

$$Z = \sum_{\nu} \exp(-E_{\nu}/T) = \sum_E \rho(E) \exp(-E/T) = \sum_E \exp(-F(E)/T), \quad (5.6)$$

and density of states $\rho(E)$, then the Monte-Carlo result for the energy histogram $h_{MC}(E)$ should fulfill $h_{MC}(E) \sim \exp(-F(E)/T)$ for an ergodic algorithm. To ensure ergodicity we

can employ entropic sampling: Instead of the weight $\exp(-E/T)$ above, we choose a Monte Carlo probability $\sim \exp(-E/T) \exp(F(E)/T) = \exp(-S) = 1/\rho(E)$ which trivially yields a flat, i.e. uniform histogram $h_{MC}(E)$. To obtain $\exp(F(E)/T) \sim 1/h(E)$, a priori unknown in detail, Wang and Landau [75] proposed an iterative scheme: Start with a uniform $h(E) = 1$ and update $h(E)$ after each Monte Carlo step connecting states with energy E and E' according to $h(E') \rightarrow h(E') + \Delta h$. Noting that we use a sampling probability $\sim \exp(-E/T)/h(E)$, this choice forces the algorithm to continuously explore unvisited states in the energy landscape. The modification factor Δh will be dynamically adjusted (decreased) during the simulation to ensure convergence.

Adaptation of this method to strong coupling QCD is straightforward: Ignoring the sign, our partition function reads

$$Z_{||} = \sum_{\{k\}} |w_k| = \sum_{\{k\}} |w_k| \frac{h_{||}(O(k))}{h_{||}(O(k))} \quad (5.7)$$

where $h_{||}(O) = \sum_{\{k'\}} |w(k')| \delta(O(k') - O)$ and O is a convenient observable such as the energy E or baryon number B . We take advantage of the algorithms of Sect.4.1.2, using now $|w(k)|/h_{||}(O(k))$ as Monte Carlo weight for the worm as well as for the local update algorithm and modify $h_{||}(O(k))$ after each worm move. In Fig.5.3(b) we show the resulting histogram $h_{||}(O)$ for $O = \epsilon^1$, obtained on a 4^4 lattice at $am_q = 0.1$ and $a\mu = 0.64, 0.65$. We comment on the important features:

- Both histograms are normalized s.t. $\max_{\epsilon} h_{||}(\epsilon) = 1$. From $a\mu = 0.64$, where the peaks in the dilute and dense phase are approximately of equal magnitude, we can extract an estimator for the surface tension of nuclear matter according to

$$a^2 \sigma_L / T = -\log(h_{\min}/h_{\max}) / 2L^2 \approx 1, \quad (5.8)$$

which is based on the derivation leading to Eq.3.11 of Sect.3.3.1.2. With $aT = 1/4$ we can extract $\sigma_{L=4} \approx 200$ MeV/fm², in rough agreement with the result in Sect.4.3.1 for $am_q = 0$ and $aT = 1/16$.

- Having obtained $h_{||}(E)$ to sufficient accuracy should permit us to simulate at the given parameter set $am_q = 0.1, a\mu = 0.64$ with fixed measure $|w_k(\mu, m_q)|/h_{||}(E(k))$ to obtain a uniformly distributed $h_{MC}(E)$. Expectation values for observables O such as $\rho_B, \bar{\psi}\psi$ can then be extracted for a range of parameters by reweighting

$$\langle O \rangle_{\mu'} = \frac{\sum_j O_j \text{sign}(j) h_{||}(E_j) w_j(\mu') / w_j(\mu)}{\sum_k \text{sign}(k) h_{||}(E_k) w_k(\mu') / w_k(\mu)}. \quad (5.9)$$

We compare our results for $O = \rho_B$ given by the red curve in Fig.5.3(a) to those obtained in [9, 42] (blue triangles), finding $a\mu_c = 0.635$ which seems plausible in view of the metastability region $0.58 < a\mu < 0.69$.

¹Strictly speaking, we use $O = 2N_{Dt} + 3N_{Bt}$, where N_{Dt} , N_{Bt} are the total number of dimer-links and (anti)-baryonic links in $\hat{0}$ -dir, respectively.

5.1.2.4 Previous Monte-Carlo results for $\mu = 0$

Using an improved version of the simple local update algorithm, Karsch et al. [76] investigated the nature of the finite temperature transition. Due to algorithmic limitations this had to happen at non-zero quark mass $am_q > 0$ and results were extracted by extrapolation to the chiral limit. Still, the authors were able to identify a second order phase transition in the $O(2)$ -universality class, in accordance with Sect.5.1.1. Fixing the temporal extent of their lattice to $N_t = 4$ and varying the anisotropy γ , the location of the transition is given by

$$2.35 < \gamma_c < 2.4. \quad (5.10)$$

In the following we will verify this result explicitly in the chiral limit.

5.2 Results in the chiral limit, $am_q = 0$

In order to vary the temperature continuously we introduce an anisotropy γ between the spatial and temporal lattice spacing. Sect.5.1.2 suggests to use

$$f(\gamma) = \gamma^2 = a/a_t. \quad (5.11)$$

We remark again that these results were obtained in an expansion in $1/(d_s)$ ($d_s = 3$), using a mean-field approximation. This should be verified using exact, non-perturbative methods (i.e. Monte-Carlo). Here, we take Eq.(5.11) as working assumption for the whole (μ, T) -plane, using lattices with $N_t = 4$ sites in the $\hat{0}$ -direction. In particular, this implies that

$$aT = \gamma^2/N_t \text{ and } a_t\mu = a\mu/\gamma^2. \quad (5.12)$$

For the finite temperature transition at $\mu = 0$, we extend the study to $N_t = 2, 6$.

Class	γ	α	ν
$d = 3, O(2)$ [77]	1.3177(5)	-0.0146(8)	0.67155(27)
$d = 3, Z_2$ [78]	1.237(4)	0.108(5)	0.631(2)
$d \geq 3$ tricritical (mean-field) [79]	1	0	$\frac{1}{2}$

Table 5.1: Critical exponents of the $d = 3, O(2), Z_2$ universality classes as well as tricritical exponents given by mean-field theory (with upper tricritical dimension $d = 3$). Note that the combination γ/ν of the upper two is hard to distinguish in practice.

5.2.1 Observables

In a finite volume, the symmetry Eq.(4.3), present for $am_q = 0$, cannot break spontaneously. As a consequence, the order parameter $\langle \bar{\psi}\psi \rangle = 0 \forall \mu, T$. Fortunately, the chiral susceptibility, $\chi_\sigma = \frac{1}{V} \frac{\partial^2}{\partial m^2} \log Z = \langle \sum_x \bar{\psi}\psi_x \bar{\psi}\psi_0 \rangle$ is accessible by an improved estimator, Eq.(4.32), which we

measure during the worm update.

The divergence of susceptibilities at a phase transition in infinite volume will turn into a rounded peak in a finite system with linear extent L . In particular

$$\chi_{\sigma,L} = L^{\gamma/\nu} \hat{\chi}(tL^{1/\nu}) = L^{\gamma/\nu} (a_0 + \mathcal{O}(tL^{1/\nu})), \quad (5.13)$$

where $t = 1 - T/T_c$ or $t = 1 - \mu/\mu_c$ is a reduced parameter for transitions in T and μ , respectively. In our case $\chi_{\sigma,L}$ will be a monotonic function owing to the vanishing order parameter. Our model has the $U(1)$ symmetry Eq.(4.3). At a continuous phase transition the correlation length ξ diverges, rendering the system with compactified $\hat{0}$ -direction effectively three dimensional. The model should thus be in the $d = 3, O(2)$ universality class where we give the for us relevant exponents in Tab.5.1. In principle, the relation Eq.(5.13) allows us to verify these exponents by means of a fit in $T_c(\mu_c), \gamma, \nu$ varying $T(\mu)$ or L . In practice, $O(2)$ - and Z_2 -critical exponents are numerically close for $d = 3$ and a clear distinction remains difficult even for lattices as large as $L = 128$ [80]. We therefore take the $O(2)$ -universality of our model as an established fact and concentrate on the determination of the critical parameter $T_c(\mu_c)$.

In view of the mean-field results on the phase diagram (Fig.5.2), we should expect the relation Eq.(5.13) to hold in the vicinity of the *tricritical* point (TCP) with tricritical exponents γ_t, ν_t . As shown in Sect.2.3 the upper critical dimension for tricritical behavior is expected to be $d = 3$ [23]. Our model describes a lattice field theory in $d = 3 + 1$ dimensions at finite temperature, the exponents γ_t, ν_t should thus be the mean-field tricritical exponents listed in Tab.5.1.

Accepting the above statements as our working hypothesis, the relation (5.13) will be helpful as it implies that

- at the critical parameter $T_c(\mu_c)$ of a continuous phase transition, i.e. at $t = 0$, the rescaled susceptibility $\chi_{\sigma,L}/L^{\gamma/\nu} = a_0 \forall L$, leading to a crossing when plotted as a function of T , see Fig.5.4(a) and the next Section.
- having an estimate for $T_c(\mu_c)$, $\chi_{\sigma,L}/L^{\gamma/\nu}$ should collapse to a universal scaling function $\hat{\chi}(tL^{1/\nu})$ when plotted as a function of $tL^{1/\nu}$.

Both statements hold, provided the appropriate critical exponents are used.

For a first order transition, the susceptibility of the order parameter diverges with exponents [81] $\gamma = \alpha = 1, \nu = 1/d$. In our case, χ_{σ} will not be peaked but rather behave monotonically decreasing for increasing T or μ beyond the transition value. We cannot expect a behavior as indicated in Eq.(5.13) as there is no universality argument at a first order transition. Chiral perturbation theory [82] however predicts

$$\chi_{\sigma,L} = \frac{1}{2} \Sigma^2(T) L^3 (1 + \mathcal{O}(1/L)), \quad (5.14)$$

with the infinite volume condensate $\Sigma = \lim_{m_q \rightarrow 0} \lim_{L \rightarrow \infty} \langle \bar{\psi} \psi \rangle$. In particular, this implies that $\chi_{\sigma,L}/L^3$ should be roughly volume independent for $T < T_c$. Due to the sign problem we are restricted to rather small lattices $L \leq 16$. Still, we make use of formula (5.14) in the following context.

First order phase transitions exhibit phase coexistence: At the transition point (say at T_c) the system contains connected domains of broken and unbroken symmetry. Borgs and Kotecky [83] found that the partition function of a system with volume L^d that contains $q + 1$ coexisting

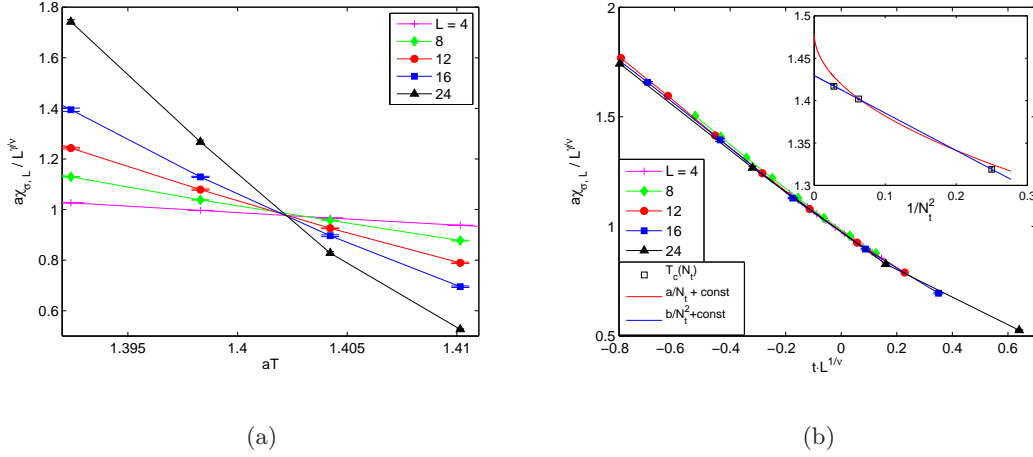


Figure 5.4: (a) The susceptibility $\chi_{\sigma,L}/L^{\gamma/\nu}$ obtained at $m_q = \mu = 0$ for systems of size $L^3 \times N_t$ with $N_t = 4$. Using $d = 3, O(2)$ critical exponents, see Tab.5.1, the crossing indicates $aT_c = 1.402(1)$ (see Eq.(5.13)). (b) Collapsing $\chi_{\sigma,L}/L^{\gamma/\nu}$ with $t = T/T_c(N_t) - 1$ for $N_t = 4$. Using $N_t = 2, 6$ -lattices we obtain $aT_c = 1.319(2), 1.417(2)$, respectively. The inset shows a linear extrapolation to $N_t \rightarrow \infty$ according to $aT(N_t) = c/N_t + aT_{c,extra}$ (red, solid line) which yields $aT_{c,extra} = 1.48(1)$, while extrapolating according $aT(N_t) = c/N_t^2 + aT_{c,extra}$ (blue curve) gives $T_{c,extra} = 1.430(2)$. Both extrapolations are plotted against $1/N_t^2$.

phases (q ordered and one disordered) can be approximated by

$$Z \sim \exp(-f^{(d)}(T)L^d/T) + q \exp(-f^{(o)}(T)L^d/T), \quad (5.15)$$

with smooth functions $f^{(o)/(d)}(T)$, obeying $f^{(o)}(T) = f(T)$ and $f^{(d)}(T) = f(T)$ for $T \leq T_c, T \geq T_c$, respectively, $f(T)$ being the free energy density of the system. In the vicinity of the transition the “metastable free energies” of the ordered and disordered phase $f^{(o)/(d)}$ are given by $f^{(o)/(d)} \approx f_0 + f^{(o)/(d),\prime}(T - T_c)$ such that $Z \sim \exp(-L^d f^{(d)}(T)/T) (1 + q \exp(-L^d \Delta f'(T - T_c)/T))$ with $\Delta f' = f^{(o),\prime} - f^{(d),\prime}$. The (integer) parameter q is the relative weight of the ordered and disordered phases at the coexistence and has to be replaced by $c \in \mathbb{R}$ in our case of a continuous broken symmetry. For observables such as χ_σ , Eq.(5.15) leads to

$$\chi_{\sigma,L}/L^3 = \frac{a/L^3 + b \exp(-L^3 \Delta f'(T - T_c)/T)}{1 + c \exp(-L^3 \Delta f'(T - T_c)/T)}, \quad (5.16)$$

where we assumed $\chi_{\sigma,L} \sim L^3$ in the ordered phase up to corrections in $1/L$ and in the approximation of weak temperature dependence, whereas $\chi_{\sigma,L}$ was taken to be regular in the disordered (chirally symmetric) phase, i.e. $\chi_{\sigma,L} = a/(1 + c)$ at the transition.

5.2.2 Results

5.2.2.1 $\mu = 0$

Taking $T = \gamma^2/N_t a$ we show in Fig.5.4 results for the chiral susceptibility $\chi_{\sigma,L}$ obtained on systems of size $L^3 \times N_t$ for $N_t = 4$. In Fig.5.4(a) $\chi_{\sigma,L}/L^{\gamma/\nu}$ is given as a function of aT , where γ, ν are the $d = 3, O(2)$ critical exponents. The volumes of linear extent $L = 4, \dots, 24$ cross at $aT = aT_c(N_t = 4) = 1.402(1)$.

Performing similar runs for $N_t = 2, 6$ we find $aT_c = 1.319(2), 1.417(2)$, respectively. In fact, values extracted for $T_c(N_t)$ will be subject to finite discretization effects: Given T_c for $N_t = 2, 4, 6$ we can at least make a qualitative statement by extrapolating to $N_t = \infty$. The inset in Fig.5.4(b) shows two extrapolations assuming $aT_c(N_t) = c/N_t + \text{const}$ and $c/N_t^2 + \text{const}$ ². The fits suggest that the error due to finite spacing in $\hat{0}$ -direction is of order $1/N_t^2$, yielding

$$aT_c^{N_t \rightarrow \infty} = 1.430(2) \quad (5.17)$$

which can be compared to the mean-field result $aT_{c,mf} = 5/3$.³ To estimate the effect of baryons in a finite temperature mean-field treatment we quote the Monte-Carlo result for $U(3)$ [80] for $aT_c^{U(3)} \approx 1.87$ ($N_t = 4$), compared to $aT_{c,mf}^{U(3)} = 5/2$. Note, that the relatively larger difference between Monte-Carlo and mean-field theory is counterintuitive, as the $1/d_s$ expansion to lowest order in d_s should yield results more accurate for a theory without baryons which, for $SU(3)$, are only suppressed by $1/\sqrt{d_s}$.

In summary, in physical units we obtain $T_c \sim 500$ MeV. To develop a feeling for the order of magnitude we revert to full lattice QCD with $N_f = 2 + 1$, i.e. two light and one heavy quark flavor, at the physical masses. There $150 \text{ MeV} < T_c < 175 \text{ MeV}$ [3] and $T_c \approx 190 \text{ MeV}$ [4], respectively, depending on the lattice action, observables and number of time slices.

5.2.2.2 Full phase diagram

Continuing our study to $\mu > 0$, the system exhibits a sign problem as pointed out in Sect.4.1.1, which however turns out to be mild for a wide range of the parameters $aT, a\mu$, s.t. systems of size up to $16^3 \times 4$ are accessible with primitive computing resources and strategies. We point to Sect.5.2.3 for a more thorough statement.

For $\mu > 0$ we can thus follow the critical line $T_c(\mu)$, monitoring the collapse of $\chi_{\sigma,L}$ using the appropriate critical exponents. We find that the transition along this line remains 2nd order up to $\gamma^2 a_t \mu = a\mu = 0.6$, where in Fig.5.5(a) $\chi_{\sigma,L}/L^{\gamma/\nu}$ is plotted as function of $t \cdot L^{1/\nu}$, using $O(2)$ -critical exponent. With a slight increase to $a\mu = 0.64$ in Fig.5.5(b) a change to tricritical behavior becomes visible: The rescaled chiral susceptibility collapses nicely on a single curve when using critical exponents (Fig.5.5(b), upper part) but does more so using tricritical exponents (lower part). No such collapse is possible when increasing the chemical potential slightly to $a\mu = 0.66$, as can be seen in Fig.5.6(a). Instead, the system shows 1st

²A full quadratic fit trivially gives an exact description of the data. Doing so we find that the linear term is consistent with zero within errors, supporting a relation $\sim 1/N_t^2 + \text{const}$.

³Note that using the weak coupling relation $\gamma = a/a_t$ our measurements would correspond to $T_c^{f(\gamma)=\gamma}(N_t) \approx 0.81, 0.59, 0.49$ for $N_t = 2, 4, 6$, respectively. A linear extrapolation in $1/N_t$ yields here $aT_c = 0.34(1)$, whereas a extrapolation $aT = c/N_t^2 + \text{const}$ only yields a poor description of the data as the missing linear term in $1/N_t$ is dominant. Taking the weak coupling relation thus implies poor convergence when increasing N_t .

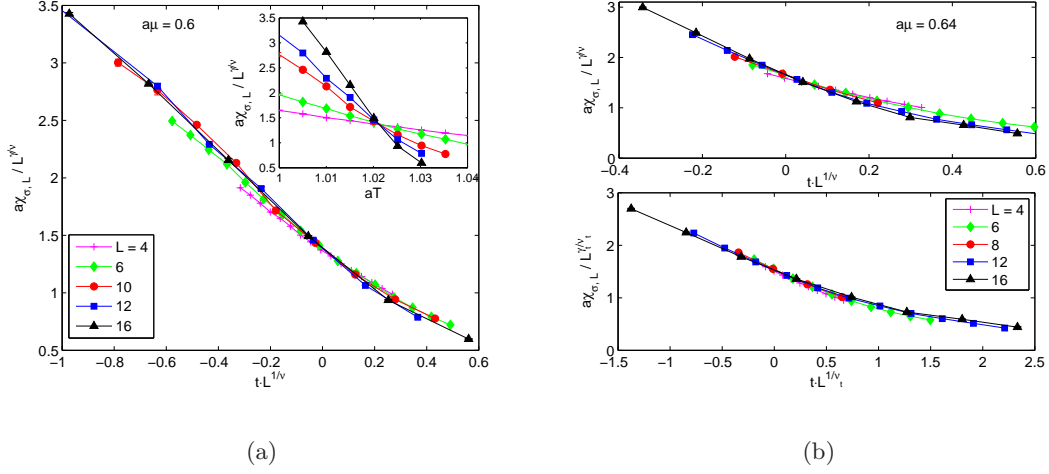


Figure 5.5: (a) Collapse of $\chi_{\sigma,L}/L^{\gamma\nu}$ at $\gamma^2 a_t \mu = a\mu = 0.6$ using $O(2)$ critical exponents for various lattice sizes. The inset shows that the transition happens at $aT_c(a\mu = 0.6) \approx 1.02$. (b) Trying the same for $a\mu = 0.64$ does yield a slightly better collapse for the available volumes when using mean-field tricritical exponents γ_t, ν_t (lower part) instead of $d = 3, O(2)$ (upper part) critical exponents, which indicates tricritical behavior.

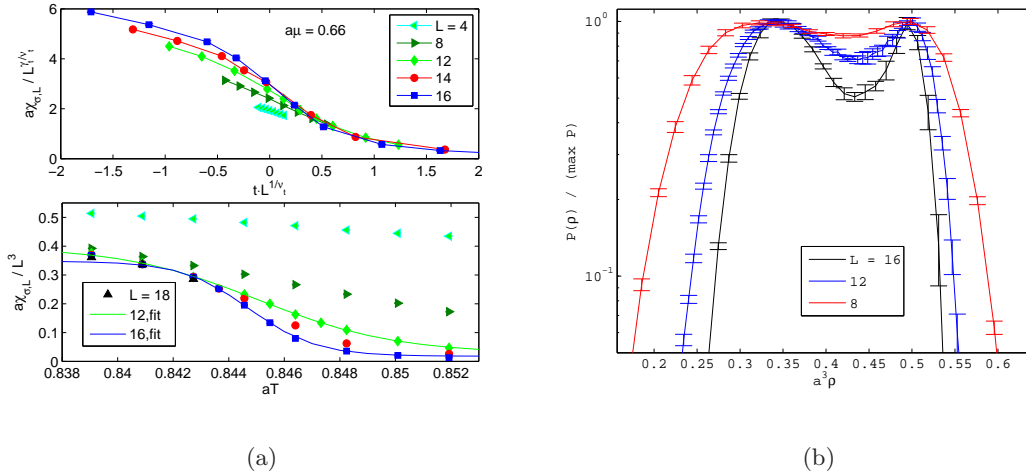


Figure 5.6: (a) Failing collapse of $\chi_{\sigma,L}/L^{\gamma_t\nu_t}$ at $a\mu = 0.66$ (upper part) using tricritical exponents. Instead, rescaling to $\chi_{\sigma,L}/L^3$ the data becomes volume independent below the transition (lower part). The solid lines are fits according to the Borgs-Kotecky ansatz, Eq.(5.16). (b) Distribution $P(\rho)$ for $a\mu \approx 0.66$, slightly reweighted in T and μ to equal peak height in the dilute and in the dense phase. Extracting an interface tension yields $a^2 \sigma_L/T = -\log(P_{\min})/2L^2 = 10^{-3}$. We are thus already in the first order region.

order behavior:

- The probability distribution $P(\rho)$ shown in Fig.5.6(b) exhibits a double peak whose locations in the dense, chirally symmetric phase remain fixed with increasing L . Moreover

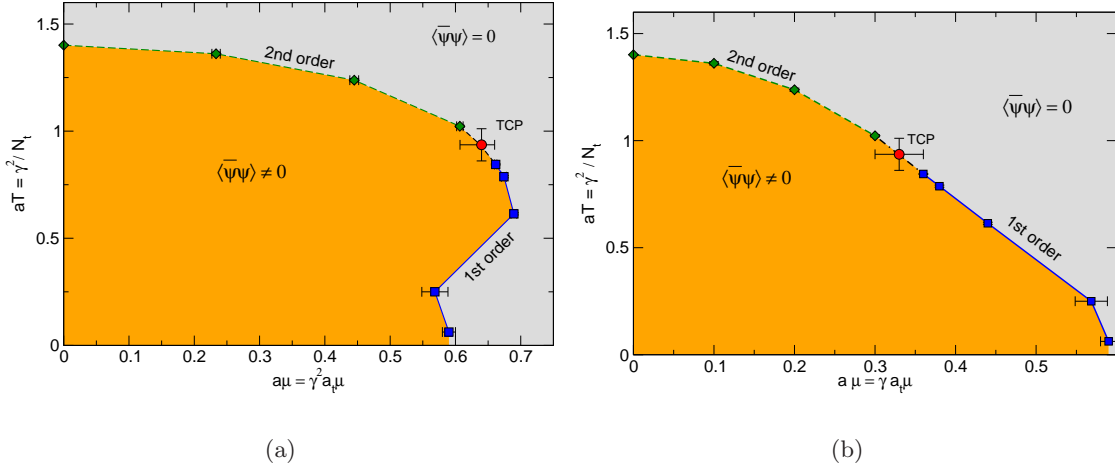


Figure 5.7: (a) Phase diagram as obtained on a $N_t = 4$ lattice with one exception: The lowest temperature point is the outcome of the snake-algorithm on $N_t = 16$ lattice with $\gamma = 1$. Throughout this section the choice $a/a_t = \gamma^2$ has been adopted. Using this convention the phase diagram shows the reentrance region predicted by mean-field theory, Eq.(5.2), and brings the Monte Carlo and mean-field estimate on TCP in rough agreement. (b) This agreement vanishes when changing the x -axis to $a_t \mu = a\mu/\gamma$ as displayed. The reentrance region is gone, now the shape of the transition line is closer to what is expected in chiral 2-flavor QCD, Fig.5.1 and closer to the mean-field phase diagram of strong coupling Lattice QCD given in [13]. A careful extrapolation $a_t \rightarrow 0$, $N_t \rightarrow \infty$ is needed for a final determination of the phase diagram.

the estimator of the surface tension σ , given by $a^2 \sigma_L / T = -\log(P_{\min}/P_{\max})/2L^2$, yields $a^2 \sigma_L / T = \text{const} \approx 10^{-3}$ for the available sizes $L = 8, 12, 16$, indicating a nonzero surface tension $\sigma = \lim_{L \rightarrow \infty} \sigma_L$, characteristic for a 1st order transition (c.f. Sect.3.3.1.2).

- For $T < T_c(a\mu = 0.66)$, $\chi_{\sigma,L}/L^3$ remains volume independent (see lower part of Fig.5.6(a)) as suggested by Eq.(5.14) and an application of the Borgs-Kotecky ansatz, Eq.(5.15), shows that the data of lattice sizes $L = 12, 16$ are well described by Eq.(5.16), a fit yielding $\chi_{\text{red}}^2 = 0.7, 1.35$, respectively.

From the available data we thus conservatively conclude for the location of the TCP

$$(a\mu_t, aT_t) = (0.64_{-0.04}^{+0.02}, 0.94(7)), \quad (5.18)$$

which we can compare to the mean-field prediction $(a\mu_{t,mf}, aT_{t,mf}) = (0.577, 0.866)$ [66] finding good agreement on which we comment below.

We conclude this subsection by giving the complete phase diagram in Fig.5.7(a) obtained for $N_t = 4$. Two more low- T measurements have been included to the transition line separating the chirally broken (orange) from the chirally symmetric, dense phase (grey): The location $a\mu_c \approx 0.6$ of the transition $aT = 1/16$ with $\gamma = 1$ is known from our treatment of the $T \approx 0$ -theory with the snake algorithm (c.f. Sect.4.2.4). For $aT = 1/4$ (also $\gamma = 1$) we state $a\mu_c(aT = 0.25) = 0.57(2)$ which was estimated from the discontinuity of the baryon density ρ , obtained by applying the Wang-Landau algorithm (c.f. Sect.5.1.2) in the chiral limit on a 4^4 lattice.

The phase diagram given in Fig.5.7(a) in particular shows the reentrance region, predicted by mean-field theory (Fig.5.2) with the important difference that the slope $dT/d\mu$ of the critical line changes sign deep in the first order region, contrary to Fig.5.2(b) and the argumentation below Eq.(5.2). Indeed, keeping $N_t = 4$ fixed implies that a_t increases as T is decreases. Thus, the corrections arising in the limit $a_t \rightarrow 0$ are expected to be larger at low temperature. We emphasize that the phase diagram crucially depends on the choice of $f(\gamma) = a/a_t$. We consistently used $f(\gamma) = \gamma^2$ throughout our study - a choice suggested by mean-field theory which we found justified at least for $\mu = 0$. For Monte-Carlo simulations of the partition function Eq.(4.12), we note that such choice assigns the physically sensible weight

$$w(\ell) \sim \exp(\pm a_3 \mu N_t / \gamma^2) = \exp(\pm 3\mu/T) \quad (5.19)$$

to the (anti)baryonic world lines in Eq.(4.13). Using instead $w(\ell) \sim \exp(\pm a_3 \mu N_t / \gamma)$ but keeping $T = \gamma^2/N_t$ leads to the phase diagram sketched in Fig.5.7(b) where the reentrant shape has vanished, along with the agreement between Monte-Carlo and mean-field results on $a\mu_{\text{TCP}}$.

A future study can resolve this issue by performing a more systematic $a_t \rightarrow 0$, $N_t \rightarrow \infty$ extrapolation which we only started for $T_c(\mu = 0)$. The sign problem is absent here, so simulations on large spatial volumes of linear extent $L \gg 24$ are feasible. For the given values $N_t = 2, 4, 6$ we observed the trend of a slight increase in the critical value aT_c . If this trends persists when performing the same extrapolation at finite μ , then the effect of the discretization is to shrink the chirally broken region. A similar extrapolation can be carried out for $T \rightarrow 0$. There the snake algorithm should allow one to find μ_c for $\gamma \neq 1$, thus providing us with a Monte-Carlo estimate for $f(\gamma)$ at $T = 0$.

However, for $\mu > 0, T > 0$, the limit $N_t \rightarrow \infty$ is more involved because of the sign problem which we want to discuss now.

5.2.3 Sign problem

The feasibility of our study not only relied on overcoming algorithmic problems present in [42] which are essentially resolved with the worm algorithm, but also on controlling the severity of the sign problem. The latter can be quantified by the ‘‘average sign’’

$$\langle \text{sign} \rangle = \frac{Z}{Z_{||}} = \exp\left(-\frac{\Delta f V_s}{T}\right) = \exp\left(-\frac{a^4 \Delta f L^3 N_t}{\gamma^2}\right) \approx \frac{\sum_K \text{sign}(K)}{N_{\text{MC}}}, \quad (5.20)$$

where the Monte-Carlo average over a sample of length N_{MC} is given in the last step. The ratio $Z/Z_{||}$ of partition functions $Z, Z_{||}$ with the weights w_k and $|w_k|$, respectively, has been rewritten using the difference in free energy density $a\Delta f = -\gamma^2 \log(Z/Z_{||})/N_t V_s$, where $\Delta f \equiv \Delta f(T, \mu, m_q)$ measures the severity of the sign problem. Taking Eq.(5.20) as the correct scaling assumption in L , we show $a^4 \Delta f$ as a function of $a\mu$ in Fig.5.8 for $T = T_t, am_q = 0$ using systems of size $L^3 \times 4$, $L = 4, 8, 12$:

- At the tricritical point $a^4 \Delta f \approx 5 \cdot 10^{-4}$ (see Fig.5.8(b)) compared to $a^4 \Delta f_{\text{HMC}} \approx a^4 (m_B - \frac{3}{2} m_\pi) \rho_B = \mathcal{O}(1)$ obtained in the conventional approach of HMC and reweighting from isospin chemical potential (see [2] for a review) where we used $am_B \approx 3$, $am_\pi(am_q = 0) = 0$ and $\rho_B(T_t, \mu_t) \approx 0.5$. It shows the mildness of the sign problem in our approach to strong coupling QCD. A possible reason lies in the exact integration over the gauge fields,

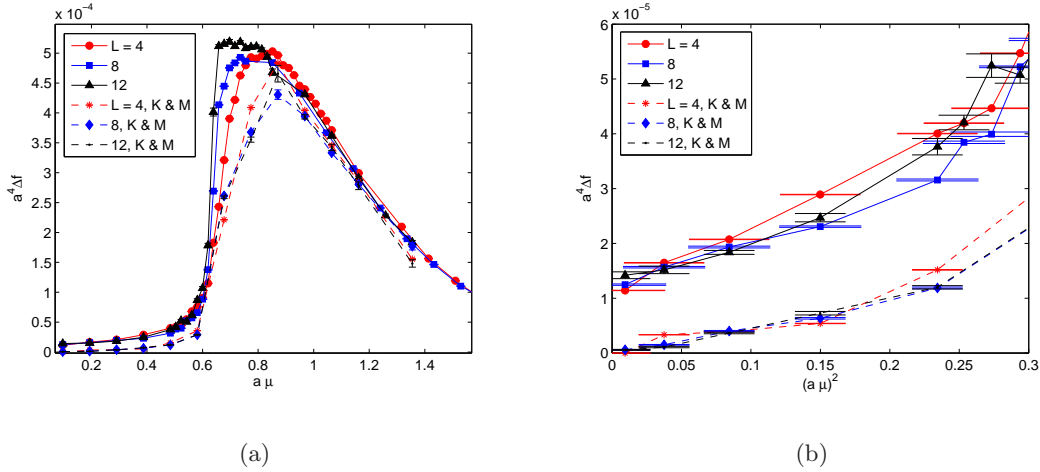


Figure 5.8: The difference in free energy $a^4\Delta f$, Eq.(5.20), as a function of $a\mu$ at $T = T_t$ ($am_q = 0$) and two different approaches: Sampling the partition function Z , Eq.(4.12) (solid lines), and using the resummation proposed by Karsch and Mütter [9], see Sect.8.4.1 (dashed lines, labelled “K&M”). As visible $a^4\Delta f$ is almost volume independent and reaches $5 \cdot 10^{-4}$ at the transition which we compare to $a^4\Delta f_{\text{HMC}} = \mathcal{O}(1)$ using the conventional approach of HMC. Thus the sign problem is mild in our approach, and further benefits from the resummation are only small. (b) $a^4\Delta f$ now as a function of $(a\mu)^2$, showing that $\Delta f \sim \mu^2$ for small $a\mu$ as expected (see text). Note that the resummation (“K&M”) resolves the sign problem at $a\mu = 0$ while $\Delta f(0, T_t, am_q = 0) \neq 0$ for the naive approach.

carried out in Eq.(4.6) which conventionally is performed stochastically. This small value of Δf yields an average sign $\langle \text{sign} \rangle \approx 0.1$ on a $16^3 \times N_t$ lattice at $(\mu, T) = (\mu_t, T_t)$.

- Comparing our approach (solid line) based on the sampling of the partition function $Z_{||}$ with weights defined in Eq.(4.12) with the approach (dashed line) based on the resummation of weights [9] (see also Sect.8.4.1), we see that the latter resolves the sign problem at $\mu = 0$ rendering it however only slightly milder for $\mu > 0$.
- Further we note that, as evident from Fig.5.8(b) $\Delta f \sim \mu^2$ for small chemical potential. That Δf must be an even function of μ follows from the fact that under the change $\mu \rightarrow -\mu$ baryons and anti-baryons only exchange their role in our one-flavor theory, leaving $\langle \text{sign} \rangle$ and thus Δf unchanged. For small $a\mu$, away from any transition, we can thus write $\Delta f = \sum_n c_n(T, m_q)\mu^{2n}$, keeping only the μ^2 term.
- For a particular value of $(a\mu, aT)$ we can increase N_t and γ , keeping $\frac{N_t}{\gamma^2} = \frac{1}{T}$ fixed. The relation $\langle \text{sign} \rangle \sim \exp(-\text{const } L^3 N_t / \gamma^2)$ (Eq.(5.20)) then implies that we can in principle take the continuum limit ($N_t, \gamma \rightarrow \infty$) in $\hat{0}$ -direction while only being limited by the spatial volume V_s . A more precise study of the phase diagram, especially in view of the open question to accurately determine $f(\gamma) = a/a_t$, seems therefore feasible.

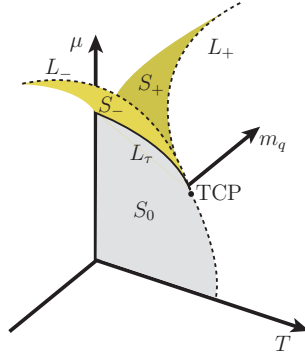


Figure 5.9: Schematic phase diagram of strong coupling QCD, in analogy to the metamagnet, Fig.2.4. Note that the T and μ -axes have been swapped. On the surface S_0 the two phases $\langle \bar{\psi}\psi \rangle \gtrless 0$ of the limits $m_q \rightarrow 0_{\pm}$ coexist. This extends to a three-phase coexistence at the triple line L_{τ} , ending in a tricritical point (TCP) where the transition turns second order (dashed line). For $m_q \neq 0$, the “wing”-lines L_{\pm} of critical end points (CEP) depart tangentially from the chiral TCP, bounding the surface S_{\pm} of dilute/dense phase coexistence.

5.3 Results for $m_q > 0$

5.3.0.1 Observables and strategy

Away from the chiral limit, the symmetry Eq.(4.3) is broken explicitly. We recapitulate the findings of mean-field theory (see Fig.5.2(a)) which proved to be accurate in the chiral limit: For $m_q > 0$ the second order line collapses to a critical endpoint (CEP) of the low temperature, first order line, leaving a crossover “trace” at high temperature and for $\mu \geq 0$.

With the help of Monte-Carlo it has been numerically verified [76] that the finite temperature transition is indeed a crossover for $am_q > 0$: The chiral susceptibility

$$\chi_{\sigma,L} = \frac{1}{L^3 N_t} \frac{\partial^2}{\partial (2m_q)^2} \log Z = \frac{1}{(2am_q)^2 L^3 N_t} (\langle N_M^2 \rangle - \langle N_M \rangle^2 - \langle N_M \rangle) \quad (5.21)$$

remains flat in the vicinity of γ_c , and a peak only develops in the limit $m_q \rightarrow 0$. On the other hand, we know that for $T \approx 0$ (actually $aT = 1/4$) and $am_q = 0.1$ the system undergoes a strong first order transition (strictly speaking only in infinite volume of course) from the hadronic to the dense phase, see Sect.5.1.2, in particular Fig.5.3. We thus conclude the mean-field scenario to be likely, i.e. the first order line must terminate in a critical end-point (CEP). There are reasons to expect $d = 3, Z_2$ (Ising) universality for this point: The phase diagram of our model in the chiral limit, Fig.5.7, resembles in some core features the expected phase diagram of continuum QCD with two massless flavors [6–8], see Fig.5.1. In particular, in a mean-field treatment of an effective model of 2-flavor QCD ref. [6] finds, for $m_q > 0$, a divergent correlation length only in a scalar channel. The corresponding effective Lagrangian is therefore that of the linear sigma model which exhibits Z_2 -symmetry. We note that besides the apparent similarities of the two phase diagrams, the transition line (dashed lines connected by tricritical point P and solid 1st order line ending in the QCD critical point E) in Fig.5.1 is to the deconfined phase. The solid line terminating in the point M represents the nuclear “liquid-gas” transition, to the right of this line nuclei are forming, in analogy with the transition

of our model. The endpoint of a generic liquid-gas transition is in the universality class of the $d = 3$ Ising model.

To locate the point of criticality in the phase diagram for $m_q > 0$ we will make use of the standard scaling, Eq.(5.13), of $\chi_{\sigma,L}$ with $d = 3$, Ising critical exponents, Tab.5.1. In particular in a finite volume the peak $\chi_{\sigma,L,\max}$ at the pseudo transition should fulfill

$$\log \chi_{\sigma,L,\max} = \frac{\gamma}{\nu} \log L + c. \quad (5.22)$$

Further, by noting that $\chi_{\sigma} = \frac{1}{V} \langle (\bar{\psi}\psi - \langle \bar{\psi}\psi \rangle)^2 \rangle$, we see that the properly normalized distribution function of the chiral condensate, $P(x_{\langle \bar{\psi}\psi \rangle})$ where $x_{\langle \bar{\psi}\psi \rangle} = (\bar{\psi}\psi - \langle \bar{\psi}\psi \rangle) \cdot L^{-\frac{\gamma/\nu+d}{2}}$, should yield the universal distribution function at the CEP for any L (see also Sect.3.3.1.1). However, within our model $\langle \bar{\psi}\psi \rangle = \langle N_M \rangle / (2am_q)$ from which Eq.(5.21) followed. Thus the monomer susceptibility χ_M is given by $\chi_M = \langle (N_M - \langle N_M \rangle)^2 \rangle / V \neq \chi_{\sigma}$. At the CEP, the divergent behavior of the monomer and baryon number susceptibility will be dominated by the larger of the two exponents, the energy (α) or magnetic exponent (γ). From $\gamma/\alpha > 10$ (Ising, $d = 3$ [78]) we conclude $\chi_{M,L} \sim L^{\gamma/\nu} \tilde{\chi}_M(t \cdot L^{1/\nu})$ which implies that the distribution $P(x_M)$ normalized to unit norm where $x_M = (N_M - \langle N_M \rangle) \cdot L^{-\frac{\gamma/\nu+d}{2}}$ should give the universal scaling function of the Ising magnetization at criticality.

5.3.0.2 Scaling in the vicinity of the TCP

Once we have located prospective CEPs for a range of quark masses, the following picture (Fig.5.9) may arise, in close analogy to the metamagnet of Sect.2.3: The area S_0 in the chiral plane represents the coexistence surface of phases $\langle \bar{\psi}\psi \rangle \geq 0$ for $m_q \rightarrow 0_{\pm}$, i.e. depending of the approach of the chiral limit in infinite volume. At the chiral first order line L_{τ} , the broken phases coexist with the chirally symmetric phase. The line thus represents a three-phase coexistence ending in a *tricritical* point. In the presence of an ordering (i.e. symmetry breaking) field $m_q \geq 0$, the low temperature transitions trace out coexistence surfaces S_{\pm} bounded by the CEPs which form the “wing” lines L_{\pm} of $d = 3$, Ising universality. In the vicinity of the TCP, these lines can be parametrized by $t = T/T_t - 1$ and are given by

$$L_{\pm} : \begin{pmatrix} a\mu(t) \\ am_q(t) \\ t \end{pmatrix} = \begin{pmatrix} b_{\mu}|t|^{\phi} - ct + a\mu_t \\ \pm b_m|t|^{\phi_1} \\ t \end{pmatrix}, \quad (5.23)$$

with the mean-field exponents $\phi_1 = \frac{5}{2}$, $\phi = 2$ [23] and $c = -\left. \frac{\partial \mu(T)}{\partial T} \right|_{T_t}$ is the negative slope of L_{τ} at $T = T_t$.

We should test if our results on the CEPs are consistent with the prediction Eq.(5.23) in which case we can use the above relation to obtain an estimate for $(a\mu_t, aT_t)$.

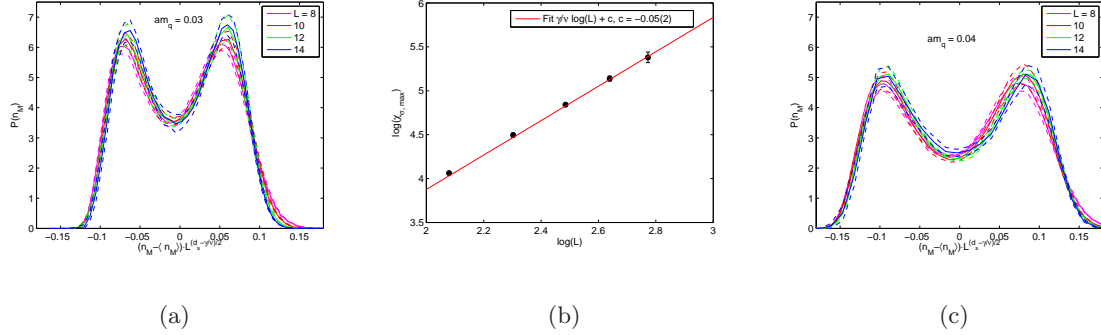


Figure 5.10: (a) Collapse of the distribution $P(x_M)$, $x_M = (N_M - \langle N_M \rangle) \cdot L^{-\frac{\gamma/\nu+d}{2}}$, signaling a CEP in the $d = 3$, Ising universality class for $am_q = 0.03$. (b) Peak of the susceptibility $\chi_{\sigma,L}$ as a function of L for $T = T_E$ and $m_q = 0.03$. The solid line corresponds to a fit of Eq.(5.22), where we fix $\gamma/\nu = 1.237/0.631$ (the $d = 3$, Ising value), showing that this criterion is consistent with the collapse of $P(x_M)$. (c) $P(x_M)$ for $am_q = 0.04$. The thus obtained CEP's are listed in Tab.5.2.

am_q	$a\mu_E$	aT_E
0	$0.64^{+0.02}_{-0.04}$	0.94(7)
0.005	0.69(1)	0.79(1)
0.01	0.70(2)	0.77(3)
0.03	0.74(1)	0.74(1)
0.04	0.76(1)	0.73(1)
0.1	0.86(1)	0.69(1)

Table 5.2: Critical end points located with the help of the collapse of $P(x_M)$ using $d = 3, Z_2$ exponents, with the exception of the (chiral) TCP (first line) where $\chi_{\sigma,L}$ was used. The error for the former was estimated conservatively by varying the reweighting parameters (μ, T) until the universal scaling disappeared visibly.

5.3.1 Results

We first have to establish criticality for a number of quark masses am_q . Due to the sign problem (Sect.5.2.3) we are practically limited to $L^3 \times N_t$ -lattices with $L \leq 16$ and work with $N_t = 4$ throughout this section. Employing as our main criterion the collapse of distributions $P_L(x_M)$, we approached for fixed quark mass $am_q > 0$ in parameter space $(a\mu, aT)$ the prospective CEP for $L = 8, 10, \dots, 16$ following the first order line. We found it natural to reweight the distributions $P_L(x_M)$ to equal peak height (a criterion suitable for a first order transition in the presence of a Z_2 symmetry), where one peak is located in the dilute (monomer rich) phase, the other in the dense (monomer depleted) phase. We then varied the parameters $(a\mu_L, aT_L)$ slightly to optimize the collapse within error bands for various L . The resulting scaling functions are shown in Fig.5.10 for $am_q = 0.03$ (a) and 0.04 (c). The resulting critical

coordinates for several masses are given in Tab.5.2.

To ascertain that this criterion to locate the CEP is consistent with others, also in view of the possible difference in scaling of χ_σ and χ_M for $am_q > 0$, we investigated the scaling of the peak $\chi_{\sigma,L,\max}$ for $am_q = 0.03$ in the vicinity of the parameters $(a\mu_E, aT_E)$ given in Tab.5.2. Reweighting to $T = T_E$, fixed, we determined the maximum of the chiral susceptibility as a function of μ , by standard reweighting techniques. In Fig.5.10(b) we plot $\log \chi_{\sigma,L,\max}$ versus $\log L$ for $L = 8, \dots, 16$ along with a fit using Eq.(5.22), fixing $\gamma/\nu = 1.967$, i.e. Ising critical exponents in $d = 3$ [78]. We obtained $c = -0.04(1)$ with $\chi_{\text{red}}^2 = 1.2$ and the fitting law seems in good agreement with the data; leaving instead γ/ν as a free parameter yields $\gamma/\nu = 1.92(1), c = 0.08(2)$ which however are largely correlated ($cov = 0.97$) and we cannot trust the fit. We thus believe that the values given in Tab.5.2 are acceptable estimates of $(a\mu_E, T_E)(m_q)$, given the small volume with $L \leq 16$ and the coarse resolution with $N_t = 4$.

The more interesting and perhaps more relevant question is about the consistency of these estimates with the mean-field scaling for lines L_\pm in the vicinity of the TCP (see the previous subsection and Sect.2.3).

The system of equations (5.23) suggests to fit $T_E(m_q)$ and to extract an estimator for T_t . In Fig.5.11(a) (upper part) we show aT_E as a function of am_q . As the scaling

$$T(m_q) = T_c - b_m m_q^{2/5} \quad (5.24)$$

is expected to hold in the vicinity of the (chiral) TCP we have checked if a fit is stable under exclusion of points of larger quark mass. Fitting the full set of points, we obtain $aT_t = 0.83(1), b_m = 0.36(5)$ ($\chi_{\text{red}}^2 \approx 1$). Excluding $am_q = 0.1$ gives the estimate $aT_t = 0.85(1), b_m = 0.45(5)$ ($\chi_{\text{red}}^2 \approx 0.5$), which remains stable under further exclusion. In view of the estimate on aT_t , Eq.(5.18), and the already established first order transition for $aT = 0.845(3)$ (see Fig.5.6), we take the fit-estimate $aT_t = 0.85(1)$ as more likely.

Using this estimate we fit (μ_E, T_E) of Tab.5.2 to the relation $\mu(t)$, Eq.(5.23) and obtain

$$b_\mu = 2.9(7), \quad c = 0.37(13), \quad a\mu_t = 0.648(6), \quad (5.25)$$

with an acceptable χ_{red}^2 . The resulting curve is shown in the lower part of Fig.5.11(a). In particular, despite its large fitting error, at least the sign of $c = -\left.\frac{\partial\mu(T)}{\partial T}\right|_{T_t} > 0$ is determined correctly. It should be noted that this sign is opposite compared to that obtained by mean-field calculations, c.f. Fig.5.2. Comparing our estimate on TCP, Eq.(5.18) with those obtained by the fit, $(0.648(6), 0.85(1))$, we see that the results are roughly consistent.⁴ We thus take the scaling of the wing lines L_\pm , Eq.(5.23), as a tenable scenario for our model whose phase diagram, now complemented by the CEPs for $m_q > 0$ (Tab.5.2) and the corresponding fit Eq.(5.23), is given in Fig.5.11(b).

5.4 Summary and Conclusions

Our findings for the phase diagram of strong coupling QCD in and off the chiral limit essentially support mean-field predictions as for the order of the transition along the transition

⁴Which comes only partially as a surprise given that we included the tricritical coordinates Eq.(5.18) in both fits. However, excluding them as well as the point $am_q = 0.1$ yields only fitting results with correlated fitting parameters with little predictive power.

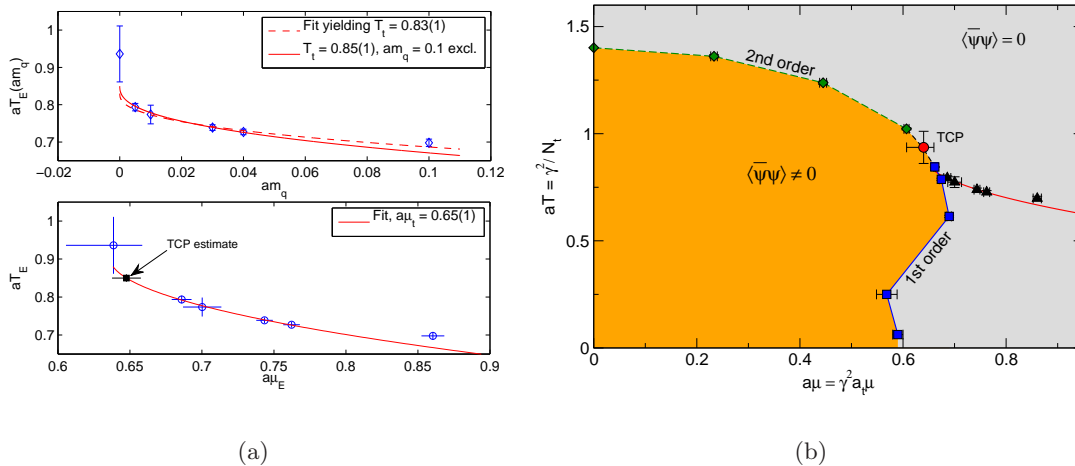


Figure 5.11: (a) Upper part: $T_E(m_q)$ as listed in Tab.5.2. The two lines correspond to fits of Eq.(5.24) with (dashed line) and without (solid) the estimate at $am_q = 0.1$. The fit remained stable under exclusion of further points $am_q < 0.1$. We thus extract $T_t = 0.85(1)$. Lower part: T_E as a function of μ_E . The solid line shows the fit to Eq.(5.23), using the above estimate on T_t , excluding $am_q = 0.1$. We observe consistency and extract $a\mu_t = 0.65(1)$. (b) The full phase diagram with choice $a/a_t = \gamma^2$, now complemented by the CEPs and the corresponding fit as it is visible in the lower part of (a).

line. For $m_q > 0$ the results are consistent with scaling predictions of Landau-Ginzburg theory (see Sect.2.3.1.2). We remark that in our study the geometry of the transition lines, including the location of the tricritical point, depend crucially on the choice of $a/a_t = f(\gamma)$, where the parameter γ allowed us to vary the temperature continuously via $f(\gamma)/N_t = aT$. The choice $f(\gamma) = \gamma^2$ (another suggestion of mean-field theory) for the entire (μ, T) -plane brought our results in qualitative and quantitative (TCP) agreement with mean-field predictions. In particular the slope $\frac{dT}{d\mu}$ is positive on part of the first order line in contrast to expectations in QCD in the chiral limit, Fig.5.1.

The weakness of the sign problem of strong coupling QCD facilitated our study: Both, the Karsch-Mütter resummation (Sect.8.4.1) and the naive sampling of the partition function Eq.(4.12) allow for systems sizes of $16^3 \times 4$. Further, a study of the phase diagram, taking the continuum limit in the $\hat{0}$ -direction ($N_t \rightarrow \infty$), seems feasible and particularly desirable in view of the yet unknown relation $a/a_t = f(\gamma)$.

Remarkably, thanks to the mild sign problem and the simple form of the partition function Eq.(4.12) and its degrees of freedom, Fig.4.1, the study was carried out using table-top computing resources which has to be contrasted with full Lattice QCD where major computing resources are involved. But: The listed advantages and achievements come of course at the high price of being really a crude approximation whose continuum limit cannot be taken.

Are there still open questions for the phase diagram at strong coupling? For zero and intermediate chemical potential it was found for the two-color theory at strong coupling [52] that its (bosonic) baryons form a superfluid whose condensate drops to zero as saturation is reached at high chemical potential. With our present investigation of the phase diagram of our model we have not excluded the possibility that baryons form a fermionic superfluid.

A further unaddressed question consists of the limit of large quark masses in our model which

however cannot be studied with the present algorithm.

6 Strong coupling Lattice QCD with $N_f = 2$ flavors

Can the strong coupling theory be as “easily” studied for a number of staggered quark flavors $N_f > 1$? Taking $N_f = 2$ and gauge group $U(1)$, i.e. QED at strong coupling, in [84] the authors were able to study the physics of pions. In the following we will investigate how this can be generalized to a non-Abelian gauge group.

6.1 Motivation

We now consider the strong coupling partition function $Z(m_u, m_d) = \int \mathcal{D}\chi \mathcal{D}\bar{\chi} \mathcal{D}U e^{S_F}$ with the staggered action

$$S_F = \sum_x \left\{ \sum_{\mu=0,d} \eta_{\hat{\mu}}(x) \left(\bar{\chi}_x^\alpha U_{\hat{\mu}}(x) \chi_{x+\hat{\mu}}^\alpha - \bar{\chi}_{x+\hat{\mu}}^\alpha U_{\hat{\mu}}^\dagger(x) \chi_x^\alpha \right) + 2am_\alpha \bar{\chi}_x^\alpha \chi_x^\alpha \right\}, \quad (6.1)$$

where the summation over the flavor index $\alpha = 1, 2$ ¹ is implicit and $U_{\hat{\mu}} \in U(N)$ or $SU(N)$. We recall that in addition to the $U(1)_V$ symmetry Eq.(4.4), this action has the global symmetry $SU_L(2) \times SU_R(2) \times U_A(1)$ in the chiral limit, $m_q^\alpha = 0$,

$$\begin{aligned} \chi_{x_e}^\alpha &\rightarrow V^{\alpha\beta} e^{i\theta_A} \chi_{x_e}^\beta & \bar{\chi}_{x_e}^\alpha &\rightarrow \bar{\chi}_{x_e}^\beta e^{i\theta_A} W^{\dagger,\beta\alpha} \\ \chi_{x_o}^\alpha &\rightarrow W^{\alpha\beta} e^{-i\theta_A} \chi_{x_o}^\beta & \bar{\chi}_{x_o}^\alpha &\rightarrow \bar{\chi}_{x_o}^\beta e^{-i\theta_A} V^{\dagger,\beta\alpha} \end{aligned} \quad (6.2)$$

with matrices $V, W \in SU(2)$ and an even-odd decomposition of our hypercubic lattice in sites x_e, x_o defined via parity $\epsilon(x_e) = 1, \epsilon(x_o) = -1$ where $\epsilon(x) = (-1)^{\sum_\mu x_\mu}$. For nonzero quark mass $m_u = m_d \neq 0$, this symmetry is reduced to $SU(2)_{L=R} \times U_V(1)$, i.e. taking $W = V$ in Eq.(6.2).

If we consider this model in the context of our earlier study of strong coupling Lattice QCD in Ch.4, it clearly means an improvement as the symmetry Eq.(6.2) is the symmetry of QCD with two massless (light) flavors. We are ultimately interested in extending our study of nuclear physics of strong coupling lattice QCD which will now be the physics of nucleons composed of u and d -quarks — far more realistic than the one-flavor model. Further, tuning the masses m_u, m_d independently, as possible using the algorithms applicable at strong coupling QCD, we naturally expect differences in the phase diagram of the two models. Introduction of a baryon chemical potential, $\mu_B/3 = \mu_u = \mu_d$ will of course lead to a sign problem like in the one-flavor case. If it remains mild — which is not excluded, thanks to the explicit integration of the gauge fields at strong coupling — we can continue our investigation of the phase diagram

¹We take the staggered quark with flavor label $\alpha = 1, 2$ to be “up” (u) and “down” (d) - quark, respectively.

in the extended parameter space $(T, m_u, m_d, \mu_B, \mu_I)$ where $\mu_I = \mu_u - \mu_d$ denotes the isospin chemical potential. Moreover, the crucial ingredient at strong coupling is the map of the partition function with action given in Eq.(6.1) onto the partition function of a dimer model. For the case of $N_f = 2$ it is carried out explicitly in the next section and can be readily generalized to $N_f > 2$, leaving thus the possibility to carry the analogy to QCD even further.

6.2 Partition function for gauge group G and N_f flavors

We recall from Sect.4.1.1 that the link integration factorizes at strong coupling. We can thus write

$$\begin{aligned} Z &= \int \prod_x \left(d\chi_x d\bar{\chi}_x e^{2am_\gamma \bar{\chi}_x^\gamma \chi_x^\gamma} \prod_\mu \left[dU_{\hat{\mu}}(x) e^{\eta_{\hat{\mu}}(x) \left(\bar{\chi}_x^\alpha U_{\hat{\mu}}(x) \chi_{x+\hat{\mu}}^\alpha - \bar{\chi}_{x+\hat{\mu}}^\beta U_{\hat{\mu}}^\dagger(x) \chi_x^\beta \right)} \right] \right) \\ &=: \int \prod_x \left(d\chi_x d\bar{\chi}_x e^{m_\gamma \bar{\chi}_x^\gamma \chi_x^\gamma} \prod_\mu z(x, \mu) \right), \end{aligned} \quad (6.3)$$

where the flavor indices α, β, γ are summed over. The *one-link integral* $z(x, \mu)$ is given again in the general form

$$z(x, \mu) = \int_G dg e^{\text{tr}(gm^\dagger + mg^\dagger)}, \quad (6.4)$$

with $g \in G$ ($G = U(N)$ or $SU(N)$) and matrices

$$(m)_{ij} = \chi_{x,i}^\alpha \bar{\chi}_{y,j}^\alpha \quad \text{and} \quad (m^\dagger)_{kl} = -\chi_{y,k}^\beta \bar{\chi}_{x,l}^\beta, \quad (6.5)$$

where $y = x + \hat{\mu}$ and the indices i, j and k, l are color indices. Note that m and m^\dagger are independent matrices as the fields χ_x and $\bar{\chi}_x$ are independent variables in an Euclidean theory.² In Sect.8.1 we show that $z(x, y)$ can be expanded in group invariants of the gauge group G . In particular one finds

$$\begin{aligned} z(x, y) &= \sum_{k_1, \dots, k_N} \alpha_{k_1 \dots k_N} (\det[mm^\dagger])^{k_1} (\text{tr}[mm^\dagger])^{k_2} \dots (\text{tr}[(mm^\dagger)^{N-1}])^{k_N} \quad (U(N)) \\ z(x, y) &= \sum_{k_1, \dots, k_{N+1}} \alpha_{k_1 \dots k_{N+1}} (\det[m])^{k_1} (\det[m^\dagger])^{k_2} (\text{tr}[mm^\dagger])^{k_3} \dots (\text{tr}[(mm^\dagger)^{N-1}])^{k_{N+1}} \quad (SU(N)). \end{aligned} \quad (6.6)$$

Here “tr” and “det” denotes the trace and determinant in color space as both, m and m^\dagger are matrices in color space. The expansion will terminate at finite order due to the Grassmann nature of $\chi, \bar{\chi}$. We can now write $\text{tr}[mm^\dagger] = \text{Tr}[M_x M_y]$ with

$$(M_z)_{\alpha\beta} = \bar{\chi}^\alpha \chi^\beta(z) \quad (6.7)$$

²Further we have neglected the staggered phases $\eta_{\hat{\mu}}(x)$ in the above definition. For the mesonic theory without isospin chemical potential as it is the case here, this is without importance. In general we can always recover the phases by letting $\bar{\chi}_x^\alpha \rightarrow \eta_{\hat{\mu}}(x) \bar{\chi}_x^\alpha$ and $\chi_x^\alpha \rightarrow \eta_{\hat{\mu}}(x) \chi_x^\alpha$ and counting the number of occurrences of a field χ_x^α or $\bar{\chi}_x^\alpha$ in the strong coupling dof $(M_x)_{\alpha\beta}$, $(B_z)_{\alpha\beta\gamma}$ and $(\bar{B}_z)_{\alpha\beta\gamma}$.

and the trace “Tr” in flavor space. In general it holds that

$$\text{tr}[(mm^\dagger)^i] = (-1)^{i+1} \text{Tr}[(M_x M_y)^i]. \quad (6.8)$$

The matrix elements $(M_z)_{\alpha\beta}$ are the generalization of $M_z = \bar{\chi}_z \chi_z$ encountered in the one-flavor case, see Eq.(4.8). In particular, for $N_f = 1$, $\text{Tr}[(M_x M_y)^i] = (M_x M_y)^i$. Then the expansion Eq.(6.6) simplifies and with the arguments presented in Sect.8.1 we find the by now familiar result

$$z_{N_f=1}(x, y) = \sum_{k=0}^N \frac{(N-k)!}{N!k!} (M_x M_y)^k + \kappa \left((-1)^N \bar{B}_y B_x + \bar{B}_x B_y \right), \quad (6.9)$$

with the fields defined in Eq.(4.8) and $\kappa = 0, 1$ for $G = U(N), SU(N)$, respectively.

For $N_f > 1$ this simplification no longer exists and the coefficients $\alpha_{k_1 \dots k_N}$ and $\alpha_{k_1 \dots k_{N+1}}$ of the expansion Eq.(6.6) have to be obtained differently. For simplicity we consider now the gauge group $G = U(3)$, i.e. a theory without baryons, and restrict the discussion to $N_f = 2$.

6.2.1 $G = U(3)$

6.2.1.1 Link Integration

In [45] the authors obtain the one-link integral $z(x, \mu)$ in closed form for $N \leq 3$ by using an explicit parametrization of the Haar measure dg appearing in Eq.(6.4). In particular for $G = U(3)$, defining the invariants

$$X = \text{tr}[mm^\dagger], \quad (6.10)$$

$$Y = \frac{1}{2} \left\{ (\text{tr}[mm^\dagger])^2 - \text{tr}[(mm^\dagger)^2] \right\}, \quad (6.11)$$

$$\tilde{Z} = \det(mm^\dagger), \quad (6.12)$$

they find

$$z(x, \mu) = 2 \sum_{j,k,l=0}^{\infty} \frac{(j+2k+4l+2)!}{[(j+2k+3l+2)!]^2} \frac{X^j Y^k \tilde{Z}^l}{(k+2l+1)! j! k! (l!)^2}. \quad (6.13)$$

The quantities X, Y, \tilde{Z} defined above are the only independent variables for $G = U(3)$. Due to the Cayley-Hamilton theorem, Eq.(8.3), all other non-trivial invariants, i.e. $\text{tr}[(mm^\dagger)^i], i > 2$, can be expressed in terms of X, Y, \tilde{Z} .

If we follow the same steps as for the one-flavor model, then we should express the invariants X, Y, \tilde{Z} in terms of traces of flavor matrices M_x, M_y , whose elements $(M_z)_{\alpha\beta}$ are (see Eq.(6.7))

- a) gauge invariant, contrary to the elements $(mm^\dagger)_{ij}$ of the expansion above.
- b) local, where we recall that m_{ij}, m_{ij}^\dagger each involved staggered fields at both, x and y , where $y = x + \hat{\mu}$, see Eq.(6.5).

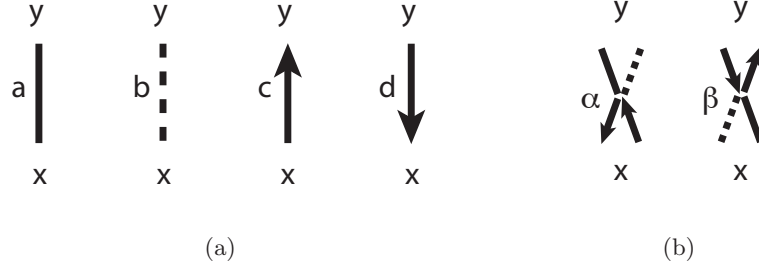


Figure 6.1: (a) Graphical definition for the four states in Eq.(6.18). (b) The link states α and β .

Doing so we obtain by using the definitions Eq.(6.10) - (6.12), the relation Eq.(6.8) and the Cayley-Hamilton-theorem Eq.(8.3)

$$X = \text{Tr}[M_x M_y], \quad (6.14)$$

$$Y = \frac{1}{2} (X^2 + \text{Tr}[(M_x M_y)^2]), \quad (6.15)$$

$$\tilde{Z} = XY + \frac{1}{3} (\text{Tr}[(M_x M_y)^3] - X^3). \quad (6.16)$$

Once $z(x, y)$ is expanded in $(M_x)_{\alpha\beta}$, $(M_y)_{\alpha\beta}$ via Eq.(6.13), we can deduce the highest non-vanishing power in the expansion. For convenience, we choose the convention $\chi^1(x) = u(x)$, $\bar{\chi}^1(x) = \bar{u}(x)$, $\chi^2(x) = d(x)$, $\bar{\chi}^2(x) = \bar{d}(x)$. Then, for gauge group $U(3)$ this will be a term $(\bar{u}u)^3(x)(\bar{d}d)^3(x)$ (and respectively for y) due to the Grassmann property of the variables u, \bar{u}, d and \bar{d} .

In fact we can simply carry out the expansion Eq.(6.13) order by order in the variables $(M_z)_{\alpha\beta} \in \{\bar{u}u_z, \bar{d}d_z, \bar{u}d_z, \bar{d}u_z\}$, $z = x, y$ by noting that

- X contributes to order $\mathcal{O}(\bar{\chi}^\alpha \chi_x^\beta \bar{\chi}^\gamma \chi_y^\delta)$
- Y contributes to order $\mathcal{O}((\bar{\chi}^\alpha \chi_x^\beta \bar{\chi}^\gamma \chi_y^\delta)^2)$
- \tilde{Z} contributes to order $\mathcal{O}((\bar{\chi}^\alpha \chi_x^\beta \bar{\chi}^\gamma \chi_y^\delta)^3)$

as can be seen from Eqs.(6.14)-(6.16). For example to first non-trivial order we obtain from Eq.(6.13)

$$z(x, y) = 1 + \frac{1}{3}X + \dots \quad (6.17)$$

where

$$X = \text{Tr}[M_x M_y] = \bar{u}u(x)u(y) + \bar{d}d(x)d(y) + \bar{u}d(x)\bar{d}u(y) + \bar{d}u(x)\bar{u}d(y) \quad (6.18)$$

$$=: a + b + c + d. \quad (6.19)$$

In analogy to the one-flavor case we can define a graphical notation. Labeling the four *link states* of Eq.(6.18) by $a - d$ as indicated in Eq.(6.19), the notation is given in Fig.6.1(a). The factor $\frac{1}{3}$ appearing Eq.(6.17) is the link *weight*. Contrary to the one-flavor model where a closed expression for the link weights could be given in terms of the occupation number of a

dimer link $k_{\hat{\mu}}$ (the factor $\frac{(N-k)!}{N!k!}$ appearing in Eq.(6.9)), for $N_f = 2$ we will obtain the numerical coefficients appearing at every order. In practice, the coefficients can be easily tabulated. It is instructive to look at terms of $O(X^2)$ in the expansion of $z(x, y)$. We see from Eq.(6.13) and the above remarks that the contributing terms will be $\sim X^2$ and $\sim Y$. To order $\mathcal{O}(X^2)$

$$z(x, y) = 1 + \frac{1}{3}X + \frac{1}{24}(X^2 + Y) + \mathcal{O}(X^3). \quad (6.20)$$

Using Eqs.(6.14) and (6.15) we obtain

$$\frac{1}{24}(X^2 + Y) = \frac{a^2}{12} + \frac{ab}{8} + \frac{b^2}{12} + \frac{ac}{6} + \frac{bc}{6} + \frac{c^2}{12} + \frac{ad}{6} + \frac{bd}{6} + \frac{cd}{8} + \frac{d^2}{12} + \frac{\alpha}{24} + \frac{\beta}{24}, \quad (6.21)$$

where we defined the additional link states

$$\alpha := \sum_{i,j,k,l=1}^3 \bar{u}_{i,x} d_{i,x} \bar{d}_{j,x} u_{j,x} \bar{u}_{k,y} u_{k,y} \bar{d}_{l,y} d_{l,y} = \bar{u} d_x \bar{d} u_x \bar{u} u_y \bar{d} d_y \quad \text{and} \quad \beta := \bar{u} u_x \bar{d} d_x \bar{u} d_y \bar{d} u_y, \quad (6.22)$$

giving a graphical shorthand in Fig.6.1(b). From Eq.(6.21) it follows for example that a link doubly occupied by a has weight $\frac{1}{12}$ while a link in state ab contributes $\frac{1}{8}$. The link states α and β will be of interest when we come to the final form of the partition function Z , after taking the remain Grassmann integral Eq.(6.3).

All other link states, i.e. those of higher power in the fields $\bar{u} u_z, \bar{d} d_z, \bar{d} u_z, \bar{u} d_z$ for $z = x, y$, will turn out to be products of powers of a, b, c, d, α and β . The remaining work is therefore to give the complete expansion of $z(x, y)$ in terms of these variables. Due to the Grassmann nature of the variables u, \bar{u}, d and \bar{d} , for higher power in X, Y, \tilde{Z} an increased number of terms vanishes. As we had found above, the highest non-vanishing term contributing to $z(x, y)$ is of order $\mathcal{O}(X^6)$. We defer the corresponding derivation to the Appendix (Sect.(8.2.1)) and now turn to the remaining Grassmann integration of Eq.(6.3).

6.2.1.2 Grassmann integration and minus sign

The (final) Grassmann integration in Eq.(6.3) is done per site x and will create constraints analogous to the constraint given in Eq.(4.11) for the theory at $N_f = 1$. For every site x the integral will be of the form

$$I = \int \prod_a [d u_a d \bar{u}_a d d_a d \bar{d}_a] e^{2am_u \bar{u} u} e^{2am_d \bar{d} d} (\bar{u} u)^{k_u} (\bar{d} d)^{k_d} (\bar{u} d)^{k_{\pi^-}} (\bar{d} u)^{k_{\pi^+}}, \quad (6.23)$$

where the index $a = 1, \dots, N$ denotes color ($N = 3$) and $k_u, k_d, k_{\pi^+}, k_{\pi^-} = 0, \dots, N$ are the link occupation numbers of the 2-flavor theory.

To evaluate I let us take $k_{\pi^+} = k_{\pi^-} = 0$ and the chiral limit $m_u = m_d = 0$ for the moment. I then has only non-vanishing contribution for $k_u = k_d = N$ due to the rules of Grassmann integration defined in Eq.(2.30). In this case $I = (N!)^2$ as $(\bar{u} u)^N = N! \prod_a \bar{u}_a u_a$ (respectively for $(\bar{d} d)^N$). Taking $m_u > 0, m_d > 0$ we see that if k_u or $k_d < N$ terms from the expansion of the exponential $e^{2m_u \bar{u} u}$ or $e^{2m_d \bar{d} d}$ to order $N - k_u, N - k_d$, respectively, are needed to have a non-vanishing contribution. Letting k_{π^+} or $k_{\pi^-} > 0$, we see that $k_{\pi^+} = k_{\pi^-}$ is needed to have non-vanishing contribution as the terms $\bar{u} u$ and $\bar{d} d$ appearing in front involve only powers in color and anti-color of one flavor each. We can therefore replace $k_{\pi^-} = k_{\pi^+}$ by $k_{\pi^\pm}/2$. Carrying

out the explicit computation we find for $N = 2, 3$ (i.e. gauge group $U(2)$ and $U(3)$)

$$I = (-1)^{k_{\pi^\pm}} p(k_{\pi^\pm}) \frac{N!}{n_u!} \frac{N!}{n_d!} (2m_u)^{n_u} (2m_d)^{n_d}, \quad (6.24)$$

$$p(k_{\pi^\pm}) = \begin{cases} 1, & k_{\pi^\pm} = 0 \text{ or } k_{\pi^\pm} = N \\ \frac{1}{N}, & \text{otherwise} \end{cases},$$

where $n_u = N - k_u - k_{\pi^\pm}$, $n_d = N - k_d - k_{\pi^\pm}$ will represent the number of u and d monomers at site x . The combinatorial factor $p(k_{\pi^\pm})$ has its origin in the number of possibilities to pair $1, \dots, N-1$ \bar{u}_a and d_a quarks (and vice versa) with each other rather than with a (anti-)color of the same flavor.

The factor $(-1)^{k_{\pi^\pm}}$ comes from the number of permutations done to get the integrand into the form $\sim \int \prod_a [du_a d\bar{u}_a dd_a d\bar{d}_a] (\bar{u}u)^N (\bar{d}d)^N = (N!)^2$. For most of the configurations that does not have to worry us: As $k_{\pi^-} = k_{\pi^+}$ we have current conservation at each site. Practically it means that the links with link states involving c, d (see Eq.(6.19)), will be members of closed loops: Each term $(\bar{u}d_x \bar{d}u_x)$ will be matched by the same contribution at neighboring sites as a loop involves an even number of sites. We call these loops *charged pion loops*, in analogy with the $U(1)$ -study [84]. The weight of such loops is positive. In Fig.(6.2(a)) we show a typical configuration exhibiting pairs of negative weights at sites x_1, \dots, x_4 .

However, besides the link states c and d , we had encountered α -links (and β -links), defined in Eq.(6.22) with shorthand shown in Fig.6.1(b). These link states will contribute minus signs in I as the term $(\bar{u}d_x \bar{d}u_x)$ (and $(\bar{u}d_y \bar{d}u_y)$), which is present for a site x (y) touched by a link with a state involving odd powers of α , comes unmatched by an equivalent pair at the neighboring site y (and v.v. x). In Fig.(6.2(b)) we show a configuration with negative weight. This configuration has been obtained by replacing the charged pion loop traversing x_2 and x_3 (actually a double link cd) in Fig.(6.2(a)) by a link with state β . It follows that our 2-flavor model has a *minus-sign* problem for $N > 1$.³

We summarize the constraints imposed by the Grassmann integral Eq.(6.24) at the site x

$$k_{\pi^-} = k_{\pi^+} = k_{\pi^\pm}/2, \quad (6.25)$$

$$n_u + k_u + k_{\pi^\pm} = N, \quad (6.26)$$

$$n_d + k_d + k_{\pi^\pm} = N, \quad (6.27)$$

where n_u and n_d represent the number of u -monomers and d -monomers at site x , in analogy with the one-flavor case.

Let us now consider a link $l = (x, \mu)$. Associated with each link l is a weight $w_l(s(l))$ which we define (in words) as the factor in the expansion of $z(l)$ occurring in front of the term corresponding to the link state $s(l)$. For example $w_l(s(l) = \text{"b"}) = 1/3$ or $w_l(s(l) = \text{"a}^3\text{")} = 1/36$ which we read off Eqs.(8.23) and (8.27), respectively. Further, a site x carries weight $w_s(x) = I(x)$, where $I(x)$ is the value of the corresponding Grassmann integral I at x . We

³For $N = 1$ we note that the link states α and β , Eq.(6.22), can be trivially rewritten as a state ab or cd with negative weight. The total link weight of the states ab and cd , as taken from the $U(1)$ equivalent of Eq.(6.21) turns out to be positive. In fact, for the non-Abelian groups we try a similar strategy by adding link weights, see below.

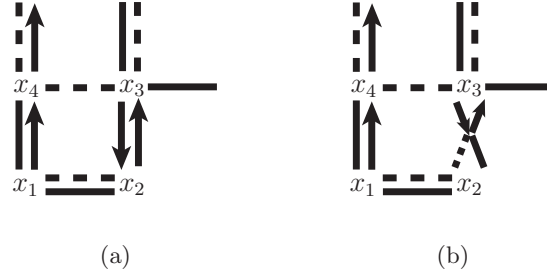


Figure 6.2: (a) A configuration involving sites x_1 - x_4 with periodic bc (upwards and to the right). The charged pion loop traversing x_1 and x_4 creates negative weights at these sites (see Eq.(6.24)), whose signs cancel each other. The same holds for the loop traversing x_2, x_3 (in this case a double link cd). (b) The double link (charged pion loop) connecting x_2 and x_3 has been replaced by a β -link. Now the site x_2 has a positive weight, while all other sites have negative weights.

now give the partition function Z in closed form:

$$Z = \prod_{\{s(l), n_u, n_d\}} \prod_{l=(x, \mu)} w_l(s(l)) \prod_x w_s(x). \quad (6.28)$$

6.2.2 Taming the sign problem

Before we try to address the sign problem, let us simplify the discussion by considering the gauge group $U(2)$ instead of $U(3)$. With the help of [45] we can carry out the link integration in a completely analogous way to Sect.6.2.1.1. We therefore defer this discussion to the Appendix (Sect.(8.2.2)) where we also define the corresponding link weights $w_l(s(l))$. In particular, we find states α, β , defined as in Eq.(6.22) with implicit sum over colors $a = 1, 2$. The partition function Z is then formally given by Eq.(6.28), with site weights $w_s(x) = I(x)$ (Eq.(6.24) with $N = 2$). In particular it has the same sign problem as demonstrated by the configurations displayed in Fig.6.3.

We start by considering the link states contributing to order $\mathcal{O}(X^2)$ (see Sect.8.2.2). There we have

$$\frac{1}{12}X^2 + \frac{1}{6}Y = \frac{a^2}{4} + \frac{ab}{3} + \frac{b^2}{4} + \frac{ac}{2} + \frac{bc}{2} + \frac{c^2}{4} + \frac{ad}{2} + \frac{bd}{2} + \frac{cd}{3} + \frac{d^2}{4} + \frac{\alpha}{6} + \frac{\beta}{6}, \quad (6.29)$$

where X and Y are $U(2)$ -invariants defined below Eq.(8.31). We can now take the link states ab, cd, α, β and show

$$\begin{aligned} \frac{1}{6}(ab + cd + \alpha + \beta) &= \frac{1}{6}(\bar{u}_{x,1}\bar{d}_{x,2} - \bar{u}_{x,2}\bar{d}_{x,1})(u_{x,1}d_{x,2} - u_{x,2}d_{x,1}) \cdot \\ &\quad \cdot (\bar{u}_{y,1}\bar{d}_{y,2} - \bar{u}_{y,2}\bar{d}_{y,1})(u_{y,1}d_{y,2} - u_{y,2}d_{y,1}) \\ &=: \frac{1}{6}\bar{D}D_x\bar{D}D_y, \end{aligned} \quad (6.30)$$

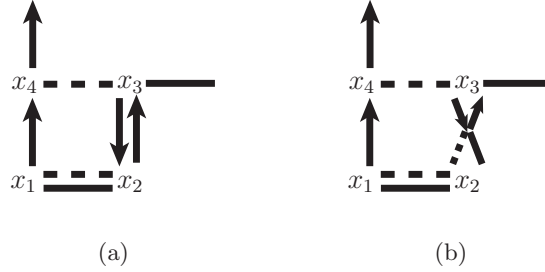


Figure 6.3: The same configurations as displayed in Fig.6.2 now adapted to $G = U(2)$. In particular we again obtain a positive weight for the configuration shown in (a), while the configuration (b) still carries a minus sign.

where we may think of $\bar{D}D_z$ as an antiquark-diquark-pair at z which can exist even in $U(2)$. We note that in this way link states containing α or β are completely removed.

Taking the Grassmann integral $I(z)$ in Eq.(6.24) and the definition of $\bar{D}D_z$ we can show that the weight $w_s(z)$ of a site z containing a $\bar{u}u_z\bar{d}d_z\bar{D}D_z$ is $w_s(z) = (N!)^2/2 = 2$ ($N = 2$). As it turns out, the weight of a site containing $\bar{u}d_z\bar{d}u_z\bar{D}D_z$ or $\bar{D}D_z\bar{D}D_z$ is also positive. Nevertheless, we still have a sign problem: Taking for example the configuration Fig.(6.4(a)) which has a positive weight, we replace the double link ab connecting x_2 and x_3 by a pair $\bar{D}D_{x_2}\bar{D}D_{x_3}$. Doing so, the sign of the weight $w_s(x_2)$ is changed and the resulting configuration has negative weight.

The solution is now to combine the link states ab and cd with $\bar{D}D$. Starting again from Eq.(6.29) which now reads (omitting its l.h.s.)

$$\frac{a^2}{4} + \frac{ab}{6} + \frac{b^2}{4} + \frac{ac}{2} + \frac{bc}{2} + \frac{c^2}{4} + \frac{ad}{2} + \frac{bd}{2} + \frac{cd}{6} + \frac{d^2}{4} + \frac{\bar{D}D_x\bar{D}D_y}{6}, \quad (6.31)$$

we write $ab = \lambda ab + (1 - \lambda)ab$ and define

$$\frac{1}{12}AB := \frac{1}{12}(2\lambda ab + \bar{D}D_x\bar{D}D_y), \quad \frac{1}{12}CD := \frac{1}{12}(2\lambda cd + \bar{D}D_x\bar{D}D_y) \quad (6.32)$$

with $0 < \lambda < 1$ some positive number to be chosen s.t. the sign is absent/minimal. The new link states AB , CD are symbolically defined in Fig.6.4(c). The link states ab , cd still exist, now with weight $\frac{1-\lambda}{6}$. Clearly, such a replacement is non-local as it will affect the site weights of x, y touched by AB (CD), this will complicate the update which is a practical question. Since it is non-local the proof of absence of the sign-problem is difficult. Setting for example $\lambda = 1/2$, on a 2×2 lattice it is essentially only the configuration displayed on the left of Fig.6.5 which has negative weight (and of course configurations obtained by rotating, reflecting this configuration, given some axis). In the figure we have also given the corresponding sum of configurations which is implied by the configuration on the left due to the definition of the link states AB and CD (Eq.(6.32)). Practically, choosing $\lambda > 0.7$ we found the sign problem to be absent.⁴

⁴Actually one can show that the configuration displayed in Fig.6.5 has positive weight for $\lambda > \frac{1}{4}(1 + \sqrt{3}) = 0.683\dots$

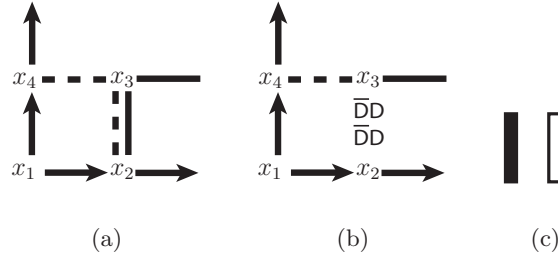


Figure 6.4: (a) A configuration with positive weight. (b) Replacing the double link ab connecting x_2 and x_3 by a pair $\bar{D}D_{x_2}\bar{D}D_{x_3}$ changes the sign at x_2 . (c) Graphical representation of the link state AB (left) and CD (right), defined in Eq.(6.32).

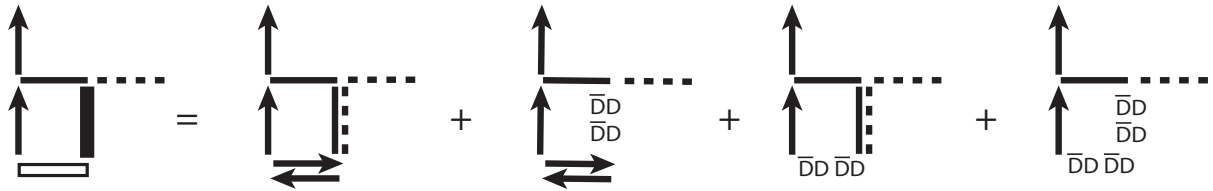


Figure 6.5: The configuration on the left is given as the sum of configurations on the right by using the definition of the link states AB and CD , defined in Eq.(6.32). Note that in this graphical sum we have omitted the site labels x_1, \dots, x_4 as well as factors involving λ .

6.3 Conclusions

In this chapter we have rewritten the partition function of Lattice QCD at strong coupling with $N_f = 2$ flavors of staggered quarks to obtain the partition function of a dimer model amenable to the worm algorithm. Using the expansion of the one-link integral in terms of group invariants [45], we found that even a mesonic theory (obtained by taking the gauge group $U(N)$) exhibits a sign problem in this formulation. Although we showed ways to tame the sign problem by practical methods for the simple case of $U(2)$, one may ask if it is not completely removed from the formulation by a change of basis. Choosing for example the “physical” variables $\sigma = \frac{1}{\sqrt{2}}(\bar{u}u + \bar{d}d)$, $\pi^0 = \frac{1}{\sqrt{2}}(\bar{u}u - \bar{d}d)$, $\pi^+ = \bar{d}u$ and $\pi^- = \bar{u}d$ this does not seem to be the case.

In the above discussion we have completely ignored the fermionic content of the original theory ($G = SU(3)$). Including baryons into the formulation will lead to another, physical sign problem at finite quark chemical potential which even persists at $\mu = 0$ where it is only solved by an explicit resummation of configurations as in the one-flavor case [9].

7 Outlook

Like in any study, there remain questions and extensions unaddressed in this thesis. They can be grouped into the more “fundamental” changes to the original theory with $N_f = 1$ flavor and questions that represent a perhaps natural continuation or deepening of the work done so far. In the following we list these points worth pursuing by starting with the latter:

- The perhaps simplest extension of our study of the phase diagram for $N_f = 1$ consists of the obvious possibility to take the continuum limit in the $\hat{0}$ -direction: The limit $\gamma \rightarrow \infty$, $N_t \rightarrow \infty$, keeping $aT = f(\gamma)/N_t$ fixed, not only means a gain in accuracy in terms of $1/N_t$ corrections to the phase diagram but in this particular limit taking $f(\gamma) = \gamma^2$ becomes a good approximation according to mean-field theory for $a\mu \geq 0$. The sign problem as quantified by the average sign, $\langle \text{sign} \rangle = c \exp(-\Delta f(T) V_s N_t / \gamma^2)$, depends only on the physical volume and will thus remain mild, making a perhaps more elaborate study of the tricritical point in the chiral limit or the critical endpoint for nonzero quark mass possible. We also note that in this limit $a_t = a/\gamma^2 = 0$ and continuous time Monte-Carlo algorithms as presented in [85] are applicable.
- In the context of the phase diagram we have not studied the behavior of gluonic observables such as the Polyakov loop P , $P(\vec{x}) = \text{Tr} \prod_t (U_{\hat{0}}(\vec{x}, t))$. In the present formulation expectation values of observables depending on the gauge links $U_{\hat{\mu}}(x)$ involve the explicit solution of the group integrals and the reformulation of the observable in terms of link variables $k_{\hat{\mu}}, b_{\hat{\mu}}$. We point to [86] for the calculation of $\langle P \rangle$ in the case of gauge group $SU(2)$.
- Another path to pursue is the introduction of an imaginary chemical potential $\mu = \pm i|\mu|$. As can be seen most clearly in the original formulation of Karsch & Mütter [9], see Sect.8.4.1, the weight $w(\ell)$ of a baryonic loop ℓ then becomes

$$w(\ell) = 1 + \sigma(\ell) \cos(\pm 3|\mu|/T) \geq 0$$

with $\sigma(\ell) = \pm 1$ and the sign problem is absent. For full Lattice QCD, i.e. at nonzero $\beta = 6/g^2$, this approach has given valuable insight e.g. in the phase diagram by analytic continuation to real μ . In the context of strong coupling QCD analytic continuation can be tested against our real- μ results thanks to the mild sign problem.

We now turn to the more fundamental changes to the model studied in the larger part of this thesis. The first important point left unfinished is the extension to $N_f > 1$ staggered quark flavors. In Ch.6 we have given the framework to map the strong coupling QCD partition function for $N_f = 2$ onto that of a dimer model which in turn is amenable to algorithmic approaches s.a. the worm algorithm. The following subjects are here of interest:

- Already in the presence of only $N_f = 2$ flavors, the nuclear physics will be the physics of four different baryons (termed Δ^{++} , p , n and Δ^-) and their respective antiparticles.



Figure 7.1: $\mathcal{O}(\beta)$ corrections: The term $M_x M_{x+\hat{j}} M_{x+\hat{k}} M_{x+\hat{j}+\hat{k}}$ in the middle, drawn in the conventional notation on the right as two single dimers between sites $x, x+\hat{j}$ and sites $x+\hat{k}, x+\hat{j}+\hat{k}$, respectively, represents a *plaquette* term (left) with weight $w \sim 1/g^2$ when $\mathcal{O}(\beta)$ corrections are included in the action. In the drawing on the left quarks and antiquarks are drawn as solid and empty circles, respectively. There are of course other, mesonic and baryonic, contributions to $\mathcal{O}(1/g^2)$ in the action. Part of the figure was taken from [87].

Clearly, the nucleon-nucleon potential, V_{NN} , will have interesting characteristics. While it is clear that for example V_{pn}, V_{pp}, V_{nn} will all exhibit a hard core, one easily sees that $V_{\Delta^{++}\Delta^-}(R=0)$ remains finite just by considering the degrees of freedom involved per site ($\Delta^{++} = u_1 u_2 u_3, \Delta^- = d_1 d_2 d_3$).

- In view of the phase diagram of the one-flavor theory, we will have a much richer phase structure in the extended parameter space $(T, m_u, m_d, \mu_u, \mu_d)$ where the quark masses $m_u \neq m_d$ can be chosen independently. If the sign problem remains mild for $\mu_B > 0$ we can explore the dense phase and study the condensation of pions for $\mu_I > m_\pi$ at finite baryon density and perhaps kaon condensation when a third quark flavor is included.

A further direction not all followed in this thesis is the inclusion of $\mathcal{O}(\beta)$ -corrections to the strong coupling action,

$$Z = \int \mathcal{D}\chi \mathcal{D}\bar{\chi} \int \mathcal{D}U e^{S_F} \left(1 - \beta \sum_{x, \mu < \nu} 1 - \frac{1}{2N} \text{tr} \left[P_{\mu\nu}(x) + P_{\mu\nu}^\dagger(x) \right] \right).$$

It is clear that formulating the theory with the $\mathcal{O}(\beta)$ term present will not only involve the link variable $k_{\hat{\mu}}, b_{\hat{\mu}}$ as degree of freedom in the resulting model but also the plaquette: Taking for example the mesonic sector to leading order in $1/d$, then a configuration drawn in Fig.7.1 will be of order $1/g^2$, as the staggered quark and antiquark can now be thought of moving independently as schematically expressed by the arrows. There are of course other, mesonic and baryonic, terms contributing with $1/g^2$ in the action. The resulting theory will have a sign problem for finite chemical potential. However, since gauge fields are integrated out exactly as in the $g = \infty$ case we expect this approach to be fruitful. In any case this theory has only been studied in a mean-field approximation [54, 87] - of course in a $1/d$ expansion and inclusion of this $\mathcal{O}(\beta)$ term offers the possibility of taking a first step towards the continuum limit, $a \rightarrow 0$. It thus certainly is a natural next step in our study.

Finally, an interesting question is: how general are the properties of our model? It is for example quite plausible that a large class of systems of hard spheres — probably the simplest model with the steric effect — shows a Yukawa-like potential and a transition to a crystalline phase. On the other hand, the phenomenological central potential between two nucleons also exhibits a hard core repulsion and has Yukawa-shape at long distance. It is therefore not excluded that nuclear matter belongs to this class of systems.

8 Appendix

8.1 One-link integral, $N_f = 1$

This section gives a derivation of the one-link integral

$$z(x, y) = \int_G dg e^{\text{tr}(gm^\dagger + mg^\dagger)}, \quad (8.1)$$

where G denotes the gauge group ($U(N)$ or $SU(N)$) with elements g . Comparing the one-link integral occurring in the staggered partition function Eq.(4.5) with N_f staggered flavors, we see that it is of the form given in Eq.(8.1) with matrices $(m)_{ij} = \chi_{x,i}^\alpha \bar{\chi}_{y,j}^\alpha$, $(m^\dagger)_{kl} = -\chi_{y,k}^\beta \bar{\chi}_{x,l}^\beta$ in color space where $i, j = 1, \dots, N$, $\alpha, \beta = 1, \dots, N_f$ and $x = y + \hat{\mu}$. It is instructive to first consider the case of arbitrary $N_f \geq 1$ and then specify to the case $N_f = 1$.

From the invariance of $z(x, y)$ under gauge transformations

$$\chi_x \rightarrow W \chi_x, \bar{\chi}_x \rightarrow \bar{\chi}_x W^\dagger, \quad \chi_y \rightarrow V \chi_y, \bar{\chi}_y \rightarrow \bar{\chi}_y V^\dagger \quad V, W \in U(N) \text{ or } SU(N) \quad (8.2)$$

we see that it is not a function of $2 \cdot 2 \cdot N_c \cdot N_f$ Grassmann variables but of the gauge invariant expressions in Tab.8.1. For any invertible $N \times N$ matrix A , $\text{tr}[A^k]$ for $k \geq N$ can be expressed

$U(N)$	$SU(N)$
$\text{tr}[mm^\dagger]$	$\text{tr}[mm^\dagger]$
\vdots	\vdots
$\text{tr}[(mm^\dagger)^k]$	$\text{tr}[(mm^\dagger)^k]$
$\det[mm^\dagger]$	$\det[m], \det[m^\dagger]$

Table 8.1: Expressions in m, m^\dagger that are invariant under the transformation given in (Eq.8.2)

by combinations of $\text{tr}[A^i]$, $i < N$ and $\det[A]$ due to the Cayley-Hamilton theorem: Given the characteristic polynomial of A , $p_c(\lambda) = \det[A - \lambda I]$, it states that $p_c(A) = 0$, i.e. A satisfies its own secular equation. The coefficients of p_c can be given in closed form. For the important case of $N = 3$, it is given by

$$p_c(A) = -A^3 + \text{tr}[A]A^2 - \frac{1}{2}((\text{tr}[A])^2 - \text{tr}[A^2])A + \det[A] = 0, \quad (8.3)$$

from which $\text{tr}[A^k]$, $k \geq 3$ can be obtained. For general N , this leaves N and $N + 1$ independent expressions for $U(N)$ and $SU(N)$, respectively, in which we can expand $z(x, y)$ to obtain

$$z(x, y) = \sum_{k_1, \dots, k_N} \alpha_{k_1 \dots k_N} (\det[mm^\dagger])^{k_1} (\text{tr}[mm^\dagger])^{k_2} \dots (\text{tr}[(mm^\dagger)^{N-1}])^{k_N} \quad (U(N)) \quad (8.4)$$

$$z(x, y) = \sum_{k_1, \dots, k_{N+1}} \alpha_{k_1 \dots k_{N+1}} (\det[m])^{k_1} (\det[m^\dagger])^{k_2} (\text{tr}[mm^\dagger])^{k_3} \dots (\text{tr}[(mm^\dagger)^{N-1}])^{k_{N+1}} \quad (SU(N)). \quad (8.5)$$

In the following we use $\text{tr}[mm^\dagger] = \text{Tr}[M_x M_y]$, defining $(M_z)_{\alpha\beta} = \bar{\chi}^\alpha \chi^\beta(z)$ where ‘‘Tr’’ denotes the trace over flavors and the summation of colors has been suppressed. Further one can show that

$$\text{tr}[(mm^\dagger)^i] = (-1)^{i+1} \text{Tr}[(M_x M_y)^i]. \quad (8.6)$$

For the present case of $N_f = 1$ we trivially have $\text{Tr}[(M_x M_y)^i] = (M_x M_y)^i$. Using this and the relation Eq.(8.6), the expressions given in Eq.(8.5) simplify to

$$\begin{aligned} z_{N_f=1}(x, y) &= \sum_{k=0}^{\infty} \alpha_k (M_x M_y)^k \quad (U(N)), \\ z_{N_f=1}(x, y) &= \sum_{i, j, k=0}^{\infty} \alpha_{ijk} (\det[m])^i (\det[m^\dagger])^j (M_x M_y)^k \quad (SU(N)), \end{aligned} \quad (8.7)$$

where $\det mm^\dagger$ appearing in the $U(N)$ relation has been expressed in color traces using the Cayley-Hamilton theorem given in Eq.(8.3) for $N = 3$. The summations appearing in Eqs.(8.7) will terminate at a finite power due to the Grassmann nature of $\bar{\chi}, \chi$ but, before, we note that

$$\begin{aligned} \det[m] &= \epsilon_{i_1 \dots i_N} m_{1i_1} \dots m_{Ni_N} = \frac{1}{N!} \epsilon_{i_1 \dots i_N} \epsilon_{j_1 \dots j_N} m_{j_1 i_1} \dots m_{j_N i_N} \\ &=: (-1)^N N! \bar{B}_y B_x \\ \det[m^\dagger] &= N! \bar{B}_x B_y \end{aligned} \quad (8.8)$$

where $B_z = \frac{1}{N!} \epsilon_{i_1 \dots i_N} \chi_{i_1} \dots \chi_{i_N}(z)$ and $\bar{B}_z = \frac{1}{N!} \epsilon_{i_1 \dots i_N} \bar{\chi}_{i_1} \dots \bar{\chi}_{i_N}(z)$. From this we see that the terms $\det[m]$, $\det[m^\dagger]$ appearing in the $SU(N)$ case can only occur as single terms to power one and as a product $\det[m] \det[m^\dagger]$ (which again is equivalent to a trace), i.e.

$$z_{N_f=1}(x, y) = \sum_{k=0}^N \alpha_k (M_x M_y)^k + \kappa \left(\tilde{\alpha} (-1)^N N! \bar{B}_y B_x + \tilde{\beta} N! \bar{B}_x B_y \right), \quad (8.9)$$

with $\kappa = 0, 1$ for $U(N)$ and $SU(N)$, respectively. To determine $\tilde{\alpha}, \tilde{\beta}$ we compare Eq.(8.9) to Eq.(8.1) in expanded form,

$$z(x, y) = \sum_{k, l} \frac{1}{k! l!} \int_{SU(N)} dU (\bar{\chi}_x U \chi_y)^k (-\bar{\chi}_y U^\dagger \chi_x)^l. \quad (8.10)$$

Because of the Grassmann property the term $\sim \bar{B}_x B_y$ can only be generated by the term $\frac{1}{N!} \int_{SU(N)} dU (\bar{\chi}_x U \chi_y)^N$ hence we can equate

$$\begin{aligned}
\tilde{\beta} \bar{B}_x B_y N! &= \frac{1}{N!} \int_{SU(N)} dU (\bar{\chi}_x U \chi_y)^N \\
&= \frac{1}{N!} \sum_{i_1 \dots i_N} \sum_{j_1 \dots j_N} \bar{\chi}_{x, i_1} \chi_{y, j_1} \dots \bar{\chi}_{x, i_N} \chi_{y, j_N} \int_{SU(N)} dU U_{i_1 j_1} \dots U_{i_N j_N} \\
&\stackrel{[88]}{=} \frac{1}{N! N!} \sum_{i_1 \dots i_N} \sum_{j_1 \dots j_N} \epsilon_{i_1 \dots i_N} \epsilon_{j_1 \dots j_N} \bar{\chi}_{x, i_1} \chi_{y, j_1} \dots \bar{\chi}_{x, i_N} \chi_{y, j_N} \\
&= \bar{B}_x B_y,
\end{aligned}$$

from which we conclude $\tilde{\beta} = \tilde{\alpha} = 1/N!$. Note that in the third line we have explicitly used the $SU(N)$ integration formulae given in [88]. The α_k occurring in Eq.(8.9) can be obtained by noting the identity

$$\int d\chi_x d\bar{\chi}_x \int dU e^{\bar{\chi} \chi_x + \bar{\chi}_x U \chi_y - \bar{\chi}_y U^\dagger \chi_x} = e^{\bar{\chi} \chi_y}.$$

Plugging in the one-link integral expression of Eq.(8.9) yields

$$\int d\chi_x d\bar{\chi}_x e^{\bar{\chi} \chi_x} \sum_{k=0}^N \alpha_k (\bar{\chi} \chi_x \bar{\chi} \chi_y)^k = \sum_{l=0}^N \alpha_l \frac{N!}{(N-l)!} (\bar{\chi} \chi_y)^l, \quad (8.11)$$

from which follows $\alpha_k = \frac{(N-k)!}{N!k!}$ by inspection. Thus, for $N_f = 1$ we are given the closed expression for the one-link integral

$$z_{N_f=1}(x, y) = \sum_{k=0}^N \frac{(N-k)!}{N!k!} (M_x M_y)^k + \kappa ((-1)^N \bar{B}_y B_x + \bar{B}_x B_y), \quad (8.12)$$

for gauge group $U(N)$ ($\kappa = 0$) and $SU(N)$ ($\kappa = 1$).

8.2 One-link integral, $N_f = 2$

8.2.1 $G = U(3)$

In [45] the authors obtain the one-link integral $z(x, \mu)$ in closed form for $N \leq 3$ by using an explicit parametrization of the Haar measure dg appearing in Eq.(6.4). For $G = U(3)$ we have the following invariants:

$$X = \text{tr}[mm^\dagger], \quad (8.13)$$

$$Y = \frac{1}{2} \left\{ (\text{tr}[mm^\dagger])^2 - \text{tr}[(mm^\dagger)^2] \right\}, \quad (8.14)$$

$$\tilde{Z} = \det(mm^\dagger). \quad (8.15)$$

The expansion Eq.(8.4) then becomes [45]

$$z(x, \mu) = 2 \sum_{j,k,l=0}^{\infty} \frac{(j+2k+4l+2)!}{[(j+2k+3l+2)!]^2} \frac{X^j Y^k \tilde{Z}^l}{(k+2l+1)! j! k! (l!)^2}. \quad (8.16)$$

We now express X, Y, \tilde{Z} in terms of M_x, M_y by using the trace property Eq.(8.6) and the Cayley-Hamilton theorem Eq.(8.3)

$$X = \text{Tr}[M_x M_y] \quad (8.17)$$

$$Y = \frac{1}{2} (X^2 + \text{Tr}[(M_x M_y)^2]) \quad (8.18)$$

$$\tilde{Z} = XY + \frac{1}{3} (\text{Tr}[(M_x M_y)^3] - X^3). \quad (8.19)$$

We can now expand $z(x, y)$ order by order in $(M_z)_{\alpha\beta}$, $z = x, y$ by noting that

- X contributes to order $\mathcal{O}(\bar{\chi}^\alpha \chi_x^\beta \bar{\chi}^\gamma \chi_y^\delta)$,
- Y contributes to order $\mathcal{O}((\bar{\chi}^\alpha \chi_x^\beta \bar{\chi}^\gamma \chi_y^\delta)^2)$,
- \tilde{Z} contributes to order $\mathcal{O}((\bar{\chi}^\alpha \chi_x^\beta \bar{\chi}^\gamma \chi_y^\delta)^3)$.

To power X^0 we trivially have

$$z(x, \mu) = 1 + \dots \quad (8.20)$$

– $\mathcal{O}(\mathbf{X})$: Here we obtain

$$z(x, \mu) = 1 + \frac{1}{3} X + \mathcal{O}(X^2). \quad (8.21)$$

From Eq.(8.17) it follows that

$$X = \text{Tr}(M_x M_y) = \bar{u}u(x)u(y) + \bar{d}d(x)\bar{d}d(y) + \bar{u}d(x)\bar{d}u(y) + \bar{d}u(x)\bar{u}d(y). \quad (8.22)$$

Again the notation of up (u) and down (d) quarks was used for $\alpha = 1, 2$, respectively.

We are done to order X . Let us denote the four terms in Eq.(8.22) by a, b, c, d , in this order. The entire $\mathcal{O}(X)$ term in the expression for $z(x, \mu)$ then simply reads

$$\frac{1}{3} X = \frac{1}{3} (a + b + c + d). \quad (8.23)$$

Just like the original work of [9] one should also introduce some graphical notation, in the order $\mathcal{O}(X)$ case this is given in Fig.8.1(a).

– $\mathcal{O}(\mathbf{X}^2)$: Here, one has two terms contributing to this order to $z(x, y)$, X^2 and Y . The X^2 being just the product of the link states of Fig.8.1(a), we immediately turn to $Y = \frac{1}{2} \{X^2 + \text{Tr}[M_x M_y M_x M_y]\}$. It is the second term that creates something new. We introduce the new notation $\alpha := \bar{u}d_x \bar{d}u_x \bar{u}u_y \bar{d}d_y$ and $\beta := \bar{u}u_x \bar{d}d_x \bar{u}d_y \bar{d}u_y$ and its graphical representation

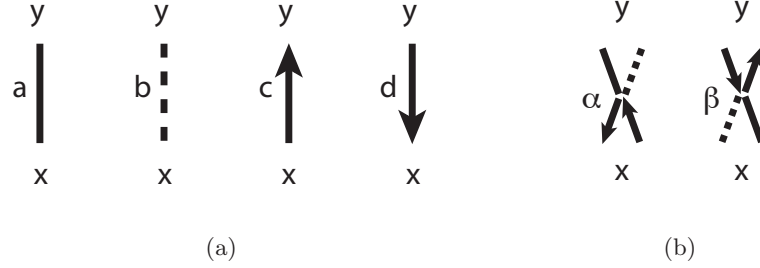


Figure 8.1: (a) Graphical definition for the four states in Eq.(8.22). (b) The link-states α and β .

in Fig.8.1(b). The complete expression to $\mathcal{O}(X^2)$ including the pre-factor then reads

$$\frac{1}{24}(X^2 + Y) = \frac{a^2}{12} + \frac{ab}{8} + \frac{b^2}{12} + \frac{ac}{6} + \frac{bc}{6} + \frac{c^2}{12} + \frac{ad}{6} + \frac{bd}{6} + \frac{cd}{8} + \frac{d^2}{12} + \frac{\alpha}{24} + \frac{\beta}{24}. \quad (8.24)$$

– $\mathcal{O}(\mathbf{X}^3)$: The contributing terms are X^3, XY, \tilde{Z} . X and Y are known from the previous powers. Using Eq.(8.19) the expression for \tilde{Z} then reads

$$\tilde{Z} = (a + b + c + d)(a^2 + b^2 + c^2 + d^2 + 2a(c + d) + 2b(c + d) + 2\alpha + 2\beta) \quad (8.25)$$

$$= X(Y - ab - cd + \alpha + \beta). \quad (8.26)$$

The total contribution to $z(x, y)$ at $\mathcal{O}(X^3)$ now sums up to

$$\begin{aligned} \frac{1}{60}\left(\frac{1}{6}X^3 + \frac{1}{2}XY + Z\right) &= \frac{a^3}{36} + \frac{a^2b}{24} + \frac{ab^2}{24} + \frac{b^3}{36} + \frac{a^2c}{12} + \frac{abc}{8} + \frac{b^2c}{12} + \frac{ac^2}{12} + \frac{bc^2}{12} \\ &+ \frac{c^3}{36} + \frac{a^2d}{12} + \frac{abd}{8} + \frac{b^2d}{12} + \frac{acd}{8} + \frac{bcd}{8} + \frac{c^2d}{24} + \frac{ad^2}{12} + \frac{bd^2}{12} \\ &+ \frac{cd^2}{24} + \frac{d^3}{36} + \frac{a\alpha}{24} + \frac{b\alpha}{24} + \frac{c\alpha}{24} + \frac{d\alpha}{24} + \frac{a\beta}{24} + \frac{b\beta}{24} + \frac{c\beta}{24} + \frac{d\beta}{24} \end{aligned} \quad (8.27)$$

which we leave in this uncanceled form to immediately read off the link weight corresponding to some link state. Having obtained the explicit expression for X, Y, \tilde{Z} , we continue by partitioning the remaining powers $\mathcal{O}(X^4)$ - $\mathcal{O}(X^6)$.

– $\mathcal{O}(\mathbf{X}^4)$: We proceed as announced

$$\begin{aligned} \frac{1}{8640}X^4 + \frac{1}{1440}X^2Y + \frac{1}{4320}Y^2 + \frac{7}{2160}XZ &= \frac{a^3b}{108} + \frac{ab^3}{108} + \frac{c^3d}{108} + \frac{cd^3}{108} + \frac{a^2bc}{24} + \frac{a^2bd}{24} + \frac{ab^2c}{24} \\ &+ \frac{ab^2d}{24} + \frac{a^2b^2}{128} + \frac{c^2d^2}{128} - \frac{\alpha^2}{384} - \frac{\beta^2}{384}. \end{aligned} \quad (8.28)$$

Here repeated use has been made of the Grassmann properties (a few terms vanish, many are equivalent). As an example, take the equivalence $a^3b = 9a^2cd$, this relation and others have been used to simplify the expression on the *l.h.s.* of the above equation resulting in the final expression Eq.(8.28). Correspondingly, in the final set of link states to occupation number 4

the state a^2cd does not occur any more. This could possibly lead to ergodicity problems for an update algorithm. Therefore, we symmetrize the final expression Eq.(8.28) between seemingly important link states and their equivalent partners, ending up with

$$\begin{aligned} \frac{1}{8640}X^4 + \frac{1}{1440}X^2Y + \frac{1}{4320}Y^2 + \frac{7}{2160}XZ &= \frac{a^3b}{216} + \frac{ab^3}{216} + \frac{c^3d}{216} + \frac{cd^3}{216} + \frac{a^2cd}{24} + \frac{b^2cd}{24} + \frac{c^2ab}{24} \\ &+ \frac{d^2ab}{24} + \frac{a^2bc}{48} + \frac{ac^2d}{48} + \frac{a^2bd}{48} + \frac{acd^2}{48} + \frac{ab^2c}{48} \\ &+ \frac{bc^2d}{48} + \frac{ab^2d}{48} + \frac{bcd^2}{48} + \frac{a^2b^2}{128} + \frac{c^2d^2}{128} - \frac{\alpha^2}{384} - \frac{\beta^2}{384}. \end{aligned}$$

– $\mathcal{O}(\mathbf{X}^5)$: Nothing special happens to this order, so we proceed as before and just state the final expression

$$\begin{aligned} \frac{1}{302400}X^5 + \frac{1}{30240}X^3Y + \frac{1}{30240}XY^2 + \frac{1}{3780}X^2Z + \frac{1}{7560}YZ &= \frac{a^3b^2 + 9a^2bcd + 9ac^2d^2}{1296} \\ + \frac{a^2b^3 + 9ab^2cd + 9bc^2d^2}{1296} + \frac{9a^2b^2c + 9abc^2d + c^3d^2}{1296} + \frac{9a^2b^2d + 9abcd^2 + c^2d^3}{1296}. \end{aligned} \quad (8.29)$$

– $\mathcal{O}(\mathbf{X}^6)$: The pre-factors in Eq.(6.13) are lengthy fractions which we denote by $d_{j,k,l}$ and the last nonzero contribution to $z(x, y)$ then becomes

$$\begin{aligned} d_{6,0,0}X^6 + d_{4,1,0}X^4Y + d_{2,2,0}X^2Y^2 + d_{3,0,1}X^3Z + d_{1,1,1}XYZ + d_{0,3,0}Y^3 + d_{0,0,2}Z^2 &= \\ \frac{a^3b^3 + 9a^2b^2cd + 9abc^2d^2 + c^3d^3}{5184}. \end{aligned} \quad (8.30)$$

8.2.2 $G = U(2)$

For $G = U(2)$ the integral $z(x, y)$ reads [45]

$$z(x, \mu) = \sum_{i,j=0}^{\infty} \frac{X^i Y^j}{(i+2j+1)!i!(j!)^2}, \quad (8.31)$$

where $X := \text{tr}(mm^\dagger)$ and $Y = \det(mm^\dagger)$. Following the same steps as for $U(3)$ we can determine $z(x, \mu)$ order by order.

– $\mathcal{O}(\mathbf{X})$: Only the term $\sim X$ contributes, hence

$$\frac{1}{2}X = \frac{1}{2}(a + b + c + d). \quad (8.32)$$

– $\mathcal{O}(\mathbf{X}^2)$: The term $\sim Y$, with $Y = \det(mm^\dagger)$ can be treated as for $U(3)$. Note that, since mm^\dagger is a 2×2 -matrix, we use $\det(mm^\dagger) = \frac{1}{2}((\text{tr}[mm^\dagger])^2 - \text{tr}[(mm^\dagger)^2])$ (a result of Cayley-Hamilton). Further we had already from $U(3)$ (and the same holds here), $\text{tr}[mm^\dagger] = \text{Tr}[M_x M_y]$

and $\text{tr}[(mm^\dagger)^2] = -\text{Tr}[(M_x M_y)^2]$, one writes therefore

$$\det(mm^\dagger) = \frac{1}{2} \left((\text{tr}[mm^\dagger])^2 - \text{tr}[(mm^\dagger)^2] \right) = \frac{1}{2} \left((\text{Tr}[M_x M_y])^2 + \text{Tr}[(M_x M_y)^2] \right) \quad (8.33)$$

$$= (\text{Tr}[M_x M_y])^2 - \det(M_x M_y) \quad (8.34)$$

$$= X^2 - ab - cd + \alpha + \beta. \quad (8.35)$$

In Eqs.(8.33) and (8.34) the Cayley-Hamilton theorem has been applied.

Computing then $\frac{1}{12}X^2 + \frac{1}{6}Y$ yields,

$$\frac{1}{12}X^2 + \frac{1}{6}Y = \frac{a^2}{4} + \frac{ab}{3} + \frac{b^2}{4} + \frac{ac}{2} + \frac{bc}{2} + \frac{c^2}{4} + \frac{ad}{2} + \frac{bd}{2} + \frac{cd}{3} + \frac{d^2}{4} + \frac{\alpha}{6} + \frac{\beta}{6}. \quad (8.36)$$

– $\mathcal{O}(\mathbf{X}^3)$: To this and the next order we will have again cancellations and equivalent pairs. We therefore symmetrize between equivalent link states and sum the contributions $\sim X^3 \sim XY$ to find

$$\frac{1}{144}X^3 + \frac{1}{24}XY = \frac{a^2b}{16} + \frac{acd}{4} + \frac{ab^2}{16} + \frac{bcd}{4} + \frac{c^2d}{16} + \frac{abc}{4} + \frac{cd^2}{16} + \frac{abd}{4}. \quad (8.37)$$

– $\mathcal{O}(\mathbf{X}^4)$: The terms that contribute are $\sim X^4, \sim X^2Y$ and $\sim Y^2$. We find

$$\frac{1}{2880}X^4 + \frac{1}{240}XY + \frac{1}{480}Y^2 = \frac{a^2b^2}{48} + \frac{1}{12}abcd + \frac{c^2d^2}{48}. \quad (8.38)$$

8.3 A useful relation

8.3.1 Relating the decay mass M and the continuum pole mass m

We take as an example the free boson propagator $G(x)_{\text{lat}}$ on an infinite hypercubic lattice in $d = 4$. The “decay” mass M is extracted from the exponential decay of $C(t) = \sum_{\vec{x}} G(x)_{\text{lat}}$ in t , $C(t) \sim \exp(-Mt)$. Using the propagator in momentum space $G(p)_{\text{lat}} = 1/(4 \sum_{\mu} \sin^2(ap_{\mu}/2) + a^2m^2)$, we can relate the masses m and M :

$$C(t) = \int_{-\pi/a}^{\pi/a} \frac{adp_0}{2\pi} \frac{e^{ip_0 t}}{4 \sin^2(ap_0/2) + a^2m^2} \stackrel{w=e^{ip_0 a}}{=} \oint \frac{dw}{2\pi i} \frac{w^{t/a}}{(2 + a^2m^2)w - w^2 - 1} \quad (8.39)$$

where the integrand has poles at $w_{1/2} = A \pm \sqrt{A^2 - 1}$, $A = \frac{2+a^2m^2}{2}$. As $A \geq 1$ only w_2 contributes through its residue to the integral over the circle around the origin in counterclockwise sense,

$$C(t) = 2\pi i \lim_{w \rightarrow w_2} (w - w_2) \frac{i}{2\pi} \frac{w^{t/a}}{(w - w_1)(w - w_2)} = \frac{(A - \sqrt{A^2 - 1})^{t/a}}{2\sqrt{A^2 - 1}}. \quad (8.40)$$

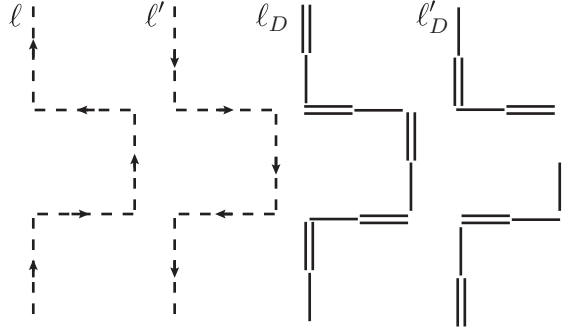


Figure 8.2: Four loops of the same geometry — the baryonic and antibaryonic loops ℓ , ℓ' (carrying positive weight) and the dimer loops ℓ_D , ℓ'_D of unit weight, Eq.(8.44).

If we define $\cosh(aM) = A = \frac{2+a^2m^2}{2}$, we obtain $C(t) = \frac{e^{-Mt}}{2\sinh(aM)}$. The decay mass M and the continuum pole mass m are hence related via

$$aM = \operatorname{acosh}\left(1 + \frac{a^2m^2}{2}\right), \quad (8.41)$$

and become equal in the limit $a \rightarrow 0$.

8.4 Algorithmic details

8.4.1 Resummation in the MDP-algorithm

For simplicity we use an isotropic lattice ($\gamma = 1$) and recall that in the partition function Z ,

$$Z = \sum_{\{k,n,\ell\}} \prod_{b=(x,\hat{\mu})} \frac{(3-k_b)!}{3!k_b!} \prod_x \frac{3!}{n_x!} (2am_q)^{n_x} \prod_{\ell} w(\ell), \quad (8.42)$$

a baryon loop ℓ contributes with weight $w(\ell)$,

$$w(\ell) = \frac{1}{\prod_{x \in \ell} 3!} \sigma(\ell) \exp(3N_t r_\ell a \mu), \quad \sigma(\ell) = (-1)^{r_\ell + N_-(\ell) + 1} \prod_{b=(x,\hat{\mu}) \in \ell} \eta_{\hat{\mu}}(x) \quad (8.43)$$

with the number of links on ℓ in negative direction, $N_-(\ell)$, and its winding number in $\pm\hat{0}$ -direction, r_ℓ . In particular, due to the geometry dependent sign $\sigma(\ell)$, even for zero chemical potential the model has a sign problem. However, by a simple trick it can be solved for $\mu = 0$ and weakened for $\mu > 0$ [9]: In Fig.8.2 we display next to a baryonic (ℓ) and antibaryonic loop (ℓ'), two dimer loops (ℓ_D, ℓ'_D) of the same shape consisting of a sequence of single and double dimers. The latter two loops have unit weight, since

$$w(\ell_D) = \prod_{b \in \ell_D} \frac{(N - k_b)!}{N!k_b!} \prod_{x \in \ell_D} N! = 1. \quad (8.44)$$

Writing formally $Z = \sum_C = w(C)$, we can now add to the configurational weight $w(C)$ of a configuration C containing a dimer loop, say the loop ℓ_D , one-half of the weight of two configurations C', C'' which are identical to C but contain the baryon loop ℓ, ℓ' respectively, instead of ℓ_D ,

$$\begin{aligned} w(C) + \frac{1}{2}(w(C') + w(C'')) &= (2am_q)^{N_M} \prod_{b \notin \ell_D} \frac{(N - k_b)!}{N!k_b!} \prod_{x \notin \ell_D} N! \\ &\cdot \left(\prod_{b \in \ell_D} \frac{(N - k_b)!}{N!k_b!} \prod_{x \in \ell_D} N! + \frac{1}{2} \prod_{x \in \ell} N! \cdot w(\ell) + \frac{1}{2} \prod_{x \in \ell'} N! \cdot w(\ell') \right) \\ &= (2am_q)^{N_M} \prod_b \frac{(N - k_b)!}{N!k_b!} \prod_x N! \left(\underbrace{1 + \sigma(\ell) \cosh(3r_\ell \mu/T)}_{w(\ell_P)} \right). \end{aligned}$$

We proceed the same way for configurations containing the loop ℓ'_D , adding now the remaining weight $\frac{1}{2}(w(C') + w(C''))$ of the configurations C' and C'' . As a configurational weight $w(C)$ factorizes into contributions from each link, site and baryonic or antibaryonic loop, this procedure holds for any number of dimer and baryon loops per configuration. We have thus eliminated the purely baryonic and antibaryonic loops from our set of degrees of freedom and defined a new (polymer) loop type ℓ_P with weight $w(\ell_P)$, thus obtaining a monomer-dimer-polymer (MDP) system. As in particular $w(\ell_P) = 1 + \sigma(\ell) \cosh(3r_\ell \mu/T) \geq 0$ for $\mu = 0$ (ℓ stands here for a baryonic or antibaryonic loop of the same shape), the sign problem is resolved here. For $\mu > 0$ we can compare the average sign obtained from simulations using the conventional formulation Eq.(8.42) and those of MDP-simulations. We point to Sect.5.8 for details.

8.4.2 Proving detailed balance for the mesonic worm

We recall that we could write the partition function Eq.(4.12) as a product of weights of active and passive sites,

$$Z = \sum_{\{n, k, b\}} \prod_{x_a} W_a(x_a) \prod_{x_p} W_p(x_p) \sigma(\{n, k, b\}), \quad (8.45)$$

where

$$W_a(x) = \prod_{\hat{\nu}=\pm\hat{0}, \dots, \pm\hat{d}} \left(\frac{(N - k_{\hat{\nu}})!}{N!k_{\hat{\nu}}!} \exp(3b_{\hat{\nu}}(\delta_{\hat{\nu}, \hat{0}} + \delta_{\hat{\nu}, -\hat{0}})a_t \mu) \right) \frac{N!}{n_x!} (2ma)^{n_x} \quad (8.46)$$

$$W_p(x) = \prod_{\hat{\nu}=\pm\hat{0}} \left(\gamma^{2k_{\hat{\nu}}+3|b_{\hat{\nu}}|} \right) \frac{N!}{n_x!} (2ma)^{n_x}. \quad (8.47)$$

with dimer link occupation number $k_{\hat{\nu}} = 0, \dots, 3$, baryonic link variables $b_{\hat{\nu}} = \pm 1, 0$ and monomer number $n_x = 0, \dots, N$.

8.4.2.1 Passive site update

For simplicity we start the proof with the update step 2 of the mesonic worm defined in Sect.4.1.2.3 and show that it fulfills detailed balance,

$$W(C)P(C'|C) = W(C')P(C|C'), \quad (8.48)$$

where $W(C) = \prod_{x_a} W_a(x_a) \prod_{x_p} W_p(x_p)$ is the configurational weight and $P(C'|C)$ the transition probability from worm configuration C to C' . Let y be a passive site, and the incoming direction be $\hat{\mu}$. We choose an outgoing direction $\hat{\rho}$ with probability $P_{\hat{\mu}\hat{\rho}}$, which according to Eq.(8.48) has to satisfy

$$\prod_{\hat{\kappa}} (\gamma^2)^{(\delta_{\hat{0},\hat{\kappa}} + \delta_{\hat{0},\hat{\kappa}})k_{\hat{\kappa}}} P_{\hat{\mu}\hat{\rho}} = \prod_{\hat{\lambda}} (\gamma^2)^{(\delta_{\hat{0},\hat{\lambda}} + \delta_{\hat{0},\hat{\lambda}})k'_{\hat{\lambda}}} P_{\hat{\rho}\hat{\mu}}. \quad (8.49)$$

Here $P_{\hat{\rho}\hat{\mu}}$ is the probability of the reverse step. During a passive update the incoming link occupation number is decreased, $k_{\hat{\mu}} \rightarrow k_{\hat{\mu}} - 1$, whereas for the outgoing direction we set $k_{\hat{\rho}} \rightarrow k_{\hat{\rho}} + 1$. In addition to Eq.(8.49), $P_{\hat{\mu}\hat{\rho}}$ has to satisfy

$$\sum_{\hat{\nu}} P_{\hat{\mu}\hat{\nu}} = 1, \quad (8.50)$$

where the sum $\sum_{\hat{\nu}}$ extends over all directions $\hat{\nu}$, for which $y + \hat{\nu}$ is a dimer site (not baryonic). The choice

$$P_{\hat{\mu}\hat{\nu}} = \frac{W_{\hat{\mu}\hat{\nu}}}{W_D^{\hat{\mu}}(y)}, \quad W_D^{\hat{\mu}}(y) = \sum_{\hat{\kappa}} W_{\hat{\mu}\hat{\kappa}} \quad (8.51)$$

with $W_{\hat{i}\pm\hat{0}} = \gamma^2 = W_{\pm\hat{0}\pm\hat{0}}$, $W_{\pm\hat{0}\hat{i}} = 1 = W_{\hat{i}\hat{j}}$ ($\hat{i}, \hat{j} = \pm 1, \dots, \pm d$) and $W_{\hat{\mu}\hat{\nu}} = 0$ for a baryonic neighboring site $y + \hat{\nu}$ fulfills detailed-balance, Eq.(8.49), and corresponds to a heatbath probability. In particular $W_D^{\hat{\mu}}(y)$ does not depend on the incoming direction, $W_D^{\hat{\mu}}(y) = W_D(y)$.

8.4.2.2 Active site update

The update of an active site allows for the exclusion of backtracking as we will see below. Let $\hat{\nu}$ and $\hat{\sigma}$ be the incoming and outgoing direction, respectively, on the active site x . An active update increases the occupation number of the incoming link $k_{\hat{\nu}} \rightarrow k_{\hat{\nu}} + 1$ while decreasing it on the outgoing link $k_{\hat{\sigma}} \rightarrow k_{\hat{\sigma}} - 1$. If we denote by $P_{\hat{\nu}\hat{\sigma}}$ the probability to choose this step (and $P_{\hat{\sigma}\hat{\nu}}$ the probability of the reverse step), then with Eq.(8.48) and the weight defined in Eq.(8.46) we must require

$$P_{\hat{\nu}\hat{\sigma}} = P_{\hat{\sigma}\hat{\nu}} \frac{(N - k_{\hat{\sigma}} + 1)k_{\hat{\sigma}}}{(N - k_{\hat{\nu}})(k_{\hat{\nu}} + 1)}. \quad (8.52)$$

Taking

$$P_{\hat{\nu}\hat{\sigma}} = \frac{k_{\hat{\sigma}}}{N - k_{\hat{\nu}}} \quad (8.53)$$

we see that Eq.(8.52) is satisfied which the corresponding choice of $P_{\hat{\sigma}\hat{\nu}} = \frac{k_{\hat{\nu}}+1}{N-k_{\hat{\sigma}}+1}$. Additionally we have to fulfill

$$\sum_{\hat{\sigma}} P_{\hat{\nu}\hat{\sigma}} + P_{\hat{\nu}x} = 1, \quad (8.54)$$

where $P_{\hat{\nu}x}$ is the probability to leave the lattice at site x by erasing a monomer. Choosing

$$P_{\hat{\nu}x} = \frac{n_x}{N - k_{\hat{\nu}}}, \quad (8.55)$$

we see from the constraint in Eq.(8.54) that this excludes backtracking: The incoming direction $\hat{\nu}$ and the outgoing direction $\hat{\sigma}$ have to be distinct, $\hat{\nu} \neq \hat{\sigma}$.

We now turn to the start of a mesonic worm update at an randomly chosen active site z . Let $P_{z\hat{\lambda}}$ be the probability to create a monomer at z (by letting $n_z \rightarrow n_z + 1$) and to decrease the link occupation number $k_{\hat{\lambda}}$ by one, $k_{\hat{\lambda}} \rightarrow k_{\hat{\lambda}} - 1$. If we denote by $P_{\hat{\lambda}z}$ the probability of the reverse step (i.e. the analog of $P_{\hat{\nu}x}$, defined in Eq.(8.55)), then we have

$$P_{z\hat{\lambda}} = P_{\hat{\lambda}z} \frac{(N - k_{\hat{\lambda}} + 1)k_{\hat{\lambda}}}{n_x + 1} \frac{1}{(2am_q)V_D}. \quad (8.56)$$

The mass factor $1/(2am_q)$ arises due to the definition of the active site weight in Eq.(8.46). We explicitly write the factor $1/V_D$ which arises as the site z has been chosen randomly from the set of all dimer sites of total number V_D . $P_{z\hat{\lambda}}$ has to satisfy the constraint $\sum_{\hat{\lambda}} P_{z\hat{\lambda}} + P_{zz} = 1$, where P_{zz} is the probability to leave the site z unchanged and the sum extends over all directions $\hat{\lambda}$ with $k_{\hat{\lambda}} > 0$. By setting

$$P_{z\hat{\lambda}} = \frac{k_{\hat{\lambda}}}{N} \text{ and } P_{zz} = \frac{n_z}{N}, \quad (8.57)$$

we see that the constraint is fulfilled. Recalling however that we had chosen $P_{\lambda z} = \frac{n_z+1}{N-k_{\hat{\lambda}}+1}$ in Eq.(8.55), now with $x = z$, $n_x = n_z + 1$ and $k_{\hat{\nu}} = k_{\hat{\lambda}} + 1$, we see that a factor $1/(NV_D 2am_q)$ remains uncanceled in the detailed balance equation (8.56). It is important to note that this factor arises for both, the beginning and the end, of the update s.t. the *sequence* of (active and passive) worm updates which transform a closed path configuration C into a closed path configuration C' indeed satisfies detailed balance (Eq.(8.48)). To see this take for example a closed path configuration C . Let the sequence of worm updates be a sequence of say 5 consecutive updates around a plaquette (the smallest nontrivial loop), leading to a closed path configuration C' . The product $W(C)P(C'|C)$ can then be written as

$$W(C)P(C'|C) = W(C) \prod_{i=0,4} P(C^{i+1}|C^i), \quad (8.58)$$

with the definition $C^0 = C, C^5 = C'$. If we take the first step to start from the closed path configuration C^0 and create a monomer at some site z , chosen uniformly from all dimer sites, to obtain the worm configuration C^1 we have by definition $W(C^0)P(C^1|C^0) = W(C^1)P(C^0|C^1) \frac{1}{V_D 2am_q N}$ due to the choice $P_{z\hat{\lambda}}$ in Eq.(8.57). The following sequence of active and passive updates fulfills detailed balance at each step, $W(C^i)P(C^{i+1}|C^i) = W(C^{i+1})P(C^i|C^{i+1})$

until the configuration C^4 is reached, we then have from Eq.(8.58)

$$\begin{aligned} W(C)P(C'|C) &= P(C^0|C^1)P(C^1|C^2)P(C^2|C^3)P(C^3|C^4)W(C^4)P(C^5|C^4)\frac{1}{V_D N 2am_q} \\ &= P(C^0|C^1)P(C^1|C^2)P(C^2|C^3)P(C^3|C^4)W(C^5)P(C^4|C^5) \\ &= W(C')P(C|C'), \end{aligned}$$

where we used $W(C^5)P(C^4|C^5) = W(C^4)P(C^5|C^4)\frac{1}{V_D N 2am_q}$ (the worm closes again) to go from the first to the second line. But the l.h.s. of the first line and r.h.s. of the last line imply detailed balance, Eq.(8.48).

All of the defined update probabilities (Eqs.(8.51), (8.53), (8.55) and (8.57)) are independent of the quark mass. The algorithm is in particular applicable in the chiral limit.

8.4.3 Mesonic worm estimators

8.4.3.1 The chiral condensate $\langle \bar{\psi}\psi \rangle$

We start the derivation by noting that the chiral condensate $\langle \bar{\psi}\psi \rangle = \frac{1}{2am_q} \langle N_M \rangle$ (with the total number of monomers N_M) can be written in the following form (defining $\hat{m} = 2am_q$ for convenience)

$$\langle \bar{\psi}\psi \rangle = \frac{1}{V} \frac{\partial}{\partial \hat{m}} \log Z = \frac{1}{V} \sum_x \langle \bar{\chi}\chi_x \rangle, \quad (8.59)$$

with

$$\langle \bar{\chi}\chi_x \rangle = \frac{1}{Z} \sum_{\{k', n', b'\}_x} \sigma(\{n', k', b'\}_x) W(\{n', k', b'\}_x) \hat{m}^n. \quad (8.60)$$

Here $\{k', n', b'\}_x$ denotes a configuration that fulfills the closed path constraint for every site z , except at x where $n_x + \sum_{\hat{\mu}} k_{\hat{\mu}} = N - 1$. $W(\{n', k', b'\}_x)$ is defined as the product over active and passive site weights, defined in Eq.(8.46) and (8.47), respectively, up to the mass-dependent weight \hat{m}^n which we have taken out explicitly.

The configuration $\{k, n, b\}_x$ is reached during a mesonic worm update at a passive site x . On the active starting site of the worm a monomer is placed to satisfy the constraint Eq.(4.11). Continuing the worm update until the path closes, say at active site y (which is not necessarily the starting site for $\hat{m} > 0$) by erasing at a monomer at y , we denote the path of the worm by α_{xy} and its probability by $P(\{n', k', b'\}_x, \alpha_{xy})$. The reverse path α_{xy}^{-1} (probability $P(\{n, k, b\}, \alpha_{xy}^{-1})$) starts from a closed path configuration $\{n, k, b\}$ by placing a monomer at y and continues the worm update until the passive site x is reached. The balance equation now reads

$$\sigma(\{n', k', b'\}_x) W(\{n', k', b'\}_x) \hat{m}^n P(\{n', k', b'\}_x, \alpha_{xy}) = \sigma(\{n, k, b\}) \frac{V_D \hat{m} N}{W_D(x)} W(\{n, k, b\}) \hat{m}^n P(\{n, k, b\}, \alpha_{xy}^{-1}). \quad (8.61)$$

The factor $V_D \hat{m} N$ already occurred in Sect.8.56 and has now to be explicitly taken into account. On the l.h.s. one additional monomer at site y is present (now including the weight \hat{m}), therefore

we need to include this factor on the right. Further, on the right, the site y was chosen with probability $1/V_D$. An additional factor $1/N$ is due to the choice Eq.(8.57) in the initial step of the worm. The factor $1/W_D(x)$ (defined in Eq.(8.51)) occurs on the r.h.s. as a passive update step at x is carried out on the path α_{xy} and therefore included in $P(\{n', k', b'\}_x, \alpha_{xy})$. This step does not happen on the reverse path α_{xy}^{-1} (we do not update x once it is reached). We have also included the sign $\sigma(\{n', k', b'\}_x)$ and $\sigma(\{n, k, b\})$ on the left and right. As the mesonic worm does not touch any baryonic site we have $\sigma(\{n', k', b'\}_x) = \sigma(\{n, k, b\})$.

Now by definition summing over all paths α_{xy} with fixed passive site x and ending at an arbitrary site y , we must have $\sum_{\alpha_{xy}} P(\{n', k', b'\}_x, \alpha_{xy}) = 1$ and therefore

$$\sigma(\{n', k', b'\}_x) W(\{n', k', b'\}_x) \hat{m}^{n'} = \sum_{\alpha_{xy}} \sigma(\{n, k, b\}) \frac{V_D \hat{m} N}{W_D(x)} W(\{n, k, b\}) \hat{m}^n P(\{n, k, b\}, \alpha_{xy}^{-1}), \quad (8.62)$$

where the configuration $\{n, k, b\}$ depends on the configuration $\{n', k', b'\}_x$ and the chosen path α_{xy} . Summing now over all configurations $\{n', k', b'\}_x$, i.e. configurations with “defect” at x , while multiplying with $1/VZ$ yields

$$\begin{aligned} \frac{1}{V} \langle \bar{\chi} \chi_x \rangle &= \frac{1}{VZ} \sum_{\{n', k', b'\}_x} \sigma(\{n', k', b'\}_x) W(\{n', k', b'\}_x) \hat{m}^{n'} \\ &= \frac{1}{Z} \sum_{\{n', k', b'\}_x} \sum_{\alpha_{xy}} \sigma(\{n, k, b\}) \frac{V_D N \hat{m}}{V W_D(x)} W(\{n, k, b\}) \hat{m}^n P(\{n, k, b\}, \alpha_{xy}^{-1}). \end{aligned} \quad (8.63)$$

But on the r.h.s. we can reorder the terms and sum over all configurations $\{n, k, b\}$ and paths α_{xy}^{-1} with arbitrary active starting point y and fixed passive site x to obtain

$$\begin{aligned} \frac{1}{V} \langle \bar{\chi} \chi_x \rangle &= \frac{1}{Z} \sum_{\{n, k, b\}} \sigma(\{n, k, b\}) \frac{\hat{m} N V_D}{V} \left(\sum_{\alpha_{xy}^{-1}} \frac{1}{W_D(x)} P(\{n, k, b\}, \alpha_{xy}^{-1}) \right) W(\{n, k, b\}) \\ &= \frac{1}{Z} \frac{\hat{m} N}{V} \sum_{\alpha_{xy}^{-1}} \sum_{\{n, k, b\}} \sigma(\{n, k, b\}) V_D \frac{1}{W_D(x)} \underbrace{P(\{n, k, b\}, \alpha_{xy}^{-1}) W(\{n, k, b\}) \hat{m}^n}_{(8.64)}. \end{aligned} \quad (8.65)$$

Now take $W_D(x) = 1 = V_D/V$ and $\sigma(\{n, k, b\}) = 1$ for simplicity. The mesonic worm update generates paths α_{xy}^{-1} with probability $P(\{n, k, b\}, \alpha_{xy}^{-1})$ starting from a configuration with weight $W(\{n, k, b\}) \hat{m}^n$. On the practical side, the underbraced term in Eq.(8.65) becomes the Monte-Carlo sampling weight. The sum $\sum_{\{n, k, b\}}$ thus becomes a histogram $I(x, y)$ of events of having the mesonic worm head and tail at x and y , respectively during a Monte-Carlo run. The partition function will receive contributions only when the worm closes. Including now the factors $W_D(x)$, V_D and $\sigma(\{n, k, b\})$, the “histogram” $I(x, y)$ will be updated at every update of a passive site, say x_1 , (let x_2 be the start of the worm) according to

$$I(x, y) = I(x, y) + \sigma(\{n, k, b\}) \frac{V_D}{W_D(x) V} \delta_{x_1, x} \delta_{x_2, y}. \quad (8.66)$$

Summing over all paths α_{xy}^{-1} with arbitrary start y , this then means

$$\frac{1}{V} \langle \bar{\chi} \chi_x \rangle = \hat{m} N \frac{\sum_y I(x, y)}{K_{CP}}. \quad (8.67)$$

Where K_{CP} is the difference of the number of closed paths on configurations with positive and negative sign. We obtain for the chiral condensate of Eq.(8.59)

$$\langle \bar{\psi} \psi \rangle = \hat{m} N \frac{\sum_{x,y} I(x, y)}{K_{CP}} = \hat{m} N \frac{O(\bar{\psi} \psi)}{K_{CP}}, \quad (8.68)$$

where we can define a worm observable $O(\bar{\psi} \psi)$ which is continuously accumulated during the passive worm update of a site z of a configuration C according to

$$O(\bar{\psi} \psi) \rightarrow O(\bar{\psi} \psi) + \frac{\sigma(C)}{W_D(z)} \frac{V_D}{V}. \quad (8.69)$$

8.4.3.2 The 2-pt function $G(x_1, x_2)$

An estimator for the 2-pt function $G(x, y)$ is given by

$$G(x, y) = \frac{\partial^2}{\partial \hat{m}_x \partial \hat{m}_y} \log Z \Big|_{\hat{m}_x = \hat{m}_y = \hat{m}} = \frac{1}{\hat{m}^2} (\langle n_x n_y \rangle - \langle n_y \delta_{x,y} \rangle - \langle n_x \rangle \langle n_y \rangle) \quad (8.70)$$

where $n_{x/y}$ denotes the number of monomers at the site $x(y)$. Going back to Eq.(8.62) we can derive a worm estimator for $G(x_1, x_2)$ by making the masses site dependent. Taking the derivative with respect to \hat{m}_z we obtain

$$\begin{aligned} \sigma(\{n', k', b'\}_x) n'_z W(\{n', k', b'\}_x) \hat{m}^{n'-1} &= \sum_{\alpha_{xy}} \sigma(\{n, k, b\}) \frac{V_D N}{W_D(x)} \delta_{y,z} W(\{n, k, b\}) \hat{m}^n P(\{n, k, b\}, \alpha_{xy}^{-1}) \\ &+ \sum_{\alpha_{xy}} \sigma(\{n, k, b\}) \frac{V_D N}{W_D(x)} W(\{n, k, b\}) \hat{m}_z \hat{m}^n P(\{n, k, b\}, \alpha_{xy}^{-1}). \end{aligned} \quad (8.71)$$

On the l.h.s. we now have a configuration contributing to the 2-pt function $G(x, z)$ as the constraint Eq.(4.11) is now violated at x and z due to the cancellation of the factor n'_z with the same factor in $1/n'_z!$ appearing in $W(\{n', k', b'\}_x)$. Repeating the same steps that lead to Eq.(8.65), we thus obtain

$$\begin{aligned} G(x, z) &= \frac{1}{Z} \sum_{\alpha_{xy}^{-1}} \sum_{\{n,k,b\}} \sigma(\{n, k, b\}) \frac{V_D N}{W_D(x)} \delta_{z,y} P(\{n, k, b\}, \alpha_{xy}^{-1}) W(\{n, k, b\}) \hat{m}^n \\ &+ \frac{1}{Z} \sum_{\alpha_{xy}^{-1}} \sum_{\{n,k,b\}} \sigma(\{n, k, b\}) \frac{V_D N}{W_D(x)} n_z P(\{n, k, b\}, \alpha_{xy}^{-1}) W(\{n, k, b\}) \hat{m}^n \end{aligned} \quad (8.72)$$

During a Monte-Carlo run this can be interpreted as follows: Suppose we have a closed path configuration contributing to the partition function Z . Starting a mesonic worm update on a configuration C at site \tilde{z} (declared active), we accumulate a histogram $I(x, \tilde{z})$ (initialized with

0 at the start) by letting

$$I(x, \tilde{z}) \rightarrow I(x, \tilde{z}) + \sigma(C) \frac{V_D}{W_D(x)} \quad (8.73)$$

every time the worm head visits the passive site x . After the worm closes we can update the observable $O(G(x_1, x_2)) \forall x_1, x_2$ by letting

$$O(G(x_1, x_2)) \rightarrow O(G(x_1, x_2)) + I(x_1, x_2). \quad (8.74)$$

This corresponds to the first term on the r.h.s. of Eq.(8.72) (up to the normalization) and means that $G(x_1, x_2)$ will only receive a contribution if $x_2 = \tilde{z}$ and x_1 was visited during the update. The second term on the r.h.s. of Eq.(8.72) implies that we get another contribution,

$$O(G(x_1, x_2)) \rightarrow O(G(x_1, x_2)) + n_{x_2} I(x_1, \tilde{z}). \quad (8.75)$$

That is, reaching the passive site x_1 during the update (i.e. $I(x_1, \tilde{z}) \neq 0$) which we take as “sink”, all other monomers on the lattice act as sources and should thus contribute to G . Practically we update the observable $O(G(x_1, x_2)) \forall x_1, x_2$ at each passive step. If head and tail are located at x, \tilde{z} , respectively, then

$$O(G(x_1, x_2)) \rightarrow O(G(x_1, x_2)) + \frac{\sigma(C)V_D}{W_D(x)} (\delta_{x,x_1} \delta_{\tilde{z},x_2} + n_{x_2} \delta_{x,x_1}). \quad (8.76)$$

Note that in the chiral limit $n_{x_2} = 0 \forall x_2 \neq \tilde{z}$ and $n_{\tilde{z}} = 1$ by construction. Finally, we obtain $G(x_1, x_2)$ by

$$G(x_1, x_2) = N \frac{O(G(x_1, x_2))}{K_{CP}}. \quad (8.77)$$

Bibliography

- [1] www.bnl.gov/today, How low can rhic go?
- [2] P. de Forcrand, PoS **LAT2009**, 010 (2009), 1005.0539.
- [3] Y. Aoki *et al.*, Nuclear Physics A **830**, 805c (2009), Quark Matter 2009 - The 21st International Conference on Ultrarelativistic Nucleus-Nucleus Collisions.
- [4] M. Cheng *et al.*, Phys. Rev. D **74**, 054507 (2006).
- [5] S. Durr *et al.*, Science **322**, 1224 (2008), 0906.3599.
- [6] J. Berges and K. Rajagopal, Nucl. Phys. **B538**, 215 (1999), hep-ph/9804233.
- [7] M. A. Stephanov, K. Rajagopal, and E. V. Shuryak, Phys. Rev. Lett. **81**, 4816 (1998), hep-ph/9806219.
- [8] J. Kogut and M. Stephanov, *The Phases of Quantum Chromodynamics: From Confinement to Extreme Environments* (Cambridge University Press, 2004).
- [9] F. Karsch and K. H. Mutter, Nucl. Phys. **B313**, 541 (1989).
- [10] N. Kawamoto and J. Smit, Nucl. Phys. **B192**, 100 (1981).
- [11] T. Z. Nakano, K. Miura, and A. Ohnishi, Prog. Theor. Phys. **123**, 825 (2010), 0911.3453.
- [12] P. H. Damgaard, D. Hochberg, and N. Kawamoto, Phys. Lett. **B158**, 239 (1985).
- [13] N. Bilic, F. Karsch, and K. Redlich, Phys. Rev. **D45**, 3228 (1992).
- [14] N. Bilic, K. Demeterfi, and B. Petersson, Nucl. Phys. **B377**, 651 (1992).
- [15] <http://www.gridpp.ac.uk/>.
- [16] <http://en.wikipedia.org/>.
- [17] K. G. Wilson, Phys. Rev. D **10**, 2445 (1974).
- [18] S. Chandrasekharan and U. J. Wiese, Prog. Part. Nucl. Phys. **53**, 373 (2004), hep-lat/0405024.
- [19] H. Georgi, *Lie Algebras In Particle Physics: from Isospin To Unified Theories* (Westview Press, 1999).
- [20] M. Peskin and D. Schroeder, *An Introduction to Quantum Field Theory* (Westview Press, 1995).
- [21] H. B. Nielsen and M. Ninomiya, Phys. Lett. **B105**, 219 (1981).

-
- [22] I. A. Montvay and G. Münster, *Quantum Fields on a Lattice (Cambridge Monographs on Mathematical Physics)* (Cambridge University Press, 1997).
- [23] C. Domb and J. Lebowitz, editors, *Phase Transitions and Critical Phenomena (Vol 9)* (Academic Press, 1984).
- [24] J. Cardy, *Scaling and Renormalization in Statistical Physics* (Cambridge University Press, 2002).
- [25] N. Prokof'ev and B. Svistunov, *Phys. Rev. Lett.* **87**, 160601 (2001).
- [26] R. H. Swendsen and J.-S. Wang, *Phys. Rev. Lett.* **58**, 86 (1987).
- [27] U. Wolff, *Phys. Rev. Lett.* **62**, 361 (1989).
- [28] M. Vettorazzo and P. de Forcrand, *Phys. Lett.* **B604**, 82 (2004), hep-lat/0409135.
- [29] B. A. Berg and A. Bazavov, *Phys. Rev.* **D74**, 094502 (2006), hep-lat/0605019.
- [30] R. B. Potts, *Proc. Cambridge Phil. Soc.* **48**, 106 (1952).
- [31] R. J. Baxter, *Journal of Physics C: Solid State Physics* **6**, L445 (1973).
- [32] F. Y. Wu, *Rev. Mod. Phys.* **54**, 235 (1982).
- [33] B. Nienhuis, A. N. Berker, E. K. Riedel, and M. Schick, *Phys. Rev. Lett.* **43**, 737 (1979).
- [34] J. Salas and A. D. Sokal, *J. Stat. Phys.* **88**, 567 (1997), hep-lat/9607030.
- [35] W. Janke and R. Villanova, *Nucl. Phys.* **B489**, 679 (1997), hep-lat/9612008.
- [36] Y. Shnidman and E. Domany, *Journal of Physics C: Solid State Physics* **14**, L773 (1981).
- [37] K. Binder, *Phys. Rev. Lett.* **47**, 693 (1981).
- [38] K. Binder, *Z. Phys.* **B43**, 119 (1981).
- [39] Y. Iwasaki, K. Kanaya, L. Karkkainen, K. Rummukainen, and T. Yoshie, *Phys. Rev.* **D49**, 3540 (1994), hep-lat/9309003.
- [40] C. Chatelain, P. E. Berche, B. Berche, and W. Janke, *Nuclear Physics B - Proceedings Supplements* **106-107**, 899 (2002).
- [41] P. Rossi and U. Wolff, *Nucl. Phys.* **B248**, 105 (1984).
- [42] R. Aloisio, V. Azcoiti, G. Di Carlo, A. Galante, and A. F. Grillo, *Nucl. Phys.* **B564**, 489 (2000), hep-lat/9910015.
- [43] D. H. Adams and S. Chandrasekharan, *Nucl. Phys.* **B662**, 220 (2003), hep-lat/0303003.
- [44] P. de Forcrand and M. Fromm, *Phys. Rev. Lett.* **104**, 112005 (2010), 0907.1915.
- [45] K. E. Eriksson, N. Svartholm, and B. S. Skagerstam, *J. Math. Phys.* **22**, 2276 (1981).
- [46] S. I. Azakov and E. S. Aliev, *Phys. Scripta* **38**, 769 (1988).
- [47] J. Hoek, *Phys. Lett.* **B102**, 129 (1981).

-
- [48] R. C. Brower and M. Nauenberg, Nucl. Phys. **B180**, 221 (1981).
- [49] F. Karsch and I. O. Stamatescu, Phys. Lett. **B227**, 153 (1989).
- [50] O. F. Syljuasen and A. W. Sandvik, Phys. Rev. **E66**, 046701 (2002).
- [51] N. V. Prokof'ev, B. V. Svistunov, and I. S. Tupitsyn, Physics Letters A **238**, 253 (1998).
- [52] S. Chandrasekharan and F.-J. Jiang, Phys. Rev. **D74**, 014506 (2006), hep-lat/0602031.
- [53] H. Kluberg-Stern, A. Morel, and B. Petersson, Nucl. Phys. **B215**, 527 (1983).
- [54] T. Jolicoeur, H. Kluberg-Stern, M. Lev, A. Morel, and B. Petersson, Nucl. Phys. **B235**, 455 (1984).
- [55] P. de Forcrand and S. Kim, Phys. Lett. **B645**, 339 (2007), hep-lat/0608012.
- [56] O. Martin and B. Siu, Physics Letters B **131**, 419 (1983).
- [57] J. Hoek, N. Kawamoto, and J. Smit, Nucl. Phys. **B199**, 495 (1982).
- [58] O. Martin, Phys. Lett. **B130**, 411 (1983).
- [59] M. F. L. Golterman, Nucl. Phys. **B273**, 663 (1986).
- [60] A. Billoire, R. Lacaze, E. Marinari, and A. Morel, Nucl. Phys. **B251**, 581 (1985).
- [61] T. DeGrand and C. DeTar, *Lattice methods for Quantum Chromodynamics* (World Scientific Pub Co., 2006).
- [62] P. H. Damgaard, N. Kawamoto, and K. Shigemoto, Phys. Rev. Lett. **53**, 2211 (1984).
- [63] P. H. Damgaard, N. Kawamoto, and K. Shigemoto, Nucl. Phys. **B264**, 1 (1986).
- [64] G. Faldt and B. Petersson, Nucl. Phys. **B265**, 197 (1986).
- [65] K. Fukushima, Prog. Theor. Phys. Suppl. **153**, 204 (2004), hep-ph/0312057.
- [66] Y. Nishida, Phys. Rev. **D69**, 094501 (2004), hep-ph/0312371.
- [67] P. de Forcrand, M. D'Elia, and M. Pepe, Phys. Rev. Lett. **86**, 1438 (2001), hep-lat/0007034.
- [68] N. Bilic and J. Cleymans, Phys. Lett. **B355**, 266 (1995), hep-lat/9501019.
- [69] Particle Data Group, C. Amsler *et al.*, Phys. Lett. **B667**, 1 (2008).
- [70] J.D.Walecka, *Theoretical Nuclear and Subnuclear Physics* (Imperial College Press and World Scientific, 2004).
- [71] A. Ohnishi and K. Miura, PoS **LATTICE2008**, 192 (2008).
- [72] M. Fromm and P. de Forcrand, PoS **LATTICE2008**, 191 (2008), 0811.1931.
- [73] M. Fromm and P. de Forcrand, (2009), 0912.2524.
- [74] A. M. Halasz, A. D. Jackson, R. E. Shrock, M. A. Stephanov, and J. J. M. Verbaarschot,

- Phys. Rev. **D58**, 096007 (1998), hep-ph/9804290.
- [75] F. Wang and D. P. Landau, Phys. Rev. Lett. **86**, 2050 (2001).
- [76] G. Boyd, J. Fingberg, F. Karsch, L. Karkkainen, and B. Petersson, Nucl. Phys. **B376**, 199 (1992).
- [77] M. Campostrini, M. Hasenbusch, A. Pelissetto, P. Rossi, and E. Vicari, Phys. Rev. **B63**, 214503 (2001), cond-mat/0010360.
- [78] M. Kolesik and M. Suzuki, Physica A Statistical Mechanics and its Applications **215**, 138 (1995), arXiv:cond-mat/9411109.
- [79] D. J. Amit and V. Martin-Mayor, *Field Theory, the Renormalization Group and Critical Phenomena: Graphs to Computers* (World Scientific Pub Co, 2005).
- [80] S. Chandrasekharan and F.-J. Jiang, Phys. Rev. **D68**, 091501 (2003), hep-lat/0309025.
- [81] K. Binder and D. P. Landau, Phys. Rev. B **30**, 1477 (1984).
- [82] P. Hasenfratz and H. Leutwyler, Nuclear Physics B **343**, 241 (1990).
- [83] C. Borgs and R. Kotecky, J. Stat. Phys. **61**, 79 (1990).
- [84] D. J. Cecile and S. Chandrasekharan, Phys. Rev. **D77**, 014506 (2008), 0708.0558.
- [85] B. B. Beard and U.-J. Wiese, Phys. Rev. Lett. **77**, 5130 (1996).
- [86] J. U. Klatke and K. H. Mutter, Nucl. Phys. **B342**, 764 (1990).
- [87] K. Miura, T. Z. Nakano, A. Ohnishi, and N. Kawamoto, Phys. Rev. **D80**, 074034 (2009), 0907.4245.
- [88] M. Creutz, J. Math. Phys. **19**, 2043 (1978).

List of Figures

1.1	Toy hadrons, BNL QCD phase diagram	1
1.2	Critical line from the lattice	2
2.1	Standard model, Beta decay	5
2.2	A simple lattice	6
2.3	Plaquette $P_{\mu\nu}$ and fundamental link $U_{\hat{\mu}}(x)$	9
2.4	Schematic phase diagram of a metamagnet.	16
2.5	Elementary link update, Potts worm	21
2.6	Sequence of worm update, Potts worm	22
3.1	Expected phase diagram, Potts model, critical exponents	27
3.2	Collapse of probability distributions $P_{N_t,L}(x_e)$, Potts model	29
3.3	Collapse of probability distributions $P_{N_t,L}(x_v)$, $N_t = 20 - 18$, Potts model	30
3.4	Collapse of probability distributions $P_{N_t,L}(x_v)$, $N_t = 17, 16$, Potts model	31
3.5	Surface tension $\sigma_{N_t,L}$ as a function of $1/L$ for $N_t = 16 - 20, 22$, Potts model	32
3.6	Collapse of the spin-spin correlation function $G(r)$, Potts model	33
4.1	Graphical notation, nuclear physics, strong coupling	37
4.2	Example configurations, nuclear physics, strong coupling	39
4.3	Example of an MDP-update, nuclear physics, strong coupling	40
4.4	Results of an exact enumeration, nuclear physics, strong coupling	46
4.5	Comparing worm, HMC and mean-field, nuclear physics, strong coupling	48
4.6	Pion correlator, nuclear physics, strong coupling	50
4.7	Mean-field effective free energy f_{eff} , nuclear physics, strong coupling	53
4.8	Meson masses from worm, HMC and mean-field, nuclear physics, strong coupling	54
4.9	Example of a static baryon and triple dimer loop, nuclear physics, strong coupling	55

4.10	Example of a pair of snake configurations, nuclear physics, strong coupling . . .	56
4.11	Steric effect in $d = 2$, nuclear physics, strong coupling	58
4.12	Determination of $\mu_{B,c}$, nuclear physics, strong coupling	58
4.13	Measuring V_{NN} , nuclear physics, strong coupling	60
4.14	Steric effect with cubes, nuclear physics, strong coupling	61
4.15	Surface tension of nuclear matter, nuclear physics, strong coupling	62
4.16	Masses of nuclei, nuclear physics, strong coupling	63
4.17	Binding energy of nuclei, nuclear physics, strong coupling	64
4.18	Distortion of energy density, $\delta\epsilon$, nuclear physics, strong coupling	66
4.19	Distortion $\delta\epsilon$ for two baryons, nuclear physics, strong coupling	68
5.1	Phase diagram, full QCD, $N_f = 2$, phase diagram, strong coupling	71
5.2	Phase diagram obtained from mean-field theory, phase diagram, strong coupling	73
5.3	Wang-Landau results, phase diagram, strong coupling	75
5.4	Chiral susceptibility χ_σ at T_c , phase diagram, strong coupling	79
5.5	Collapse of $\chi_{\sigma,L}$ at $a\mu = 0.6, 0.64$, phase diagram, strong coupling	81
5.6	Failing Collapse of $\chi_{\sigma,L}$ at $a\mu = 0.66$, phase diagram, strong coupling	81
5.7	Complete chiral phase diagram, strong coupling	82
5.8	Quantifying the sign problem, phase diagram, strong coupling	84
5.9	Schematic massive phase diagram, strong coupling	85
5.10	Collapse of distributions $P(x_M)$, phase diagram, strong coupling	87
5.11	Scaling of CEP, phase diagram, strong coupling	89
6.1	Graphical notation, $N_f = 2$, strong coupling	94
6.2	Sign problem for gauge group $U(3)$, $N_f = 2$, strong coupling	97
6.3	Sign problem gauge group $U(2)$, $N_f = 2$, strong coupling	98
6.4	Introducing new links $\bar{D}D_x\bar{D}D_y$, $N_f = 2$, strong coupling	99
6.5	Resumming link configurations, $N_f = 2$, strong coupling	99
7.1	Example configuration with weight $\sim 1/g^2$, conclusions	102
8.1	Graphical notation, $N_f = 2$, appendix, strong coupling	5

8.2 Resummation trick, appendix, strong coupling 8

List of Tables

2.1	Critical and tricritical exponents of the classical theory.	18
4.1	The sign g_x^D of staggered correlators, nuclear physics, strong coupling	49
4.2	Comparing masses, worm, HMC, mean-field, nuclear physics, strong coupling	57
5.1	$O(2), Z_2$ critical exponents for $d = 3$, phase diagram, strong coupling	77
5.2	Coordinates of critical endpoints, phase diagram, strong coupling	87
8.1	Group invariants of gauge group $U(N), SU(N)$, appendix, strong coupling	1

Acknowledgments

First and foremost I would like to thank my supervisor Philippe de Forcrand for suggesting this conceptually interesting topic to me. His intuition and tireless curiosity for the world “at finite density” have fueled the work from the beginning to the very end. I am also indebted to Matthias Troyer for his efficiency and his group, in particular Evgeny Kozik for physics related discussions. Similarly, Peter Anders and Christian May should be thanked for providing my officemates and me with their interpretation of Bobby McFerrin’s “Don’t worry, be happy.” Urs Wenger deserves special thanks for helping with the start at ETH and giving advise on both, physics and the Swiss administration.

I particularly enjoyed the discussions with my officemates, Marco Panero and Aleksi Kurkela. Marco’s profound knowledge, experience and curiosity on the scientific side but also his “Bioladen”-stories — numerous as they were — on the side of non-physics entertainment have contributed to the atmosphere in the office. Not to lesser extent did Aleksi assist to make the office our “home”. In particular, his relentless striving for clarity when it came to physics related questions, which was only matched in its scale by his consumption of coffee, provided constant fuel for an inspiring atmosphere.

A deep thanks goes of course to the staff of the institute of theoretical physics, especially Irene Urbanetti who with her efficiency and humor helped getting through the every day duties at the institute.

Without the constant support of my family progress would have been hardly possible. Born at the beginning of our time here in Zurich, we have seen our son growing up to be now a proud 3-year old, sparkling of life and tirelessly playing. Isa, I thank you for your loving support and for having tolerated my inclination to late working hours. Finally, I am grateful to my parents who have always encouraged me in my decisions.

Curriculum Vitae

Personal Data

- **Name:** Michael Fromm
- **Date of Birth:** 13.03.1981
- **Place of Birth:** Lübben, Germany
- **Nationality:** German

Education

- 06/2007-09/2010: Ph.D. student at ETH Zurich, advisors Dr. Ph. de Forcrand (CERN and ETH Zurich) and Prof. Dr. M. Troyer (ETH Zurich), Ph.D. thesis on “Lattice QCD at strong coupling: thermodynamics and nuclear physics”
- 01/2006-01/2007: Diploma thesis at Eberhard-Karls-University, Tübingen, Germany, advisors Prof. Dr. H. Reinhardt (Tübingen) and Dr. K. Langfeld (Tübingen), title “ $SU(2)$ projection of $SU(3)$ gauge theory”
- 10/2000-01/2007: Eberhard-Karls-University, Tübingen, Diploma studies in physics
- 09/2003-06/2004: University of Washington, Seattle, USA, studies in physics within an exchange program
- 08/1991-07/1999: High School, Staatliches Gymnasium, Heilbad Heiligenstadt, Germany

Publications

Refereed Journal Articles

- P. de Forcrand and **M. Fromm**, “Nuclear Physics from lattice QCD at strong coupling” Phys. Rev. Lett. 104, 112005, (2010) [arXiv:0907.1915 [hep-lat]].

Conference Proceedings

- **M. Fromm** and P. de Forcrand, “Nuclear Physics from strong coupling QCD” PoS LATTICE2009, (2009) [arXiv:0912.2524 [hep-lat]].
- **M. Fromm**, “Chiral restoration of strong coupling QCD at finite temperature and baryon density” Nucl. Phys. A 820, 179C (2009).
- **M. Fromm** and P. de Forcrand, “Revisiting strong coupling QCD at finite temperature and baryon density” PoS LATTICE2008, (2008) [arXiv:0811.1931 [hep-lat]].